POLITECNICO
MILANO 1863

PhD Program in Mathematical Models and Methods in Engineering

Mathematical and numerical models for the fluid dynamics of the human heart

Doctoral dissertation of: **Alberto Zingaro**

Advisor: Prof. Alfio Quarteroni
Co-advisor: Prof. Luca Dede'
Chair of the PhD Program: Prof. Irene Sabadini

XXXIV cycle, February 2022

Abstract

Computer-based numerical simulations – also known as in silico simulations – of the heart and blood circulation represent a valuable tool to analyze the cardiac function and to enhance the understanding of cardiovascular diseases. In this thesis, we introduce a Computational Fluid Dynamics (CFD) approach for the numerical simulation of the whole heart hemodynamics in both physiological and pathological conditions, by accounting for all the physical processes that influence cardiac flows: moving domain and interaction with electromechanics, transitional-turbulent flows, cardiac valves and coupling with the external circulation.

We propose a volume-based displacement model for the left atrium in physiological conditions and we simulate the atrial hemodynamics by considering both idealized and patient specific-geometries. A lumped-parameter (0D) closed-loop circulation model serves as input to provide the CFD simulations with flowrates, pressures and atrial displacement. We further extend the computational model to account for atrial fibrillation in patient-specific CFD simulations by devising a parametric displacement field. We investigate the effects of atrial fibrillation on the left atrium hemodynamics and we quantify an increasing blood stasis, especially in the left atrial appendage, where a dramatic washout reduction is observed.

The transitional blood flow regime is simulated by means of the Variational Multiscale - Large Eddy Simulation (VMS-LES) method, which acts as both a stabilization and a turbulence model. We investigate the role of the VMS-LES method in transitional hemodynamic flows by considering the atrial CFD simulation in physiological conditions: if relatively coarse meshes are used, numerical results suggest that the additional stabilization terms introduced by the VMS-LES method allow to better predict transitional effects and cycle-to-cycle blood flow variations than the standard Streamline Upwind Petrov Galerkin (SUPG) method. To enhance the accuracy of the stabilization methods, we propose a novel computational strategy based on Artificial Neural Networks (ANNs) to predict the optimal stabilization parameter. Numerical tests carried out on the SUPG method for advection-diffusion problems show that the ANNs-based approach leads to more accurate solutions than standard methods.

We simulate the hemodynamics of the left heart and we integrate the electromechanical activity in the CFD model by employing a 3D cardiac electromechanical model of

the left ventricle coupled to a 0D circulation model. We propose a novel preprocessing procedure that combines the harmonic extension of the ventricular electromechanical displacement with the motion of the left atrium based on the 0D model. To better match the 3D CFD with the remaining blood circulation, we devise a coupled 3D-0D model made of the 3D CFD model of the left heart and the 0D circulation model: from a numerical point of view, we solve the coupled model by a segregated scheme, and we develop algorithms to solve the integrated system comprising fluid dynamics, displacement, valves and circulation models. Numerical simulations on a healthy left heart show that biomarkers and flow patterns are accurately reproduced when compared with in-vivo data; the flexibility of the model allows to simulate also pathological scenarios as mitral valve regurgitation. We then expand our computational model to the hemodynamics of the four heart chambers: the displacement field is computed through a biventricular electromechanical simulation and then extended on the whole heart following the same methodology proposed for the left part, finally bringing to an integrated multiscale CFD model of the whole human heart.

Key-words: In-silico models, heart, cardiac hemodynamics, cardiac valves, circulation, transitional flows, atrial fibrillation, mitral valve regurgitation, computational fluid dynamics, variational multiscale, large eddy simulation, stabilization methods, multiscale models, finite element method.

This PhD Thesis has been supported by the ERC Advanced Grant iHEART, "An Integrated Heart Model for the simulation of the cardiac function", 2017–2022, P.I. A. Quarteroni (ERC-2016-ADG, project ID: 740132).

«Colui che volse il sesto
a lo stremo del mondo, e dentro ad esso
distinse tanto occulto e manifesto, ... »

Dante Alighieri
Paradiso, Canto XIX

Contents

1 | Introduction

The study of cardiac blood flow aims at enhancing the knowledge of the heart physiology, assessing the pathological conditions, and possibly improving clinical treatments and therapeutics. In the clinical routine, blood flow analysis is conventionally assessed through imaging and experimental techniques, sometimes relying on a contrast medium to improve the clarity of the images acquired. In diagnostic procedures, the gold standard for the assessment of the cardiac function is cardiac magnetic resonance (CMR) imaging, by which the patient-specific geometry and motion of the heart can be reconstructed [140]. To analyze the blood flows, color Doppler echocardiography [104, 143] provides measurements of blood velocity in specific directions, such as normally to the plane of a valve; whereas a particular phase-contrast magnetic resonance imaging technique called 4D flow MRI (Magnetic Resonance Imaging) provides time-dependent flow data in the three spatial directions [166]. However, the space and time resolution of these techniques is not accurate enough to capture small scales features as recirculation regions, possibile regions of transition to turbulence and small coherent structures [180]. Moreover, standard imaging techniques cannot provide relevant fluid dynamics indicators such as wall shear stress (WSS), turbulent kinetic energy dissipation or the oscillatory stress index, which are correlated with the function and remodeling of the heart and vessels [51, 124, 180, 213, 288]. On the other hand, computer based numerical simulations – also known as in silico simulations – of the heart stand as a valuable tool to analyze the cardiac function and to deepen our understanding of cardiovascular diseases. Specifically, patient-specific numerical simulations can provide clinicians with quantitative information that might be helpful to support decision making [48, 218].

The objective of this thesis is to develop a Computational Fluid Dynamics (CFD) model of the whole human heart comprising all the main features impacting on cardiac flows. We propose a CFD model of the left atrium (LA) hemodynamics by considering either idealized and patient-specific geometries. We extend the computational model to account for atrial fibrillation (AF) by means of a lumped-parameter closed-loop model of the blood circulation. We analyse the effect of stabilization methods-turbulence models in transitional cardiac flows and we then propose a novel computational strategy based on Artificial Neural Networks (ANNs) to predict the optimal stabilization parameter involved in the formulation of stabilization methods. We devise a multiphysics and

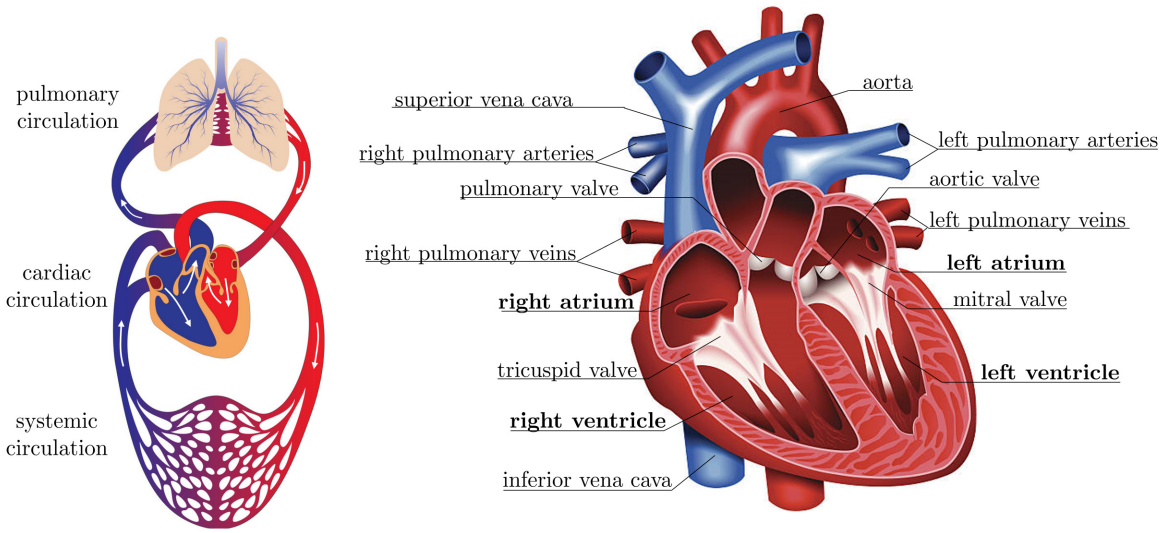

Figure 1.1: Blood circulation and heart anatomy.

multiscale CFD model of the left heart (LH), in which the displacement is driven by a 3D cardiac electromechanics (EM) model of the left ventricle (LV) coupled to the remaining circulation described by the 0D model. We account for the atrial motion by introducing a novel preprocessing strategy that combines the extension of the LV displacement on the whole LH geometry and a volume-based displacement model of the LA. We couple our 3D CFD model of the LH to the surrounding circulation and we solve the multiscale 3D-0D problem by means of a segregated numerical scheme. We carry out numerical simulations on a healthy heart and we show that the computational model can predict and reproduce biomarkers and flow patterns characterizing the LH hemodynamics. We then cover the pathological scenario of mitral valve regurgitation. Eventually, we extend our multiphysics and multiscale computational model to the whole human heart.

In Section 1.1, we briefly describe the cardiac function and the physiology of heart hemodynamics. Section 1.2 is devoted to illustrate the main challenges characterizing cardiac flows from a computational point of view and to recall the main modeling paradigms adopted in the scientific community. Finally, in Section 1.3 we present the outline of the thesis.

1.1. Physiology of cardiac blood flows

The heart is composed of two sides, the left (LH) and the right (RH) part and it is linked to the pulmonary and systemic blood circulation as displayed in Figure 1.1. Each side is made of two chambers: the atria (LA, RA) and the ventricles (LV, RV). The blood coming from the systemic circulation is pushed in the RA through the venae

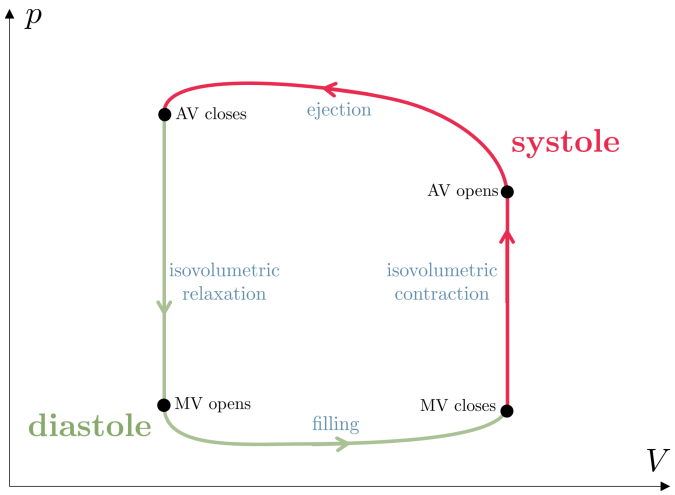

Figure 1.2: Pressure-volume loop of the LV.

cave (inferior and superior) and it fills the RV; the deoxygenated blood is then pushed towards the lungs through the pulmonary artery to pick up oxygen and get rid of carbon dioxide. The oxygenated blood coming from the lungs (pulmonary circulation) flows in the LA through the pulmonary veins (left and right) and it fills the LV; the latter pushes the blood in the systemic circulation through the aorta. The heart is made of four valves: the mitral valve (MV) separates the LA from the LV; the aortic valve (AV) the LV from the aorta. On the right side of the heart, the tricuspid valve (TV) separates the RA from the RV and the pulmonary valve (PV) the RV from the pulmonary artery.

The heart function is the result of the interplay among several physical processes that take place at different spatio-temporal scales. The contraction of the cardiac muscle – which produces the ejection of the blood in the external circulation – is caused by the intracellular mechanical activation that causes the shortening of the muscle fibers. The latter are triggered by an electric wave propagating throughout the tissue (action potential). The interplay between the electrophysiology (that drives the action potential) and the mechanics (both passive and active) is commonly referred to as electromechanical activity of the heart [106, 132, 134, 187].

The heart cycle is made of two phases: systole and diastole. The former corresponds to the contraction phase of the ventricles and can be split in the isovolumetric contraction and the ejection phase; the diastole is made of the isovolumetric relaxation and the filling stage. We display in Figure 1.2 the pressure–volume (pV) loop of the LV, which links the pressure p with the volume V of the blood in the cavity under examination. By considering the LV (analogous description is valid for the RV), during the isovolumetric contraction, both the valves (MV and AV) are closed, the pressure increases and the ventricular volume remains constant. When the LV pressure overcomes the systemic arterial pressure, the AV opens: the ejection phase starts and the ventricular volume

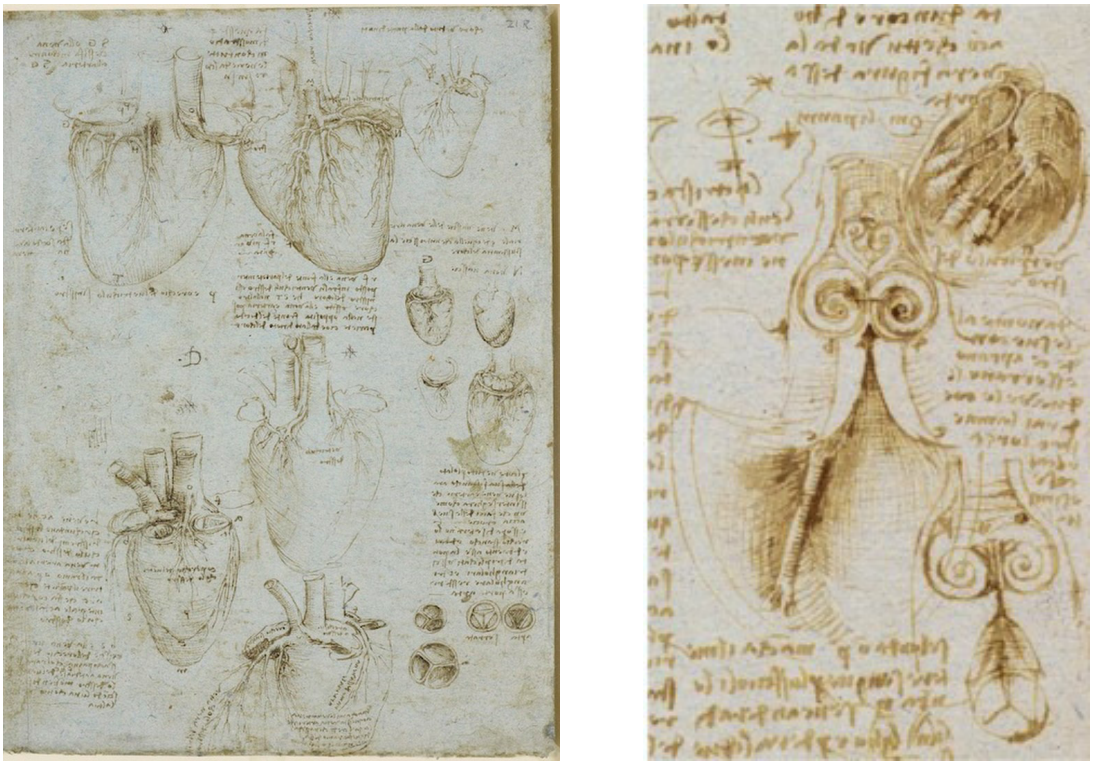

(a) (b)

Figure 1.3: Leonardo da Vinci's drawings on his studies on the heart anatomy and the blood motion in the human body: (a) study on the coronary vessels and cardiac valves; (b) vortices formation downwind the AV. Credit: The Royal Collection, Her Majesty Queen Elizabeth II.

decreases. The ejection phase ends with the closing of the AV, and this moment marks the beginning of the isovolumetric relaxation in which both valves are closed and the intraventricular pressure decreases. As the MV opens, the filling phase starts: the pressure in the LA overcomes the ventricular one, the blood flows from the LA to the LV and the ventricular volume increases. The phase ends with the closing of the MV and a new cycle starts [132, 134, 187].

We recall the definition of the Reynolds number as

$$\mathrm{Re} = \frac{\rho U L}{\mu}, \tag{1.1}$$

being ρ and μ the fluid density and kinematic viscosity respectively; U and L the characteristic velocity and characteristic length respectively. At low Reynolds number, the flow is laminar; on the contrary, when the Reynolds number increases, the inertial forces become predominant with respect to the viscous ones and the flow is said to

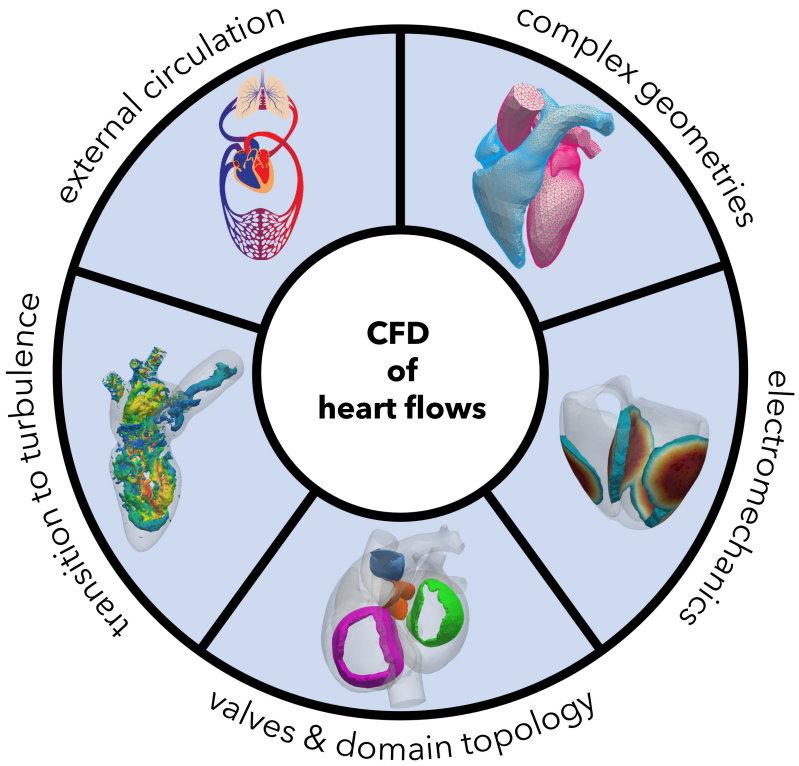

Figure 1.4: Main challenges of CFD of heart flows.

be turbulent. During the heart cycle, the Reynolds flow regime continuously changes due to a cyclic production and dissipation of energy. An open issue in the blood fluid dynamics is whether a transition to turbulence occurs whenever the blood velocity increases and the interactions among vortices are strong. Back in the 16^{th} century, Leonardo da Vinci already guessed through experiments the presence of vortices downwind the AV in his study on the blood motion in the human body (see Figure 1.3) [142]. During systole, in normal subjects the peak Reynolds number downwind the AV is about 8′000 and it can become even higher in pathological conditions as aortic stenosis [241].

1.2. Fluid dynamics modeling of heart flows

In the last decades, the role of mathematical models in the study of cardiac hemodynamics has increasingly gained relevance, for their non-invasiveness and flexibility with respect to geometries and flow conditions [51, 67, 100, 139, 170, 248, 249, 258–260, 272]. CFD is largely employed to provide a fully detailed description of cardiac flows and to estimate hemodynamic indicators as the WSS that standard image-based techniques might not capture.

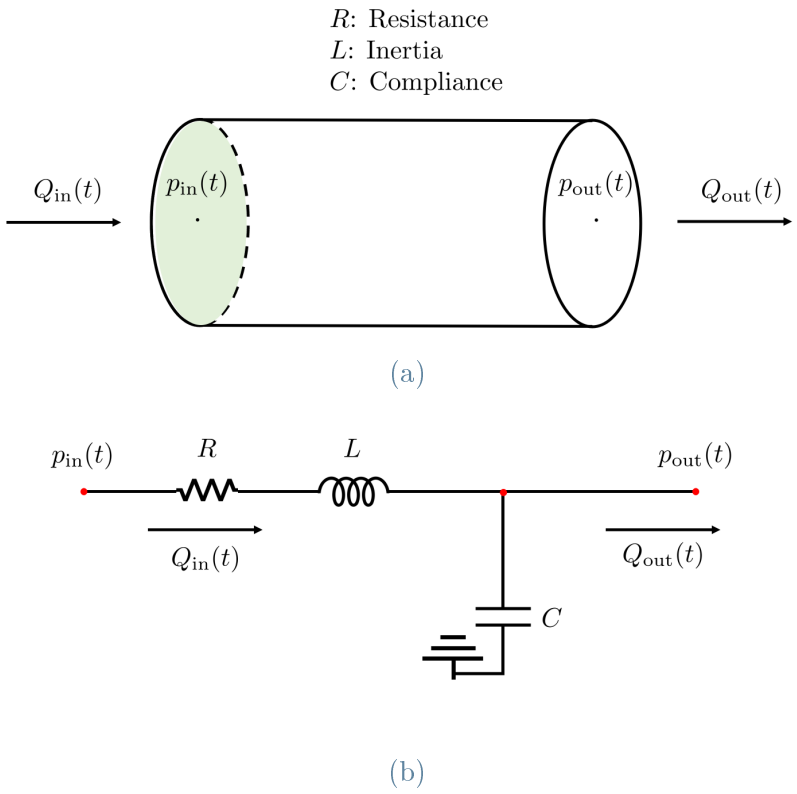

Figure 1.5: Analogy between blood vessel and electrical circuit adopted in the lumped-parameter representation on the cardiovascular system.

The numerical simulations of cardiac blood flows should account for several aspects that characterize heart's hemodynamics. As a matter of fact, the mathematical problem is defined in complex geometries and there exists a strong interaction between the fluid and the structure due to the electromechanical activity of the heart. This yields a complex coupled problem involving several processes: electrophysiology, mechanics and fluid dynamics. Furthermore, the domain changes its topology during the heartbeat due to the presence of cardiac valves, whose presence also affects the dynamic of the intracardiac flow itself. In addition, the blood flow regime is known to be neither laminar, nor fully turbulent but rather transitional [39, 269, 271, 291]. Among several challenges of modeling cardiac flows, it should also be mentioned the strict coupling of the heart's flow with the blood flow of the surrounding circulatory system (pulmonary and systemic circulation). We summarize the main challenges characterizing heart's fluid dynamics modeling in Figure 1.4. In the following, we cover all these aspects showing possible modelling choices adopted by the scientific community.

To model heart fluid dynamics, several mathematical models have been adopted, with different levels of complexity. On the one hand, *lumped-parameter* models [37, 105, 123, 191, 224, 239] consist in reduced models that are well suited to provide quick in-

formation about the whole cardiovascular system. A lumped-parameter approximation of the cardiovascular system brings to 1D or 0D models. With the latter we refer to models where the dependence of the spatial coordinates is completely neglected, and hence uniform spatial distribution of pressures and flowrates in a specific compartment is assumed [211, 238]. Moreover, as we display in Figure 1.5, 0D models establish an analogy among the fluid dynamics of the vessels (and the heart chambers) with the electrical components of an electric circuit, and they are described by sets of ordinary differential equations (ODEs). However, even if these models are suitable to quickly provide macroscopic information of fluid properties, they do not provide local details on the flow as the spatial distribution of velocity, pressure and all derived quantities commonly of interest from an hemodynamic view point, as the wall shear stress (WSS).

On the other hand, 3D CFD models can provide a fully detailed description of cardiac flows with a higher computational cost. Specifically, in large vessels, as well as in the heart chambers, blood can be regarded as a Newtonian incompressible fluid despite the presence of small particles suspended and carried by the plasma. Thus, heart flows can be modelled with the incompressible *Navier-Stokes* (NS) equations [198, 213, 252, 253]. A critical issue in 3D cardiovascular hemodynamics modeling is however the prescription of boundary conditions (BCs) at inlet and outlet sections. Since boundary data are generally unavailable (indeed, inlet and outlet boundaries are not real, they have just set for computational purposes), a possible approach is the one called *geometric multiscale modeling* [211]. The specific region of interest (a vessel or a heart chamber) is represented by a 3D model, while the remaining part of the circulation is addressed by means of lumped-parameters models as 0D [37, 144, 174, 211, 237] or 1D [91, 92, 211, 263] models. Different coupling strategy can be devised ensuring continuity of pressures and flowrates on the "artificially chopped" boundaries of the 3D domain.

A key aspect in heart CFD simulation is the modeling of the cardiac valves. They can be treated in principle by considering a (3D or 2D) structural models for the solid (leaflets of the valve and possibly its chordae tendinae) and a fluid dynamics model for the surrounding blood flow. This approach yields a coupled system commonly denoted as *Fluid-Structure-Interaction* (FSI) problem. The coupling conditions at the interfaces of the two problems are the continuity of the velocity (kinematic condition: perfect adherence between particles of fluid and the structure), the third Newton's law (dynamic condition: the forces exerted by the fluid on the interface must be compensated by the structural forces) and the perfect adherence between the fluid and the structure geometries (geometric conditions). Several works concern FSI simulations of cardiac valves [47, 65, 103, 154, 159, 244] and we can group them into four main categories [86]: models based on the *Arbitrary Lagrangian Eulerian* (ALE) formulation (see Section 4.1) [49, 50, 167]; the *Immersed Boundary* (IB) method [29, 111, 200]; the *Fictitious Domain* (FD) method [65, 265] and formulations which mix the aforementioned methods [138, 157]. In methods based on the ALE formulation, the conservation laws of the FSI problem are recast in an arbitrary reference framework; it was introduced in

[76] and developed in an attempt to combine the advantages of the Lagrangian (commonly used in structural mechanics) and Eulerian (commonly used in fluid dynamics) approaches. Differently, the main idea behind IB methods – originally developed by C. Peskin in the context of cardiac valves [199], and inspired by the pioneering work [270] – is to immerse the structure in the fluid and to account for the solid deformation by introducing a forcing term which models the forces exerted on the fluid. Differently from the ALE method, the fluid mesh is not deformed since an Eulerian framework is still employed, thus problems as mesh smoothing or remeshing (characterizing instead the ALE method) are avoided. However, the indirect representation of the structure in the fluid domain brings to a loss of accuracy compared to the ALE method [122, 201]. Similarly to IB, in the FD method the structure and fluids are expressed in Lagrangian and Eulerian frameworks respectively, and they are discretized independently. The method is introduced in [109], and the coupling conditions are enforced by means of Lagrange multipliers. FSI models are characterized by a huge computational burden to be added to the overall cost of the heart CFD simulation. In this respect, the effects of the valves in the blood can be mimicked by considering the valves as *immersed surfaces* inside the fluid domain [25, 67, 86, 87, 100, 259] or as *mixed-time varying BCs* [249, 291] in the case of single chambers numerical simulations. We use both methods in this thesis; specifically, for the case of multiple chambers study, we employ the *Resistive Immersed Implicit Surface* (RIIS) method [86, 100]. This method is inspired by the *Resistive Immersed Surface* (RIS) method: introduced in [87] to model a porous medium in a fluid, and then applied to cardiac valves in [25, 259]. The RIIS method was introduced in [86] and then extended in [100] to model the systolic anterior motion of the MV. It lays in the class of IB-FD methods, and it allows to account for a moving immersed surface in an Eulerian framework without requiring the use of a surface-conforming mesh.

An additional key point in 3D CFD models is how to treat boundary displacement since it drives the blood motion in heart chambers. Boundary displacement can be accounted for in the CFD simulation mainly according to two paradigms: FSI problems and CFD simulations with prescribed motion. In the following we describe the two approaches, summarizing the main pros and cons.

1. FSI problems: the myocardium motion is modelled via an *electromechanics* (EM) model and the blood flow via a fluid dynamics model, with the enforcement of kinematic, dynamic and geometric coupling conditions at the interface between the blood and the myocardium. This approach gives rise to a coupled problem, with the disadvantage of a higher computational effort compared to the second paradigm (see e.g. [52, 106, 272–274]). For instance, a complete FSI model of the LH requires about 48 hours to simulate a whole heartbeat on 192 cores (M. Bucelli, private communication and [44]).

2. CFD simulations with prescribed displacement: the influence of the cardiac walls motion can be prescribed either using analytical laws [27, 67, 75, 235, 247, 248,

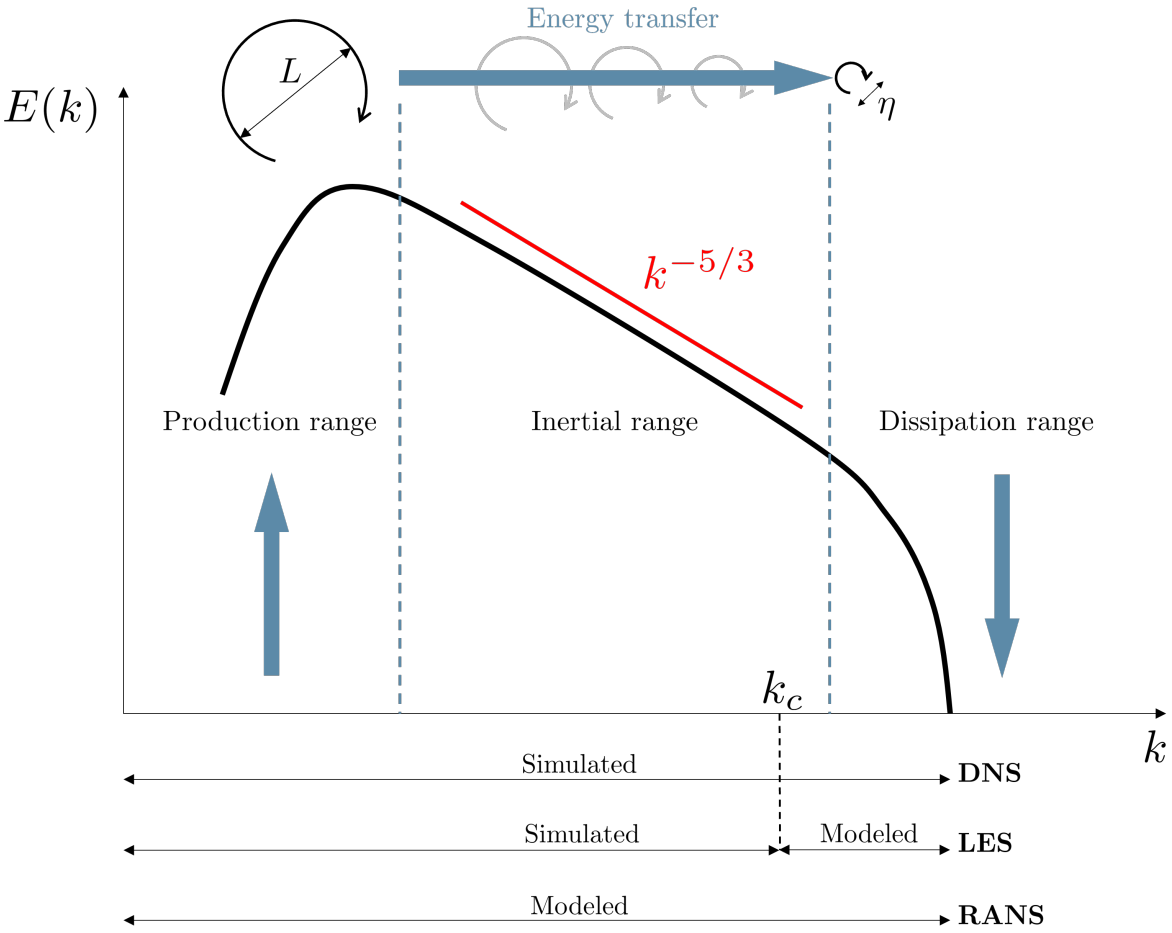

Figure 1.6: Energy cascade of turbulence; scales simulated and modeled by different turbulence models.

289, 291], by patient-specific image-based reconstructions [51, 100, 168–170, 260], or via the displacement field computed from a previous EM simulation [26, 139, 258, 259]. The latter corresponds to a "one-way coupled" approach between EM and CFD, since a kinematic coupling only is enforced, without any dynamic feedback from the fluid dynamics to the structural problem. One may refer to this approach also with the expression "kinematic uncoupling" [258, 259].

As highlighted in Section 1.1, an additional feature characterizing cardiac (and cardiovascular) flows is the blood Reynolds regime that changes during the cycle ranging from laminar, transitional and turbulent. In Figure 1.6, we display the energy cascade of turbulence which puts in relation the energy contained by eddies $E(k)$ with the wavenumber k. Turbulent flows are characterized by a full spectrum of energies and spatio-temporal scales, and the energy is transferred from the largest scale to the smallest ones [28, 205, 279]. In the production range, the energy is injected in the system due to BCs and forcing term (which may cause gradients in the flow). We found the largest

eddies in the production range, characterized by the largest part of energy associated; the length of these eddies can be directly associated to the characteristic length of the problem L and their characteristic velocity U. On the contrary, the smallest eddies are located in the dissipation range, and it is where the viscosity and the dissipation D play a major role. In the inertial range, the energy transfers from the largest to the smallest eddies and, by denoting with η the smallest (or Kolmogorov) length scale, Kolmogorov showed that the relation among the two lengths can be expressed in terms of the Reynolds number as [148]:

$$\frac{\eta}{L} = Re^{-3/4}. \tag{1.2}$$

From a numerical viewpoint, Equation (1.2) shows an important result: by discretizing each spatial direction with n equally–spaced points of size h (such that $L = (n-1)h$), the following number of grid points are required to simulate all the possible spatio–temporal scales involved in a turbulence field:

$$n^3 \sim Re^{9/4}. \tag{1.3}$$

A *Direct Numerical Simulation* (DNS) explicitly solves all the scales involved, requiring hence the spatial resolution in Equation (1.3). Analogous considerations can be done for the temporal scales, for which we refer the reader for instance to [28, 228, 279]. By considering the case of the LV, where approximately a peak of $Re = 8'000$ can be estimated on its outlet section (systolic peak), Equation (1.3) would require $n^3 \sim 6 \cdot 10^8$ and hence 2.4 billions of degrees of freedom (DOFs) for the spatial discretization of the incompressible NS equations ($\#\text{DOFs} = 4n^3$). This simple example clearly shows that the spatial and temporal resolutions required to fully capture the details of the flow features through a DNS for the discretized NS equations would require prohibitive computational resources [279]. For this reason, a turbulence model is usually employed, like e.g. the *Reynolds-Averaged Navier-Stokes equations* (RANS) and the *Large Eddy Simulation* (LES) [107, 171, 205, 279]. In RANS models, one solves for an average flow field in which only the large scale eddies containing the highest energy are considered, while the effect of the inertial range and of the fine-scales is accounted by an extra term, called Reynolds stress, to be added to the momentum balance equation of the NS equations [205, 279]. When using isotropic models, the overall effect of the Reynolds stress term is to increase the viscosity of the fluid with a turbulent viscosity that is added to the physical one. RANS models may become too dissipative and yielding unrealistic flows when used in transitional or even laminar conditions, being thus not very appropriate for the cardiac flows. On the other hand, LES models aim at explicitly solving the large eddies of the flow by reaching the inertial range, while modeling the effect of the smallest eddies by exploiting self-similarity properties of the flow [205, 279]. As displayed in Figure 1.6, LES models are based on a scale separation at a certain cutoff wavenumber k_c: all the scales below k_c are modeled by means of subgrid-scale

models which account for the effects of the fine-scales (modeled) on the coarse one (resolved) [28, 228]. The general idea behind LES models can be summed up in three main steps: splitting of the small by the large scales through a filtering procedure bringing to "filtered" NS equations; modeling of the small scales inside the filtered NS equations; numerical solution of the "modeled filtered" NS equations. Examples of LES models for cardiac and cardiovascular flows can be found in [51, 67, 156, 181, 242, 268].

In 2000, the LES formulation was developed from the *Variational Multiscale* (VMS) method by T.J.R. Hughes et al. [126]. The main idea was to use variational projections (at the basis of the VMS method) instead of classing filtering techniques and hence to avoid many of the drawbacks commonly associated to filters (see [31, 126]). Specifically, by considering a generic differential problem in the unknown u, the VMS method assumes a direct sum decomposition of the solution in a coarse and fine-scale solution as

$$u = u^h + u', \tag{1.4}$$

where the coarse-scale u^h is directly associated to the numerical discretization of the problem (and belonging thus to a finite dimensional space) and the fine-scale u', originally belonging to an infinite dimensional function space, is then modelled in terms of u^h. Thus, the modeling side inside these methods is bounded only on the way fine-scale terms are approximated. Furthermore, LES models based on VMS formulation, that we will denote from now on as VMS-LES methods, allow to obtain a solution inf-sup stable, free of numerical instabilities (due to a possible advection dominated regime) and contextually yielding a LES model [31, 125, 127, 127, 129, 130].

Literature is abundant concerning the fluid dynamics of the whole circulatory system, the study of heart valves, specific arteries and biomedical devices [97, 149, 150, 163, 182, 212, 213, 277, 287]. By far, the most studied part of the heart is the left part [67, 272–274], in particular the LV, that has been considered from the electromechanical and fluid dynamical viewpoints, both for idealized and patient-specific data [96, 163, 235, 236, 246, 247, 249, 289]. Compared to the LV, the LA is far less investigated, at least in normal conditions [70, 147, 168–170, 266]. Few works concern the CFD simulation of the RH and many of them are devoted the hemodynamics of the RV [58, 162, 280]. At the best of our knowledge, CFD simulations of the whole heart have been addressed so far only in the following three works:

1. In [172] a whole heart CFD model is proposed by the Siemens group. The displacement is obtained by patient-specific image based reconstructions and the mathematical problem is solved in a level-set framework [189]. However, since the left and right sides were not connected to the circulation, they performed simulations separately on the left and right part.

2. In [185], it is reported an FSI simulation of the whole heart through the UT-Heart simulator developed at the University of Tokyo.

3. FSI simulations of the whole heart have been performed in the context of the

Living Heart Project [7] through the FlowVision software in [190].

1.3. Organization of the PhD thesis

This thesis is organized in two parts: Part I is devoted to the presentation of the mathematical models and numerical methods for the description of transitional and turbulent flows; in Part II we consider the CFD of blood flows in the human heart.

Part I: *Numerical methods for transitional and turbulent flows.*

- In Chapter 2, we introduce the approximation of the incompressible NS equations in a fixed domain, the VMS-LES method and we verificate and validate the latter on two benchmark problems for turbulent flows. Specifically, we consider the Taylor-Green Vortex for the verification, and the nozzle test proposed by Food and Drug Administration for the validation.
- In Chapter 3, we present a novel computational method to predict the optimal parameters involved in stabilization methods by means of machine-learning algorithms [176]. Specifically, we limit ourselves to the simpler case of the SUPG method for the advection-dominated advection diffusion problems.

Part II: *Application to the cardiac problem.*

- Chapter 4 is devoted to the computational model we employ to simulate the fluid dynamics of heart: we present the NS equations in ALE framework with RIIS modeling of valves. We then apply the VMS-LES method to this mathematical model.
- In Chapter 5, we propose a computational model of the LA. We first consider an idealized geometry in physiological conditions and we investigate the role of VMS-LES on transitional flows. We further extend the computational model to patient-specific geometries and we study the effects of atrial fibrillation on the LA hemodynamics.
- In Chapter 6, we devise a novel a computational model of the left heart driven by the electromechanics model coupled to the external circulation. We cover both the physiological case and the pathological case of mitral regurgitation.
- In Chapter 7, we extend the previous model to the whole heart, introducing finally a complete CFD model of the whole human heart.

Conclusions and further developments follow in Chapter 8.

Part I

Numerical methods for transitional and turbulent flows

2 Mathematical models and numerical methods

In this chapter, we introduce the mathematical models and the numerical methods we use for the description of transitional and turbulent flows. Specifically, in Section 2.1, we recall the incompressible NS equations, and in Section 2.2 its weak formulation. In Section 2.3 we present the VMS-LES method, and in Section 2.4 the time discretization scheme employed along with methods for non-linearities. In Section 2.5, we provide a compact formulation along with details on the implementation of the numerical scheme and resolution of the linear system arising from. Section 2.6 is devoted to the validation and verification of the VMS-LES method on turbulence benchmarks. Eventually, in Section 2.7 we draw our concluding remarks.

2.1. The Navier-Stokes equations

Let $\Omega \subset \mathbb{R}^d$ be the spatial fluid domain, with $d = 2, 3$ the dimension, provided with a sufficiently regular boundary $\Gamma \equiv \partial\Omega$, with $\boldsymbol{n}$ the outward directed pointing normal unit vector. We denote as Γ^D and Γ^N the portions of the boundary where respectively Dirichlet and Neumann type BCs are prescribed, with $\Gamma = \overline{\Gamma^D} \cup \overline{\Gamma^N}$ and $\overset{\circ}{\Gamma}{}^D \cap \overset{\circ}{\Gamma}{}^N = \emptyset$. Let $(0, T_f)$ be the time domain, with T_f the final time. We consider a fluid of constant density ρ and, by denoting with $\boldsymbol{u} : \Omega \times (0, T_f) \to \mathbb{R}^d$ the fluid velocity field and $p : \Omega \times (0, T_f) \to \mathbb{R}$ the pressure field, the incompressible NS equations read:

$$\rho\left(\frac{\partial \boldsymbol{u}}{\partial t} + (\boldsymbol{u} \cdot \nabla)\,\boldsymbol{u}\right) - \nabla \cdot \boldsymbol{\sigma}(\boldsymbol{u}, p) = \boldsymbol{f} \qquad \text{in } \Omega \times (0, T_f), \tag{2.1a}$$

$$\nabla \cdot \boldsymbol{u} = 0 \qquad \text{in } \Omega \times (0, T_f). \tag{2.1b}$$

Equation (2.1a) is the momentum balance equation. In the first term of Equation (2.1a), $\dfrac{\partial \boldsymbol{u}}{\partial t}$ is the unsteady term and $(\boldsymbol{u} \cdot \nabla)\boldsymbol{u}$ the non-linear convective term.

They can also be expressed through the total derivative in an Eulerian framework as

$$\frac{D\boldsymbol{u}}{Dt} = \frac{\partial \boldsymbol{u}}{\partial t} + (\boldsymbol{u}\cdot\nabla)\boldsymbol{u}. \tag{2.2}$$

The second term in Equation (2.1a) is the divergence of the total (Cauchy's) stress tensor. The latter is defined as the sum of two contributes:

$$\boldsymbol{\sigma}(\boldsymbol{u},p) = -p\boldsymbol{I} + \boldsymbol{\tau}(\boldsymbol{u}), \tag{2.3}$$

where the first term represents the surface forces with hydrodynamic pressure p and the second the viscous stress tensor. Specifically, by considering an incompressible and Newtonian fluid, the following linear relation among $\boldsymbol{\tau}(\boldsymbol{u})$ and the strain-rate tensor $\boldsymbol{\epsilon}(\boldsymbol{u})$ holds:

$$\boldsymbol{\tau}(\boldsymbol{u}) = 2\mu\boldsymbol{\epsilon}(\boldsymbol{u}), \tag{2.4}$$

being μ is the dynamic viscosity (assumed to be constant) and $\boldsymbol{\epsilon}(\boldsymbol{u})$ the strain-rate tensor defined as

$$\boldsymbol{\epsilon}(\boldsymbol{u}) = \frac{1}{2}\left(\nabla\boldsymbol{u} + (\nabla\boldsymbol{u})^T\right). \tag{2.5}$$

With the aforementioned hypotheses, the divergence of the Cauchy's stress tensor in Equation (2.1a) can also be expressed as:

$$\nabla\cdot\boldsymbol{\sigma}(\boldsymbol{u},p) = -\nabla p + \mu\Delta\boldsymbol{u}. \tag{2.6}$$

The term $\boldsymbol{f}:\Omega\times(0,T_f)\to\mathbb{R}^d$ in Equation (2.1a) is the forcing term representing the body forces. Equation (2.1b) is the continuity equation (or mass conservation) also known as divergence-free constraint. Equation (2.1) is complemented with BCs and initial condition for the velocity as follows:

$$\boldsymbol{u} = \boldsymbol{g} \qquad \text{on } \Gamma^D\times(0,T_f), \tag{2.7a}$$

$$\boldsymbol{\sigma}(\boldsymbol{u},p)\boldsymbol{n} = \boldsymbol{h} \qquad \text{on } \Gamma^N\times(0,T_f), \tag{2.7b}$$

$$\boldsymbol{u} = \boldsymbol{u}_0 \qquad \text{in } \Omega\times\{0\}. \tag{2.7c}$$

Equations (2.7a) and (2.7b) are the Dirichlet and Neumann BCs, and $\boldsymbol{g}:\Gamma^D\times(0,T_f)\to\mathbb{R}^d$ and $\boldsymbol{h}:\Gamma^N\times(0,T_f)\to\mathbb{R}^d$ Dirichlet and Neumann data respectively. Finally, Equation (2.7c) is the initial condition, and $\boldsymbol{u}_0:\Omega\to\mathbb{R}^d$ the initial datum.

2.2. Weak formulation

To write the weak formulation of Equation (2.1), we introduce the infinite dimensional function spaces [208]:

$$\mathcal{V}_{\boldsymbol{g}} := \{\boldsymbol{v}\in[H^1(\Omega)]^d : \boldsymbol{v} = \boldsymbol{g} \text{ on } \Gamma^D\}, \quad \mathcal{Q} := L^2(\Omega), \tag{2.8}$$

and we denote with $\boldsymbol{\mathcal{V}_g} := \mathcal{V}_g \times \mathcal{Q}$. The weak formulation of Equation (2.1) reads [208]:

given $\boldsymbol{u}_0$, for any $t \in (0, T_f)$, find $(\boldsymbol{u}, p) \in \mathcal{V}_g \times \mathcal{Q}$ s.t.

$$\left(\boldsymbol{v}, \rho\frac{\partial \boldsymbol{u}}{\partial t}\right) + (\boldsymbol{v}, \rho\boldsymbol{u}\cdot\nabla\boldsymbol{u}) + (\nabla\boldsymbol{v}, \mu\nabla\boldsymbol{u}) - (\nabla\cdot\boldsymbol{v}, p) + (q, \nabla\cdot\boldsymbol{u}) = (\boldsymbol{v}, \boldsymbol{f}) + (\boldsymbol{v}, \boldsymbol{h})_{\Gamma^N}, \quad \text{for all } (\boldsymbol{v}, q) \in \mathcal{V}_{\mathbf{0}} \times \mathcal{Q}. \tag{2.9}$$

We denoted by $(\cdot,\cdot)$ and $(\cdot,\cdot)_{\Gamma^N}$ the L^2 inner product with respect to Ω and Γ^N respectively.

Equivalently, by defining $\boldsymbol{U} = (\boldsymbol{u}, p)^T$ and $\boldsymbol{V} = (\boldsymbol{v}, q)^T$, with $\boldsymbol{U} \in \boldsymbol{\mathcal{V}_g}$ and $\boldsymbol{V} \in \boldsymbol{\mathcal{V}_0}$, we can express the weak formulation in a compact form as

given $\boldsymbol{u}_0$, for any $t \in (0, T_f)$, find $\boldsymbol{U} \in \boldsymbol{\mathcal{V}_g}$ s.t.

$$A(\boldsymbol{V}, \boldsymbol{U}) = F(\boldsymbol{V}), \quad \text{for all } \boldsymbol{V} \in \boldsymbol{\mathcal{V}_0}, \tag{2.10}$$

being

$$A(\boldsymbol{V}, \boldsymbol{U}) = A_1(\boldsymbol{V}, \boldsymbol{U}) + A_2(\boldsymbol{V}, \boldsymbol{U}, \boldsymbol{U}), \tag{2.11a}$$

$$A_1(\boldsymbol{V}, \boldsymbol{U}) = \left(\boldsymbol{v}, \rho\frac{\partial \boldsymbol{u}}{\partial t}\right) + (\nabla\boldsymbol{v}, \mu\nabla\boldsymbol{u}) - (\nabla\cdot\boldsymbol{v}, p) + (q, \nabla\cdot\boldsymbol{u}), \tag{2.11b}$$

$$A_2(\boldsymbol{U}, \boldsymbol{V}, \boldsymbol{W}) = (\boldsymbol{u}, \rho\boldsymbol{v}\cdot\nabla\boldsymbol{w}), \tag{2.11c}$$

$$F(\boldsymbol{V}) = (\boldsymbol{v}, \boldsymbol{f}) + (\boldsymbol{v}, \boldsymbol{h})_{\Gamma^N}. \tag{2.11d}$$

2.3. Space discretization: the Variational Multiscale - LES method

For the spatial discretization of Equation (2.9), we consider $\mathcal{T}^h$: a triangulation of Ω into tetrahedra or hexaedra. We introduce the function space of Finite Element (FE) with piecewise Lagrangian polynomial of degree $r \geq 1$ over $\mathcal{T}^h$ as

$$X_r^h = \{v^h \in C^0(\overline{\Omega}) : v^h|_K \in \mathbb{Q}_r, \text{ for all } K \in \mathcal{T}^h\}, \tag{2.12}$$

h being the diameter of the grid element $K \in \mathcal{T}^h$. In the VMS method, we assume a direct sum decomposition of both trial and test function spaces into *coarse* and *fine* scales subspaces as

$$\boldsymbol{\mathcal{V}_g} = \boldsymbol{\mathcal{V}_g^h} \oplus \boldsymbol{\mathcal{V}_g'}, \tag{2.13a}$$

$$\boldsymbol{\mathcal{V}_0} = \boldsymbol{\mathcal{V}_0^h} \oplus \boldsymbol{\mathcal{V}_0'}. \tag{2.13b}$$

Specifically, $\boldsymbol{\mathcal{V}}_{\boldsymbol{g}}^h = \mathcal{V}_{\boldsymbol{g}}^h \times \mathcal{Q}^h$, $\boldsymbol{\mathcal{V}}_{\boldsymbol{0}}^h = \mathcal{V}_{\boldsymbol{0}}^h \times \mathcal{Q}^h$ are the coarse-scale function spaces, i.e. finite-dimensional spaces directly associated to the spatial discretization of the problem. In particular, $\mathcal{V}_{\boldsymbol{g}}^h = \mathcal{V}_{\boldsymbol{g}} \cap [X_r^h]^d$, $\mathcal{V}_{\boldsymbol{0}}^h = \mathcal{V}_{\boldsymbol{0}} \cap [X_r^h]^d$ and $\mathcal{Q}^h = \mathcal{Q} \cap X_r^h$. On the contrary, $\boldsymbol{\mathcal{V}}_{\boldsymbol{g}}' = \mathcal{V}_{\boldsymbol{g}}' \times \mathcal{Q}'$, $\boldsymbol{\mathcal{V}}_{\boldsymbol{0}}' = \mathcal{V}_{\boldsymbol{0}}' \times \mathcal{Q}'$ are the infinite-dimensional function spaces which represent the fine-scale solution [31, 93, 125–127, 129, 130].

In this way, we introduce an a-priori splitting of the solution (and test functions) into coarse and fine-scales as [125–127, 129, 130]:

$$\boldsymbol{U} = \boldsymbol{U}^h + \boldsymbol{U}', \tag{2.14a}$$

$$\boldsymbol{V} = \boldsymbol{V}^h + \boldsymbol{V}'. \tag{2.14b}$$

Accordingly, the superscripts $(\cdot)^h$ and $(\cdot)'$ denote the projections of $\boldsymbol{U}$ and $\boldsymbol{V}$ on coarse-scale and fine-scale solution spaces respectively, with $\boldsymbol{U}^h \in \boldsymbol{\mathcal{V}}_{\boldsymbol{g}}^h$, $\boldsymbol{U}' \in \boldsymbol{\mathcal{V}}_{\boldsymbol{g}}'$, $\boldsymbol{V}^h \in \boldsymbol{\mathcal{V}}_{\boldsymbol{0}}^h$ and $\boldsymbol{V}' \in \boldsymbol{\mathcal{V}}_{\boldsymbol{0}}'$. By plugging the decomposition (2.14) in Equation (2.10), one gets the following coupled equations [31]: given $\boldsymbol{u}_0$, for any $t \in (0, T_f)$,

$$\begin{aligned} &\text{find } \boldsymbol{U}^h \in \boldsymbol{\mathcal{V}}_{\boldsymbol{g}}^h \text{ s.t.} \\ &A(\boldsymbol{V}^h, \boldsymbol{U}^h + \boldsymbol{U}') = F(\boldsymbol{V}^h), \text{ for all } \boldsymbol{V}^h \in \boldsymbol{\mathcal{V}}_{\boldsymbol{0}}^h, \text{ with } \boldsymbol{U}' \in \boldsymbol{\mathcal{V}}_{\boldsymbol{g}}', \end{aligned} \tag{2.15}$$

$$\begin{aligned} &\text{find } \boldsymbol{U}' \in \boldsymbol{\mathcal{V}}_{\boldsymbol{g}}' \text{ s.t.} \\ &A(\boldsymbol{V}', \boldsymbol{U}^h + \boldsymbol{U}') = F(\boldsymbol{V}'), \text{ for all } \boldsymbol{V}' \in \boldsymbol{\mathcal{V}}_{\boldsymbol{0}}', \text{ with } \boldsymbol{U}^h \in \boldsymbol{\mathcal{V}}_{\boldsymbol{g}}^h. \end{aligned} \tag{2.16}$$

Equations (2.15) and (2.16) are the *coarse-scale equation* and *fine-scale equation* respectively. By expressing all the terms in $A(\cdot,\cdot)$ according to Equation (2.11a), and by exploiting bilinearity, Equation (2.15) is rearranged as: given $\boldsymbol{u}_0$, for any $t \in (0, T_f)$, find $\boldsymbol{U}^h \in \boldsymbol{\mathcal{V}}_{\boldsymbol{g}}^h$ s.t.

$$\begin{aligned} &A_1(\boldsymbol{V}^h, \boldsymbol{U}^h) + A_1(\boldsymbol{V}^h, \boldsymbol{U}') + \\ &+ A_2(\boldsymbol{V}^h, \boldsymbol{U}^h, \boldsymbol{U}^h) + A_2(\boldsymbol{V}^h, \boldsymbol{U}^h, \boldsymbol{U}') + A_2(\boldsymbol{V}^h, \boldsymbol{U}', \boldsymbol{U}^h) + A_2(\boldsymbol{V}^h, \boldsymbol{U}', \boldsymbol{U}') \\ &= F(\boldsymbol{V}^h), \text{ for all } \boldsymbol{V}^h \in \boldsymbol{\mathcal{V}}_{\boldsymbol{0}}^h, \text{ with } \boldsymbol{U}' \in \boldsymbol{\mathcal{V}}_{\boldsymbol{g}}'. \end{aligned} \tag{2.17}$$

In the equation above, $A_2(\boldsymbol{V}^h, \boldsymbol{U}^h, \boldsymbol{U}')$ and $A_2(\boldsymbol{V}^h, \boldsymbol{U}', \boldsymbol{U}^h)$ are the *cross-stress* terms, while $A_2(\boldsymbol{V}^h, \boldsymbol{U}', \boldsymbol{U}')$ the *Reynolds-stress* term [31]. By making the following assumptions [31]:

- $\dfrac{\partial \boldsymbol{v}^h}{\partial t} = \boldsymbol{0}$ in Ω;
- $\boldsymbol{u}' = \boldsymbol{0}$ on Γ;
- $\left(\nabla \boldsymbol{v}^h, \mu \nabla \boldsymbol{u}'\right) = \boldsymbol{0}$ in Ω,

we integrate by parts fine-scale terms in Equation (2.17), and it can be shown that the latter reduces to the following *semi–discrete* VMS-LES formulation of the NS equations

[31]:

given $\boldsymbol{u}_0$, for any $t \in (0, T_f)$, find $(\boldsymbol{u}^h, p^h) \in \mathcal{V}_{\boldsymbol{g}}^h \times \mathcal{Q}^h$ s.t.

$$\begin{aligned}
&\left(\boldsymbol{v}^h, \rho\frac{\partial \boldsymbol{u}^h}{\partial t}\right) + \left(\boldsymbol{v}^h, \rho(\boldsymbol{u}^h \cdot \nabla)\boldsymbol{u}^h\right) + \left(\nabla \boldsymbol{v}^h, \mu \nabla \boldsymbol{u}^h\right) - \left(\nabla \cdot \boldsymbol{v}^h, p^h\right) \\
&+ \left(q^h, \nabla \cdot \boldsymbol{u}^h\right) \underbrace{- \left(\rho \boldsymbol{u}^h \cdot \nabla \boldsymbol{v}^h + \nabla q^h, \boldsymbol{u}'\right) - \left(\nabla \cdot \boldsymbol{v}^h, p'\right)}_{\text{(I)}} \underbrace{- \left(\rho \boldsymbol{u}^h \cdot (\nabla \boldsymbol{v}^h)^T, \boldsymbol{u}'\right)}_{\text{(II)}} \\
&\underbrace{- \left(\rho \nabla \boldsymbol{v}^h, \boldsymbol{u}' \otimes \boldsymbol{u}'\right)}_{\text{(III)}} = \left(\boldsymbol{v}^h, \boldsymbol{f}\right) + \left(\boldsymbol{v}^h, \boldsymbol{h}\right)_{\Gamma^N}, \\
&\text{for all } (\boldsymbol{v}^h, q^h) \in \mathcal{V}_{\boldsymbol{0}}^h \times \mathcal{Q}^h, \text{ with } (\boldsymbol{u}', p') \in \mathcal{V}_{\boldsymbol{g}}' \times \mathcal{Q}'.
\end{aligned} \tag{2.18}$$

Equation (2.18) contains stabilization terms in addition to the standard NS equations, namely (I) the Streamline Upwind Petrov Galerkin (SUPG) term[1], (II) an additional stabilization term arising from the VMS method and (III) the LES term which models the Reynolds stress [31, 93].

From this point of view, the standard SUPG stabilization method can be considered as an intermediate step towards the fully stabilized formulation [31]. In this thesis, we will adopt either the VMS-LES method, i.e. the whole formulation in Equation (2.18), and the SUPG method, i.e. the formulation in Equation (2.18) without the additional terms VMS and LES (terms II and III respectively).

On the one hand, both the SUPG and VMS-LES methods allow to control instabilities in the velocity field arising from convection-dominated (i.e. high Reynolds number) regimes and instabilities due to the fact that equal order FE spaces ($\mathbb{P}_r - \mathbb{P}_r$ or $\mathbb{Q}_r - \mathbb{Q}_r$) would not satisfy the *inf-sup* (or LBB) condition, yielding numerical oscillations of the pressure field [31, 41, 93]. On the other hand, the VMS-LES method – as the name itself emphasizes and differently from SUPG – also yields a LES-type modeling [31, 93, 125–127, 129, 130] to account for the transitional-nearly turbulent flow regime that typically occurs for instance in cardiac hemodynamics, which will be the subject of the next chapters and specifically of the Part II of this thesis.

From Equation (2.18), we also observe that the fine-scale solution $(\boldsymbol{u}', p')$ is still defined in an infinite dimensional function space. Let consider now the fine-scale Equation (2.16), in an analogous fashion it can be expressed as: given $\boldsymbol{u}_0$, for any $t \in (0, T_f)$,

[1] In the whole manuscript, we will use the term SUPG to indicate, more precisely, the SUPG-PSPG type stabilization applied to the NS equations [256]. The SUPG method is designed to avoid velocity instabilities in the advection dominated regime; the PSPG (Pressure Stabilized Petrov-Galerkin) method is designed to circumvent the lack of inf-sup stability.

find $\boldsymbol{U}' \in \boldsymbol{\mathcal{V}}'_{\boldsymbol{g}}$ s.t.

$$\begin{aligned} &A_1(\boldsymbol{V}', \boldsymbol{U}^h) + A_1(\boldsymbol{V}', \boldsymbol{U}') + \\ &+ A_2(\boldsymbol{V}', \boldsymbol{U}^h, \boldsymbol{U}^h) + A_2(\boldsymbol{V}', \boldsymbol{U}^h, \boldsymbol{U}') + A_2(\boldsymbol{V}', \boldsymbol{U}', \boldsymbol{U}^h) + A_2(\boldsymbol{V}', \boldsymbol{U}', \boldsymbol{U}') \\ &= F(\boldsymbol{V}'), \text{ for all } \boldsymbol{V}' \in \boldsymbol{\mathcal{V}}'_{\boldsymbol{0}}, \text{ with } \boldsymbol{U}^h \in \boldsymbol{\mathcal{V}}^{\boldsymbol{h}}_{\boldsymbol{g}}. \end{aligned} \tag{2.19}$$

By rearranging terms in Equation (2.19), we get:

$$\begin{aligned} &A_1(\boldsymbol{V}', \boldsymbol{U}') + A_2(\boldsymbol{V}', \boldsymbol{U}^h, \boldsymbol{U}') + A_2(\boldsymbol{V}', \boldsymbol{U}', \boldsymbol{U}^h) + A_2(\boldsymbol{V}', \boldsymbol{U}', \boldsymbol{U}') \\ &= F(\boldsymbol{V}') - A_1(\boldsymbol{V}', \boldsymbol{U}^h) - A_2(\boldsymbol{V}', \boldsymbol{U}^h, \boldsymbol{U}^h), \text{ for all } \boldsymbol{V}' \in \boldsymbol{\mathcal{V}}'_{\boldsymbol{0}}, \text{ with } \boldsymbol{U}^h \in \boldsymbol{\mathcal{V}}^{\boldsymbol{h}}_{\boldsymbol{g}}. \end{aligned} \tag{2.20}$$

where the right-hand-side of Equation (2.20) represents the residual of the coarse-scale Equation (2.17) projected onto the fine-scale space $\boldsymbol{\mathcal{V}}'_{\boldsymbol{0}}$. We denote the coarse-scale residual as $\boldsymbol{R}(\boldsymbol{U}^h)$ and Equation (2.20) is hence rearranged as

$$A_1(\boldsymbol{V}', \boldsymbol{U}') + A_2(\boldsymbol{V}', \boldsymbol{U}^h, \boldsymbol{U}') + A_2(\boldsymbol{V}', \boldsymbol{U}', \boldsymbol{U}^h) + A_2(\boldsymbol{V}', \boldsymbol{U}', \boldsymbol{U}') = (\boldsymbol{V}', \boldsymbol{R}(\boldsymbol{U}^h)). \tag{2.21}$$

The solution $\boldsymbol{U}'$ of Equation (2.21) can be represented as a functional of the coarse-scale solution $\boldsymbol{U}^h$ and the coarse-scale residual $\boldsymbol{R}(\boldsymbol{U}^h)$ [31]:

$$\boldsymbol{U}' = \boldsymbol{\mathcal{F}}'(\boldsymbol{U}^h, \boldsymbol{R}(\boldsymbol{U}^h)). \tag{2.22}$$

The latter can be plugged in Equation (2.15) to close finally the coarse-scale equation:

$$\text{find } \boldsymbol{U}^h \in \boldsymbol{\mathcal{V}}^h_{\boldsymbol{g}} : \quad A(\boldsymbol{V}^h, \boldsymbol{U}^h + \underbrace{\boldsymbol{\mathcal{F}}'(\boldsymbol{U}^h, \boldsymbol{R}(\boldsymbol{U}^h))}_{\boldsymbol{U}'}) = F(\boldsymbol{V}^h), \text{ for all } \boldsymbol{V}^h \in \boldsymbol{\mathcal{V}}^h_{\boldsymbol{0}}. \tag{2.23}$$

In order to find a numerical solution of the problem above, we need to approximate the functional with $\widetilde{\boldsymbol{\mathcal{F}}'} \approx \boldsymbol{\mathcal{F}}'$, which will lead to an approximation of both coarse and fine-scale solutions, namely $\widetilde{\boldsymbol{U}^h} \approx \boldsymbol{U}^h$ and $\widetilde{\boldsymbol{U}'} \approx \boldsymbol{U}'$. However, for notational convenience, from now on we will simply refer to functional and solutions without $\sim$, but implicitly denoting their approximations.

2.3.1. Quasi-static approximation of fine-scales

For the approximation of the functional $\boldsymbol{\mathcal{F}}'$, by using analogous arguments of [31, 93], we employ a *quasi-static* approach. Equation (2.22) is approximated as:

$$\boldsymbol{U}' \approx -\boldsymbol{\tau}(\boldsymbol{U}^h)\boldsymbol{R}(\boldsymbol{U}^h), \tag{2.24}$$

being [31, 93]

$$\boldsymbol{R}(\boldsymbol{U}^h) = \begin{Bmatrix} \boldsymbol{r}_{\mathrm{M}}(\boldsymbol{u}^h, p^h) \\ r_{\mathrm{C}}(\boldsymbol{u}^h) \end{Bmatrix}, \quad \boldsymbol{\tau}(\boldsymbol{U}^h) = \begin{bmatrix} \tau_{\mathrm{M}}(\boldsymbol{u}^h)\boldsymbol{I}_{3\times 3} & \boldsymbol{0}_{3\times 3} \\ \boldsymbol{0}^T_{3\times 3} & \tau_{\mathrm{C}}(\boldsymbol{u}^h) \end{bmatrix}. \tag{2.25}$$

Hence, the fine-scale velocity and pressure are approximated as

$$\boldsymbol{u}' \approx -\tau_{\mathrm{M}}(\boldsymbol{u}^h)\boldsymbol{r}_{\mathrm{M}}(\boldsymbol{u}^h, p^h), \tag{2.26a}$$

$$p' \approx -\tau_{\mathrm{C}}(\boldsymbol{u}^h) r_{\mathrm{C}}(\boldsymbol{u}^h). \tag{2.26b}$$

For additional details on the quasi-static approximation of fine-scales, we refer to [31]. $\boldsymbol{r}_{\mathrm{M}}(\boldsymbol{u}^h, p^h)$ and $r_{\mathrm{C}}(\boldsymbol{u}^h)$ are the strong residuals of the coarse-scale momentum and continuity equations defined respectively as:

$$\boldsymbol{r}_{\mathrm{M}}(\boldsymbol{u}^h, p^h) = \rho\left(\frac{\partial \boldsymbol{u}^h}{\partial t} + \boldsymbol{u}^h \cdot \nabla \boldsymbol{u}^h\right) + \nabla p^h - \mu \Delta \boldsymbol{u}^h - \boldsymbol{f}, \tag{2.27a}$$

$$r_{\mathrm{C}}(\boldsymbol{u}^h) = \nabla \cdot \boldsymbol{u}^h. \tag{2.27b}$$

Many definitions of the stabilization parameters $\tau_{\mathrm{M}}(\boldsymbol{u}^h)$ and $\tau_{\mathrm{C}}(\boldsymbol{u}^h)$ can be found in literature. Many of them are designed for one-dimensional problems and then extended to multidimensional problems straightforwardly, incorporating some (empirical) dependence on numerical settings [40, 43, 54–56, 94, 101, 195, 217, 233, 234, 257]. We address this issue in Chapter 3, and we propose a novel computational strategy to find an optimal form stabilization parameter via ANNs. Specifically, we limit ourselves to the case of the SUPG method for advection-diffusion problems. For the NS equations instead, we set the stabilization parameters as [31, 93]

$$\tau_{\mathrm{M}}(\boldsymbol{u}^h) = \left(\frac{\sigma_t^2 \rho^2}{\Delta t^2} + \rho^2 \boldsymbol{u}^h \cdot \overline{\boldsymbol{G}} \boldsymbol{u}^h + C_r \mu^2 \overline{\boldsymbol{G}} : \overline{\boldsymbol{G}}\right)^{-\frac{1}{2}}, \tag{2.28a}$$

$$\tau_{\mathrm{C}}(\boldsymbol{u}^h) = \left(\tau_{\mathrm{M}}(\boldsymbol{u}^h)\overline{\boldsymbol{g}} \cdot \overline{\boldsymbol{g}}\right)^{-1}. \tag{2.28b}$$

In Equation (2.28), σ_t is a constant equal to the order of the time discretization scheme employed (see Section 2.4), Δt the time-step size and $C_r = 15 \cdot 2^r$ is a constant obtained by an inverse inequality depending on the polynomial degree r [31, 93].

Let $\boldsymbol{x} = \{x_i\}_{i=1}^d$ be the coordinates of the mesh element K in the physical space and $\boldsymbol{\xi} = \{\xi_i\}_{i=1}^d$ the coordinates of element $\widehat{K}$ in the parametric space, as displayed for example in Figure 2.1. Let $\boldsymbol{x} = \boldsymbol{x}(\boldsymbol{\xi}) : \widehat{K} \to K$ be a continuous and differentiable mapping from the parametric to the physical space, with a continuously differentiable inverse. Denoting by $\boldsymbol{J} = \frac{\partial \boldsymbol{x}}{\partial \boldsymbol{\xi}}$ the Jacobian of the mapping $\boldsymbol{x}(\boldsymbol{\xi})$, $\overline{\boldsymbol{G}}$ and $\overline{\boldsymbol{g}}$ appearing in Equation (2.28) are respectively the metric tensor and metric vector [31]:

$$\overline{\boldsymbol{G}} = \boldsymbol{J}^{-T}\boldsymbol{J}^{-1}, \ \overline{\boldsymbol{g}} = \boldsymbol{J}^{-T}\boldsymbol{1}. \tag{2.29}$$

From Equation (2.28), as $\Delta t = \mathcal{O}(h/|\boldsymbol{u}^h|)$, the stabilization parameters do not degenerate; however, in the limit $\Delta t \to 0$, for fixed $h/|\boldsymbol{u}^h|$, the first term in Equation (2.28a) becomes predominant over the remaining two: as a result, $\tau_{\mathrm{M}} \to 0$ and $\tau_{\mathrm{C}} \to \infty$ [31, 57].

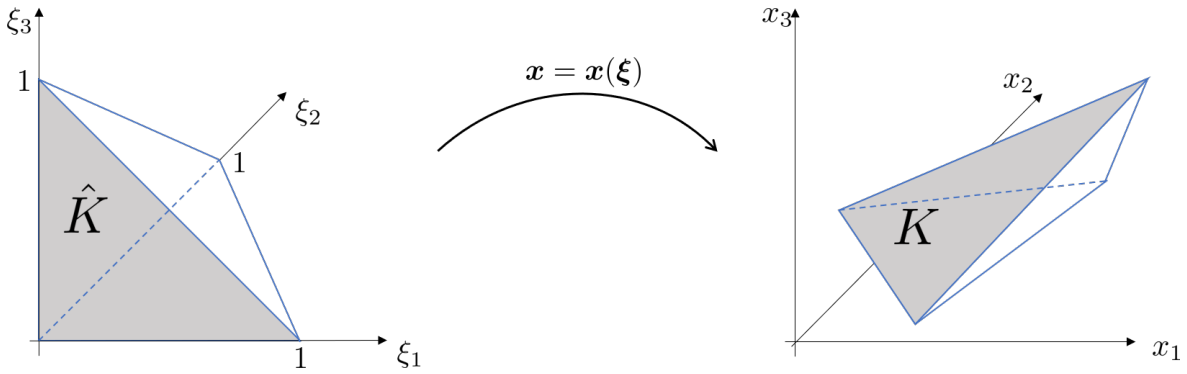

Figure 2.1: Mapping $\boldsymbol{x} = \boldsymbol{x}(\boldsymbol{\xi}) : \widehat{K} \to K$ from the parametric element $\widehat{K}$ to the physical one K.

A possible solution to address this drawback is to rely on a *dynamic* approximation of the fine-scale solution, where an additional ODE is solved to advance in time the fine-scale. For a dynamic VMS-LES, we refer for instance to [57, 84].

By using the quasi-static approximation of the fine-scales (2.24) in Equation (2.18), the *semi-discrete* VMS-LES formulation of the NS equations with a *quasi-static* approximation of the fine-scales finally reads:

given $\boldsymbol{u}_0$, for any $t \in (0, T_f)$, find $(\boldsymbol{u}^h, p^h) \in \mathcal{V}_{\boldsymbol{g}}^h \times \mathcal{Q}^h$ s.t.

$$
\begin{aligned}
&\left(\boldsymbol{v}^h, \rho \frac{\partial \boldsymbol{u}^h}{\partial t}\right) + \left(\boldsymbol{v}^h, \rho\left(\boldsymbol{u}^h \cdot \nabla\right)\boldsymbol{u}^h\right) + \left(\nabla \boldsymbol{v}^h, \mu \nabla \boldsymbol{u}^h\right) \\
&- \left(\nabla \cdot \boldsymbol{v}^h, p^h\right) + \left(q^h, \nabla \cdot \boldsymbol{u}^h\right) \\
&+ \left(\rho \boldsymbol{u}^h \cdot \nabla \boldsymbol{v}^h + \nabla q^h,\, \tau_{\mathrm{M}}(\boldsymbol{u}^h)\boldsymbol{r}_{\mathrm{M}}(\boldsymbol{u}^h, p^h)\right) + \left(\nabla \cdot \boldsymbol{v}^h, \tau_{\mathrm{C}}(\boldsymbol{u}^h) r_{\mathrm{C}}(\boldsymbol{u}^h)\right) \\
&+ \left(\rho \boldsymbol{u}^h \cdot (\nabla \boldsymbol{v}^h)^T, \tau_{\mathrm{M}}(\boldsymbol{u}^h)\boldsymbol{r}_{\mathrm{M}}(\boldsymbol{u}^h, p^h)\right) \\
&- \left(\rho \nabla \boldsymbol{v}^h, \tau_{\mathrm{M}}(\boldsymbol{u}^h)\boldsymbol{r}_{\mathrm{M}}(\boldsymbol{u}^h, p^h) \otimes \tau_{\mathrm{M}}(\boldsymbol{u}^h)\boldsymbol{r}_{\mathrm{M}}(\boldsymbol{u}^h, p^h)\right) = \\
&\left(\boldsymbol{v}^h, \boldsymbol{f}\right) + \left(\boldsymbol{v}^h, \boldsymbol{h}\right)_{\Gamma^N}, \qquad \text{for all } (\boldsymbol{v}^h, q^h) \in \mathcal{V}_{\boldsymbol{0}}^h \times \mathcal{Q}^h.
\end{aligned}
\tag{2.30}
$$

2.4. Time discretization and non-linearities treatment

We discretize in time Equation (2.30) by means of *Backward Differentiation Formula* (BDF) [64] of order $\sigma_t = 1, 2, 3$. We partition the time domain $(0, T_f)$ into N_t subintervals of equal size $\Delta t = \frac{T_f}{N_t}$ and we denote with the subscript n quantities related to the time-step n, with $n = 0, \ldots, N_t$. The approximation of the velocity time derivative

reads [93]:

$$\left.\frac{\partial \boldsymbol{u}^h}{\partial t}\right|_{n+1} \approx \frac{\alpha_{\mathrm{BDF}}\boldsymbol{u}^h_{n+1} - \boldsymbol{u}^h_{n,\mathrm{BDF}}}{\Delta t}, \text{ for } n = \sigma_t - 1, \ldots, N_t - 1. \tag{2.31}$$

being

$$\boldsymbol{u}^h_{n,\mathrm{BDF}} = \begin{cases} \boldsymbol{u}^h_n, & \text{if } n \geq 0, \text{ for } \sigma_t = 1 \text{ (BDF1)}, \\ 2\boldsymbol{u}^h_n - \frac{1}{2}\boldsymbol{u}^h_{n-1}, & \text{if } n \geq 1, \text{ for } \sigma_t = 2 \text{ (BDF2)}, \\ 3\boldsymbol{u}^h_n - \frac{3}{2}\boldsymbol{u}^h_{n-1} + \frac{1}{3}\boldsymbol{u}^h_{n-2}, & \text{if } n \geq 2, \text{ for } \sigma_t = 3 \text{ (BDF3)}, \end{cases} \tag{2.32}$$

and

$$\alpha_{\mathrm{BDF}} = \begin{cases} 1, & \text{for } \sigma_t = 1 \text{ (BDF1)}, \\ \frac{3}{2}, & \text{for } \sigma_t = 2 \text{ (BDF2)}, \\ \frac{11}{6}, & \text{for } \sigma_t = 3 \text{ (BDF3)}. \end{cases} \tag{2.33}$$

2.4.1. Fully implicit, BDF, quasi-static VMS-LES formulation

By using the BDF discretization (2.31) in Equation (2.30), we get the following *fully-discrete fully-implicit* BDF VMS-LES formulation of the NS equations with *quasi-static* approximation of fine-scales:

given $\boldsymbol{u}^h_n, \ldots, \boldsymbol{u}^h_{n+1-\sigma_t}$, for any $n = 0, \ldots, N_t - 1$, find $(\boldsymbol{u}^h_{n+1}, p^h_{n+1}) \in \mathcal{V}^h_{\boldsymbol{g}} \times \mathcal{Q}^h$ s.t.

$$\begin{aligned} &\left(\boldsymbol{v}^h, \rho\frac{\alpha_{\mathrm{BDF}}\boldsymbol{u}^h_{n+1} - \boldsymbol{u}^h_{n,\mathrm{BDF}}}{\Delta t}\right) + \left(\boldsymbol{v}^h, \rho\left(\boldsymbol{u}^h_{n+1}\cdot\nabla\right)\boldsymbol{u}^h_{n+1}\right) + \left(\nabla\boldsymbol{v}^h, \mu\nabla\boldsymbol{u}^h_{n+1}\right) \\ &- \left(\nabla\cdot\boldsymbol{v}^h, p^h_{n+1}\right) + \left(q^h, \nabla\cdot\boldsymbol{u}^h_{n+1}\right) \\ &+ \left(\rho\boldsymbol{u}^h_{n+1}\cdot\nabla\boldsymbol{v}^h + \nabla q^h,\ \tau_{\mathrm{M}}(\boldsymbol{u}^h_{n+1})\boldsymbol{r}_{\mathrm{M}}(\boldsymbol{u}^h_{n+1}, p^h_{n+1})\right) \\ &+ \left(\nabla\cdot\boldsymbol{v}^h, \tau_{\mathrm{C}}(\boldsymbol{u}^h_{n+1})r_{\mathrm{C}}(\boldsymbol{u}^h_{n+1})\right) \\ &+ \left(\rho\boldsymbol{u}^h_{n+1}\cdot(\nabla\boldsymbol{v}^h)^T, \tau_{\mathrm{M}}(\boldsymbol{u}^h_{n+1})\boldsymbol{r}_{\mathrm{M}}(\boldsymbol{u}^h_{n+1}, p^h_{n+1})\right) \\ &- \left(\rho\nabla\boldsymbol{v}^h, \tau_{\mathrm{M}}(\boldsymbol{u}^h_{n+1})\boldsymbol{r}_{\mathrm{M}}(\boldsymbol{u}^h_{n+1}, p^h_{n+1}) \otimes \tau_{\mathrm{M}}(\boldsymbol{u}^h_{n+1})\boldsymbol{r}_{\mathrm{M}}(\boldsymbol{u}^h_{n+1}, p^h_{n+1})\right) \\ &= \left(\boldsymbol{v}^h, \boldsymbol{f}_{n+1}\right) + \left(\boldsymbol{v}^h, \boldsymbol{h}_{n+1}\right)_{\Gamma^N}, \qquad \text{for all } \ (\boldsymbol{v}^h, q^h) \in \mathcal{V}^h_{\boldsymbol{0}} \times \mathcal{Q}^h, \qquad \text{for all } n \geq \sigma_t - 1. \end{aligned} \tag{2.34}$$

In the equation above, $\boldsymbol{f}_{n+1} = \boldsymbol{f}(t_{n+1})$ and $\boldsymbol{h}_{n+1} = \boldsymbol{h}(t_{n+1})$. After time discretization,

the stabilization parameters and the strong residuals are defined as:

$$\tau_{\mathrm{M}}(\boldsymbol{u}^h_{n+1}) = \left(\frac{\sigma_t^2\rho^2}{\Delta t^2} + \rho^2\boldsymbol{u}^h_{n+1}\cdot\overline{\boldsymbol{G}}\boldsymbol{u}^h_{n+1} + C_r\mu^2\overline{\boldsymbol{G}}:\overline{\boldsymbol{G}}\right)^{-\frac{1}{2}}, \tag{2.35a}$$

$$\tau_{\mathrm{C}}(\boldsymbol{u}^h_{n+1}) = \left(\tau_{\mathrm{M}}(\boldsymbol{u}^h_{n+1})\overline{\boldsymbol{g}}\cdot\overline{\boldsymbol{g}}\right)^{-1}, \tag{2.35b}$$

$$\begin{aligned}\boldsymbol{r}_{\mathrm{M}}(\boldsymbol{u}^h_{n+1}, p^h_{n+1}) = \rho\left(\frac{\alpha_{\mathrm{BDF}}\boldsymbol{u}^h_{n+1} - \boldsymbol{u}^h_{n,\mathrm{BDF}}}{\Delta t} + \boldsymbol{u}^h_{n+1}\cdot\nabla\boldsymbol{u}^h_{n+1}\right) + \nabla p^h_{n+1} \\ - \mu\Delta\boldsymbol{u}^h_{n+1} - \boldsymbol{f}_{n+1},\end{aligned} \tag{2.36a}$$

$$r_{\mathrm{C}}(\boldsymbol{u}^h_{n+1}) = \nabla\cdot\boldsymbol{u}^h_{n+1}. \tag{2.36b}$$

A fully-implicit numerically scheme generally leads to a stable time discretization method. However, Equation (2.34) yields the solution, at each discrete time t_n, of a non linear problem. The non linearity might be numerically solved for instance via the Newton method, increasing hence the computational burden of the overall simulation. As a matter of fact, the Newton method requires – until convergence – the assembly of the residual vector and the Jacobian matrix, and the solution of the associated linear system. To mitigate the computational burden associated to this numerical scheme, in the following section we recall the semi-implicit formulation [93].

2.4.2. Semi-implicit, BDF, quasi-static VMS-LES formulation

The *semi-implicit* BDF scheme is derived from its implicit counterpart in Equation (2.34) by extrapolating the non linear terms by means of the Newton-Gregory backward polynomials of order $\sigma_t = 1, 2, 3$ for the variables $\boldsymbol{u}^h_{n+1}$ and p^h_{n+1}. Extrapolated variables are denoted with subscript "$n+1,\mathrm{EXT}$" and, based on the BDF order adopted for the time discretization, they are expressed as [93]:

$$\boldsymbol{u}^h_{n+1,\mathrm{EXT}} = \begin{cases}\boldsymbol{u}^h_n, & \text{if } n \geq 0, \text{ for } \sigma_t = 1 \text{ (BDF1)},\\ 2\boldsymbol{u}^h_n - \boldsymbol{u}^h_{n-1}, & \text{if } n \geq 1, \text{ for } \sigma_t = 2 \text{ (BDF2)},\\ 3\boldsymbol{u}^h_n - 3\boldsymbol{u}^h_{n-1}, +\boldsymbol{u}^h_{n-2} & \text{if } n \geq 2, \text{ for } \sigma_t = 3 \text{ (BDF3)},\end{cases} \tag{2.37a}$$

$$p^h_{n+1,\mathrm{EXT}} = \begin{cases}p^h_n, & \text{if } n \geq 0, \text{ for } \sigma_t = 1 \text{ (BDF1)},\\ 2p^h_n - p^h_{n-1}, & \text{if } n \geq 1, \text{ for } \sigma_t = 2 \text{ (BDF2)},\\ 3p^h_n - 3p^h_{n-1} + p^h_{n-2}, & \text{if } n \geq 2, \text{ for } \sigma_t = 3 \text{ (BDF3)}.\end{cases} \tag{2.37b}$$

By expanding each term of Equation (2.34), by linearising each non-linear terms by means of Newton-Gregory backward polynomials, and by gathering terms to re-define the strong residuals, we get the following *fully-discrete semi-implicit* BDF VMS-LES formulation of the NS equations with *quasi-static* approximation of fine-scales:

given $\boldsymbol{u}_n^h, \dots, \boldsymbol{u}_{n+1-\sigma_t}^h$, for any $n = 0, \dots, N_t - 1$, find $(\boldsymbol{u}_{n+1}^h, p_{n+1}^h) \in \mathcal{V}_{\boldsymbol{g}}^h \times \mathcal{Q}^h$ s.t.

$$
\begin{aligned}
&\left(\boldsymbol{v}^h, \rho \frac{\alpha_{\mathrm{BDF}} \boldsymbol{u}_{n+1}^h - \boldsymbol{u}_{n,\mathrm{BDF}}^h}{\Delta t}\right) + \left(\boldsymbol{v}^h, \rho \left(\boldsymbol{u}_{n+1,\mathrm{EXT}}^h \cdot \nabla\right) \boldsymbol{u}_{n+1}^h\right) + \left(\nabla \boldsymbol{v}^h, \mu \nabla \boldsymbol{u}_{n+1}^h\right) \\
&- \left(\nabla \cdot \boldsymbol{v}^h, p_{n+1}^h\right) + \left(q^h, \nabla \cdot \boldsymbol{u}_{n+1}^h\right) \\
&+ \left(\rho \boldsymbol{u}_{n+1,\mathrm{EXT}}^h \cdot \nabla \boldsymbol{v}^h + \nabla q^h,\ \tau_{\mathrm{M}}(\boldsymbol{u}_{n+1,\mathrm{EXT}}^h) \boldsymbol{r}_{\mathrm{M,EXT}}(\boldsymbol{u}_{n+1}^h, p_{n+1}^h)\right) \\
&+ \left(\nabla \cdot \boldsymbol{v}^h, \tau_{\mathrm{C}}(\boldsymbol{u}_{n+1,\mathrm{EXT}}^h) r_{\mathrm{C}}(\boldsymbol{u}_{n+1}^h)\right) \\
&+ \left(\rho \boldsymbol{u}_{n+1,\mathrm{EXT}}^h \cdot (\nabla \boldsymbol{v}^h)^T, \tau_{\mathrm{M}}(\boldsymbol{u}_{n+1,\mathrm{EXT}}^h) \boldsymbol{r}_{\mathrm{M,EXT}}(\boldsymbol{u}_{n+1}^h, p_{n+1}^h)\right) \\
&- \left(\rho \nabla \boldsymbol{v}^h, \tau_{\mathrm{M}}(\boldsymbol{u}_{n+1,\mathrm{EXT}}^h) \boldsymbol{r}_{\mathrm{M,EXT}}^{\mathrm{LHS}}(\boldsymbol{u}_{n+1}^h, p_{n+1}^h) \otimes \right. \\
&\left. \tau_{\mathrm{M}}(\boldsymbol{u}_{n+1,\mathrm{EXT}}^h) \boldsymbol{r}_{\mathrm{M,EXT}}(\boldsymbol{u}_{n+1,\mathrm{EXT}}^h, p_{n+1,\mathrm{EXT}}^h)\right) \\
&+ \left(\rho \nabla \boldsymbol{v}^h, \tau_{\mathrm{M}}(\boldsymbol{u}_{n+1,\mathrm{EXT}}^h) \boldsymbol{r}_{\mathrm{M}}^{\mathrm{RHS}} \otimes \tau_{\mathrm{M}}(\boldsymbol{u}_{n+1,\mathrm{EXT}}^h) \boldsymbol{r}_{\mathrm{M,EXT}}(\boldsymbol{u}_{n+1}^h, p_{n+1}^h)\right) \\
&= \left(\boldsymbol{v}^h, \boldsymbol{f}_{n+1}\right) + \left(\boldsymbol{v}^h, \boldsymbol{h}_{n+1}\right)_{\Gamma^N}, \qquad \text{for all } \ (\boldsymbol{v}^h, q^h) \in \mathcal{V}_{\boldsymbol{0}}^h \times \mathcal{Q}^h \qquad \text{for all } \ n \geq \sigma_t - 1.
\end{aligned}
\tag{2.38}
$$

In the formulation above, we have adopted the extrapolated strong residual of the momentum equation i.e. with the extrapolated advection velocity:

$$
\begin{aligned}
\boldsymbol{r}_{\mathrm{M,EXT}}(\boldsymbol{u}_{n+1}^h, p_{n+1}^h) = &\rho \left(\frac{\alpha_{\mathrm{BDF}} \boldsymbol{u}_{n+1}^h - \boldsymbol{u}_{n,\mathrm{BDF}}^h}{\Delta t} + \boldsymbol{u}_{n+1,\mathrm{EXT}}^h \cdot \nabla \boldsymbol{u}_{n+1}^h\right) \\
&+ \nabla p_{n+1}^h - \mu \Delta \boldsymbol{u}_{n+1}^h - \boldsymbol{f}_{n+1}.
\end{aligned}
\tag{2.39}
$$

Moreover, we have split its definition in two contributes, namely a left-hand-side and a right-hand-side term:

$$
\boldsymbol{r}_{\mathrm{M,EXT}}(\boldsymbol{u}_{n+1}^h, p_{n+1}^h) = \boldsymbol{r}_{\mathrm{M,EXT}}^{\mathrm{LHS}}(\boldsymbol{u}_{n+1}^h, p_{n+1}^h) - \boldsymbol{r}_{\mathrm{M}}^{\mathrm{RHS}},
\tag{2.40}
$$

with

$$
\begin{aligned}
\boldsymbol{r}_{\mathrm{M,EXT}}^{\mathrm{LHS}}(\boldsymbol{u}_{n+1}^h, p_{n+1}^h) = &\rho \left(\frac{\alpha_{\mathrm{BDF}} \boldsymbol{u}_{n+1}^h}{\Delta t} + \boldsymbol{u}_{n+1,\mathrm{EXT}}^h \cdot \nabla \boldsymbol{u}_{n+1}^h\right) \\
&+ \nabla p_{n+1}^h - \mu \Delta \boldsymbol{u}_{n+1}^h,
\end{aligned}
\tag{2.41a}
$$

$$
\boldsymbol{r}_{\mathrm{M}}^{\mathrm{RHS}} = \rho \frac{\boldsymbol{u}_{n,\mathrm{BDF}}^h}{\Delta t} + \boldsymbol{f}_{n+1}.
\tag{2.41b}
$$

On the basis of this splitting, we observe in Equation (2.38) that the LES term is decomposed into two terms after linearisation. Moreover, one should see that the extrapolated residual defined in Equation (2.39) is evaluated in Equation (2.38) either with variables at the current time-step and extrapolated.

2.5. Implementation of the numerical scheme

For the sake of an efficient implementation, denoting by $\boldsymbol{u}_*^h$:

$$\boldsymbol{u}_*^h = \begin{cases} \boldsymbol{u}_{n+1}^h, & \text{if implicit,} \\ \boldsymbol{u}_{n+1,\text{EXT}}^h & \text{if semi-implicit,} \end{cases} \tag{2.42}$$

we can express Equations (2.34) and (2.38) in a compact form as

given $\boldsymbol{u}_n^h, \dots, \boldsymbol{u}_{n+1-\sigma_t}^h$, for any $n = 0, \dots, N_t - 1$, find $(\boldsymbol{u}_{n+1}^h, p_{n+1}^h) \in \mathcal{V}_{\boldsymbol{g}}^h \times \mathcal{Q}^h$ s.t.

$$\begin{aligned} &\left(\boldsymbol{v}^h, \rho \frac{\alpha_{\text{BDF}} \boldsymbol{u}_{n+1}^h - \boldsymbol{u}_{n,\text{BDF}}^h}{\Delta t}\right) + \left(\boldsymbol{v}^h, \rho \left(\boldsymbol{u}_*^h \cdot \nabla\right) \boldsymbol{u}_{n+1}^h\right) + \left(\nabla \boldsymbol{v}^h, \mu \nabla \boldsymbol{u}_{n+1}^h\right) \\ &- \left(\nabla \cdot \boldsymbol{v}^h, p_{n+1}^h\right) + \left(q^h, \nabla \cdot \boldsymbol{u}_{n+1}^h\right) + \mathcal{S}(\boldsymbol{v}^h, q^h, \boldsymbol{u}_{n+1}^h, \boldsymbol{u}_*^h, p_{n+1}^h, p_{n+1,\text{EXT}}^h) \\ &= \left(\boldsymbol{v}^h, \boldsymbol{f}_{n+1}\right) + \left(\boldsymbol{v}^h, \boldsymbol{h}_{n+1}\right)_{\Gamma^N}, \qquad \text{for all } \ (\boldsymbol{v}^h, q^h) \in \mathcal{V}_{\boldsymbol{0}}^h \times \mathcal{Q}^h, \qquad \text{for all } n \geq \sigma_t - 1. \end{aligned} \tag{2.43}$$

The form $\mathcal{S}$ includes all the stabilization and turbulence terms introduced in Equations (2.34) and (2.38). Specifically, according to the stabilization method employed (SUPG or VMS-LES), the stabilization term $\mathcal{S}$ can assume one of the following forms:

$$\mathcal{S}(\boldsymbol{v}^h, q^h, \boldsymbol{u}_{n+1}^h, \boldsymbol{u}_*^h, p_{n+1}^h, p_{n+1,\text{EXT}}^h) =$$

$$\begin{cases} \mathcal{S}_{\text{SUPG}}(\boldsymbol{v}^h, q^h, \boldsymbol{u}_{n+1}^h, \boldsymbol{u}_*^h, p_{n+1}^h), & \text{if SUPG} \\ \mathcal{S}_{\text{SUPG}}(\boldsymbol{v}^h, q^h, \boldsymbol{u}_{n+1}^h, \boldsymbol{u}_*^h, p_{n+1}^h) + \mathcal{S}_{\text{VMS}}(\boldsymbol{v}^h, \boldsymbol{u}_{n+1}^h, \boldsymbol{u}_*^h, p_{n+1}^h) & \\ + \mathcal{S}_{\text{LES}}(\boldsymbol{v}^h, q^h, \boldsymbol{u}_{n+1}^h, \boldsymbol{u}_*^h, p_{n+1}^h, p_{n+1,\text{EXT}}^h), & \text{if VMS-LES} \end{cases} \tag{2.44}$$

being

$$\begin{aligned} \mathcal{S}_{\text{SUPG}}(\boldsymbol{v}^h, q^h, \boldsymbol{u}_{n+1}^h, \boldsymbol{u}_*^h, p_{n+1}^h) &= \left(\rho \boldsymbol{u}_*^h \cdot \nabla \boldsymbol{v}^h + \nabla q^h, \, \tau_{\text{M}}(\boldsymbol{u}_*^h) \boldsymbol{r}_{\text{M}}(\boldsymbol{u}_{n+1}^h, p_{n+1}^h)\right) \\ &\quad + \left(\nabla \cdot \boldsymbol{v}^h, \tau_{\text{C}}(\boldsymbol{u}_*^h) r_{\text{C}}(\boldsymbol{u}_{n+1}^h)\right), \end{aligned} \tag{2.45}$$

$$\mathcal{S}_{\text{VMS}}(\boldsymbol{v}^h, q^h, \boldsymbol{u}_{n+1}^h, \boldsymbol{u}_*^h, p_{n+1}^h) = \left(\rho \boldsymbol{u}_*^h \cdot (\nabla \boldsymbol{v}^h)^T, \tau_{\text{M}}(\boldsymbol{u}_*^h) \boldsymbol{r}_{\text{M}}(\boldsymbol{u}_{n+1}^h, p_{n+1}^h)\right), \tag{2.46}$$

and

$$\mathcal{S}_{\text{LES}}(\boldsymbol{v}^h, q^h, \boldsymbol{u}^h_{n+1}, \boldsymbol{u}^h_*, p^h_{n+1}, p^h_{n+1,\text{EXT}}) =$$
$$\begin{cases} -(\rho\nabla\boldsymbol{v}^h, \tau_{\text{M}}(\boldsymbol{u}^h_{n+1})\boldsymbol{r}_{\text{M}}(\boldsymbol{u}^h_{n+1}, p^h_{n+1})\otimes \\ \tau_{\text{M}}(\boldsymbol{u}^h_{n+1})\boldsymbol{r}_{\text{M}}(\boldsymbol{u}^h_{n+1}, p^h_{n+1})), & \text{if non-linearities in implicit,} \\ -(\rho\nabla\boldsymbol{v}^h, \tau_{\text{M}}(\boldsymbol{u}^h_{n+1,\text{EXT}})\boldsymbol{r}^{\text{LHS}}_{\text{M,EXT}}(\boldsymbol{u}^h_{n+1}, p^h_{n+1})\otimes \\ \tau_{\text{M}}(\boldsymbol{u}^h_{n+1,\text{EXT}})\boldsymbol{r}_{\text{M,EXT}}(\boldsymbol{u}^h_{n+1,\text{EXT}}, p^h_{n+1,\text{EXT}})) \\ +(\rho\nabla\boldsymbol{v}^h, \tau_{\text{M}}(\boldsymbol{u}^h_{n+1,\text{EXT}})\boldsymbol{r}^{\text{RHS}}_{\text{M}}\otimes \\ \tau_{\text{M}}(\boldsymbol{u}^h_{n+1,\text{EXT}})\boldsymbol{r}_{\text{M,EXT}}(\boldsymbol{u}^h_{n+1}, p^h_{n+1})), & \text{if non-linearities in semi-implicit.} \end{cases} \tag{2.47}$$

We implemented the formulation of Equation (2.43) in life$^{\text{x}}$ [6], a C++ finite element library developed within the iHEART project [2] and based on the deal.II finite element core [4]. The fully implicit version of the method, bringing to a non linearity to be solved at each time-step, is solved via the Newton method. The linear system arising at each Newton iteration of each time-step is solved by the GMRES method. The linear system is preconditioned with the aSIMPLE preconditioner [69] and its blocks are preconditioned with an algebraic multigrid preconditioner based on Trilinos [12]. On the contrary, the semi-implicit formulation brings to a single linear system to be solved at each time-step that we precondition and solve in the same fashion.

2.6. Verification and validation

In this section, we verificate and validate the VMS-LES method by considering two benchmarks: the Taylor-Green vortex (TGV) in Section 2.6.1 and the FDA nozzle in Section 2.6.2.

The process of verification aims at ensuring that the mathematical model is implemented correctly and accurately solved. Specifically, according to [24], numerical code verification is performed by comparing numerical solutions to exact benchmarks solutions that are analytical or semi-analytical. In this context, we demonstrate the correct implementation of the VMS-LES method by comparing our numerical results with high-fidelity DNS data.

Differently, according to [24], the process of validation consists of assessing the degree to which the mathematical model and the numerical methods employed are an appropriate representation of the reality. Thus, validation is performed by comparing numerical solutions with in vitro or in vivo data. In this work, we validate the VMS-LES method

[2] *iHEART - An Integrated Heart model for the simulation of the cardiac function*, European Research Council (ERC) grant agreement No 740132, P.I. Prof A. Quarteroni.

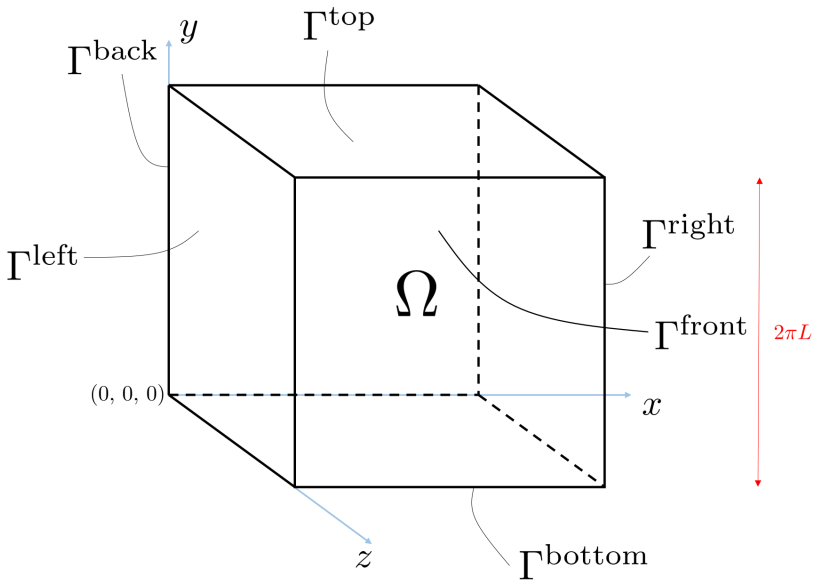

Figure 2.2: The cubic domain Ω for the TGV problem.

by comparing numerical solutions against experimental data. Furthermore, we also compare our numerical solutions with additional numerical results that we found in literature.

These works are performed during the MSc theses of Tommaso Tassi and Sara Perdoncin, for which I have been co-advisor. Specifically, Section 2.6.1 contains material from [250] and Section 2.6.2 from [197].

2.6.1. Numerical verification: the Taylor-Green vortex

The TGV is an unsteady flow describing the decaying of vortex in a cube. Firstly introduced in 1937 by G.I. Taylor and A.E. Green [254], nowadays the TGV represents a well established benchmark problem that allows to verify the correct implementation of the computational models and also to compare different turbulence models and numerical schemes [34, 59, 81, 83, 151, 283] against DNS data [42, 178].

The TGV problem is described by the NS equations with periodic BCs defined in the cubic domain $\overline{\Omega} = [0, 2\pi L]^3 \subset \mathbb{R}^3$ bounded by $\Gamma = \Gamma^{\text{top}} \cup \Gamma^{\text{bottom}} \cup \Gamma^{\text{front}} \cup \Gamma^{\text{back}} \cup \Gamma^{\text{left}} \cup \Gamma^{\text{right}}$ as displayed in Figure 2.2. We set *periodic BCs* along the three dimensions, meaning that a fluid particle passing from a cube boundary appears with the same velocity on the opposite side: For all $t \in (0, T_f)$, the periodic BCs read

$$\boldsymbol{u}|_{\Gamma^{\text{left}}} = \boldsymbol{u}|_{\Gamma^{\text{right}}}, \tag{2.48a}$$

$$\boldsymbol{u}|_{\Gamma^{\text{top}}} = \boldsymbol{u}|_{\Gamma^{\text{bottom}}}, \tag{2.48b}$$

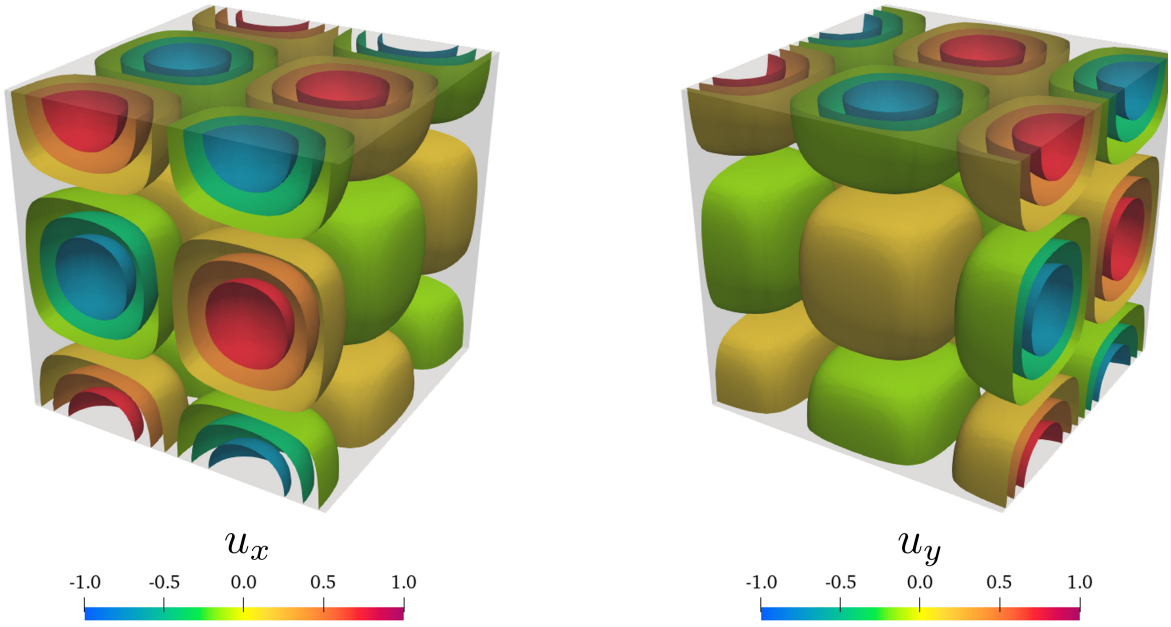

Figure 2.3: Initial condition of the TGV problem as reported in Equation (2.49): iso–contours of x and y components of velocity field.

$$\boldsymbol{u}|_{\Gamma^{\text{front}}} = \boldsymbol{u}|_{\Gamma^{\text{back}}}. \tag{2.48c}$$

The initial condition of the problem is expressed as

$$\boldsymbol{u}_0 = \boldsymbol{u}_0(\boldsymbol{x}) = \begin{bmatrix} U\sin(x/L)\cos(y/L)\cos(z/L) \\ -U\cos(x/L)\sin(y/L)\cos(z/L) \\ 0 \end{bmatrix} \quad \text{in } \Omega \times \{0\}, \tag{2.49}$$

being U and L the characteristic velocity and length. The latter are used also for the definition of the Reynolds number introduced in Equation (1.1). Specifically, we consider the case $U = 1$ m/s and $L = 1$ m, bringing to $\text{Re} = 1/\nu$, being $\nu = \frac{\mu}{\rho}$ the kinematic viscosity. Specifically, our numerical tests are performed by considering $\text{Re} = 1600$. Furthermore, coherently with the DNS data of [42, 178], we select as final time $T_f = 10$ s. Note that, since both L and U are set to unity, we will consider the time $t/(L/U)$ as a dimensionless quantity. In Figure 2.3 we display the initial condition in Equation (2.49).

The DNS data provided by [42, 178] consist in the temporal evolution of statistical properties of the flow, namely the normalized kinetic energy $\widetilde{E}_k$ and normalized dissi-

pation rate $\widetilde{D}$ expressed as:

$$\widetilde{E}_k(t) = \frac{1}{|\Omega|}\int_\Omega \frac{1}{2}|\boldsymbol{u}(\boldsymbol{x},t)|_2^2 \,\mathrm{d}\boldsymbol{x}, \tag{2.50}$$

and

$$\widetilde{D}(t) = -\frac{\mathrm{d}\widetilde{E}_k(t)}{\mathrm{d}t}. \tag{2.51}$$

being $|\Omega|$ the measure of Ω and $|\cdot|_2$ the Euclidean norm of a vector. We generated a structured mesh of the cube made of $N_{\text{el}} = n_{\text{el}}^3$ elements, being n_{el} the number of elements along each Cartesian direction. The reference data are obtained carrying out DNS on a mesh made of $N_{\text{el}} = 512^3$ [42, 178].

We carry out numerical simulations in life$^\times$ in a parallel framework[3]. Numerical simulations required from 20 up to 64 cores by employing meshes of different sizes. A preliminary study carried out with $\mathbb{Q}1$ - $\mathbb{Q}1$ FE spaces showed that accurate results are achieved if very fine grids are used ($N_{\text{el}} = 128^3$), significantly increasing the cost of our numerical simulations. On the contrary, we found that the usage of higher order FE allows to converge faster to the DNS data. For instance, in Figure 2.4 we compare the numerical results obtained with $\mathbb{Q}1$ - $\mathbb{Q}1$ and $\mathbb{Q}2$ - $\mathbb{Q}2$ FE spaces. By adopting a mesh made of $N_{\text{el}} = 32^3$, we found that the solution with linear FE is very far from the reference DNS data. On the contrary, quadratic elements allow to better capture the statistical flow properties.

Moreover, in Figure 2.5, we display the numerical solutions obtained with $\mathbb{Q}_2$–$\mathbb{Q}_2$ FE spaces and BDF3 with different resolution of the mesh, namely 32^3 and 64^3. We see that refining the grid the solution becomes more accurate either in terms of kinetic energy and dissipation rate.

We split the velocity gradient $\nabla\boldsymbol{u}$ into its symmetric $\boldsymbol{\epsilon}(\boldsymbol{u})$ and skew-symmetric $\boldsymbol{\omega}(\boldsymbol{u})$ parts:

$$\nabla\boldsymbol{u} = \frac{1}{2}\left(\nabla\boldsymbol{u} + (\nabla\boldsymbol{u})^T\right) + \frac{1}{2}\left(\nabla\boldsymbol{u} - (\nabla\boldsymbol{u})^T\right) = \boldsymbol{\epsilon}(\boldsymbol{u}) + \boldsymbol{\omega}(\boldsymbol{u}), \tag{2.52}$$

being respectively the strain-rate tensor (Equation (2.8)) and the rotation tensor. In order to identify coherent vortex structures, we introduce the scalar function [131]:

$$\mathsf{Q}(\boldsymbol{u}) = \frac{1}{2}\left(|\boldsymbol{\omega}(\boldsymbol{u})|_{\text{F}}^2 - |\boldsymbol{\epsilon}(\boldsymbol{u})|_{\text{F}}^2\right), \tag{2.53}$$

where $|\cdot|_{\text{F}}$ is the Frobenius norm of a tensor. If $\mathsf{Q}(\boldsymbol{u}) > 0$, the rotation of a fluid element becomes dominant over its stretching: the Q-criterion consists in analysing the isosurfaces of the positive part of $\mathsf{Q}(\boldsymbol{u})$ [131].

[3]Numerical simulations are performed on the cluster of the Department of Mathematics, Politecnico di Milano (5 nodes of 20 Intel Xeon E5-4610v2 @2.30GHz with a total number of 160 cores and 6 nodes of 12 Intel Xeon E5-2640v4 @2.40GHz with 120 cores)

We report the volume rendering of the velocity magnitude in Figure 2.6, and we display iso-contours of Q-criterion ($\mathsf{Q} = 0.25$ Hz^2) coloured according to velocity magnitude at different time instants in Figure 2.7. In Figure 2.7a we observe the eight-fold symmetry of the TGV at the initial time; as the time advances, the vortices descend on the symmetry plane forming vortex sheets (Figures 2.7b, 2.7c). The latter experience instability, and the flow starts to dissipate kinetic energy and the coherent structures previously observed are lost (Figure 2.7d). From that time, the flow becomes very chaotic, with interaction among smaller and smaller structures and the symmetry of the flow is lost.

VMS-LES showed a good agreement with reference data in the verification process carried out on the TGV benchmark problem. We found that if sufficiently coarse grid are employed, VMS-LES correctly reproduces reference data if at least second order FE spaces are considered.

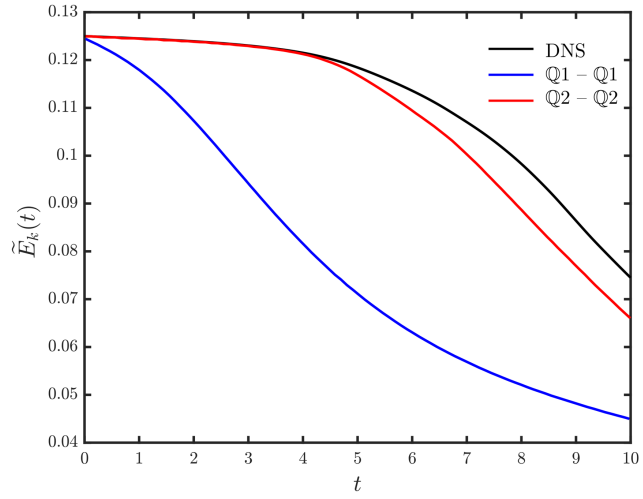

(a) Kinetic energy

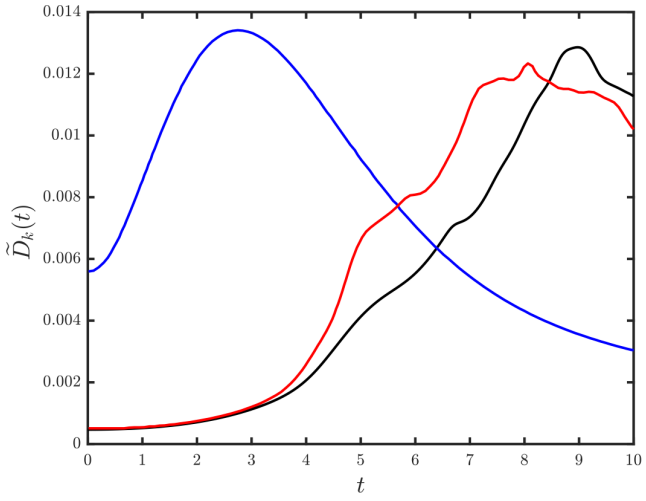

(b) Dissipation rate

Figure 2.4: Comparison between numerical results and DNS data [42, 178] using different FE spaces. VMS-LES, semi-implicit, $\Delta t = 2 \cdot 10^{-3}$, BDF1, $N_{\text{el}} = 32^3$. (a) kinetic energy; (b) dissipation rate.

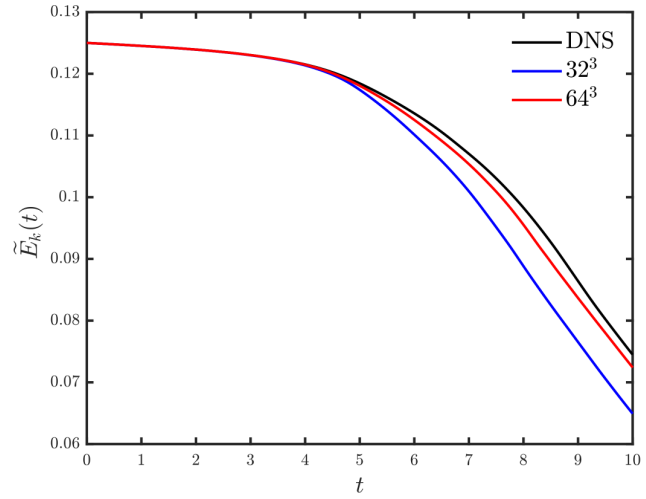

(a) Kinetic energy

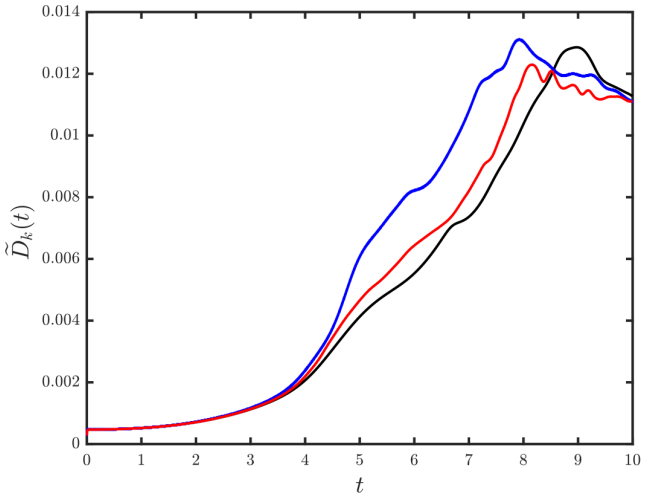

(b) Dissipation rate

Figure 2.5: Comparison between numerical results and DNS data [42, 178] using different grid resolutions. $\mathbb{Q}_2$ - $\mathbb{Q}_2$ VMS-LES, semi-implicit, $\Delta t = 2 \cdot 10^{-3}$, BDF3. (a) kinetic energy; (b) dissipation rate.

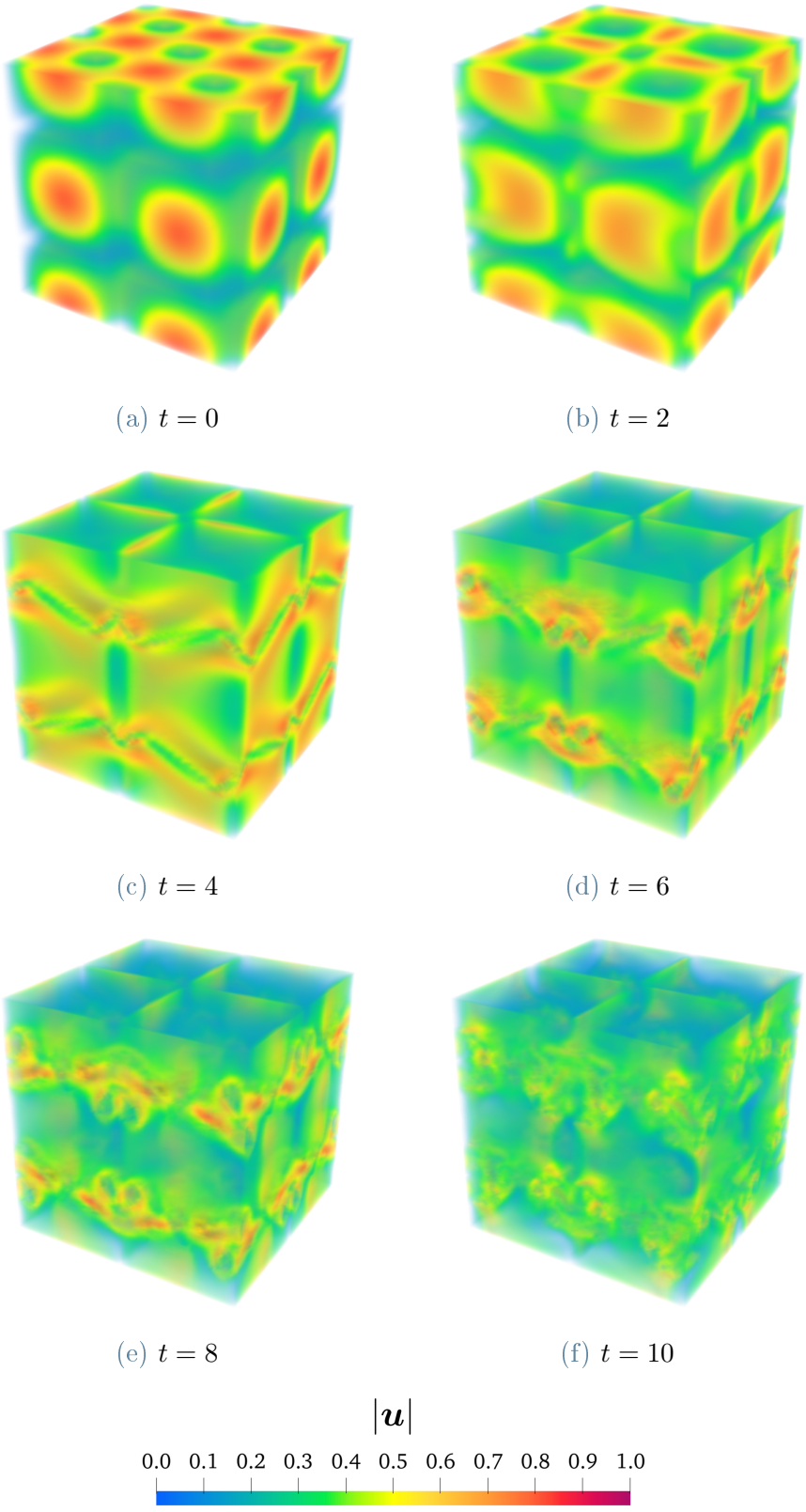

(a) $t = 0$ (b) $t = 2$

(c) $t = 4$ (d) $t = 6$

(e) $t = 8$ (f) $t = 10$

Figure 2.6: Volume rendering of velocity magnitude at different time instants.

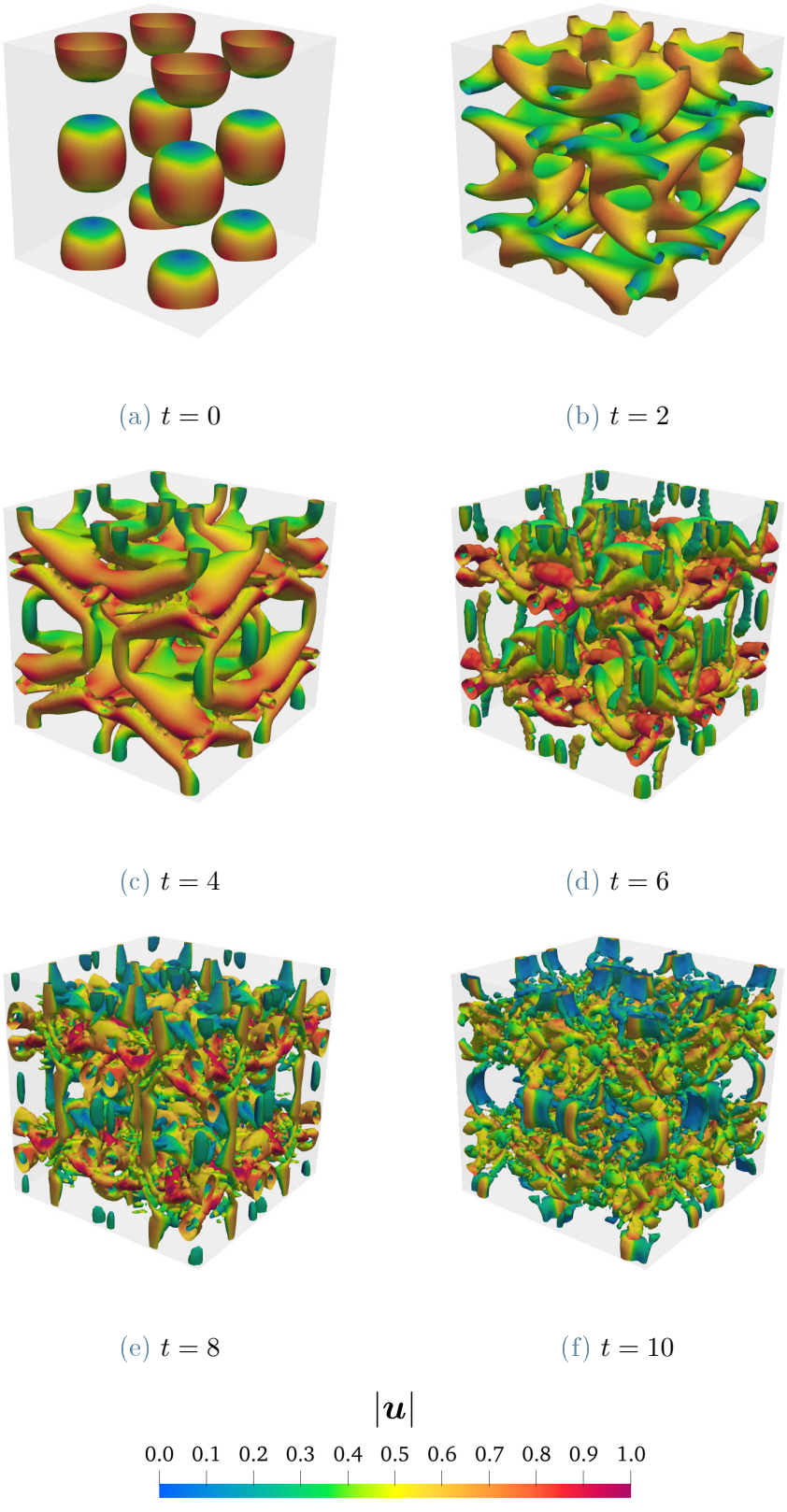

(a) $t = 0$ (b) $t = 2$

(c) $t = 4$ (d) $t = 6$

(e) $t = 8$ (f) $t = 10$

Figure 2.7: Iso-contours of Q-criterion with $\mathsf{Q} = 0.25$ Hz^2 coloured according to velocity magnitude at different time instants.

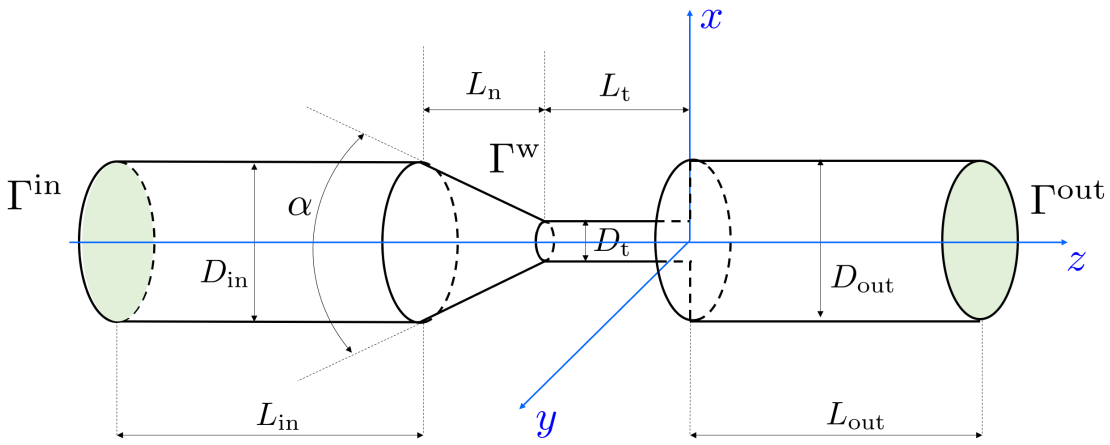

Figure 2.8: The FDA nozzle model.

D_{in} [mm]	D_t [mm]	D_{out} [mm]	L_{in} [mm]	L_n [mm]	L_t [mm]	L_{out} [mm]	α [°]
12	4	12	120	22.685	40	144	20

Table 2.1: Sizes of the FDA nozzle model.

2.6.2. Validation: the FDA nozzle

A critical issue in the cardiovascular modeling community is the validation of CFD models and methods, especially when transitional and turbulent regimes are involved. In this respect, the US *Food and Drug Administration* (FDA) launched in 2004 the "Critical Path Initiative" [5] proposing several benchmarking tests with features that characterize real medical devices. Specifically, to validate CFD models and methods, FDA proposed two benchmarks: the nozzle model (or sudden expansion case) and a blood pump model [161].

The nozzle benchmark proposed by the FDA [117] is geometrically sketched in Figure 2.8, and consists of an axisymmetric geometry. It is made of an inlet part of length L_{in} and diameter D_{in}; a conical convergent section (nozzle) of length L_n and characterized by the angle α; a throat of length L_t and diameter D_t and a sudden expansion region with length L_{out} and diameter D_{out}. Sizes of these lengths are provided in Table 2.1.

The fluid considered is the blood, modeled as an incompressible, viscous and Newtonian fluid of density $\rho = 1.056 \cdot 10^3\,\mathrm{kg/m^3}$ and dynamic viscosity $\mu = 3.5 \cdot 10^{-3}\,\mathrm{Pa \cdot s}$ [213]. The blood flow enters from the conical collector and exits from the expansion region. This benchmark is interesting from an hemodynamic point of view since it presents flow characteristics responsible for blood damage as flow separation, adverse pressure gradients, transition to turbulence and recirculation areas.

Re	Q [m^3/s]
500	$5.2062{\cdot}10^{-6}$
3500	$3.6444{\cdot}10^{-5}$

Table 2.2: Reynolds numbers and corresponding volumetric flow rates for the simulated flow regimes.

Let $\Omega \subset \mathbb{R}^3$ be the spatial domain – displayed in Figure 2.8 – bounded by $\Gamma = \Gamma^{\text{in}} \cup \Gamma^{\text{w}} \cup \Gamma^{\text{out}}$, being Γ^{in}, Γ^{out} and Γ^{w} the inlet, outlet sections and wall respectively. For this benchmark problem, the Reynolds number is referred to the throat section and hence defined as:

$$\text{Re} = \frac{\rho \overline{u}_{z,\text{t}} D_{\text{t}}}{\mu} = \frac{4\rho Q}{\pi D_{\text{t}} \mu}. \tag{2.54}$$

We denoted with $\overline{u}_{z,\text{t}}$ the mean axial velocity in the throat region and Q the volumetric flow rate, with $Q = \overline{u}_{z,\text{t}} \pi \frac{D_t^2}{4}$. In order to reproduce different operating conditions of medical devices, the FDA collected experimental data for this benchmark at different Reynolds regimes. Specifically, we considered two different Reynolds numbers namely Re = 500 and 3500 that correspond to a laminar and turbulent flow respectively. We report in Table 2.2 the Reynolds number and the corresponding volumetric flow rates.

Problem setup

For the FDA nozzle benchmark, we set a null initial condition $\boldsymbol{u}_0 = \boldsymbol{0}$ and no body forces are employed ($\boldsymbol{f} = \boldsymbol{0}$). Regarding the BCs, on the inlet section we set a Dirichlet BC; specifically, by considering that the flow is always laminar on Γ^{in}, we prescribe a Poiseuille velocity profile. Moreover, since the typical wall roughness value for medical devices is less than 0.5 microns, we prescribe a no-slip BC on Γ^{w}, as suggested in [293]. Concerning the outlet section Γ^{out}, as in [68], we prescribe a homogeneous Neumann BC. Thus, the BCs for the FDA benchmark problem reads:

$$\boldsymbol{u} = \boldsymbol{u}^{\text{in}} \qquad \text{on } \Gamma^{\text{in}} \times (0, T_f), \tag{2.55}$$

$$\boldsymbol{u} = \boldsymbol{0} \qquad \text{on } \Gamma^{\text{w}} \times (0, T_f), \tag{2.56}$$

$$\boldsymbol{\sigma}(\boldsymbol{u}, p)\boldsymbol{n} = \boldsymbol{0} \qquad \text{on } \Gamma^{\text{out}} \times (0, T_f). \tag{2.57}$$

Specifically, for the inlet BC, we define $\boldsymbol{u}^{\text{in}}$ as

$$\boldsymbol{u}^{\text{in}}(\boldsymbol{x}, t) = -\frac{2Q}{\pi(D_{\text{in}}/2)^2} \left(1 - \frac{r^2(\boldsymbol{x})}{(D_{\text{in}}/2)^2}\right) u(t)\boldsymbol{n}, \tag{2.58}$$

being $r(\boldsymbol{x})$ the radial position and $u(t)$ a scalar time dependent function that brings the inlet velocity from the null initial condition to the regime value in a time equal to

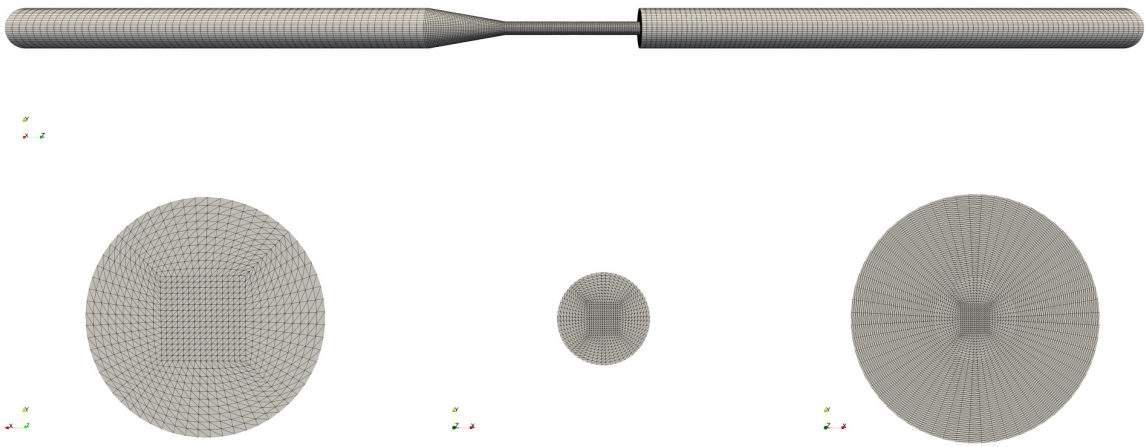

Figure 2.9: Hexaedral mesh of the FDA nozzle. On the top: frontal view; on the bottom: focus on three cross-sections: inlet, throat and outlet sections.

T_{load}:

$$u(t) = \begin{cases} \frac{1}{2}\left(1 - \cos\left(\frac{\pi t}{T_{\text{load}}}\right)\right), & \text{if } t < T_{\text{load}}, \\ 1, & \text{if } t \geq T_{\text{load}}. \end{cases} \tag{2.59}$$

We generate hexaedral meshes of the nozzle by employing gmsh [108]. Specifically, for the sections of the nozzle we use OH grid topology [38] and we refine more the throat and outlet sections since the validation is carried out mainly on these areas. The wall of the nozzle is then obtained by extruding the cross-sections. We report a mesh of the FDA in Figure 2.9.

Numerical results

We present numerical results of the validation for two different Reynolds regimes, namely laminar (Re = 500) and turbulent (Re = 3500). All the comparison are made on dimensionless fluid properties, as reported in [116]. Specifically, the velocity is normalized with respect to the average velocity in the inlet section $\overline{u}_{\text{in}} = Q/\left(\pi(D_{\text{in}}/2)^2\right)$ as

$$\boldsymbol{u}^{\text{norm}} = \frac{\boldsymbol{u}}{\overline{u}_{\text{in}}}. \tag{2.60}$$

The validation in terms of pressure is carried out by means of a normalized pressure drop defined as

$$\Delta p^{\text{norm}} = \frac{p - p_{z=0}}{\frac{1}{2}\rho\overline{u}_{\text{t}}^2}, \tag{2.61}$$

		Coarse	Medium	Fine
Number of cells		7'325	36'128	152'700
DOFs $\mathbb{Q}1$-$\mathbb{Q}1$	$\boldsymbol{u}^h$	24'696	116'442	478'410
	p^h	8'232	38'814	159'470
	total	32'928	155'256	637'880
h_{min} [m]		$2.31 \cdot 10^{-3}$	$1.26 \cdot 10^{-3}$	$6.00 \cdot 10^{-4}$
h_{avg} [m]		$6.20 \cdot 10^{-3}$	$3.10 \cdot 10^{-3}$	$1.53 \cdot 10^{-3}$
h_{max} [m]		$8.38 \cdot 10^{-3}$	$4.10 \cdot 10^{-3}$	$2.08 \cdot 10^{-3}$

Table 2.3: Case Re = 500: specifics on the three grid levels employed.

being $p_{z=0}$ the pressure in $z = 0$ (see Figure 2.8) and $\overline{u}_{\text{t}} = Q/\left(\pi(D_{\text{t}}/2)^2\right)$ the average velocity in the throat section.

We perform numerical simulations in life$^{\text{x}}$ in a parallel framework[4]. Numerical simulations required from 20 up to 64 cores by employing meshes of different sizes and different Reynolds regimes.

Laminar case: Re = 500

We present a mesh convergence study for the case Re = 500. For all the following simulations, we set $\Delta t = 10^{-3}$ s, $T_{\text{load}} = 0.01$ s and $T_f = 2$ s. This choice of the final time allows to get a fully developed flow. Non linearities are treated in a semi-implicit fashion and $\mathbb{Q}_1 - \mathbb{Q}_1$ FE spaces are set for velocity and pressure. We use the BDF method of order 1 and the VMS-LES method as stabilization method.

We consider three mesh levels, namely coarse, medium and fine mesh; in Table 2.3 we report specifics on the three grid levels used. In Figure 2.10 we report velocity magnitude, pressure and a surface Line Integral Convolution (LIC) visualization on a slice using the fine mesh at the final time. The flow regime is laminar throughout the domain, and the velocity increases in the conical and throat regions and it decreases in the expansion region. Nor breaking down of the jet, nor flow instabilities are observed. Figure 2.10c shows symmetric recirculation regions in the proximity of the wall. The pressure, almost constant in the inlet region, experiences a fast decrease in the conical collector and a slower decrease in the throat.

In Figure 2.11 we compare the numerical results with the experimental data in terms of normalized axial velocity (Figure 2.11a) and normalized pressure drop (Figure 2.11b). Concerning axial velocity, all the numerical simulations show a good match with the

[4]Numerical simulations are performed on the cluster of the Department of Mathematics, Politecnico di Milano (5 nodes of 20 Intel Xeon E5-4610v2 @2.30GHz with a total number of 160 cores and 6 nodes of 12 Intel Xeon E5-2640v4 @2.40GHz with 120 cores)

	DNS [193]	LES [68]	RANS [243]	VMS-LES (present study)
Δp^{norm} on Γ^{in} [–]	3.50	4.17	3.16 ÷ 4.10	3.49

Table 2.4: Case Re = 500: normalized pressure drop computed on the inlet section: comparison between numerical results obtained with different turbulence models available in literature and the results obtained in the present study on the fine grid.

reference data and no noticeable discrepancies are observed between the grid levels. The coarse solution mainly differs from the finer ones in region downstream the sudden expansion. In terms of normalized pressure drop, experimental data show a huge variability of the solution making hence the comparison with the numerical results not very significant. The same issue is met also in other groups that carried out CFD simulations on this benchmark [68, 193, 243], and this mismatch among experimental data might be related to experimental errors at the normalization point [243]. In Table 2.4, we list the normalized pressure drop computed on the inlet section compared with the results obtained by the aforementioned groups. We found that the numerical results obtained with VMS-LES are very accurate compared to the other CFD groups and in line with the DNS results of [193].

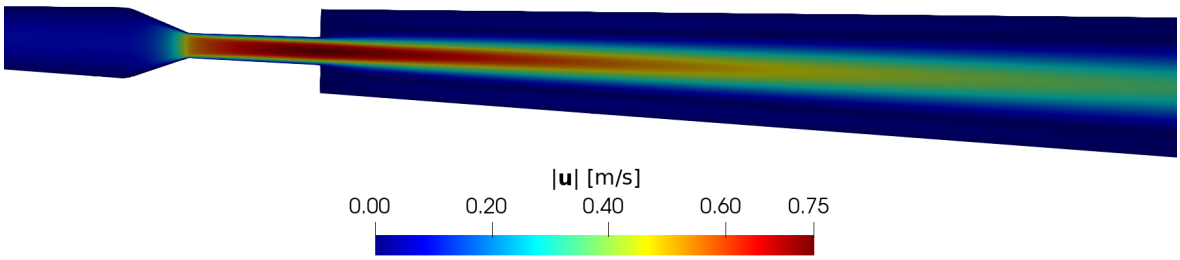

(a) velocity magnitude

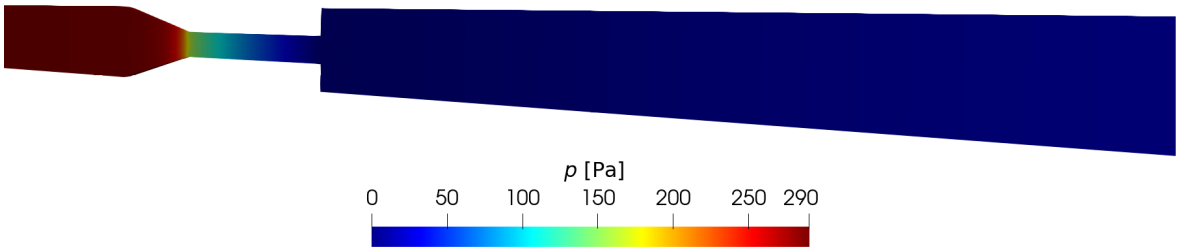

(b) pressure

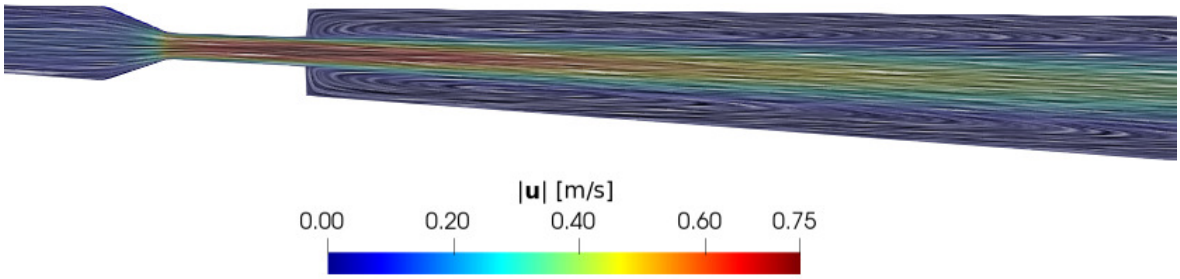

(c) Surface LIC

Figure 2.10: Case Re = 500, results on a slice using the fine mesh at $T_f = 2.0$ s. (a) velocity magnitude; (b) pressure; (c) surface LIC visualization colored according to velocity magnitude. Images from [197].

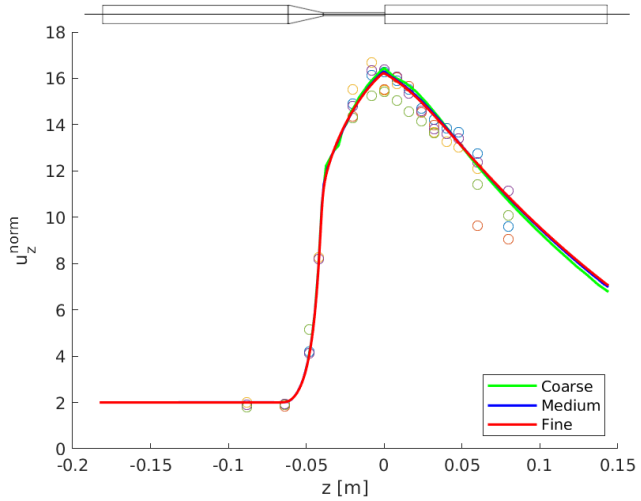

(a) Normalized axial velocity

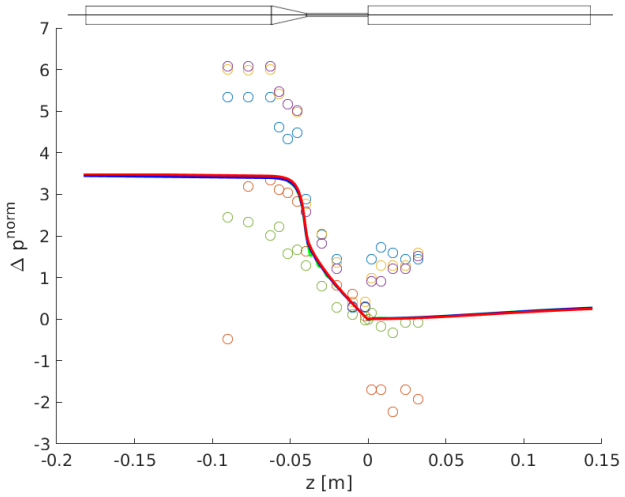

(b) Normalized pressure drop

Figure 2.11: Case Re = 500, comparison between experimental data (circles) and numerical results (lines) along the centerline using three mesh levels. (a) normalized axial velocity; (b) normalized pressure drop. Legend in (a) is common to both subfigures. Images from [197].

h [m]			cells	DOFs ($\mathbb{Q}_1 - \mathbb{Q}_1$)		
min	avg	max		$\boldsymbol{u}$	p	total
$4.83 \cdot 10^{-4}$	$1.39 \cdot 10^{-3}$	$2.13 \cdot 10^{-3}$	461'925	1'420'560	473'520	1'894'080

Table 2.5: Case Re = 3500: specifics on the mesh.

Turbulent case: Re = 3500

For the simulation with Re = 3500, surely most involving than the laminar case, we use a mesh with 1.8 million of DOFs ($\mathbb{Q}1$ - $\mathbb{Q}1$). Specifics on the mesh adopted are reported in Table 2.5. We set $\Delta t = 10^{-4}$ s and, following [193], we consider as final time $T_f = 0.5$ s. Flow statistics are gathered in the last 0.1 seconds. The simulation considered for the numerical results took about two weeks using 32 cores.

In Figures 2.12a and 2.12b we report velocity magnitude and pressures on a slice. Differently from the laminar case, we observe a higher speed jet that breaks down in the sudden expansion region. This gives rise to turbulence effects, that are directly reflected also in the pressure field. We visualize the formation of vortices by means of iso-contours of Q-criterion [131] coloured with vorticity magnitude.

We compare the VMS-LES numerical results achieved with experimental data and, when available, with DNS and LES data respectively taken from [193] and [68]. We compare the results in terms of radial distribution of normalized axial velocity at different positions along the nozzle centerline in Figure 2.13. VMS-LES correctly reproduces the Poiseuille velocity profile measured in the inlet part of the nozzle (Figure 2.13a). We display the results in the throat section in Figure 2.13b: the VMS-LES shows a typical flat, turbulent profile in good agreement with the experimental data and also with the DNS results of [193]. The LES results of [68] are in line with our results and accurate with respect to experiments; however they underestimate the velocity peak of about 6% with respect to the peak predicted by DNS. We show in Figures 2.13c and 2.13d the comparison in the sudden expansion region. We found this was the most difficult part to reproduce, since the position of the jet breakdown is strongly influenced by the setup of our simulation. In Figure 2.13c, we observe that the VMS-LES results underestimate the velocity peak measured with experiments but they better agree with the DNS data: the velocity trend near the wall is well captured but, in the central region, both numerical results show a profile flatter then experiments. In Figure 2.13d we observe that both LES and VMS-LES results are quite accurate, almost reproducing the flat profile described by experiments. Specifically, VMS-LES and LES have a maximum discrepancies with experiments of 9% and 13% respectively.

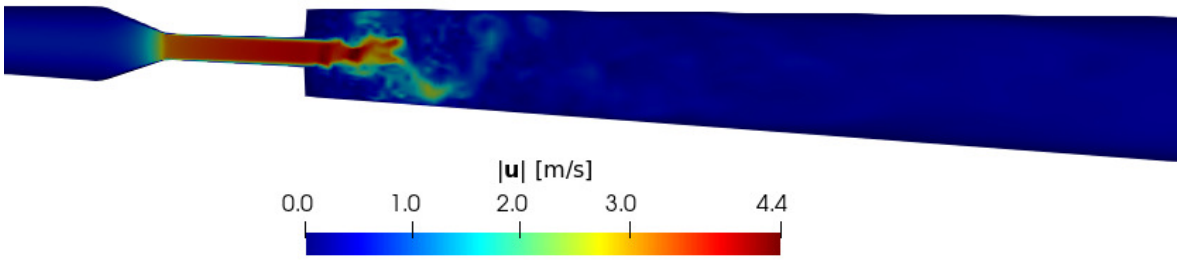

(a) velocity magnitude

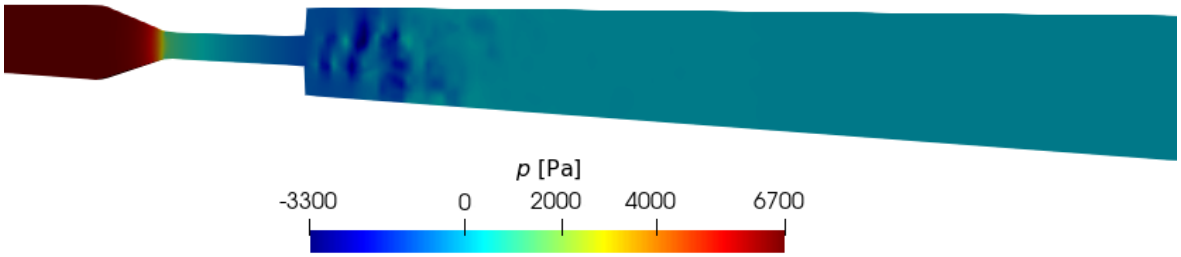

(b) pressure

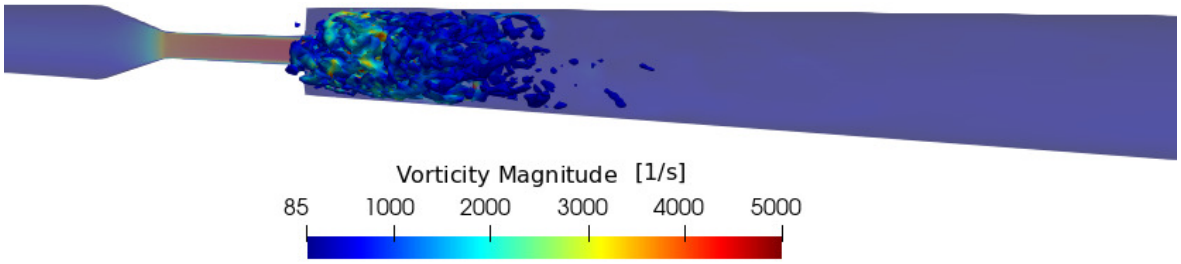

(c) Q-criterion

Figure 2.12: Case Re = 3500, results at $T_f = 0.5$ s. (a) velocity magnitude; (b) pressure; (c) iso–contours of Q-criterion coloured with vorticity magnitude. Images from [197].

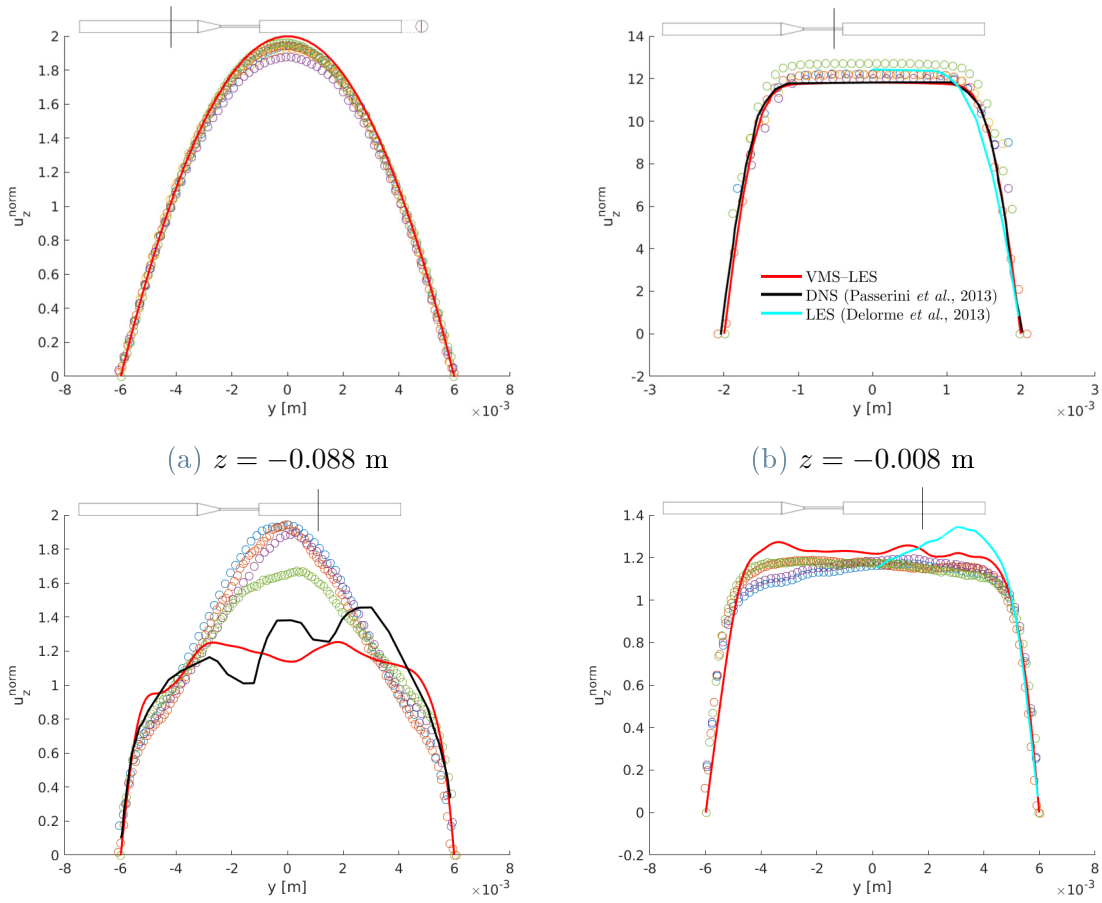

(a) $z = -0.088$ m

(b) $z = -0.008$ m

(c) $z = 0.06$ m

(d) $z = 0.08$ m

Figure 2.13: Case Re = 3500, comparison between experimental data (circles) and numerical results (lines) for the radial distribution of normalized axial velocity at different positions along the nozzle centerline. DNS and LES data are respectively taken from [193] and [68]. Legend in (b) is common to (c) and (d). Images from [197].

Finally, in Figure 2.14 we compare the numerical results with experimental data in terms of normalized axial velocity and pressure drop along the centerline. In Figure 2.14a, we observe that VMS-LES results are in accordance with experimental data, DNS and LES results in the inlet and conical regions: they correctly reproduce the laminar inlet and the increasing velocity due to the convergent part of the nozzle. In the throat, our results are in good agreement with DNS, but they slightly underestimate LES and experimental data of about 6%. As previously mentioned, the huge differences are observed in the region downstream the sudden expansion: the VMS-LES underestimates the location of the jet breakdown, bringing to lower velocities.

In terms of pressure, in Figure 2.14b, we observe that in the inlet region there is an excellent agreement between experiments, DNS and VMS-LES results. LES overestimates the pressure values of about 12 %, even if it remains in the range of experimental data. The fast pressure decrease is correctly captured by all the simulations; in the sudden expansion region we recognize two plateau and VMS-LES well reproduces both of them, even if the comparison for the second one can be made only in terms of other numerical simulations, since experimental data are not available.

2.7. Concluding remarks

We presented the mathematical models and the numerical methods describing transitional and turbulent flows that we will adopt throughout this thesis. We introduced the VMS-LES method that we implemented in the FE library life^{x}. A verification process is performed by comparing the numerical results against DNS data on the TGV benchmark problem; validation is carried out through CFD simulations of the FDA nozzle. VMS-LES showed a good agreement with reference data in both benchmarks considered. For the TGV problem, if relatively coarse grids are employed, VMS-LES correctly reproduces reference data if at least second order FE spaces are considered. A good agreement with $\mathbb{Q}_1 - \mathbb{Q}_1$ FE spaces is obtained if the underlying grid is fine enough. In the FDA nozzle problem, we found that VMS-LES is fully effective also in the laminar case producing an excellent agreement with experiments and DNS results. In the turbulent case, we found that the main issue was related in accurately predicting the velocity profiles in the region close to the jet breakdown, and the position of the latter is strongly influenced by the parameters used for the numerical discretization of the problem, as the time-step size and the granularity of the mesh employed.

The accuracy of VMS-LES method (and residual-based stabilization methods in general) is strongly related to the way the fine-scale terms are approximated: a quasi-static approach may bring to the divergence of the stabilization parameters, and a possibile solution is to rely on a fine-scales dynamic approximation [57, 84]. Moreover, a critical issue in these methods is the choice of the stabilization parameters: many definitions can be found in literature and they are tipically designed for 1D problems and then extended to 3D problems in a straightforward fashion [195]. However, differently from

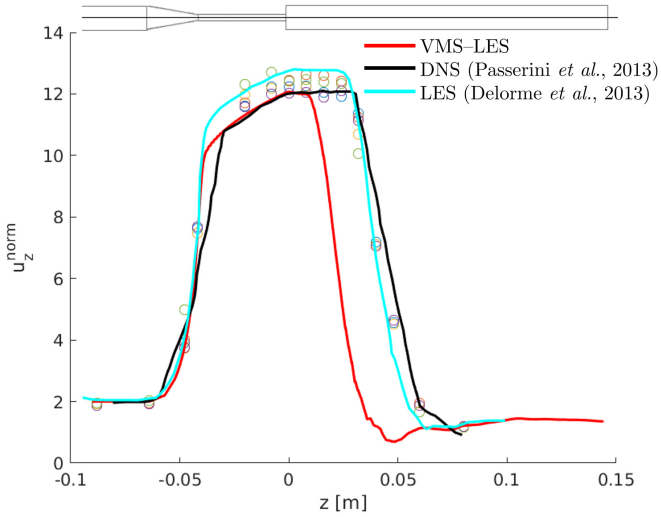

(a) Normalized axial velocity

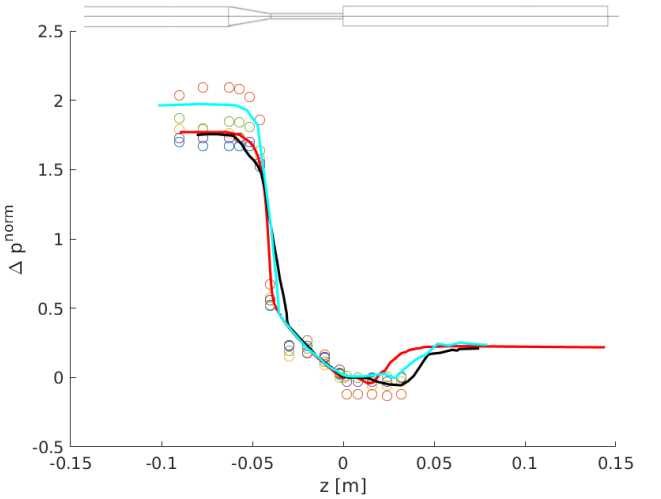

(b) Normalized pressure drop

Figure 2.14: Case Re = 3500, comparison between experimental data (circles) and numerical results (lines) along the centerline: (a) normalized axial velocity; (b) normalized pressure drop. DNS and LES data are respectively taken from [193] and [68]. Legend in (a) is common to both subfigures. Images from [197].

the 1D case, the extension to 2D and 3D problems does not guarantee nodally exact solution, neither in the case of simpler PDEs as the advection–diffusion problem. In Chapter 3, with the aim of enhancing the accuracy of stabilization methods, we present a machine-learning based strategy to provide optimal stabilization parameters.

3 | A machine-learning based stabilization method

In the following, we present a machine-learning based strategy to enhance the accuracy of stabilization methods. Specifically, we consider the simple case of the SUPG method for the advection-diffusion equation.

This chapter is organized as follows: in Section 3.1 we describe the general context in terms of stabilization methods for advection-dominated problems and the role played by machine learning (ML) in the scientific computing to enhance numerical methods and CFD models. In Section 3.2, we recall the SUPG stabilization method for advection-diffusion equations; in Section 3.3, we present our numerical strategy. We validate our strategy in Section 3.4 and in Section 3.5 we present the numerical results. Concluding remarks are drawn in Section 3.6.

The content of this chapter is reported in [251].

3.1. Stabilization methods for advection diffusion problems and ANNs

The Galerkin FE method applied to PDEs with advection terms dominating over diffusion ones may suffer of numerical instability [128, 207]. These numerical instabilities cause the numerical solution to exhibit oscillations that increase in amplitude with a local increment of the transport dominance over diffusion, i.e. as soon as the local Pèclet number becomes larger than one. In order to eliminate (or at least mitigate) numerical instabilities, a general employed strategy is to consider the generalized Galerkin method, i.e. the Galerkin method with additional stabilization terms [207]. Examples of stabilization methods to reduce numerical oscillations in the advection dominated regimes are for instance the upwind and streamline-diffusion method, both methods that are not strongly consistent. Instead, examples of strongly consistent methods are the Galerkin-Least-Squares, the SUPG, and the Douglas-Wang methods [43, 207, 226]. In particular, as we saw for the VMS-LES method for the NS equations in Chapter 2, for

these strongly consistent stabilization method, the formulation depends on the residual of the PDE (in strong formulation), other than on the stabilization parameter whose definition is crucial for the success of the stabilization strategies. Determining the values of such parameter is not straightforward, especially for 2D and 3D problems. In addition, a universal formulation of such parameter is lacking, especially as it is strongly dependent on data of the model and the numerical setting used for the FE approximation of the PDEs, e.g. low and high order FE methods, spectral element methods, isogeometric methods, etc. [45, 62, 232]. Some of the formulations for the stabilization parameter have been derived from analytical considerations on the differential problem in 1D, others are suitable only for a specific numerical approximation method, while the most comprehensive ones incorporate some (empirical) dependence on numerical setting, as e.g. the order of the FE [40, 43, 54–56, 94, 101, 217, 233, 234, 257].

In the following, we propose using Machine Learning (ML) [110, 176, 284] to make computers learn autonomously the values of the stabilization parameter for the FE approximation of advection dominated PDEs. ANNs [155, 184], are widely popular in ML and Deep Learning for a wide array of applications: they are indeed very versatile tools that are increasingly finding their way in scientific computing [179], especially in the context of numerical approximation of PDEs. For instance, as substitute to standard numerical methods, ANNs can be employed as meshless methods in Physics Informed Neural Networks (PINNs) to directly approximate the solution of the PDE as it is trained by minimizing the (strong) residual of the PDE [214–216]. ANNs are also largely employed in a data-driven fashion in the context of model order reduction for parametric PDEs [98, 99, 114, 120, 219, 286] and to enhance the stability properties of numerical methods for PDEs [71, 137]. In fluid dynamics modelling, ANNs are massively adopted for flow features extractions, modelling, optimization and control. For flow features extractions through clustering and classification to classify wake topologies [60]; for modeling fluid dynamics by reconstructing specific flows such as the near wall field in a turbulent flow [173] and for flow optimization [183], and control for aerodynamics applications [33]. ANNs are also used in a data-driven framework as a manner for providing alternative closure models for RANS' stress tensor [79], for sub-grid scale models in LES turbulence models [281, 282, 290], or for model learning input-output relationships in complex physical processes [220].

3.2. The SUPG method for advection-diffusion problems

We briefly recall the advection-diffusion differential problem and the SUPG stabilization method for the advection dominated regime. Let $\Omega \in \mathbb{R}^d$, $d = 1, 2, 3$ be the physical domain with $\partial\Omega$ being its boundary. We consider the following problem in

the unknown function u:

$$\begin{cases} -\nabla \cdot (\mu \nabla u) + \boldsymbol{\beta} \cdot \nabla u = f & \text{in } \Omega, \\ u = g & \text{on } \partial\Omega, \end{cases} \tag{3.1}$$

where μ, $\boldsymbol{\beta}$, and f are assigned functions or constants, with $\mu \in L^\infty(\Omega)$, $\boldsymbol{\beta} \in [L^\infty(\Omega)]^d$, with $\nabla \cdot \boldsymbol{\beta} \in L^2(\Omega)$, and $f \in L^2(\Omega)$. The Dirichlet datum on the boundary is $g \in H^{1/2}(\partial\Omega)$. Let $V_g = \{v \in H^1(\Omega) : v|_{\partial\Omega} = g\}$ and $V_0 = H_0^1(\Omega)$, the weak formulation of Equation (3.1) reads

$$\text{find } u \in V_g \ : \ a(v,u) = (v,f) \quad \text{for all } v \in V_0. \tag{3.2}$$

with the bilinear form $a(v,u)$ defined as:

$$a(v,u) := (\nabla v,\, \mu\, \nabla u) + (v,\, \boldsymbol{\beta} \cdot \nabla u)\,,$$

We consider a family of function spaces $v^h \subset V$ (either for V_g and V_0) dependent on a parameter h such that $\dim(v^h) = N_h < \infty$. Let $X_r^h = \{v^h \in C^0(\overline{\Omega}) : v^h|_K \in \mathbb{P}_r, \text{ for all } K \in \mathcal{T}^h\}$ be the function space of the FE discretization with piecewise Lagrange polynomials of degree $r \geq 1$, $\mathcal{T}^h$ a triangulation of Ω and h the characteristic size of the mesh, comprised of elements $K \in \mathcal{T}^h$. By setting $v^h = \mathring{X}_h^r \bigcap V_0$, the Galerkin FE method applied to Equation (3.2) reads

$$\text{find } u^h \in V_g^h \ : \ a(u^h, v^h) = F(v^h) \quad \text{for all } v^h \in V^h, \tag{3.3}$$

where $V_g^h = X_r^h \bigcap V_g$. The standard Galerkin-FE method in Equation (3.3) can generate numerical oscillations on u^h if the problem is dominated by the advection term. In particular, these numerical instabilities can arise if the local Péclet number is $\mathbb{P}\mathrm{e}_h > 1$, where

$$\mathbb{P}\mathrm{e}_h = \frac{|\boldsymbol{\beta}| h}{2\mu}. \tag{3.4}$$

The generalized Galerkin method ([209]) allows eliminating or mitigating numerical oscillations by adding stabilization terms to the standard Galerkin formulation as

$$\text{find } u^h \in V_g^h \ : \ a(v^h, u^h) + b_h(v^h, u^h) = (v^h, f) \quad \text{for all } v^h \in V^h. \tag{3.5}$$

In the SUPG method, the additional stabilization term reads:

$$b_h(v^h, u^h) = \left(\frac{1}{2} \left(\nabla \cdot (\boldsymbol{\beta} v^h) + \boldsymbol{\beta} \cdot \nabla v^h \right),\, \tau R(u^h) \right) \tag{3.6}$$

where $R(u^h)$ stands as the residual in strong formulation of Equation (3.1), which is defined as:

$$R(u^h) := -\nabla \cdot (\mu \nabla u^h) + \boldsymbol{\beta} \cdot \nabla u^h - f.$$

The term τ, appearing in Equation (3.6), is the *stabilization parameter*, which is the focus of this work. A universal and optimal definition of τ in terms of the problem data, numerical settings like the mesh size and FE degree is lacking. An extensive review of stabilization parameters for the SUPG method is reported in [135]. The most common choices for τ come from an analytic derivation made for the advection-diffusion problem in 1D with $f = 0$ and approximated by means of linear finite elements, which reads:

$$\widetilde{\tau}_1 = \frac{h}{2|\boldsymbol{\beta}|}\,\xi(\mathbb{P}\mathrm{e}_h), \tag{3.7}$$

where $\xi(\theta)$ is the upwind function:

$$\xi(\theta) = \coth(\theta) - \frac{1}{\theta}, \quad \theta > 0.$$

The stabilization parameter $\widetilde{\tau}_1$ is generally defined locally, i.e. mesh element by element. If a uniform mesh is used, as we consider in this chapter, then the value of h is uniform over $\mathcal{T}^h$; if in addition $\boldsymbol{\beta}$ is a constant, then this implies that τ is uniform over $\mathcal{T}^h$. The choice of τ made in Eq. (3.7) represents an optimal choice of the stabilization parameter as it yields a nodally exact numerical solution for the 1D advection-diffusion problem if $f = 0$ and the FE polynomial order is $r = 1$ [101, 207]. Thus, the stabilization parameter of Eq. (3.7) may not be fully effective to provide the optimal stabilization for a general advection-diffusion problem, e.g. to guarantee a nodally exact solution in 2D/3D or when using FE degrees larger than $r = 1$. A commonly used generalization of the formula of Eq. (3.7) to higher FE degrees ($r > 1$) is presented in [101] and reads:

$$\widetilde{\tau}_r = \frac{h}{2|\boldsymbol{\beta}|r}\,\xi\left(\frac{\mathbb{P}\mathrm{e}_h}{r}\right). \tag{3.8}$$

Differently from Eq. (3.7), the stabilization parameter $\widetilde{\tau}_r$ in Eq. (3.8) takes into account the contribute of higher polynomial degrees r. Still, this formula is not optimal as it does not guarantee a nodally exact numerical solution. Our goal is to find a general and optimal expression of the stabilization parameter holding for advection-diffusion problems and FE approximations of degree $r \geq 1$ to be dependent on: the dimension d, the FE degree r, the mesh size h, the forcing term f, the diffusion coefficient μ and the transport coefficient β.

3.3. ANN-based approach for determining the optimal stabilization parameter

We present our approach to determine the optimal stabilization parameter τ for the SUPG stabilization method by using an ANN. We consider as features (inputs) of our ANN: the degree of finite element r, the mesh size h and the global Péclet number

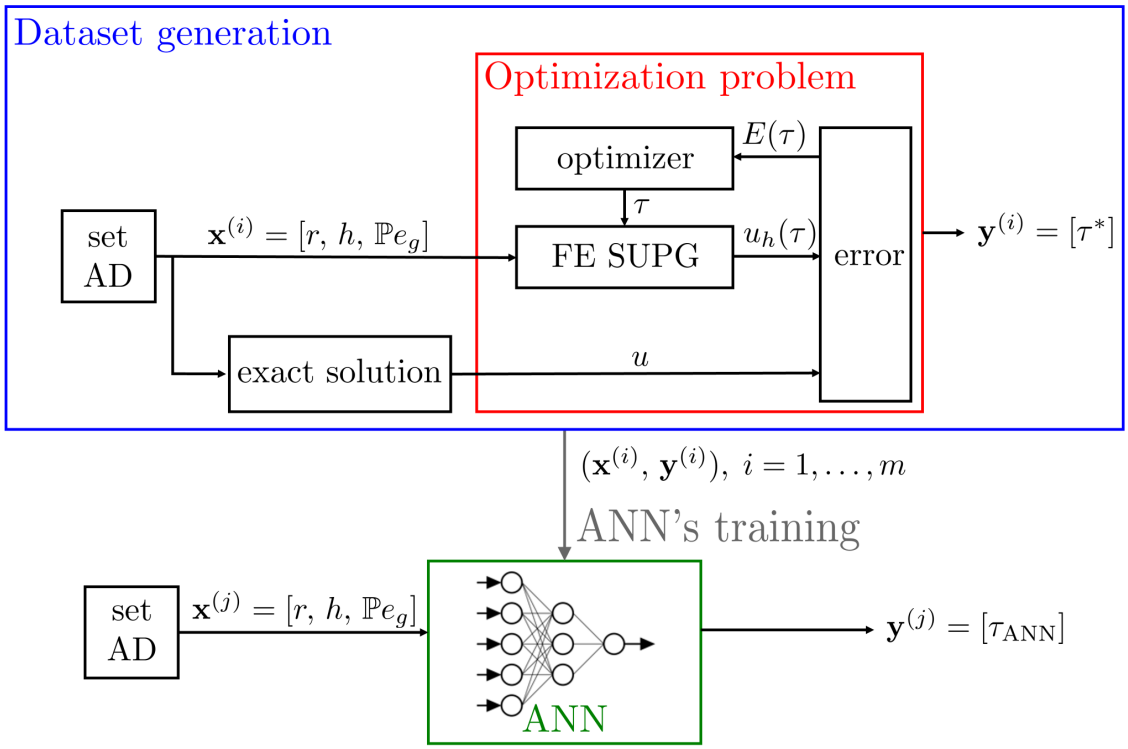

Figure 3.1: Representation of the strategy used for learning the the relation among τ and the advection-diffusion parameters and numerical settings

$\mathbb{P}e_g := |\boldsymbol{\beta}|L/(2\mu)$ of the advection-diffusion problem, where L is the characteristic length of the problem. As we consider $\boldsymbol{\beta}$ to be uniform and fixed, using $\mathbb{P}\mathrm{e}_g$ as input corresponds to varying the value of the diffusion coefficient μ. The features (input) of the ANN read:

$$\mathbf{x}^{(i)} = [r,\, h,\, \mathbb{P}\mathrm{e}_g]\,, \tag{3.9}$$

the *target* (output) of interest is the optimal SUPG stabilization parameter that we denote with τ^*:

$$\mathbf{y}^{(i)} = [\tau^*]\,. \tag{3.10}$$

The first step consist in generating the dataset, i.e. pairs of inputs and outputs to be used for training the ANN (*data generation* step). This consists in choosing repeatedly and randomly values of the features $\mathbf{x}^{(i)}$ in given ranges. These features are used to feed an *optimization problem* that, through an optimizer and a suitable error measure, provide an optimal stabilization parameter $\mathbf{y}^{(i)}$, i.e. the target of the given feature. Such optimization problem considers as error measure $E(\tau)$: the mismatch between the numerical solution u^h and the exact one u over the nodes of the FE mesh. $E(\tau)$

reads as:

$$E(\tau) = \sum_{k=1}^{K_h} |\, e(\boldsymbol{x}_k, \tau)\,|, \qquad e(\boldsymbol{x}_k, \tau) = u^h(\boldsymbol{x}_k; \tau) - u(\boldsymbol{x}_k). \tag{3.11}$$

being $\boldsymbol{x}_k$ the k-th node of the FE mesh $\mathcal{T}^h$ and K_h its number. To find the minimum of $E(\tau)$ for different problem configurations we solve, for each instance of the input parameters $\mathbf{x}^{(i)}$, the following optimization problem:

$$\text{find } \tau^* \;:\quad \min_{\tau} E(\tau). \tag{3.12}$$

Thus, the dataset generated consists of m pairs of inputs-outputs $(\mathbf{x}^{(i)}, \mathbf{y}^{(i)})$, with $i = 1, \dots, m$. The latter is used for *training* the ANN. The latter will be then used to predict the optimal stabilization parameter $\mathbf{y}^{(j)} = \tau_{\text{ANN}}$ to be used for the FE approximation of the advection-diffusion problem in the settings provided by $\mathbf{x}^{(j)}$.

We report in Figure 3.1 a sketch of the procedure used to build the ANN for the prediction of the optimal stabilization parameter for any new feature $\mathbf{x}^{(j)}$.

3.4. Numerical validation

In this section, we validate the proposed numerical strategy by means of a 1D advection-diffusion problem from which the expression of $\widetilde{\tau}_1$ in Eq. (3.7) has been derived. In particular, we consider the advection-diffusion problem in Eq. (3.1) with $\Omega = (0, 1)$, $f = 0$ and with Dirichlet BCs $u = 0$ on $x = 0$ and $u = 1$ on $x = 1$. It admits the following exact solution:

$$u(x) = \frac{\exp\left(\frac{\beta}{\mu}x\right) - 1}{\exp\left(\frac{\beta}{\mu}\right) - 1}.$$

We recall that the stabilization parameter $\widetilde{\tau}_1$ of Eq. (3.7) yields a nodally exact numerical solution if Eq. (3.1) is solved by linear FE ($r = 1$).

We plot in Figure 3.2 the error measure $E(\tau)$ against the value of the stabilization parameter τ, with $h = 1/20$, $\mathbb{P}\text{e}_h = 12.5$ and by using $r = 1$ (Figure 3.2a) and $r = 3$ (Figure 3.2b). We observe that $E(\tau)$ shows a minimum in τ^*, thus suggesting the possibility to use an optimization algorithm to solve the problem. Specifically, we employ the L-BFGS-B optimization algorithm from SciPy, an open source library for Python [275]. Instead, the advection-diffusion problem has been solved using the FE open source library FEniCS [19], by applying the SUPG method on a uniform mesh. Particularly, the optimal value τ^* found for the case $r = 1$ corresponds to the one provided by the theory in Eq. (3.7). For the case $r = 3$, we observe a optimal value of τ^* for which the error is minimized: in this case, it does not corresponds to the stabilization parameter $\widetilde{\tau}_r$ provided by the theory in Eq. (3.8): as a matter of fact, the latter arises from empirical considerations to extend the parameter $\widetilde{\tau}_1$ in Eq. (3.7) to

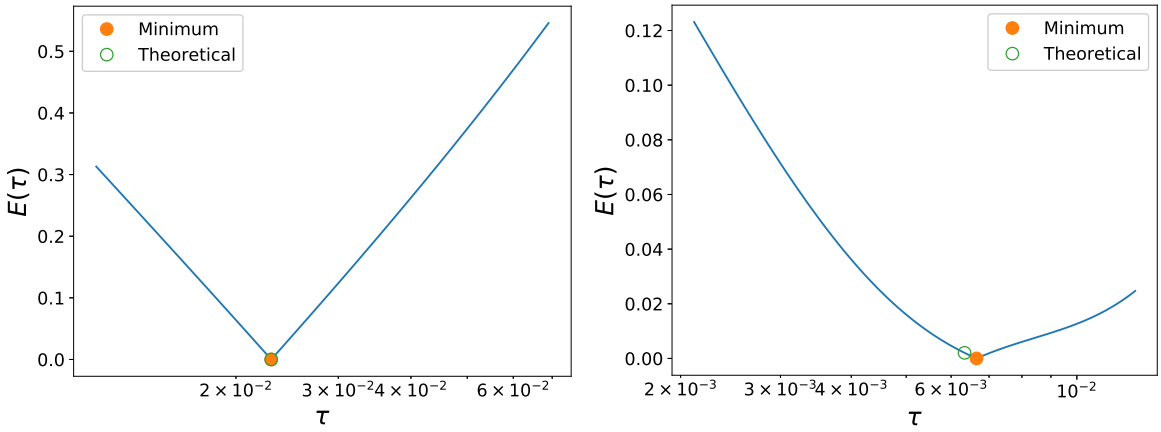

(a) $r = 1$ (b) $r = 3$

Figure 3.2: Error (3.11) of numerical solutions with SUPG method vs. the stabilization parameter τ for the 1D problem in Section 3.4 with $h = 1/20$ and $\mathbb{P}\mathrm{e}_h = 12.5$; comparison between the theoretical value $\widetilde{\tau}_r$ of Eq. (3.8) and the optimal one τ^*

polynomials degrees $r > 1$. However, this does not ensure a nodally exact numerical solution.

We solve the optimization problem for different values of the local Péclet number $1 \leq \mathbb{P}\mathrm{e}_h \leq 250$ and we plot in Figure 3.3 the optimal stabilization parameter τ^* against the local Péclet number for $r = 1, 2$, and 3.

Figure 3.3a shows that, by employing a linear FE space $r = 1$, the optimal stabilization parameter τ^* obtained by minimizing $E(\tau)$ exactly matches the theoretical one $\widetilde{\tau}_1$ for every value of $\mathbb{P}\mathrm{e}_h$, thus confirming the findings of Figure 3.2a. This also serves as validation of the optimization procedure that we proposed. By recalling that $\widetilde{\tau}_1$ of Eq. (3.7) guarantees the numerical solution to be exact at nodes for this particular advection-diffusion problem and $r = 1$, we can infer that the optimization procedure is meaningful and it can be therefore exploited further, for example for $r > 1$. On the other hand, Figures 3.3b and 3.3c show instead a mismatch between the theoretical $\widetilde{\tau}_r$ of Eq. (3.8) and the optimal one τ^*, thus confirming the findings reported in Figure 3.2b.

In order to better appreciate the differences in the numerical solutions due to the choice of the stabilization parameters, we report, in Figure 3.4, a comparison of the error $E(\tau)$ obtained by means of the optimal τ^* and theoretical $\widetilde{\tau}_r$ stabilization parameters for $r = 2$ and 3. Moreover, we report in Figure 3.5 a comparison among the exact solution u, the SUPG-stabilized numerical solution u_*^h obtained with the optimal stabilization parameter τ^*, and the numerical solution $\widetilde{u}^h$ obtained with theoretical one $\widetilde{\tau}_r$. Specifically, we consider FE of degree $r = 3$ and two different values of $\mathbb{P}\mathrm{e}_h$. In both these cases, the optimal parameter τ^* leads to a more accurate solution with respect to using the theoretical parameter $\widetilde{\tau}_r$. In particular, when $\mathbb{P}\mathrm{e}_h$ is "small", $\widetilde{\tau}_r$

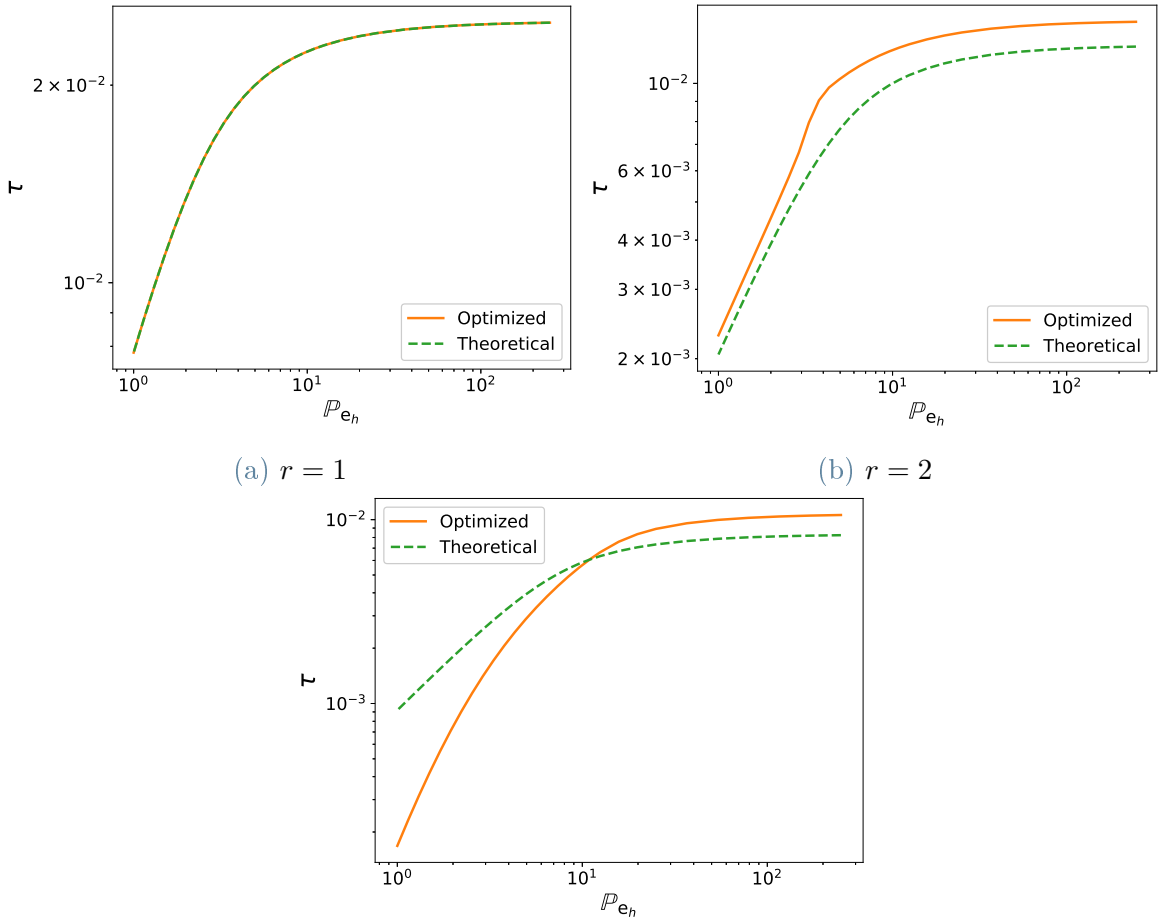

(a) $r = 1$ (b) $r = 2$

(c) $r = 3$

Figure 3.3: Comparison of the optimal stabilization parameter τ^* (full line) and the theoretical one $\widetilde{\tau}_r$ of Eq. (3.8) (dashed line) against $\mathbb{P}e_h$, with $h = 1/20$. Results are referred to the 1D advection-diffusion problem described Section 3.4

leads to overshooting in the numerical solution, while if $\mathbb{P}e_h$ is "large" the theoretical stabilization parameter leads to undershooting. Conversely, the optimal parameter τ^* accurately intercepts the exact solution at the nodes.

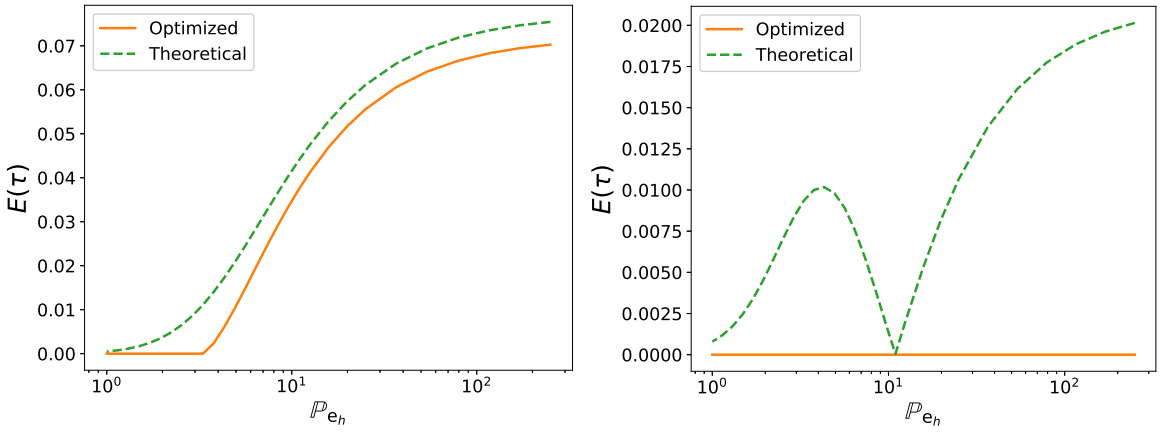

(a) $r = 2$ (b) $r = 3$

Figure 3.4: Comparison of the error of Eq.(3.11) obtained with the optimal τ^* (full line) and theoretical $\widetilde{\tau}_r$ (dashed line) for varying $\mathbb{P}e_h$ with $h = 1/20$. Results referred to the 1D advection-diffusion problem of Section 3.4.

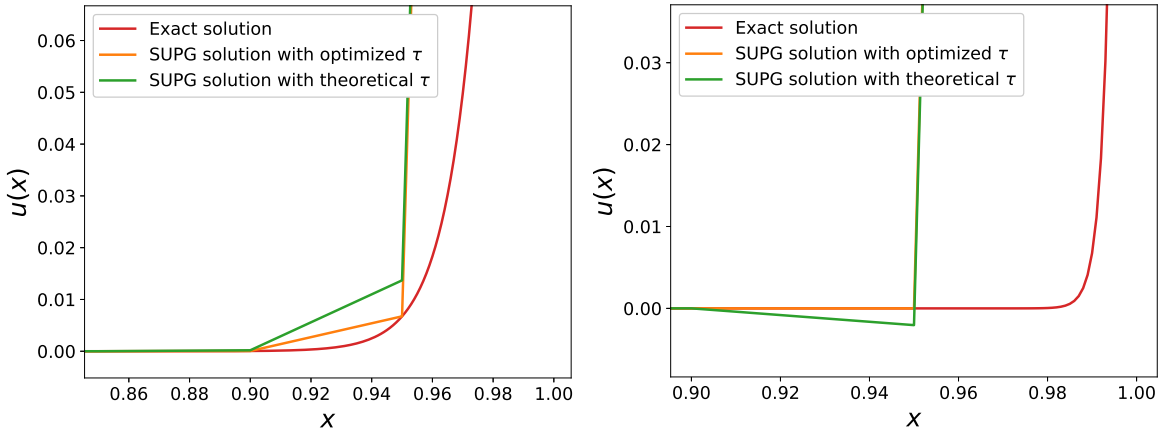

(a) $\mathbb{P}e_h = 2.5$ (b) $\mathbb{P}e_h = 12.5$

Figure 3.5: Boundary layers of the numerical solutions u_*^h and $\widetilde{u}^h$ obtained with the SUPG method with optimal τ^* and theoretical one $\widetilde{\tau}_r$ for $h = 1/20$ and $r = 3$, respectively; comparison with the exact solution u (u_*^h is nodally exact at the node in $x = 0.95$). Results are referred to the 1D advection-diffusion problem of Section 3.4

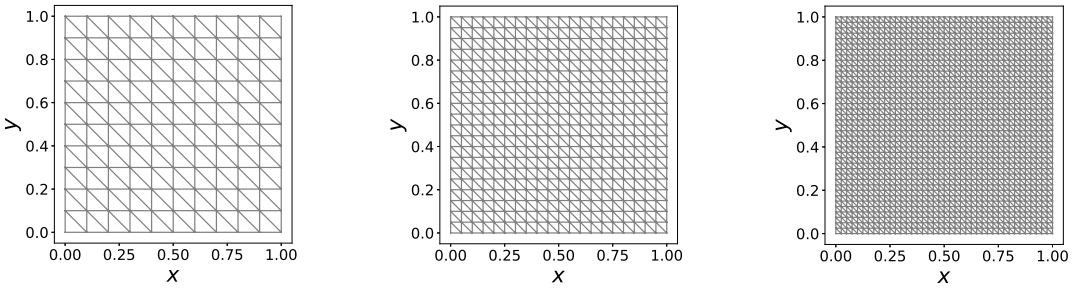

(a) $h = \sqrt{2}/10$ (b) $h = \sqrt{2}/20$ (c) $h = \sqrt{2}/40$

Figure 3.6: Structured mesh with different resolutions employed for 2D-advection-diffusion problem

3.5. Numerical results

We first introduce the training set of our problem and we detail the setup of the ANN that we use in this work. Then, we show the prediction of the stabilization parameter by means of the ANN on different advection-diffusion problems.

3.5.1. Training an ANN on a 2D problem

We apply the strategy presented so far to a 2D advection-diffusion problem to generate the dataset for the training of the ANN. Specifically, we consider in Eq. (3.1): $\Omega = (0,1)^2$, $f = 0$, and $\boldsymbol{\beta} = (1,1)$. We prescribe the following exact solution on the whole boundary $\partial\Omega$:

$$u(x,y) = \frac{e^{(x/\mu)} - 1}{e^{(1/\mu)} - 1} + \frac{e^{(y/\mu)} - 1}{e^{(1/\mu)} - 1}. \tag{3.13}$$

We generate in Ω a structured mesh $\mathcal{T}^h$ of triangles with FEniCS [19], as shown in Figure 3.6. We generate the dataset by repeatedly solving the optimization problem of Eq. (3.12) for varying set of features as described in Section 3.3; specifically, we choose the features as reported in Eq. (3.9). The complete dataset contains $m = 900$ examples with $r = \{1,2,3\}$, $h = \left\{\frac{\sqrt{2}}{10}, \frac{\sqrt{2}}{20}, \frac{\sqrt{2}}{40}\right\}$ and values of $\mathbb{P}\mathrm{e}_g$ randomly chosend in the range $[7, 70'710]$ (uniform distribution), which yields $\mu \in [10^{-5}, 10^{-1}]$. We summarize the details for generating the dataset in Table 3.1. Figure 3.7 provides an overview of the dataset used to the training of the ANN, specifically the features $\mathbf{x}^{(i)} = [r,\ h,\ \mathbb{P}e_g]$ and the target $\mathbf{y}^{(i)} = [\tau^*]$. In this case, the characteristic length L is fixed and set equal to $L = 1$.

We train a fully-connected feed-forward ANN on the generated dataset by using the open source library Keras [53] built on top of TensorFlow [16]. We divide the dataset into two parts: a training dataset that takes 80% of the examples to be used for the

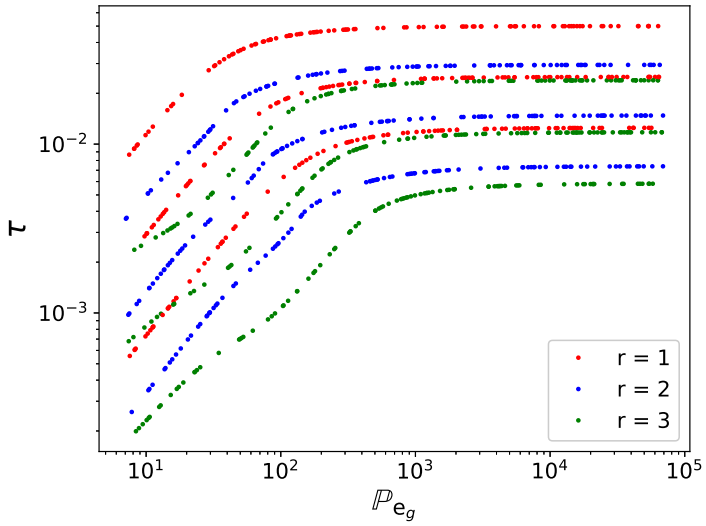

Figure 3.7: Visualization of the dataset used for the ANN training: target τ^* against feature $\mathbb{P}e_g$ colored by feature $r = 1$ (red), 2 (blue), and 3 (green) for different values of the feature h (increasing values of h from bottom to top) as listed in Table 3.1

Data set (m)	Training set	Validation set	r	h	$\mathbb{P}e_g$
900	720 (80%)	180 (20%)	$\{1, 2, 3\}$	$\left\{\frac{\sqrt{2}}{10}, \frac{\sqrt{2}}{20}, \frac{\sqrt{2}}{40}\right\}$	randomly in $[7, 70'710]$.

Table 3.1: Data set details.

ANN training and a validation dataset that takes the remaining 20%. We choose the loss function as the mean squared error that measures, for each training feature, the squared mismatch between the prediction of the ANN $\widehat{y}^{(j)}$ and the actual target $y^{(j)}$. Specifically, the loss function is defined as

$$\mathcal{J} = \frac{1}{2m} \sum_{j=1}^{m} \left(\widehat{y}^{(j)} - y^{(j)}\right)^2. \tag{3.14}$$

We normalize the features by subtracting their mean and dividing by their standard deviation in order to help the weights to better adapt to the different scales of the features. Moreover, the targets and the feature $\mathbb{P}e_g$ need special care as built on a logarithmic scale; specifically, the features are normalized by applying base 10 logarithm. The normalized features and targets read:

$$\widetilde{\mathbf{x}} = \left[\frac{r-\overline{r}}{\sigma_r}, \frac{h-\overline{h}}{\sigma_h}, \frac{\log_{10}(\mathbb{P}e_g) - \overline{\log_{10}(\mathbb{P}e_g)}}{\sigma_{\log_{10}(\mathbb{P}e_g)}} \right], \qquad \widetilde{\mathbf{y}} = \left[-\log_{10}(\tau^*) \right],$$

where $\overline{r}$, $\overline{h}$, $\overline{\log_{10}(\mathbb{P}e_g)}$ are the mean of the training features r, h and the logarithm of

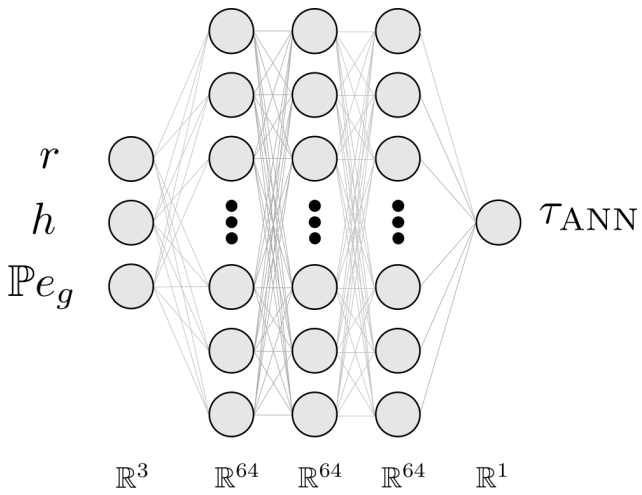

Figure 3.8: Architecture of the feed-forward fully-connected ANN.

$\mathbb{P}\text{e}_g$ respectively, while σ_r, σ_h and $\sigma_{\log_{10}(\mathbb{P}\text{e}_g)}$ are their standard deviations.

In order to find the best performing ANN architecture, we carried out a study by testing different numbers of hidden layers, nodes per layer, optimization algorithm, its learning rate, and batch size. Finally, we choose an ANN with 3 hidden layers, 64 nodes per layer and an output layer with a single node, all using a rectified linear unit ($ReLU$) activation function. We display the ANN architecture in Figure 3.8. We trained the ANN with the SGD optimization algorithm, a constant learning rate of 0.01, and mini-batch size of 32 examples. Moreover, we employed a momentum of 0.9 in the optimization algorithm to update the weights. The trained ANN is available in the GitLab repository [2].

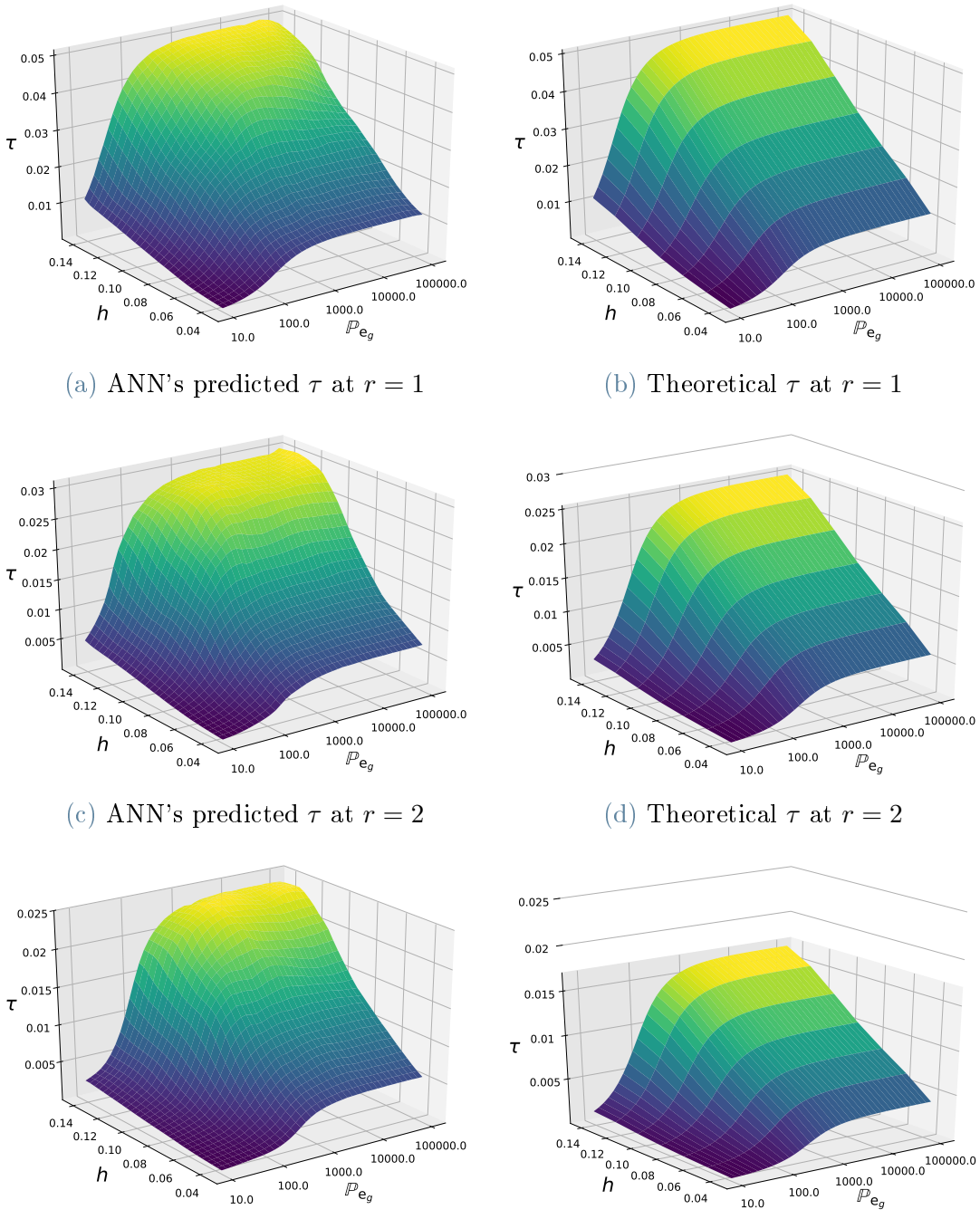

(a) ANN's predicted τ at $r = 1$

(b) Theoretical τ at $r = 1$

(c) ANN's predicted τ at $r = 2$

(d) Theoretical τ at $r = 2$

(e) ANN's predicted τ at $r = 3$

(f) Theoretical τ at $r = 3$

Figure 3.9: Stabilization parameter τ_{ANN} predicted by the ANN and theoretical one $\widetilde{\tau}_r$ for varying $\mathbb{P}\text{e}_g$ and h at different FE degrees $r = 1, 2$, an 3 for the 2D advection-diffusion problem of Section 3.5.1

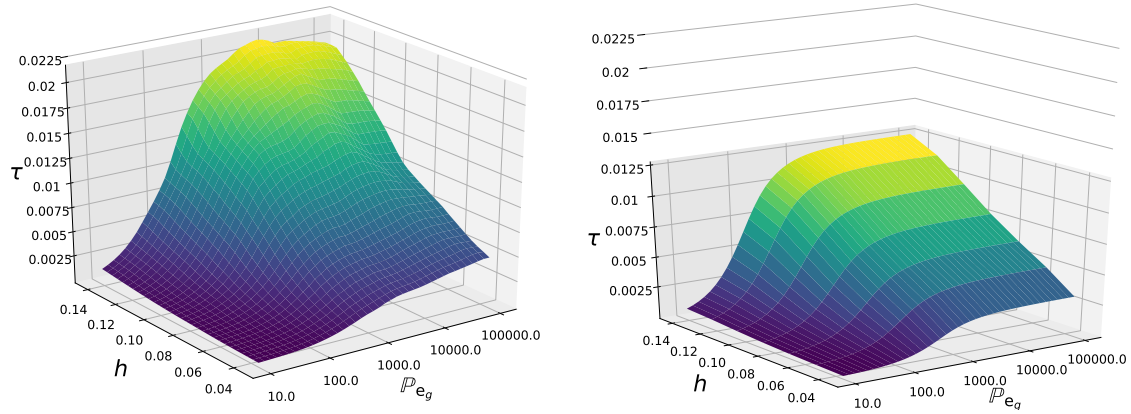

(a) ANN's predicted τ at $r = 4$

(b) Theoretical τ at $r = 4$

Figure 3.10: Stabilization parameter τ_{ANN} predicted by the ANN and theoretical one $\widetilde{\tau}_r$ for varying $\mathbb{P}\text{e}_g$ and h with FE degree $r = 4$ for the 2D advection-diffusion problem of Section 3.5.1

3.5.2. Predictions of the stabilization parameter by ANN

Now, we compare the predictions of the ANN with the theoretical stabilization parameter $\widetilde{\tau}_r$ of Eq. (3.8) [101, 207]. We show in Figure 3.9 (left) the stabilization parameter τ_{ANN} predicted by the ANN by varying mesh size h and global Péclet number $\mathbb{P}e_g$. For comparison, we report in Figure 3.9(right) the corresponding theoretical stabilization parameter $\widetilde{\tau}_r$. We observe that the overall behavior of the trained ANN's predictions are qualitatively similar of the theoretical stabilization parameter $\widetilde{\tau}_r$. Nevertheless, it can be inferred that the values of the stabilization parameters are almost completely matched with linear FE ($r = 1$), while they quantitatively differ for $r = 2$ and $r = 3$. This was expected as $\widetilde{\tau}_r$ for $r > 1$ is an empirical extension of the formula for the case $r = 1$.

The ANN allows to make predictions with features outside the range of values for which it has been trained, that is for unseen values of such features. With this aim, we report in Figure 3.10 the comparison of the ANN's predictions τ_{ANN} with $\widetilde{\tau}_r$ for the FE degree $r = 4$. This comparison shows a clear difference between the theoretical and ANN's τ for $r = 4$ even though the general trend is maintained similar.

Predictions for the problem used in the ANN's training

We compare the numerical solutions u_h^{ANN} and $\widetilde{u}_h$ obtained by means of the SUPG stabilization method with the parameter τ_{ANN} predicted by the ANN and the theoretical one $\widetilde{\tau}_r$, respectively; the comparison also involves the exact solution u (3.13) of the 2D advection-diffusion problem used for the training of the ANN. In particular,

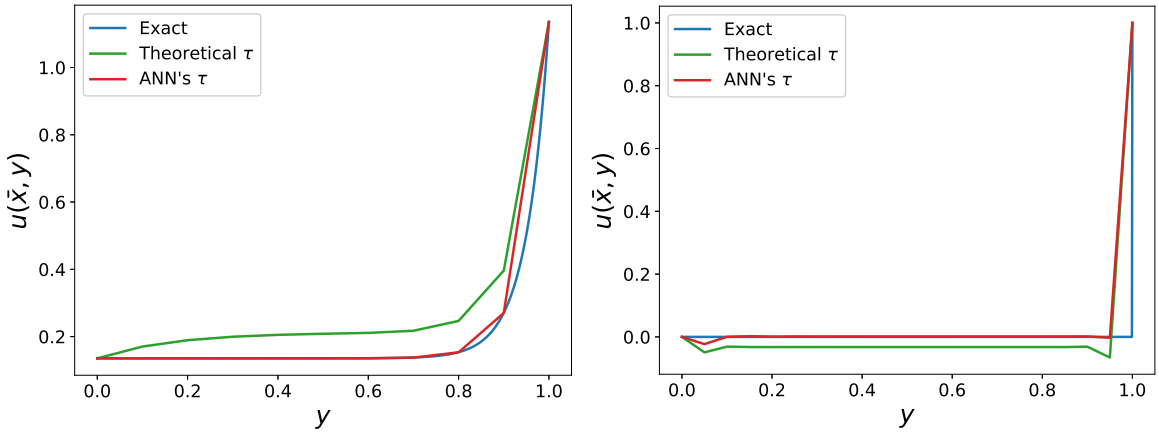

(a) $\mathbb{P}\mathrm{e}_h = 2$, $h = \sqrt{2}/10$, $r = 1$ (b) $\mathbb{P}\mathrm{e}_h = 500$, $h = \sqrt{2}/20$, $r = 3$

Figure 3.11: Comparison of the solutions u (blue), $\widetilde{u}^h$ (green), and u^h_{ANN} (red) of the 2D advection-diffusion problem along the line $(1-h, y)$ for any $y \in [0,1]$

we display the comparison of the former 2D solutions in Figure 3.11 along the line $(1-h, y)$ for any $y \in [0,1]$ with: (a) $\mathbb{P}\mathrm{e}_h = 2$, $r = 1$, and $h = \sqrt{2}/10$ (Figure 3.11a); (b) $\mathbb{P}\mathrm{e}_h = 500$, $r = 3$, and and $h = \sqrt{2}/20$ (Figure 3.11b). We notice that in both the cases, the numerical solution u^h_{ANN} involving the stabilization parameter τ_{ANN} provides more accurate results than with the theoretical stabilization paramter $\widetilde{\tau}_r$. In particular, in the case (a), $\widetilde{u}^h$ involves a much smoother boundary layer and overshoots the exact solutions u, conversely to the nearly nodally exact numerical solution u^h_{ANN}. In the case (b), u^h_{ANN} provides a much better representation of the bundary layer, without the undershooting of the solution u exhibited by $\widetilde{u}_h$.

Predictions for an unseen problem

We check the model generalization of the ANN trained for the 2D advection-diffusion problem with exact solution u of Eq. 3.13 by predicting τ_{ANN} for an unseen 2D advection-diffusion problem. In particular, we consider the advection-diffusion problem of Eq. (3.1) in $\Omega = (0,1)^2$, with $f = 1$ and $\boldsymbol{\beta} = (1,1)$. We prescribe the following exact solution on the whole boundary $\partial\Omega$:

$$u(x,y) = \frac{1}{2}(x+y) + \frac{1 - \frac{1}{2}(e^{(x/\mu)} + e^{(y/\mu)})}{e^{(1/\mu)} - 1}. \tag{3.15}$$

We compare in Figure 3.12 the numerical solutions u_h^{ANN} and $\widetilde{u}_h$ with the novel exact solution u. As for the previous numerical tests, the stabilization parameter τ_{ANN} predicted by the network provides more accurate numerical solutions u^h_{ANN} than with the theoretical stabilization parameter $\widetilde{\tau}_r$. In particular, the boundary layers and overall

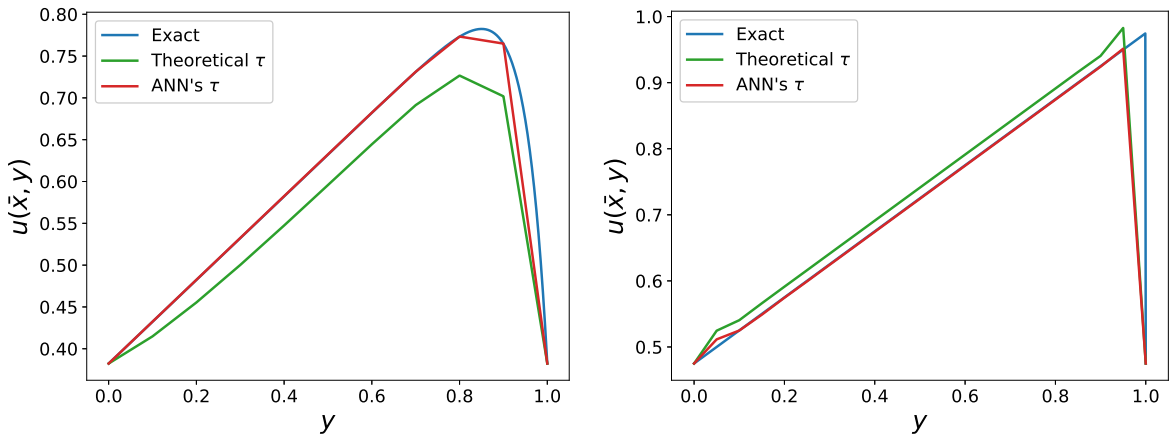

(a) $\mathbb{P}\mathrm{e}_h = 2$, $h = \sqrt{2}/10$, $r = 1$ (b) $\mathbb{P}\mathrm{e}_h = 500$, $h = \sqrt{2}/20$, $r = 3$

Figure 3.12: Comparison of the solutions u (3.15) (blue), $\widetilde{u}^h$ (green), and u^h_{ANN} (red) of the *unseen* 2D advection-diffusion problem along the line $(1-h, y)$ for any $y \in [0, 1]$

solution behaviours are better represented.

We better investigate assess the former qualitative consideration, by computing the error $E(\tau)$ associated with the numerical solutions with SUPG stabilization for the parameters τ_{ANN} and $\widetilde{\tau}_r$; different values of $\mathbb{P}\mathrm{e}_g$ and r are considered. In particular, Figure 3.13 compares $E(\tau)$ against $\mathbb{P}\mathrm{e}_g$ (in logarithmic scale) for different values of r: the error obtained by using τ_{ANN} is always lower than the one achieved with $\widetilde{\tau}_r$. These results indicate that τ_{ANN}, although trained on a specific advection-diffusion problem, can be used to make predictions of the optimal τ for an unseen advection-diffusion problem in place of the theoretical stabilization parameter.

3.6. Concluding remarks

In this chapter, we presented a novel strategy to compute the optimal stabilization parameter in stabilization methods through ANNs. We considered advection-diffusion problems discretized with FE method, and we stabilized the advection-dominated regime by means of the SUPG stabilization method, whose stabilization parameter has still not a universal and optimal definition. We propose a computational strategy aimed at employing the stabilization parameter predictedy by an ANN. The latter has been previously trained by means of optimal stabilization parameters computed by minimizing the distance between the numerical and the exact solution for different instances of our input parameter. Specifically,

- we validated our methodology showing that for the 1D case with null forcing term and linear FE space, the optimization algorithm matches the theoretical stabilization parameter that, for this simple case, yields a nodally exact solution. Instead,

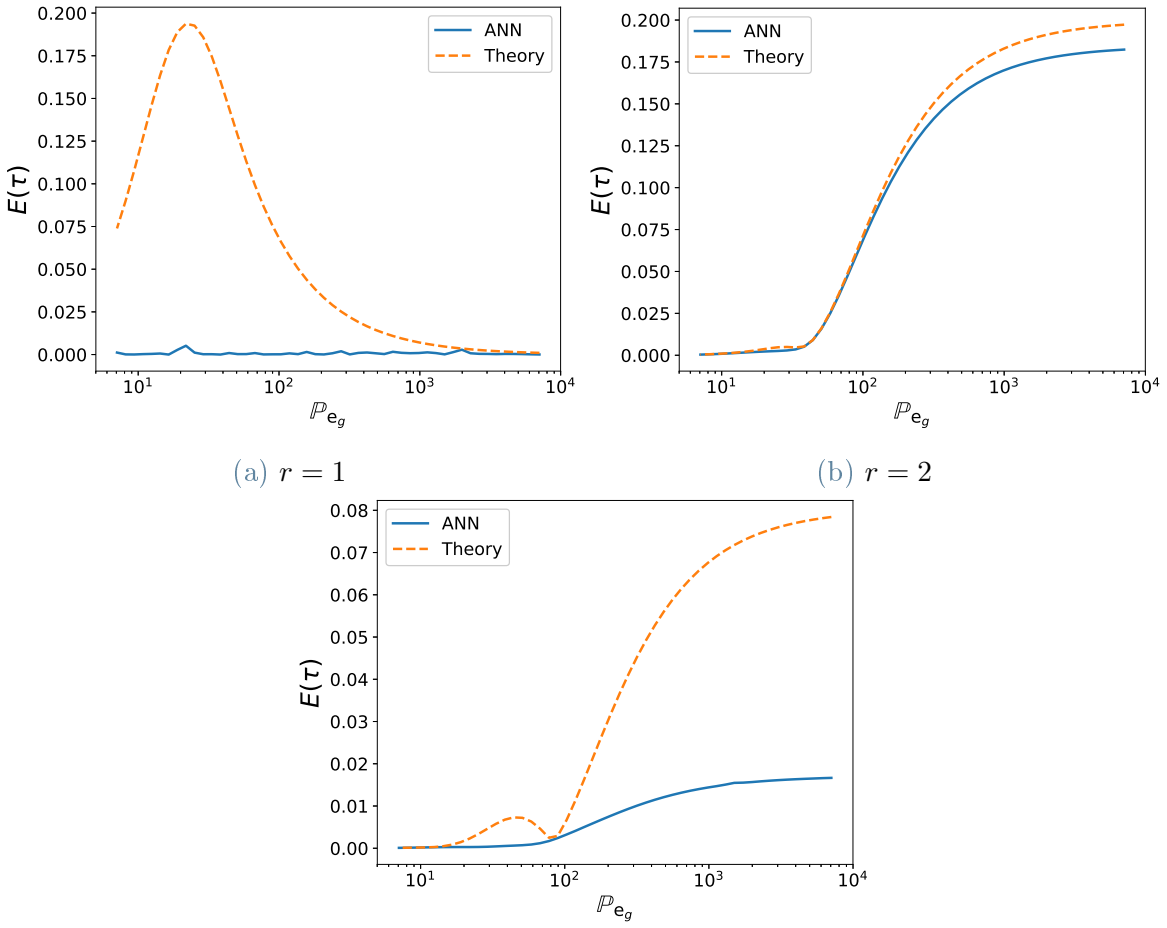

(a) $r = 1$ (b) $r = 2$

(c) $r = 3$

Figure 3.13: Comparison of errors $E(\tau)$ in Eq. (3.11) obtained with τ_{ANN} (blue, full line) and $\widetilde{\tau}_r$ (orange, ashed line) applied to the useen 2D advection-diffusion problem with the exact solution u (3.15); $E(\tau)$ against $\mathbb{P}\text{e}_g$ with $h = \sqrt{2}/10$ and FE degrees $r = 1, 2$, and 3

for higher polynomials degrees, remarkable differences are observed among theoretical and optimal parameter: we observed better accuracy and stabilization properties of the numerical solution with the optimized stabilization parameter with respect to the theoretical one.

- Our numerical results showed that the adopted strategy to use an ANN to reproduce the optimal stabilization parameter has the potential to surpass the accuracy provided by current employed strategies relying on analytical expressions.

The work presented in this chapter represents a step towards the enhancements of stabilization methods for the FE approximation of advection-dominated differential

problems. In particular, this work is limited to few features for the ANN-based stabilization parameter and provides as output a single optimal stabilization parameter meant for the whole mesh FE $\mathcal{T}^h$. Natural extensions of this work will therefore involve local stabilization parameters, i.e. element by element over the mesh $\mathcal{T}^h$, to better account for non-uniform meshes, differential problems with varying coefficients, and capturing the local behaviour of the solution.

Finally, we believe this study can be considered a valuable basis to apply a similar methodology for more complex equations as the NS equations with VMS-LES modeling. As a matter of fact, as we described in Chapter 2, its stabilization parameters are often defined empirically and the enhancing of standard methods through ML based technique would bring to considerable advantages in terms of accuracy and stability of the numerical solution.

Part II

Application to the cardiac problem

4 | CFD models and methods for cardiac hemodynamics

In this chapter, we present the mathematical models describing the fluid dynamics of heart's chambers. Specifically, in Section 4.1 we express the NS equations in the ALE framework. To model the presence of the cardiac valves in the fluid domain, in Section 4.2 we present the RIIS method. Finally, in Section 4.4 we introduce a 0D circulation model of the whole cardiovascular system.

4.1. NS equations in ALE framework

In large vessels, as well as in the heart chambers, blood can be regarded as a Newtonian incompressible fluid in spite of the presence of small particles suspended and carried by the plasma; thus, we model it with the NS equations already introduced in Section 2.1 [198, 213, 252, 253]. The physical parameters for blood are density $\rho = 1.056 \cdot 10^3$ kg/m^3 and dynamic viscosity $\mu = 3.5 \cdot 10^{-3}$ kg/(m·s).

The heart chambers are subjected to a motion and hence, the equations governing the motion of blood flow must be expressed in a domain that changes in time. A convenient way to model a fluid problem in a moving domain is to express the NS equations in a moving frame of reference, leading to the ALE framework. The ALE framework dates back to 1982 and was introduced by J. Donea et al. [76] in the context of FSI problems, and it was developed in an attempt to combine the advantages of the Lagrangian and the Eulerian fraweworks [77].

As displayed in Figure 4.1, we denote with $\Omega_t \subset \mathbb{R}^d$ the moving domain at a specific time $t > 0$, i.e. the domain in *current configuration*. By recalling the notation introduced in Section 2.1, we denote as Γ_t^D and Γ_t^N the portions of the boundary where respectively Dirichlet and Neumann type BCs are prescribed, with $\Gamma_t = \overline{\Gamma_t^D} \cup \overline{\Gamma_t^N}$ and $\overset{\circ}{\Gamma}{}_t^D \cap \overset{\circ}{\Gamma}{}_t^N = \emptyset$.

Let $\widehat{\Omega} \subset \mathbb{R}^d$ be the domain in *reference configuration* and $\partial\widehat{\Omega} \equiv \widehat{\Gamma}$ its sufficiently regular boundary. We introduce the ALE map $\mathcal{A}_t$ which associates at each $t \in (0, T_f)$ a point

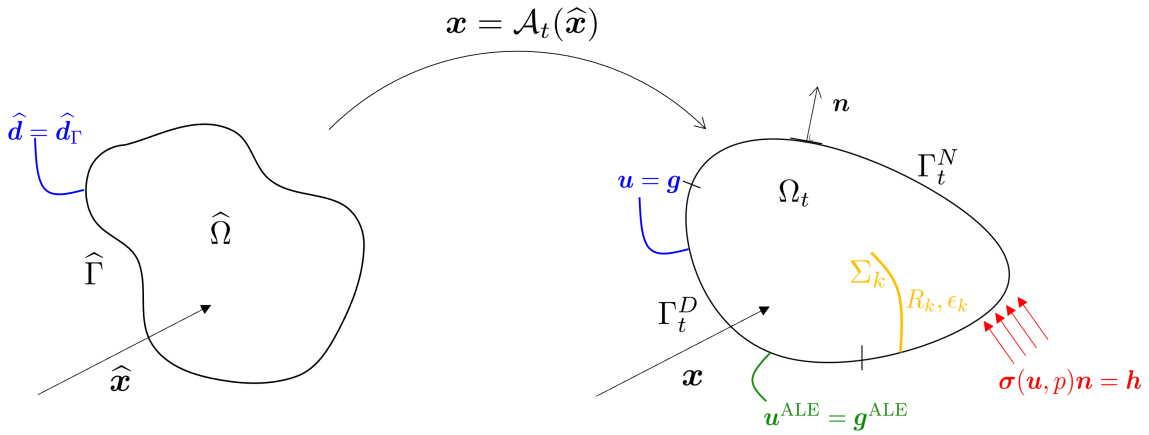

Figure 4.1: Domain in reference configuration (left), ALE map $\boldsymbol{x} = \mathcal{A}_t(\widehat{\boldsymbol{x}})$ and domain in current configuration (right). In the current configuration, the domain Ω_t is bounded by $\Gamma_t = \Gamma_t^D \cup \Gamma_t^N$; Σ_k is an immersed surface modeled by means of the RIIS method (see Section 4.2).

$\widehat{\boldsymbol{x}} \in \widehat{\Omega}$ to a point $\boldsymbol{x} \in \Omega_t$ [90]:

$$\mathcal{A}_t : \widehat{\Omega} \to \Omega_t : \quad \boldsymbol{x} = \mathcal{A}_t(\widehat{\boldsymbol{x}}) = \widehat{\boldsymbol{x}} + \widehat{\boldsymbol{d}}(\widehat{\boldsymbol{x}}, t), \tag{4.1}$$

being $\widehat{\boldsymbol{d}}$ the domain displacement with respect to the reference configuration $\widehat{\Omega}$. The spatial coordinate in the reference configuration $\widehat{\boldsymbol{x}}$ is also known as *ALE coordinate*; $\boldsymbol{x}$ is the *Eulerian coordinate* [90]. Given the reference configuration, at each time step the current domain can be computed through the ALE map as

$$\Omega_t = \mathcal{A}_t(\widehat{\Omega}). \tag{4.2}$$

For every function w defined in the current configuration, we denote with $\widehat{w} = w \circ \mathcal{A}_t$ the corresponding function in the reference frame as [90]

$$\widehat{w} : \widehat{\Omega} \times (0, T_f) \to \mathbb{R}, \quad \widehat{w}(\widehat{\boldsymbol{x}}) = w(\mathcal{A}_t(\widehat{\boldsymbol{x}}), t). \tag{4.3}$$

Viceversa, $w = \widehat{w} \circ \mathcal{A}_t^{-1}$.

Assuming now the displacement $\widehat{\boldsymbol{d}}_\Gamma(\widehat{\boldsymbol{x}}, t) : \widehat{\Gamma} \times (0, T_f) \to \mathbb{R}^d$ to be known on the whole boundary $\widehat{\Gamma}$ at any time $t \in (0, T_f)$, we can recover the displacement of the inner domain $\widehat{\boldsymbol{d}}$ by harmonically extending the datum on the boundary. Specifically, the boundary datum is defined $\widehat{\boldsymbol{d}}_\Gamma(\widehat{\boldsymbol{x}}, t) : \widehat{\Gamma} \to \Gamma_t$, and we extend it to the domain $\widehat{\Omega}$ by

solving – at each time step – the following harmonic extension problem:

$$-\nabla\cdot\left(\boldsymbol{K}\nabla\widehat{\boldsymbol{d}}\right)=\boldsymbol{0} \qquad \text{in } \widehat{\Omega}, \tag{4.4a}$$

$$\widehat{\boldsymbol{d}}=\widehat{\boldsymbol{d}}_{\Gamma} \qquad \text{on } \widehat{\Gamma}. \tag{4.4b}$$

In Equation (4.4a), $\boldsymbol{K}$ is a positive-definite tensor that can be properly set to better tune the harmonic extension operator, for example depending on the mesh size as done in [136]. In this work however, we set $\boldsymbol{K}$ equal to the identity tensor, and Eq. (4.4) resembles hence a standard vectorial Laplacian problem in the unknown $\boldsymbol{d}$.

We denote the time derivative in the ALE frame as $\frac{\partial}{\partial t}\Big|_{\widehat{\boldsymbol{x}}}$ written in the Eulerian coordinate as [90]

$$\frac{\partial w}{\partial t}\bigg|_{\widehat{\boldsymbol{x}}}:\Omega_t\times(0,T_f)\to\mathbb{R}, \quad \frac{\partial w}{\partial t}\bigg|_{\widehat{\boldsymbol{x}}}(\boldsymbol{x},t)=\frac{\partial\widehat{w}}{\partial t}(\widehat{\boldsymbol{x}},t), \tag{4.5}$$

being

$$\widehat{\boldsymbol{x}}=\mathcal{A}_t^{-1}(\boldsymbol{x}). \tag{4.6}$$

The domain velocity, that we call *ALE velocity*, is defined as

$$\boldsymbol{u}^{\mathrm{ALE}}(\boldsymbol{x},t)=\frac{\partial\boldsymbol{x}}{\partial t}\bigg|_{\widehat{\boldsymbol{x}}}, \tag{4.7}$$

or, analogously via the displacement, as

$$\boldsymbol{u}^{\mathrm{ALE}}=\left(\frac{\partial\widehat{\boldsymbol{d}}}{\partial t}\right)\circ\mathcal{A}_t^{-1}. \tag{4.8}$$

In order to express the NS equations (2.1) in the ALE framework, let us consider first a simplified first order time evolution problem in the unknown $u:\Omega_t\times(0,T_f)\to\mathbb{R}$ expressed in conservative form as

$$\frac{\partial u}{\partial t}\bigg|_{\boldsymbol{x}}+\mathcal{L}(u)=0, \tag{4.9}$$

being $\mathcal{L}$ a generic differential operator. Equation (4.9) is expressed in the Eulerian framework (space variable $\boldsymbol{x}$). To recast Equation (4.9) in the ALE framework, we consider the ALE time derivative of u (Equation (4.5)), that can be expressed via chain rule as:

$$\frac{\partial u}{\partial t}\bigg|_{\widehat{\boldsymbol{x}}}(\boldsymbol{x},t)=\frac{\partial u}{\partial t}\bigg|_{\widehat{\boldsymbol{x}}}(\boldsymbol{x}(\widehat{\boldsymbol{x}},t),t)=\frac{\partial u}{\partial t}\bigg|_{\boldsymbol{x}}+\frac{\partial\boldsymbol{x}}{\partial t}\bigg|_{\widehat{\boldsymbol{x}}}\cdot\nabla_{\boldsymbol{x}}u, \tag{4.10}$$

where we used $\nabla_{\boldsymbol{x}}$ to denote the gradient with respect to $\boldsymbol{x}$. Moreover, by using

Equation (4.7), we get:

$$\left.\frac{\partial u}{\partial t}\right|_{\widehat{\boldsymbol{x}}} = \left.\frac{\partial u}{\partial t}\right|_{\boldsymbol{x}} + \boldsymbol{u}^{\mathrm{ALE}} \cdot \nabla_{\boldsymbol{x}} u. \tag{4.11}$$

Thus, solving Equation (4.11) for $\left.\frac{\partial u}{\partial t}\right|_{\boldsymbol{x}}$ allows to express Equation (4.9) in the ALE configuration as:

$$\left.\frac{\partial u}{\partial t}\right|_{\widehat{\boldsymbol{x}}} - \boldsymbol{u}^{\mathrm{ALE}} \cdot \nabla_{\boldsymbol{x}} u + \mathcal{L}(u) = 0. \tag{4.12}$$

Hence, the main difference among Equation (4.9) and (4.12) is the appearance of a convective term due to the motion of the domain [90]. To keep the notation simpler, from now on we will denote the ALE time derivative as $\frac{\widehat{\partial} u}{\widehat{\partial} t} := \left.\frac{\partial u}{\partial t}\right|_{\widehat{\boldsymbol{x}}}$ and, as in Section 2.1, the gradient in the Eulerian coordinate simply as $\nabla := \nabla_{\boldsymbol{x}}$.

The result in Equation (4.12) allows to express the NS equations in Equation (2.1) in the ALE framework as:

$$\rho\left(\frac{\widehat{\partial}\boldsymbol{u}}{\widehat{\partial} t} + \left(\left(\boldsymbol{u} - \boldsymbol{u}^{\mathrm{ALE}}\right) \cdot \nabla\right)\boldsymbol{u}\right) - \nabla \cdot \boldsymbol{\sigma}(\boldsymbol{u}, p) = \boldsymbol{f} \qquad \text{in } \Omega_t \times (0, T_f), \tag{4.13a}$$

$$\nabla \cdot \boldsymbol{u} = 0 \qquad \text{in } \Omega_t \times (0, T_f), \tag{4.13b}$$

complemented with suitable initial conditions and BCs. We recall that, for each time, Equation (4.13) must be solved with the geometric problem in Equation (4.4) to recover the displacement in the fluid domain $\boldsymbol{d}$; the ALE velocity $\boldsymbol{u}^{\mathrm{ALE}}$ is instead recovered through Equation (4.8).

4.2. Valves modelling: the RIIS method

To model the presence of the cardiac valves, as well as their effects on the fluid, we employ the RIIS method [86, 100]: we introduce into the momentum balance of the NS equations (Equation (2.1a) or (4.13a) for the ALE counterpart) the following resistive additional term:

$$\sum_{k=1}^{m} \frac{R_k}{\varepsilon_k} \delta_{\Sigma_k, \varepsilon_k}(\varphi_k) \left(\boldsymbol{u} - \boldsymbol{u}_{\Sigma_k}\right). \tag{4.14}$$

The latter penalizes a kinematic condition, i.e. the adherence of the fluid to m immersed moving surfaces Σ_k defined as

$$\Sigma_k = \{\boldsymbol{x} \,:\, \varphi_k(\boldsymbol{x}) = 0\}, \text{ with } k = 1, \ldots, m. \tag{4.15}$$

being $\varphi_k(\boldsymbol{x})$ a signed-distance function that implicitly describe Σ_k. The resistive term has support in a narrow layer around Σ_k represented by a smoothed Dirac delta type

function:

$$\delta_{\Sigma_k,\varepsilon_k}(\varphi_k(\boldsymbol{x})) = \begin{cases} \dfrac{1+\cos(\pi\varphi_k(\boldsymbol{x})/\varepsilon_k)}{2\varepsilon_k} & \text{if } |\varphi_k| \le \varepsilon_k, \\ 0 & \text{if } |\varphi_k| > \varepsilon_k. \end{cases} \tag{4.16}$$

In Figure 4.1, we represent an immersed surface Σ_k in the fluid domain Ω_t. In particular, in the term (4.14) we have denoted with R_k the resistance coefficient and with $\varepsilon_k > 0$ a suitable parameter representing half of thickness of the immersed surface. In order to accurately represent the valve by means of the RIIS method, the mesh size h should be chosen small enough in the immersed surface region. Specifically, the minimum value of h should be chosen such that ε_k is at least 1.5 times h [86].

$\boldsymbol{u}_{\Sigma_k}$ is the immersed surface velocity that can be prescribed (for instance through medical images and measurements) or computed by solving a structural problem. For the sake of simplicity, and similarly to [100], we consider a *quasi-static* approach by taking $\boldsymbol{u}_{\Sigma_k} = \boldsymbol{0}$ throughout this thesis. We refer to [86, 100] for additional details on the RIIS method.

By expressing the NS equations in the ALE framework and by introducing the resistive term in Equation (4.14) provided by the RIIS method, allows to get the NS-ALE-RIIS equations as

$$\begin{aligned}
&\rho\frac{\widehat{\partial}\boldsymbol{u}}{\widehat{\partial}t} + \rho\left(\left(\boldsymbol{u}-\boldsymbol{u}^{\mathrm{ALE}}\right)\cdot\nabla\right)\boldsymbol{u} - \nabla\cdot\boldsymbol{\sigma}(\boldsymbol{u},p) + \\
&+\sum_{k=1}^{m}\frac{R_k}{\varepsilon_k}\delta_{\Sigma_k,\varepsilon_k}(\varphi_k)\left(\boldsymbol{u}-\boldsymbol{u}_{\Sigma_k}\right) = \boldsymbol{f} && \text{in } \Omega_t\times(0,T_f), && (4.17a)\\
&\nabla\cdot\boldsymbol{u} = 0 && \text{in } \Omega_t\times(0,T_f), && (4.17b)\\
&\boldsymbol{u} = \boldsymbol{g} && \text{on } \Gamma_t^D\times(0,T_f), && (4.17c)\\
&\boldsymbol{\sigma}(\boldsymbol{u},p)\boldsymbol{n} = \boldsymbol{h} && \text{on } \Gamma_t^N\times(0,T_f), && (4.17d)\\
&\boldsymbol{u} = \boldsymbol{u}_0 && \text{in } \Omega_0\times\{0\}. && (4.17e)
\end{aligned}$$

4.3. Numerical methods

We present the numerical methods to solve the NS-ALE-RIIS equations (Equation (4.17)) and the geometric problem introduced in Section 4.1.

4.3.1. Space and time discretization of the NS-ALE-RIIS equations and VMS-LES method

We introduce the infinite-dimensional function spaces

$$\mathcal{V}_{\boldsymbol{g}} := \left\{ \boldsymbol{v} \in [H^1(\Omega_t)]^d : \boldsymbol{v} = \boldsymbol{g} \text{ on } \Gamma_t^D \right\}, \quad \mathcal{Q} := L^2(\Omega_t). \tag{4.18}$$

and, by denoting with $(\cdot,\cdot)_{\Omega_t}$ and $(\cdot,\cdot)_{\Gamma_t^N}$ the L^2 inner product over Ω_t and Γ_t^N respectively, we define the weak formulation of the NS-ALE-RIIS equations as

given $\boldsymbol{u}(\boldsymbol{x},0) = \boldsymbol{u}_0$, for any $t \in (0,T_f)$, find $(\boldsymbol{u},p) \in \mathcal{V}_{\boldsymbol{g}} \times \mathcal{Q}$ s.t. :

$$\begin{aligned}
&\left(\boldsymbol{v}, \rho \frac{\widehat{\partial}\boldsymbol{u}}{\widehat{\partial} t}\right)_{\Omega_t} + \left(\boldsymbol{v}, \rho(\boldsymbol{u}-\boldsymbol{u}^{\mathrm{ALE}})\cdot\nabla\boldsymbol{u}\right)_{\Omega_t} + (\nabla\boldsymbol{v}, \mu\nabla\boldsymbol{u})_{\Omega_t} - (\nabla\cdot\boldsymbol{v}, p)_{\Omega_t} \\
&+ (q, \nabla\cdot\boldsymbol{u})_{\Omega_t} + \left(\boldsymbol{v}, \sum_{k=1}^{m} \frac{R_k}{\varepsilon_k}\delta_{\Sigma_k,\varepsilon_k}(\boldsymbol{u}-\boldsymbol{u}_{\Sigma_k})\right)_{\Omega_t} \\
&= (\boldsymbol{v},\boldsymbol{f})_{\Omega_t} + (\boldsymbol{v},\boldsymbol{h})_{\Gamma_t^N}, \quad \forall\,(\boldsymbol{v},q) \in \mathcal{V}_{\boldsymbol{0}} \times \mathcal{Q}.
\end{aligned} \tag{4.19}$$

For the spatial and temporal discretizations of Equation (4.19), we refer to the numerical methods presented in Chapter 2. Specifically, we refer to the compact formulation presented in Section 2.5; however, differently from Equation (2.42), here we include in $\boldsymbol{u}_*^h$ the ALE velocity:

$$\boldsymbol{u}_*^h = \begin{cases} \boldsymbol{u}_{n+1}^h - \boldsymbol{u}_{n+1}^{\mathrm{ALE},h} & \text{if implicit,} \\ \boldsymbol{u}_{n+1,\mathrm{EXT}}^h - \boldsymbol{u}_{n+1}^{\mathrm{ALE},h} & \text{if semi-implicit.} \end{cases} \tag{4.20}$$

The fully discrete BDF VMS-LES formulation for the NS-ALE-RIIS equations with a quasi-static approximation of fine scales reads:

given $\boldsymbol{u}_n^h, \ldots, \boldsymbol{u}_{n+1-\sigma_t}^h$, for any $n = 0, \ldots, N_t - 1$, find $(\boldsymbol{u}_{n+1}^h, p_{n+1}^h) \in \mathcal{V}_{\boldsymbol{g}}^h \times \mathcal{Q}^h$ s.t. :

$$\begin{aligned}
&\left(\boldsymbol{v}^h, \rho\frac{\alpha_{\mathrm{BDF}}\boldsymbol{u}_{n+1}^h}{\Delta t}\right)_{\Omega_{n+1}} + \left(\boldsymbol{v}^h, \rho\left(\boldsymbol{u}_*^h\cdot\nabla\right)\boldsymbol{u}_{n+1}^h\right)_{\Omega_{n+1}} + \left(\nabla\boldsymbol{v}^h, \mu\nabla\boldsymbol{u}_{n+1}^h\right)_{\Omega_{n+1}} \\
&- \left(\nabla\cdot\boldsymbol{v}^h, p_{n+1}^h\right)_{\Omega_{n+1}} + \left(q^h, \nabla\cdot\boldsymbol{u}_{n+1}^h\right)_{\Omega_{n+1}} \\
&+ \left(\boldsymbol{v}^h, \sum_{k=1}^{m}\frac{R_k}{\varepsilon_k}\delta_{\Sigma_k,\varepsilon_k}(\varphi_k)\left(\boldsymbol{u}_{n+1}^h - \boldsymbol{u}_{\Sigma_k,n+1}\right)\right)_{\Omega_{n+1}} \\
&+ \mathcal{S}(\boldsymbol{v}^h, q^h, \boldsymbol{u}_{n+1}^h, \boldsymbol{u}_*^h, p_{n+1}^h, p_{n+1,\mathrm{EXT}}^h)_{\Omega_{n+1}} \\
&= \left(\boldsymbol{v}^h, \boldsymbol{f}_{n+1}\right)_{\Omega_{n+1}} + \left(\boldsymbol{v}^h, \boldsymbol{h}_{n+1}\right)_{\Gamma_{n+1}^N} + \left(\boldsymbol{v}^h, \rho\frac{\boldsymbol{u}_{n,\mathrm{BDF}}^h}{\Delta t}\right)_{\Omega_n}, \\
&\text{for all } (\boldsymbol{v}^h, q^h) \in \mathcal{V}_{\boldsymbol{0}}^h \times \mathcal{Q}^h, \quad \text{for all } n \geq \sigma_t - 1.
\end{aligned} \tag{4.21}$$

The stabilization term $\mathcal{S}$ is defined as in Equation (2.44) and all the terms in Equation (2.44) are still defined as in Equations (2.45), (2.46) and (2.47). However, we recall that $\boldsymbol{u}_*^h$ is defined as in Equation (4.20) and that different definitions of the stabilization parameters and the strong residuals hold. Specifically, the stabilization parameters are now defined as

$$\tau_{\mathrm{M}}(\boldsymbol{u}_*^h) = \left(\frac{\sigma_t^2 \rho^2}{\Delta t^2} + \rho^2 \boldsymbol{u}_*^h \cdot \overline{\boldsymbol{G}} \boldsymbol{u}_*^h + C_r \mu^2 \overline{\boldsymbol{G}} : \overline{\boldsymbol{G}} + \sum_{k=1}^{m} \frac{R_k^2}{\varepsilon_k^2} \delta_{\Sigma_k, \varepsilon_k}^2(\varphi_k) \right)^{-\frac{1}{2}}, \tag{4.22a}$$

$$\tau_{\mathrm{C}}(\boldsymbol{u}_*^h) = \left(\tau_{\mathrm{M}}(\boldsymbol{u}_*^h) \overline{\boldsymbol{g}} \cdot \overline{\boldsymbol{g}} \right)^{-1}, \tag{4.22b}$$

and the strong residuals as:

$$\begin{aligned} \boldsymbol{r}_{\mathrm{M}}(\boldsymbol{u}_{n+1}^h, p_{n+1}^h) = \rho & \left(\frac{\alpha_{\mathrm{BDF}} \boldsymbol{u}_{n+1}^h - \boldsymbol{u}_{n,\mathrm{BDF}}^h}{\Delta t} + \boldsymbol{u}_*^h \cdot \nabla \boldsymbol{u}_{n+1}^h \right) + \nabla p_{n+1}^h \\ & - \mu \Delta \boldsymbol{u}_{n+1}^h + \sum_{k=1}^{m} \frac{R_k}{\varepsilon_k} \delta_{\Sigma_k, \varepsilon_k}(\varphi_k) \left(\boldsymbol{u}_{n+1}^h - \boldsymbol{u}_{\Sigma_k, n+1} \right) - \boldsymbol{f}_{n+1}, \end{aligned} \tag{4.23a}$$

$$r_{\mathrm{C}}(\boldsymbol{u}_{n+1}^h) = \nabla \cdot \boldsymbol{u}_{n+1}^h. \tag{4.23b}$$

Finally, the strong residual of the momentum balance equation for the definition of the LES term in the semi–implicit case (Equation (2.47)) is defined as

$$\begin{aligned} & \boldsymbol{r}_{\mathrm{M,\ EXT}}(\boldsymbol{u}_{n+1}^h, p_{n+1}^h) = \\ & \rho \left(\frac{\alpha_{\mathrm{BDF}} \boldsymbol{u}_{n+1}^h - \boldsymbol{u}_{n,\mathrm{BDF}}^h}{\Delta t} + \left(\boldsymbol{u}_{n+1,\mathrm{EXT}}^h - \boldsymbol{u}_{n+1}^{\mathrm{ALE},h} \right) \cdot \nabla \boldsymbol{u}_{n+1}^h \right) \\ & + \nabla p_{n+1}^h - \mu \Delta \boldsymbol{u}_{n+1}^h + \sum_{k=1}^{m} \frac{R_k}{\varepsilon_k} \delta_{\Sigma_k, \varepsilon_k}(\varphi_k) \left(\boldsymbol{u}_{n+1}^h - \boldsymbol{u}_{\Sigma_k, n+1} \right) - \boldsymbol{f}_{n+1}, \end{aligned} \tag{4.24}$$

which can be decomposed – as in Equation (2.40) – in a RHS and a LHS terms respectively defined as:

$$\begin{aligned} \boldsymbol{r}_{\mathrm{M,EXT}}^{\mathrm{LHS}}(\boldsymbol{u}_{n+1}^h, p_{n+1}^h) = & \rho \left(\frac{\alpha_{\mathrm{BDF}} \boldsymbol{u}_{n+1}^h}{\Delta t} + \left(\boldsymbol{u}_{n+1,\mathrm{EXT}}^h - \boldsymbol{u}_{n+1}^{\mathrm{ALE},h} \right) \cdot \nabla \boldsymbol{u}_{n+1}^h \right) \\ & + \nabla p_{n+1}^h - \mu \Delta \boldsymbol{u}_{n+1}^h + \sum_{k=1}^{m} \frac{R_k}{\varepsilon_k} \delta_{\Sigma_k, \varepsilon_k}(\varphi_k) \boldsymbol{u}_{n+1}^h, \end{aligned} \tag{4.25a}$$

$$\boldsymbol{r}_{\mathrm{M}}^{\mathrm{RHS}} = \rho \frac{\boldsymbol{u}_{n,\mathrm{BDF}}^h}{\Delta t} + \boldsymbol{f}_{n+1} + \sum_{k=1}^{m} \frac{R_k}{\varepsilon_k} \delta_{\Sigma_k, \varepsilon_k}(\varphi_k) \boldsymbol{u}_{\Sigma_k, n+1}. \tag{4.25b}$$

4.3.2. Space discretization of the geometric problem

For the ALE lifting problem in Equation (4.4), we introduce the infinite-dimensional function space

$$\boldsymbol{\mathcal{V}}_{\widehat{\boldsymbol{d}}_\Gamma} := \left\{ \boldsymbol{v} \in \left[H^1(\widehat{\Omega}) \right]^d : \boldsymbol{v} = \widehat{\boldsymbol{d}}_\Gamma \text{ on } \widehat{\Gamma} \right\} \tag{4.26}$$

to get the following weak formulation:

$$\text{for any } t \in (0, T_f), \ \text{ find } \widehat{\boldsymbol{d}} \in \boldsymbol{\mathcal{V}}_{\widehat{\boldsymbol{d}}_\Gamma} \text{ s.t. } \left(\boldsymbol{K} \nabla \widehat{\boldsymbol{d}}, \nabla \widehat{\boldsymbol{w}} \right) = 0 \quad \forall \, \widehat{\boldsymbol{w}} \in \boldsymbol{\mathcal{V}}_{\boldsymbol{0}}. \tag{4.27}$$

The Galerkin approximation of Equation (4.27) is expressed as

$$\text{for any } n = 0, \dots, N_t, \ \text{ find } \widehat{\boldsymbol{d}}_n^h \in \boldsymbol{\mathcal{V}}_{\widehat{\boldsymbol{d}}_\Gamma}^h \text{ s.t. } \left(\boldsymbol{K} \nabla \widehat{\boldsymbol{d}}_n^h, \nabla \widehat{\boldsymbol{w}}^h \right) = 0 \quad \forall \, \widehat{\boldsymbol{w}}^h \in \boldsymbol{\mathcal{V}}_{\boldsymbol{0}}^h. \tag{4.28}$$

The ALE velocity in the reference configuration is recovered discretizing Equation (4.7) with the Backward Euler Method, as

$$\widehat{\boldsymbol{u}}_n^{\text{ALE},h} = \frac{\widehat{\boldsymbol{d}}_n^h - \widehat{\boldsymbol{d}}_{n-1}^h}{\Delta t}. \tag{4.29}$$

Finally, we move the domain Ω_n and the mesh $\mathcal{T}_n^h$ according to the ALE map $\mathcal{A}_n(\boldsymbol{x}) = \widehat{\boldsymbol{x}} + \widehat{\boldsymbol{d}}_n^h$ defined in Equation (4.1), which gives:

$$\Omega_n = \mathcal{A}_n(\widehat{\Omega}), \quad \mathcal{T}_n^h = \mathcal{A}_n(\widehat{\mathcal{T}^h}). \tag{4.30}$$

4.4. A 0D circulation model of the whole cardiovascular system

The closed-loop lumped-parameter (0D) circulation model that we employ in this thesis was recently proposed in [224] and inspired by [37, 123]. The 0D model establishes an analogy among the fluid-dynamics and the electrical components of a circuit. As displayed in Figure 4.2, the role of the flowrate $Q(t)$ is played by the current, while the pressure $p(t)$ by the voltage. The electric resistance R models viscosity effects, the inductance L inertial effects and finally the conductance C the compliance of vessels. As represented in Figure 4.3, the closed-loop model consists of the systemic and pulmonary circulations modelled with resistance-inductance-capacitance (RLC) circuits, one for the arterial part and the other one for the venous part. The four heart chambers (cardiac circulation) are modeled by time-varying elastance elements $E(t)$ and the four valves by non-ideal diodes. Let $V_{\text{LA}}(t)$, $V_{\text{LV}}(t)$, $V_{\text{RA}}(t)$, $V_{\text{RV}}(t)$, $p_{\text{LA}}(t)$, $p_{\text{LV}}(t)$, $p_{\text{RA}}(t)$, $p_{\text{RV}}(t)$ and $E_{\text{LA}}(t)$, $E_{\text{LV}}(t)$, $E_{\text{RA}}(t)$, $E_{\text{RV}}(t)$ be respectively the volumes, pressures and elastances of the LA, LV, RA, RV; $Q_{\text{MV}}(t)$, $Q_{\text{AV}}(t)$, $Q_{\text{TV}}(t)$ and $Q_{\text{PV}}(t)$ the flowrates in the MV, AV, TV and PV. $Q_{\text{AR}}^{\text{SYS}}(t)$, $Q_{\text{VEN}}^{\text{SYS}}(t)$ and $p_{\text{AR}}^{\text{SYS}}(t)$, $p_{\text{VEN}}^{\text{SYS}}(t)$ are the flowrates

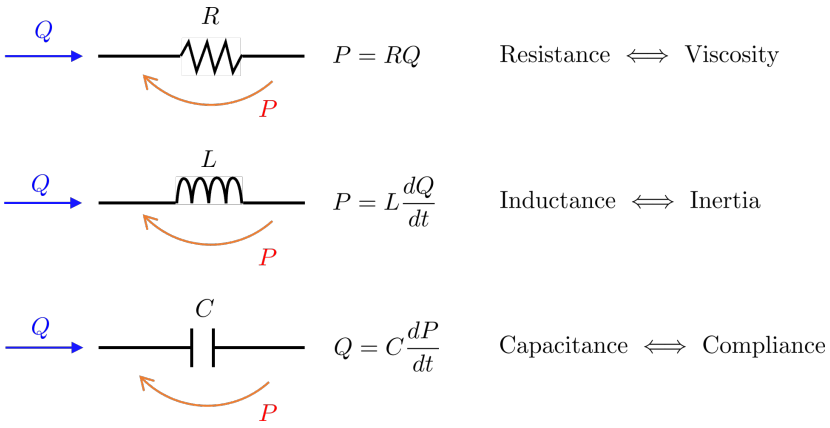

Figure 4.2: Analogy between the electrical components of a circuit and the fluid dynamics.

and pressures in the systemic circulation respectively in the arterial and venous parts; analogously for $Q_{\mathrm{AR}}^{\mathrm{PUL}}(t)$, $Q_{\mathrm{VEN}}^{\mathrm{PUL}}(t)$ and $p_{\mathrm{AR}}^{\mathrm{PUL}}(t)$, $p_{\mathrm{VEN}}^{\mathrm{PUL}}(t)$ in the pulmonary circulation.

The 0D closed-loop circulation model of the whole cardiovascular system reads [224]: for any $t \in (0, T_f)$:

$$\frac{\mathrm{d}V_{\mathrm{LA}}(t)}{\mathrm{d}t} = Q_{\mathrm{VEN}}^{\mathrm{PUL}}(t) - Q_{\mathrm{MV}}(t), \tag{4.31a}$$

$$\frac{\mathrm{d}V_{\mathrm{LV}}(t)}{\mathrm{d}t} = Q_{\mathrm{MV}}(t) - Q_{\mathrm{AV}}(t), \tag{4.31b}$$

$$\frac{\mathrm{d}V_{\mathrm{RA}}(t)}{\mathrm{d}t} = Q_{\mathrm{VEN}}^{\mathrm{SYS}}(t) - Q_{\mathrm{TV}}(t), \tag{4.31c}$$

$$\frac{\mathrm{d}V_{\mathrm{RV}}(t)}{\mathrm{d}t} = Q_{\mathrm{TV}}(t) - Q_{\mathrm{PV}}(t), \tag{4.31d}$$

$$C_{\mathrm{AR}}^{\mathrm{SYS}} \frac{\mathrm{d}p_{\mathrm{AR}}^{\mathrm{SYS}}(t)}{\mathrm{d}t} = Q_{\mathrm{AV}}(t) - Q_{\mathrm{AR}}^{\mathrm{SYS}}(t), \tag{4.31e}$$

$$C_{\mathrm{VEN}}^{\mathrm{SYS}} \frac{\mathrm{d}p_{\mathrm{VEN}}^{\mathrm{SYS}}(t)}{\mathrm{d}t} = Q_{\mathrm{AR}}^{\mathrm{SYS}}(t) - Q_{\mathrm{VEN}}^{\mathrm{SYS}}(t), \tag{4.31f}$$

$$C_{\mathrm{AR}}^{\mathrm{PUL}} \frac{\mathrm{d}p_{\mathrm{AR}}^{\mathrm{PUL}}(t)}{\mathrm{d}t} = Q_{\mathrm{PV}}(t) - Q_{\mathrm{AR}}^{\mathrm{PUL}}(t), \tag{4.31g}$$

$$C_{\mathrm{VEN}}^{\mathrm{PUL}} \frac{\mathrm{d}p_{\mathrm{VEN}}^{\mathrm{PUL}}(t)}{\mathrm{d}t} = Q_{\mathrm{AR}}^{\mathrm{PUL}}(t) - Q_{\mathrm{VEN}}^{\mathrm{PUL}}(t), \tag{4.31h}$$

$$\frac{L_{\mathrm{AR}}^{\mathrm{SYS}}}{R_{\mathrm{AR}}^{\mathrm{SYS}}} \frac{\mathrm{d}Q_{\mathrm{AR}}^{\mathrm{SYS}}(t)}{\mathrm{d}t} = -Q_{\mathrm{AR}}^{\mathrm{SYS}}(t) - \frac{p_{\mathrm{VEN}}^{\mathrm{SYS}}(t) - p_{\mathrm{AR}}^{\mathrm{SYS}}(t)}{R_{\mathrm{AR}}^{\mathrm{SYS}}}, \tag{4.31i}$$

$$\frac{L_{\mathrm{VEN}}^{\mathrm{SYS}}}{R_{\mathrm{VEN}}^{\mathrm{SYS}}} \frac{\mathrm{d}Q_{\mathrm{VEN}}^{\mathrm{SYS}}(t)}{\mathrm{d}t} = -Q_{\mathrm{VEN}}^{\mathrm{SYS}}(t) - \frac{p_{\mathrm{RA}}(t) - p_{\mathrm{VEN}}^{\mathrm{SYS}}(t)}{R_{\mathrm{VEN}}^{\mathrm{SYS}}}, \tag{4.31j}$$

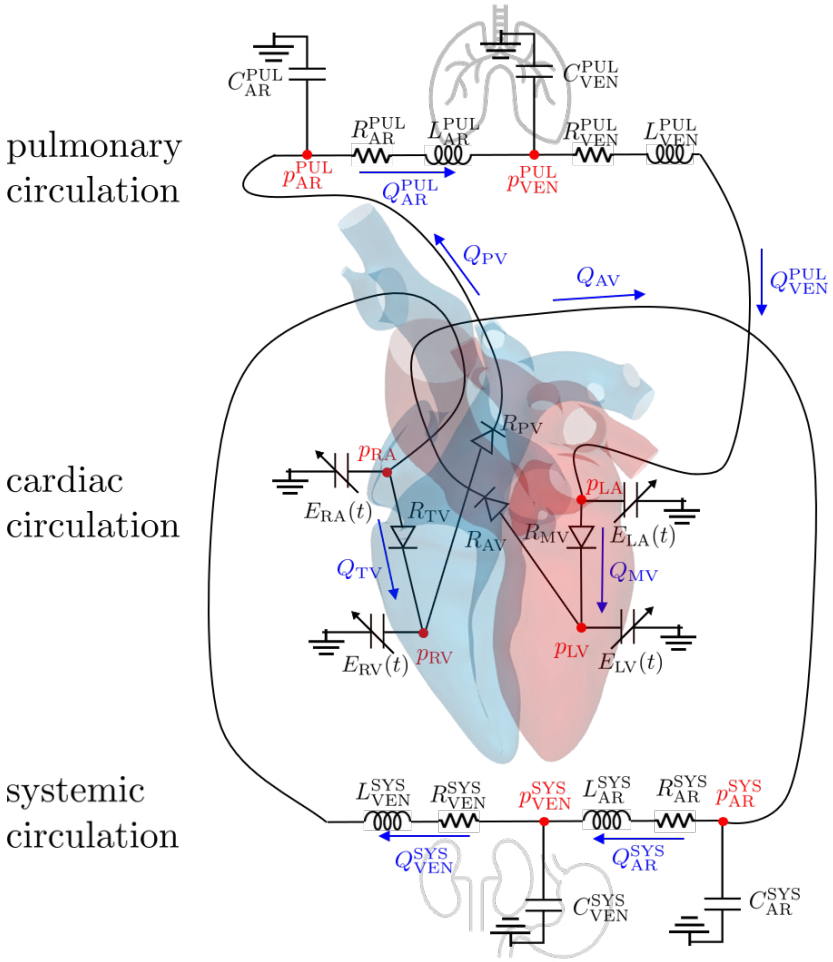

Figure 4.3: The 0D circulation model of the whole cardiovascular system.

$$\frac{L_{AR}^{PUL}}{R_{AR}^{PUL}}\frac{dQ_{AR}^{PUL}(t)}{dt} = -Q_{AR}^{PUL}(t) - \frac{p_{VEN}^{PUL}(t) - p_{AR}^{PUL}(t)}{R_{AR}^{PUL}}, \tag{4.31k}$$

$$\frac{L_{VEN}^{PUL}}{R_{VEN}^{PUL}}\frac{dQ_{VEN}^{PUL}(t)}{dt} = -Q_{VEN}^{PUL}(t) - \frac{p_{LA}(t) - p_{VEN}^{PUL}(t)}{R_{VEN}^{PUL}}, \tag{4.31l}$$

being

$$p_{LA}(t) = p_{EX}(t) + E_{LA}(t)\,(V_{LA}(t) - V_{0,LA})\,, \tag{4.32a}$$

$$p_{LV}(t) = p_{EX}(t) + E_{LV}(t)\,(V_{LV}(t) - V_{0,LV})\,, \tag{4.32b}$$

$$p_{RA}(t) = p_{EX}(t) + E_{RA}(t)\,(V_{RA}(t) - V_{0,RA})\,, \tag{4.32c}$$

$$p_{RV}(t) = p_{EX}(t) + E_{RV}(t)\,(V_{RV}(t) - V_{0,RV})\,, \tag{4.32d}$$

and

$$Q_{\mathrm{MV}}(t) = \frac{p_{\mathrm{LA}}(t) - p_{\mathrm{LV}}(t)}{R_{\mathrm{MV}}(p_{\mathrm{LA}}(t), p_{\mathrm{LV}}(t))}, \tag{4.33a}$$

$$Q_{\mathrm{AV}}(t) = \frac{p_{\mathrm{LV}}(t) - p_{\mathrm{AR}}^{\mathrm{SYS}}(t)}{R_{\mathrm{AV}}(p_{\mathrm{LV}}(t), p_{\mathrm{AR}}^{\mathrm{SYS}}(t))}, \tag{4.33b}$$

$$Q_{\mathrm{TV}}(t) = \frac{p_{\mathrm{RA}}(t) - p_{\mathrm{RV}}(t)}{R_{\mathrm{TV}}(p_{\mathrm{RA}}(t), p_{\mathrm{RV}}(t))}, \tag{4.33c}$$

$$Q_{\mathrm{PV}}(t) = \frac{p_{\mathrm{RV}}(t) - p_{\mathrm{AR}}^{\mathrm{PUL}}(t)}{R_{\mathrm{PV}}(p_{\mathrm{RV}}(t), p_{\mathrm{AR}}^{\mathrm{PUL}}(t))}, \tag{4.33d}$$

The elastances $E(t)$ of cardiac chambers are analytically prescribed and calibrated on the basis of physiological data; the valves are represented by diodes of resistance $R_k(p_{\mathrm{up}}^{(k)}, p_{\mathrm{down}}^{(k)})$, being $p_{\mathrm{up}}^{(k)}$, $p_{\mathrm{down}}^{(k)}$ the pressure upwind and downwind the valve k, with k = MV, AV, TV, PV. The system of ODEs in Equation (4.31) is complement with initial conditions.

As in [223], we solve the system of ODEs in Equation (4.31) with a 4^{th} order explicit Runge-Kutta method. The choice of a high-order time discretization scheme is motivated by the stiffness of the circulation model [210, 223]. For further details on the 0D closed-loop model used, the interested reader can refer to [223, 224].

5 | Computational hemodynamics of the left atrium

In this chapter, we numerically simulate the hemodynamics of the LA. Specifically, in Section 5.1 we present a computational model of a healthy LA by considering an idealized geometry, in Section 5.2 we investigate the role of VMS–LES in transitional flows by adopting the aforementioned LA model. In Section 5.3, we consider patient-specific geometries and we study the effects of the atrial fibrillation in the LA hemodynamics by analysing several hemodynamic indicators with a physiological patient-specific case. Eventually, we report our concluding remarks in Section 5.4.

The content of Sections 5.1 and 5.2 is partially reported in [291]; Section 5.3 contains material from the MSc thesis of Mattia Corti [61], for which I have been co-advisor.

5.1. Hemodynamics of an idealized left atrium in physiological conditions

Idealized geometries for the numerical simulation of blood flows offer the possibility of building a parametrized model that allows to obtain medical indicators for several patients without the need of performing expensive patient-specific simulations. To take into account the large geometrical inter-patient variability, an accurate idealized computational model of the LA can be parametrized based on patient-specific image acquisitions. Another motivation behind the use of an idealized geometry with a prescribed kinematics, which we deduce from the Wiggers diagram [175, 278], lays in the fact that patient-specific data for the atria in normal (physiological) conditions are scarce. Moreover, even if good quality kinematics images of the LA may become available, these would be typically acquired in individuals affected by pathological conditions, such as atrial fibrillation [168–170].

In the following, we present a computational model of the human LA based on the incompressible NS equations expressed in the ALE formulation introduced in Section 4.1; specifically, we prescribe a law of contraction and relaxation of the LA coherent with

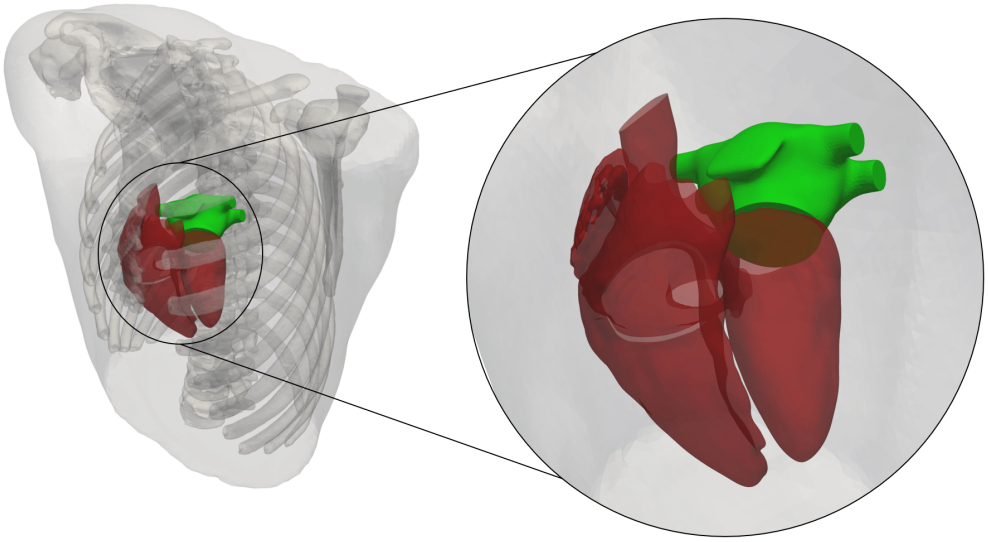

Figure 5.1: Position of the LA inside the torso. The idealized LA geometry is in green and the remaining heart's chambers in red. The 3D torso model is taken for visualization purposes from the repository CoMMLab [3, 88].

the features of the cardiac cycle.

The LA is a chamber located in the left part of the heart anchored on the top of the LV, connected to the pulmonary circulation system through the pulmonary veins and to the LV through the MV. The position, size and even the number of pulmonary veins is specific to the individual, but there are usually four veins situated in the upper part of the LA in a perpendicular direction with respect to the MV axis. The left atrial appendage (left auricle) is a small secondary cavity located on one side of the LA and connected to the main cavity through an orifice. In Figure 5.1 we highlight the position of the LA inside a human torso, while in Figure 5.2 we report the geometry of the idealized chamber that we use for the numerical simulations.

The LA boundary Γ_t is split into six portions: four pulmonary veins sections $\Gamma^{\mathrm{PVein}_i}$, $i = 1, \dots, 4$, the MV section Γ_t^{MV} and the LA endocardium Γ_t^{w}. The pulmonary veins are considered equal sized and the left atrial appendage is labelled as LAA. The section area of the MV is 6.74 cm^2, while the area of each vein is 0.78 cm^2, if the former were to be considered circular, their diameters would be 2.93 cm and 1 cm respectively.

In physiological conditions, during diastole, blood is ejected from the LA into the LV through the open MV with a first strong ejection and a second weaker one, strengthened by the LA contraction known also as atrial kick. This process is characterized by a volume reduction of about 25% of the initial volume. The first blood ejection from the LA is called Early wave (E-wave) while the atrial kick is also known as After wave

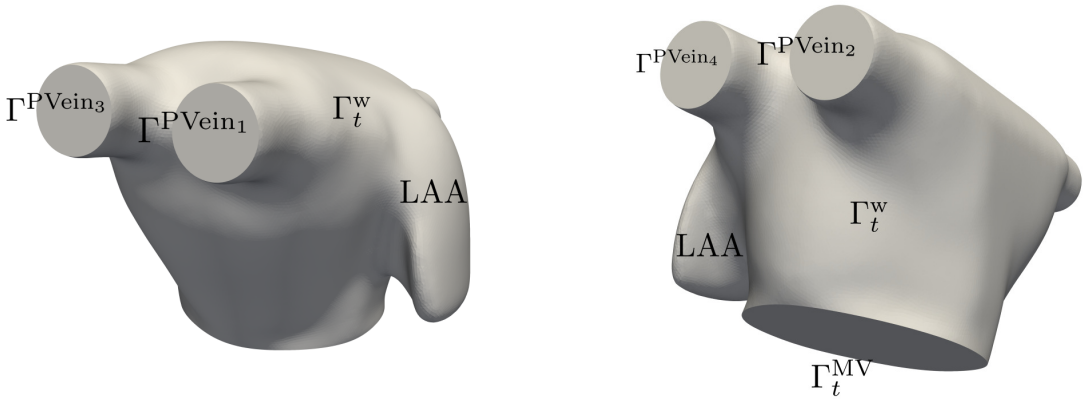

Figure 5.2: The idealized LA geometry from two different angles. The domain boundary is $\Gamma_t = \Gamma_t^{\text{w}} \cup \Gamma_t^{\text{MV}} \cup \left(\bigcup_{i=1}^{4} \Gamma^{\text{PVein}_i}\right)$.

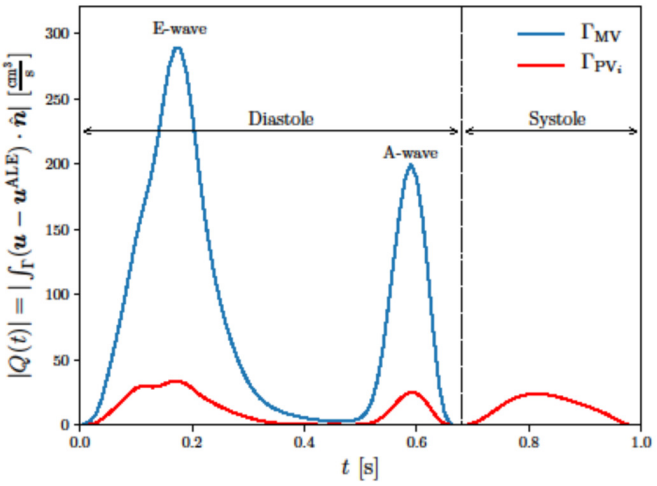

Figure 5.3: Absolute values of flowrates through the MV section (Γ_t^{MV}) and in each PV (Γ^{PVein_i}, $i = 1, \ldots, 4$) vs. time

(A-wave). During systole the MV closes and the LA is filled with blood coming from the pulmonary veins, enlarging to reach the original volume.

In literature, the MV flow has been studied and measured in both physiological and pathological conditions [51, 146, 213, 236, 248, 266]. In Figure 5.3 we report the inlet (pulmonary veins section) and outlet (MV section) absolute values of flowrates against time. The first peak during diastole is the E-wave, while the second one is the A-wave. During systole the flow through the MV is zero because the valve is closed. The heart cycle considered in this work corresponds to a rest condition at 60 bpm, i.e. the period is equal to $T_{\text{HB}} = 1$ s. The diastole lasts for $T_{\text{dias}} = 0.68$ s and the systole for

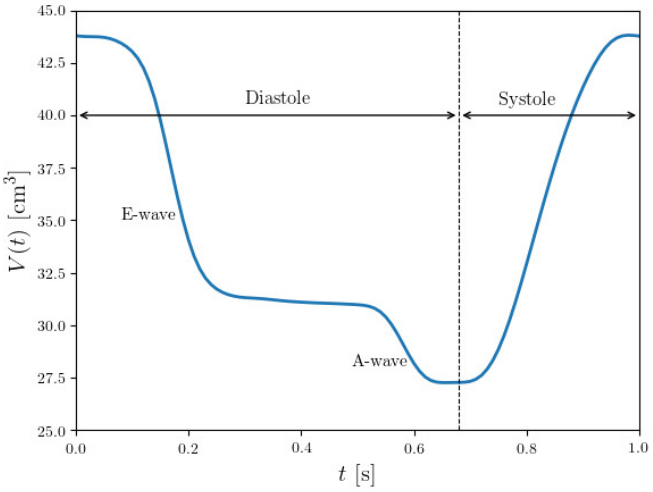

Figure 5.4: Idealized LA volume vs. time.

the remaining $T_{\text{syst}} = 0.32$ s; a whole heartbeat lasts $T_{\text{HB}} = T_{\text{dias}} + T_{\text{syst}}$. We simulate respectively diastole and systole, so that the initial time corresponds to the end systolic phase. The volume variation of the LA is based on the ejection phases, so the volume decrease is modeled in two phases corresponding to the E and A-waves. The LA filling phase is shorter and is accomplished with the volume increasing of the chamber. The LA volume as a function of time $V(t)$ is reported in Figure 5.4 [147].

5.1.1. Displacement modeling

As explained in Section 4.1, we prescribe a displacement field $\widehat{\boldsymbol{d}}_\Gamma$ on $\widehat{\Gamma}$ and we extend it to the fluid domain by means of an harmonic extension. Similarly, the same problem in Equation (4.4) can be expressed also in terms of the ALE velocity. Thus, we prescribe a velocity $\boldsymbol{g}^{\text{ALE}}$ on the boundary Γ_t and we extend it harmonically to get the ALE velocity $\boldsymbol{u}^{\text{ALE}}$ in Ω_t. In particular, we compute the ALE velocity on the LA boundary by assuming separation of variables as:

$$\boldsymbol{g}^{\text{ALE}}(\boldsymbol{x}, t) = \boldsymbol{f}^{\text{ALE}}(\boldsymbol{x})\, g^{\text{ALE}}(t) \quad \text{on } \Gamma_t, \tag{5.1}$$

where $\boldsymbol{f}^{\text{ALE}}(\boldsymbol{x})$ contains the directions of $\boldsymbol{g}^{\text{ALE}}$ and $g^{\text{ALE}}(t)$ is a time-dependent function. We design $\boldsymbol{f}^{\text{ALE}}$ to decrease the wall velocity near the pulmonary veins ($\boldsymbol{g}^{\text{ALE}} = \boldsymbol{0}$ on Γ^{PVein_i}, $i = 1, \dots, 4$). Let $\boldsymbol{e}_{\text{G}}(\boldsymbol{x})$ be the unit vector directed towards the LA center of mass, we define the function $\boldsymbol{f}^{\text{ALE}}$ as:

$$\boldsymbol{f}^{\text{ALE}}(\boldsymbol{x}) = F(z)\boldsymbol{e}_{\text{G}}(\boldsymbol{x}), \tag{5.2}$$

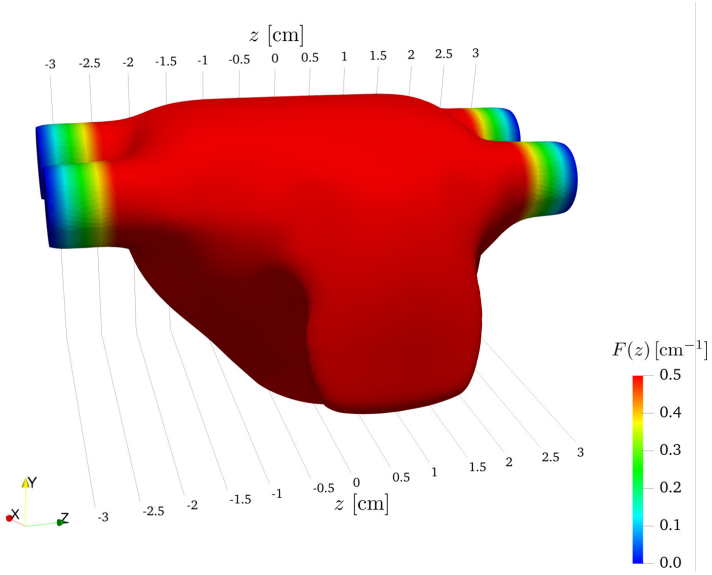

Figure 5.5: Function $F(z)$ (in Equation (5.3)) on the LA surface

with

$$F(z) = \begin{cases} 0.5 & \text{if } |z - z_G| \in [0, 2.5] \text{ cm}, \\ 0.5\left(\dfrac{2.5 - |z - z_G|}{0.72} + 1\right) & \text{if } |z - z_G| \in [2.5, 3.22] \text{ cm}, \\ 0 & \text{if } |z - z_G| \in [3.22, 10] \text{ cm}. \end{cases} \tag{5.3}$$

The function F is represented in Figure 5.5 and it is designed as in Equation (5.3) to be null on the pulmonary veins and positive and constant in the main chamber, increasing linearly in the transition regions. In order to get the time variation of the prescribed ALE velocity $g^{\text{ALE}}(t)$, we consider the LA volume time derivative and we use the *Reynolds transport theorem* (RTT) [153] and Equation (5.1) to get

$$\frac{\mathrm{d}V(t)}{\mathrm{d}t} = \frac{d}{\mathrm{d}t}\int_{\Omega_t} \mathrm{d}\Omega \overset{\text{RTT}}{=} \int_{\Gamma_t} \boldsymbol{g}^{\text{ALE}} \cdot \boldsymbol{n} \mathrm{d}\,\Gamma \overset{\text{Equation (5.1)}}{=} g^{\text{ALE}}(t) \int_{\Gamma_t} \boldsymbol{f}^{\text{ALE}} \cdot \boldsymbol{n} \mathrm{d}\,\Gamma, \tag{5.4}$$

which gives the following definition of g^{ALE}:

$$g^{\text{ALE}}(t) = \frac{1}{\int_{\Gamma_t} \boldsymbol{f}^{\text{ALE}} \cdot \boldsymbol{n} \mathrm{d}\Gamma} \frac{\mathrm{d}V(t)}{\mathrm{d}t}. \tag{5.5}$$

To better appreciate the LA deformation, in Figure 5.6 we overlap the geometry of the LA in its relaxed and contracted configurations, at the beginning and at the end of diastole, where the maximum LA contraction is met, respectively. By defining the displacement as explained, we measured a maximum mitral annular area equal to

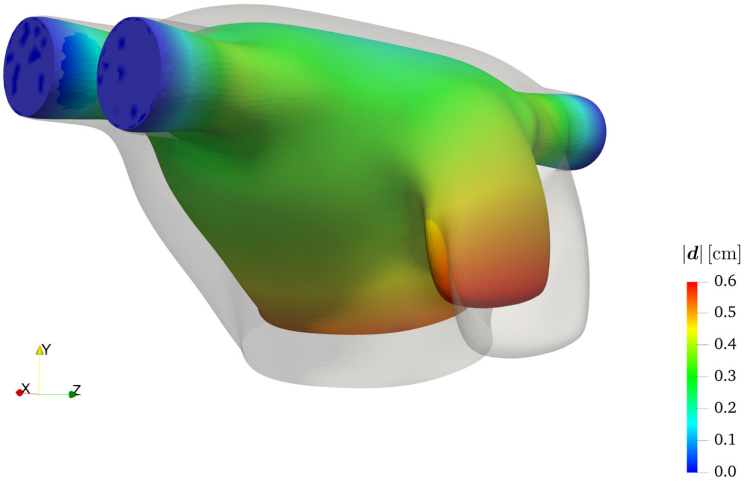

Figure 5.6: LA geometry at its maximum contraction at end diastole: the colors in the deformed geometry highlight the magnitude of the displacement field $|\boldsymbol{d}|$.

6.6 cm^2 and a minimum area equal to 4.8 cm^2, bringing to a percentage reduction equal to 27.3 % ((maximum area - minimum area)/maximum area). Our results are consistent with the clinical findings of [188], where they measured maximum mitral annular in the range 7.1 ± 1.3 cm^2 and a percentage reduction in the range 26 ± 3 %.

5.1.2. Boundary conditions

In terms of BCs, during diastole (MV is open), we set a homogeneous Neumann BC on the MV section and we prescribe Poiseuille profiles on the pulmonary veins. We do this by using, for each vein, a parabolic velocity profile and imposing the inlet flowrate $Q_{\text{PVein}_i}(t)$, $i = 1, \dots, 4$ that fulfils the mass balance[1].:

$$\sum_{i=1}^{4} Q_{\text{PVein}_i}(t) + Q_{\text{MV}}(t) + \frac{\mathrm{d}V(t)}{\mathrm{d}t} = 0, \tag{5.6}$$

whereas the flowrates are defined as:

$$Q_{\text{PVein}_i}(t) = \int_{\Gamma^{\text{PVein}_i}} \left(\boldsymbol{u} - \boldsymbol{u}^{\text{ALE}}\right) \cdot \boldsymbol{n} \, \mathrm{d}\boldsymbol{x}, \quad i = 1, \dots, 4, \tag{5.7}$$

$$Q_{\text{MV}}(t) = \int_{\Gamma_t^{\text{MV}}} \left(\boldsymbol{u} - \boldsymbol{u}^{\text{ALE}}\right) \cdot \boldsymbol{n} \, \mathrm{d}\boldsymbol{x}. \tag{5.8}$$

[1] We use the convection of the sign of the flow rate defined according to the outward unit normal $\boldsymbol{n}$. Thus, an inlet flow rate (entering velocity) will be, by definition, negative.

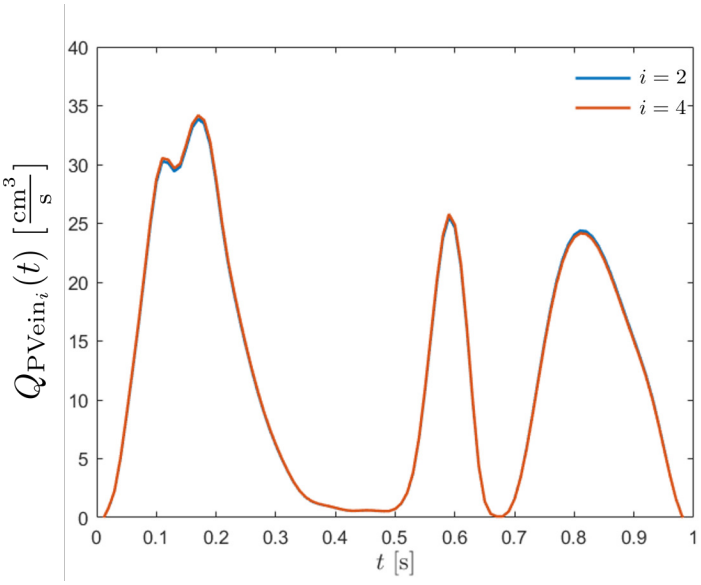

Figure 5.7: Inlet flowrates on $\Gamma^{\mathrm{PVein}_2}$ and $\Gamma^{\mathrm{PVein}_4}$.

During systole, the MV is closed ($Q_{\mathrm{MV}}(t) = 0$), so we switch the BC on Γ_t^{MV} to a Dirichlet one to model the closed behaviour of the valve: $\boldsymbol{u} = \boldsymbol{g}^{\mathrm{ALE}}$. The sudden switch of BCs from natural to essential and viceversa – aimed at replicating the rapid closing and opening stages of the MV – may potentially introduce some artifacts on the numerical solution, even if these are negligible in our experience. However, we observed that, during systole, numerical oscillations would arise by keeping Dirichlet BCs on all the inlet sections (as done during diastole) and on the MV section. For this reason, unlike diastole, we use a homogeneous Neumann BC on one of the pulmonary veins (specifically, we choose $\Gamma^{\mathrm{PVein}_4}$) while keeping a Dirichlet BC with assigned flowrate given by Equation (5.6) on the other three. As a matter of fact, from the simulation results, we found that numerical oscillations are strongly reduced using this boundary setting. In addition, we have found that during systole the flow is always entering in the domain (as for the remaining inlet sections), with a flowrate on $\Gamma^{\mathrm{PVein}_4}$ almost equal to the remaining sections where Dirichlet boudary is prescribed. We show this in Figure 5.7 where we compare the flowrate prescribed on inlet portion $\Gamma^{\mathrm{PVein}_2}$, where a Dirichlet BC is set for the whole heartbeat, and the flowrate computed on $\Gamma^{\mathrm{PVein}_4}$, where the homogeneous Neumann BC is prescribed in systole and a Dirichlet one in diastole. Mass balance condition in Equation (5.6) is hence always satisfied. By setting the BCs as explained, we finally obtain the fluxes through the MV section and through each PV as reported in Figure 5.3.

Thus, the problem consists in solving Equation (4.13) with the following set of boundary

and initial conditions:

$$
\begin{aligned}
&\boldsymbol{u} = \frac{2Q_{\mathrm{PVein}_i}}{|\Gamma^{\mathrm{PVein}_i}|}\left(1-\frac{r^2}{R_i^2}\right)\boldsymbol{n}_i && \text{on } \Gamma^{\mathrm{PVein}_i}\times(0,T_{\mathrm{dias}}],\ i=1,\dots,4,\\
&\boldsymbol{\sigma}(\boldsymbol{u},p)\boldsymbol{n} = \boldsymbol{0} && \text{on } \Gamma_t^{\mathrm{MV}}\times(0,T_{\mathrm{dias}}],\\
&\boldsymbol{u} = \boldsymbol{g}^{\mathrm{ALE}} && \text{on } \Gamma_t^{\mathrm{w}}\times(0,T_{\mathrm{dias}}],\\
&\boldsymbol{u} = \frac{2Q_{\mathrm{PVein}_i}}{|\Gamma^{\mathrm{PVein}_i}|}\left(1-\frac{r^2}{R_i^2}\right)\boldsymbol{n}_i && \text{on } \Gamma^{\mathrm{PVein}_i}\times(T_{\mathrm{dias}},T_{\mathrm{HB}}),\ i=1,2,3\\
&\boldsymbol{\sigma}(\boldsymbol{u},p)\boldsymbol{n} = \boldsymbol{0} && \text{on } \Gamma^{\mathrm{PVein}_4}\times(T_{\mathrm{dias}},T_{\mathrm{HB}}),\\
&\boldsymbol{u} = \boldsymbol{g}^{\mathrm{ALE}} && \text{on } \Gamma_t^{\mathrm{w}}\cup\Gamma_t^{\mathrm{MV}}\times(T_{\mathrm{dias}},T_{\mathrm{HB}}),\\
&\boldsymbol{u} = \boldsymbol{0} && \text{in } \Omega_0\times\{0\},
\end{aligned}
$$

in the Dirichlet inflow BC, $r(\boldsymbol{x}) = |\boldsymbol{x}|$, R_i is the radius of the i–th PV section and $\boldsymbol{n}_i$ its outward directed unit vector normal to. Moreover, a backflow-stabilization is introduced in all the homogeneous Neumann-type BCs in order to weakly penalize the reverse flow [32]:

$$
\boldsymbol{\sigma}(\boldsymbol{u},p)\boldsymbol{n} = \rho(\{(\boldsymbol{u}-\boldsymbol{u}^{\mathrm{ALE}})\cdot\boldsymbol{n}\}_-)\,(\boldsymbol{u}-\boldsymbol{u}^{\mathrm{ALE}}) \qquad \text{on } \Gamma_t^N, \tag{5.9}
$$

being $\{(\boldsymbol{u}-\boldsymbol{u}^{\mathrm{ALE}})\cdot\boldsymbol{n}\}_-$ the negative part of $(\boldsymbol{u}-\boldsymbol{u}^{\mathrm{ALE}})\cdot\boldsymbol{n}$:

$$
\{(\boldsymbol{u}-\boldsymbol{u}^{\mathrm{ALE}})\cdot\boldsymbol{n}\}_- = \begin{cases} (\boldsymbol{u}-\boldsymbol{u}^{\mathrm{ALE}})\cdot\boldsymbol{n} & \text{if } (\boldsymbol{u}-\boldsymbol{u}^{\mathrm{ALE}})\cdot\boldsymbol{n} < 0,\\ 0 & \text{if } (\boldsymbol{u}-\boldsymbol{u}^{\mathrm{ALE}})\cdot\boldsymbol{n} \geq 0. \end{cases} \tag{5.10}
$$

5.1.3. Mesh generation

The LA endocardium that we use was originally built by means of NURBS with the purpose of modeling the electric potential wavefront [194]. In particular, the LA endocardium is built as a single NURBS patch starting from B-splines basis functions of degree 2; the LA fluid mesh is then obtained by filling the obtained surface. For further details on the idealized LA geometrical representation we refer the interested reader to [194] and references there in. We generate three meshes, namely a coarse, medium and a fine one, denoted respectively as $\mathcal{T}_{h_1}$, $\mathcal{T}_{h_2}$ and $\mathcal{T}_{h_3}$. As shown in Figure 5.8 and reported in Table 5.1, for $\mathcal{T}_{h_1}$ and $\mathcal{T}_{h_2}$, a non-uniform distribution of mesh element size is considered in order to have a well resolved LAA. In particular, we employ for all mesh levels the same minimum cell-size $h_{\min} = 0.05$ cm in the lower corner of the LAA and we increase it linearly through an appropriate distance function (for $\mathcal{T}_{h_1}$ and $\mathcal{T}_{h_2}$ only). $\mathcal{T}_{h_3}$ instead keeps uniform grid cells sizes $h_{\min} = h_{\max} = 0.05$ cm. Furthermore, in order to accurately catch viscous effects near the wall, we introduce a boundary layer made of n_{layers} layers with linearly variable element thicknesses. In particular, we set for all the meshes the same boundary layer thickness $\delta_{\mathrm{BL}} = 0.05$ cm, while we increase the

	Mesh	$\mathcal{T}_{h_1}$	$\mathcal{T}_{h_2}$	$\mathcal{T}_{h_3}$
	# elements	575'220	1'711'622	8'344'030
# DOFs ($\mathbb{P}1-\mathbb{P}1$)	$\boldsymbol{u}^h$	291'561	830'517	4'030'227
	p^h	97'187	276'839	1'343'409
	total	388'748	1'107'356	5'373'636
Internal elements	$h_{\min}$[cm]	0.05	0.05	0.05
	$h_{\max}$ [cm]	0.2	0.1	0.05
Boundary layer	δ_{BL} [cm]	0.05	0.05	0.05
	n_{layers}	3	4	5
	χ_{BL}	0.8	0.8	0.8

Table 5.1: Details on the three meshes $\mathcal{T}_{h_i}$, $i = 1, \ldots, 3$: number of elements; number of degrees of freedom (DOFs) using Lagrangian linear elements (for velocity, pressure and total number); minimum and maximum cell size for the inner elements of the mesh; boundary layer: boundary layer thickness δ_{BL}, number of layers n_{layers} and ratio among successive layers' thicknesses χ_{BL}.

.

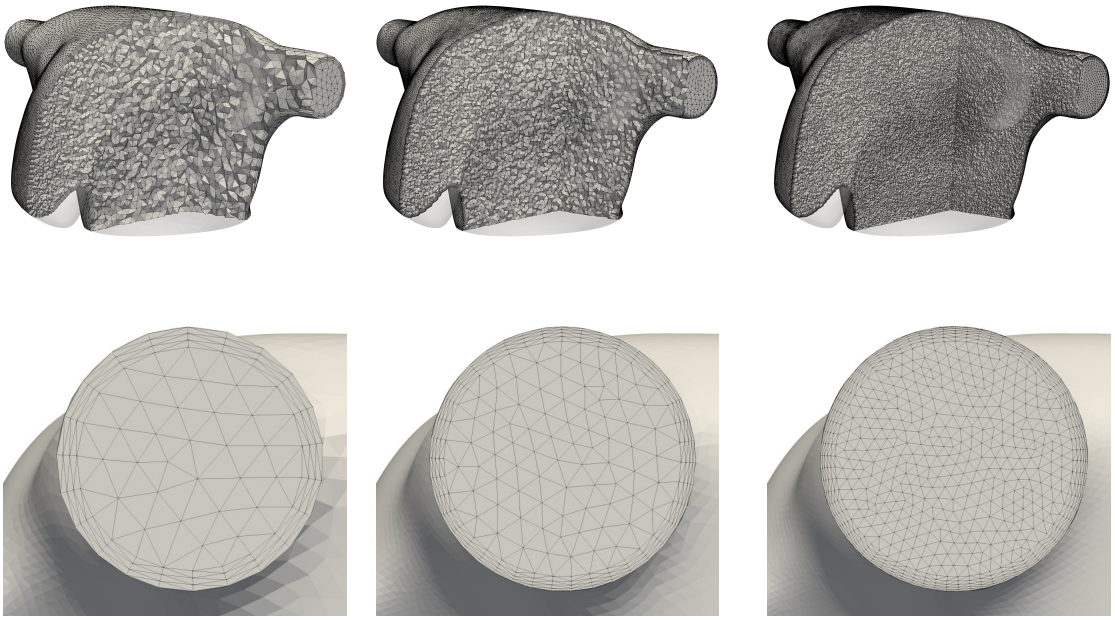

(a) mesh $\mathcal{T}_{h_1}$ (b) mesh $\mathcal{T}_{h_2}$ (c) mesh $\mathcal{T}_{h_3}$

Figure 5.8: The three meshes $\mathcal{T}_{h_i}$, $i = 1, \ldots, 3$ adopted for the CFD simulations of the idealized LA geometry with a focus on a inlet section.

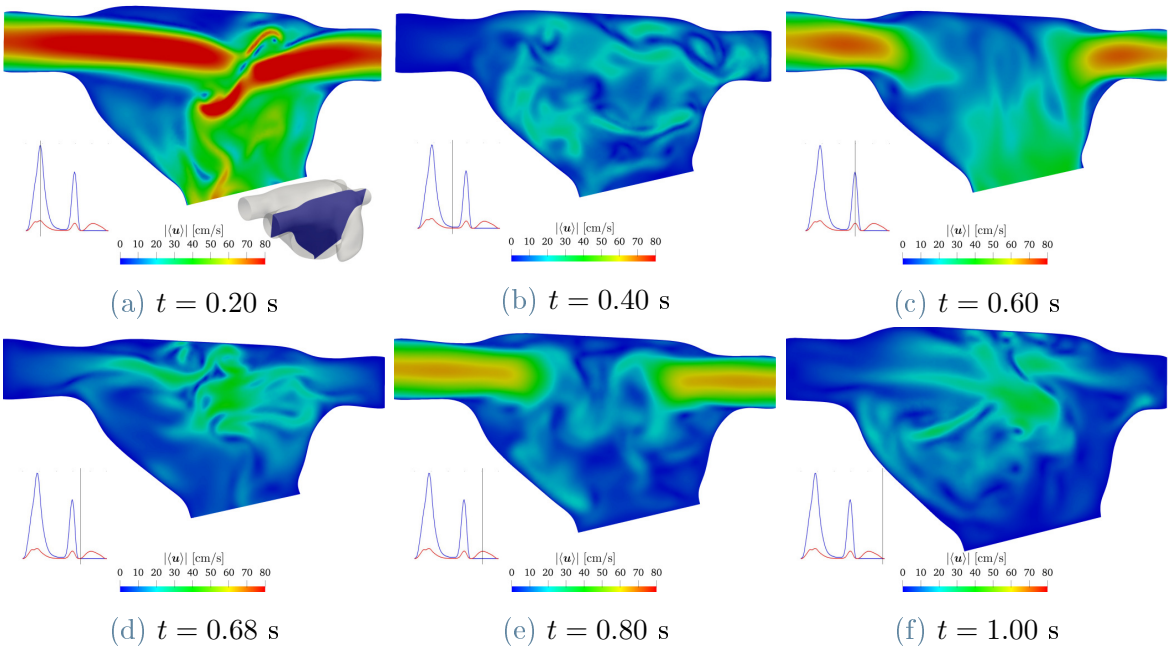

(a) $t = 0.20$ s (b) $t = 0.40$ s (c) $t = 0.60$ s

(d) $t = 0.68$ s (e) $t = 0.80$ s (f) $t = 1.00$ s

Figure 5.9: Reference solution: phase-averaged velocity magnitude $|\langle \boldsymbol{u} \rangle|$ on a slice cutting two pulmonary veins (top-left) at different time instants.

number of layers – going from a mesh level to another – keeping the same ratio among successive layers' thicknesses χ_{BL}. Table 5.1 lists quantitative information about the three meshes. Mesh generation is performed by exploiting the VMTK library [20, 85]. Meshes are uploaded to a GitLab repository and publicly accessible [9].

5.1.4. Numerical results and discussion

We report the numerical results obtained performing numerical simulations[2] by the FE library LifeV [1, 35] for the solution of the fluid dynamics in the idealized LA.

For each $\mathcal{T}_{h_i}$, $i = 1, \dots, 3$, we simulate six heartbeats, starting from the initial condition $\boldsymbol{u}_0 = \boldsymbol{0}$. Due to the periodicity in time of the BCs of the problem, we analyse the output of the numerical simulations with a phase-averaging filter in order to get averaged quantities on one representative cycle. Furthermore, in order to remove the influence the unphysical initial condition $\boldsymbol{u}_0 = \boldsymbol{0}$, we discard the first two heartbeats. Hence, referring to $N_{\text{HB}} = 4$ heartbeats, with period $T_{\text{HB}} = 1$ s, we introduce the phase-

[2]Numerical simulations were run on the cluster iHEART (Lenovo SR950 8 x 24-Core Intel Xeon Platinum 8160, 2100 MHz and 1.7TB RAM) available at MOX, Dipartimento di Matematica, Politecnico di Milano. Furthermore, simulations on the mesh $\mathcal{T}_{h_3}$ were run on the cluster GALILEO supercomputer (IBM NeXtScale cluster, 1022 nodes (Intel Broadwell), 2 x 18-Cores Intel Xeon E5-2697 v4 at 2.30 GHz, 36 cores/node, 26.572 cores in total with 128 GB/node) by CINECA.

averaging filter for the velocity as:

$$\langle \boldsymbol{u}(\boldsymbol{x},t)\rangle = \frac{1}{N_{\mathrm{HB}}}\sum_{n=1}^{N_{\mathrm{HB}}} \boldsymbol{u}(\boldsymbol{x},t+(n-1)T_{\mathrm{HB}}). \tag{5.11}$$

First, we present the results achieved with the mesh $\mathcal{T}_{h_3}$ using the SUPG stabilization method, which will represent our reference solution. Then, in Section 5.2 we perform a mesh convergence study using both SUPG and VMS-LES methods and we compare the two methods in terms of fluid dynamics indicators with the results achieved with the reference solution.

We report the results obtained with the mesh $\mathcal{T}_{h_3}$ by adopting a SUPG stabilization method, with a time step $\Delta t = 6.25 \cdot 10^{-5}$ s. The numerical solution correspondingly obtained is denoted as our reference solution. We remark that the results that will present are referred to the phase-averaged velocity $\langle \boldsymbol{u}\rangle$ which is representative of a heartbeat defined in the time domain $[0, T_{\mathrm{HB}}]$.

In Figure 5.9, we report the phase-averaged velocity magnitude of the blood on a slice cutting two pulmonary veins at six time instants corresponding to the diastolic peak of the E-wave ($t = 0.20$ s), the plateau between E and A-waves ($t = 0.40$ s), the A-wave ($t = 0.60$ s), the beginning of systole ($t = 0.68$ s), the filling phase during systole ($t = 0.80$ s) and the end of systole ($t = 1.00$ s). The peak velocity attained in our simulations is around 90 cm/s during the E-wave. The jets coming from the pulmonary veins impact one on each other, as it can be seen at time 0.20 s.

In Figure 5.10, we report volume rendering of the phase-averaged velocity magnitude at different time instants. The flow shows quite complex features, in particular we observe that the jets impact during the heartbeat in three peculiar instants: the E-wave (Figure 5.10a), the A-wave (Figure 5.10b) and during the filling phase of systole (Figure 5.10e).

In Figure 5.11, we display the Q-criterion by plotting the isosurfaces corresponding to $\mathsf{Q} = 2000$ Hz^2 coloured with the phase-averaged vorticity magnitude $|\nabla \times \langle \boldsymbol{u}\rangle|$. The main feature of this flow is the formation of vortex rings out of the pulmonary veins when the blood enters in the LA. These rings mutually interact when the corresponding jets impact and then form structures that become smaller and smaller until disappearing by dissipating their energy. In Figure 5.11a, we highlight the impact among the strong jets during the E-wave. Then, at time $t = 0.40$ s (Figure 5.11b), the structures become smaller and they have nearly disappeared as new jet enters at time $t = 0.60$ s (Figure 5.11c) forming four well visible vortex rings around the pulmonary veins sections (A-wave). In the refilling phase of systole ($t = 0.80$ s), the vortex rings are again visible with some residual structures still present at the center of the chamber.

By focusing on the impact during the E-wave we show, in Figure 5.12, the projection of the phase-averaged vorticity $\nabla \times \langle \boldsymbol{u}\rangle$ on the normal direction of a slice cutting two

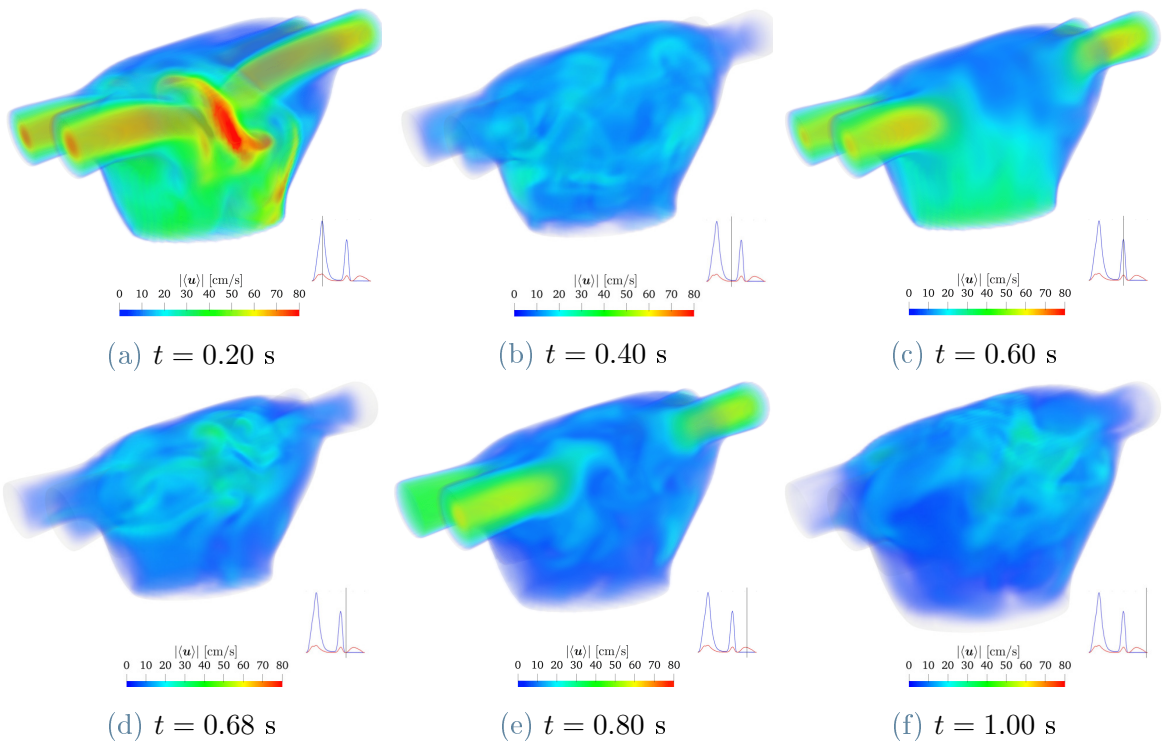

(a) $t = 0.20$ s (b) $t = 0.40$ s (c) $t = 0.60$ s

(d) $t = 0.68$ s (e) $t = 0.80$ s (f) $t = 1.00$ s

Figure 5.10: Reference solution: volume rendering of phase-averaged velocity magnitude $|\langle \boldsymbol{u} \rangle|$ at different time instants.

pulmonary veins. We observe the formation of shear layers from the pulmonary veins (Figure 5.12a), a early-stage interaction in Figure 5.12b along with some recirculation regions. Then, from $t = 0.18$ s, we observe perturbed shear layers with a coalescence of vortices and a dispersion of the organized flow pattern previously seen (Figures 5.12c, 5.12d). In particular, the vortices breakdown propagates in the rest of the chamber, towards the MV section (Figures 5.12e, 5.12f).

The velocity profile at the MV is an interesting output of this computation since it can be used as input for the simulation of the LV hemodynamics [248, 249]. In Figure 5.13, we report glyphs of velocity vector at the MV section during diastole (i.e. when the MV is open) on a slice coloured with $\langle \boldsymbol{u} \rangle \cdot \boldsymbol{n}_{\mathrm{MV}}$, i.e. the scalar product among the phase-averaged velocity and the outward pointing unit vector normal to the MV section. We notice that the velocity profile that we obtain is highly variable in time and, more importantly, the velocity shows a flat profile only at some specific times, such as at $t = 0.10$ s (Figure 5.13a). Even when the flow is intense, such as at $t = 0.20$ s or $t = 0.60$ s, the velocity profile is never flat but, on the contrary, the presence of vortices located above the MV section produces low velocity regions as shown in Figures 5.13b and 5.13f. During the time between the two waves, the flowrate is positive, as can be seen in Figures 5.13c, 5.13d and 5.13e, but some recirculating velocities are visible in some

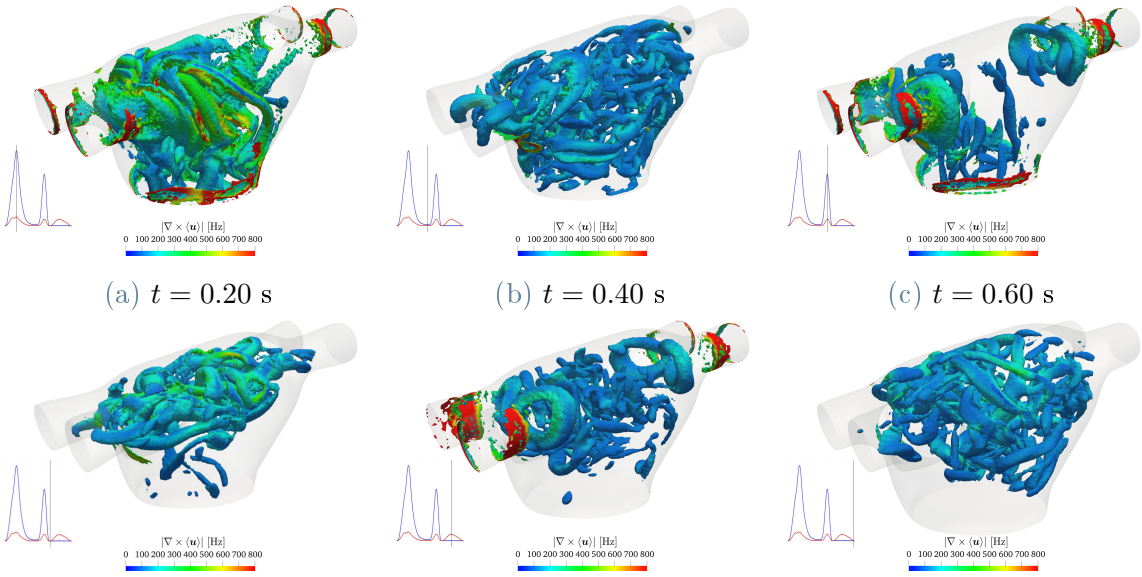

(a) $t = 0.20$ s (b) $t = 0.40$ s (c) $t = 0.60$ s

(d) $t = 0.68$ s (e) $t = 0.80$ s (f) $t = 1.00$ s

Figure 5.11: Reference solution: isosurfaces of Q-criterion $\mathsf{Q} = 2000$ Hz^2 coloured by phase-averaged vorticity magnitude $|\nabla \times \langle \boldsymbol{u} \rangle|$ at different time instants.

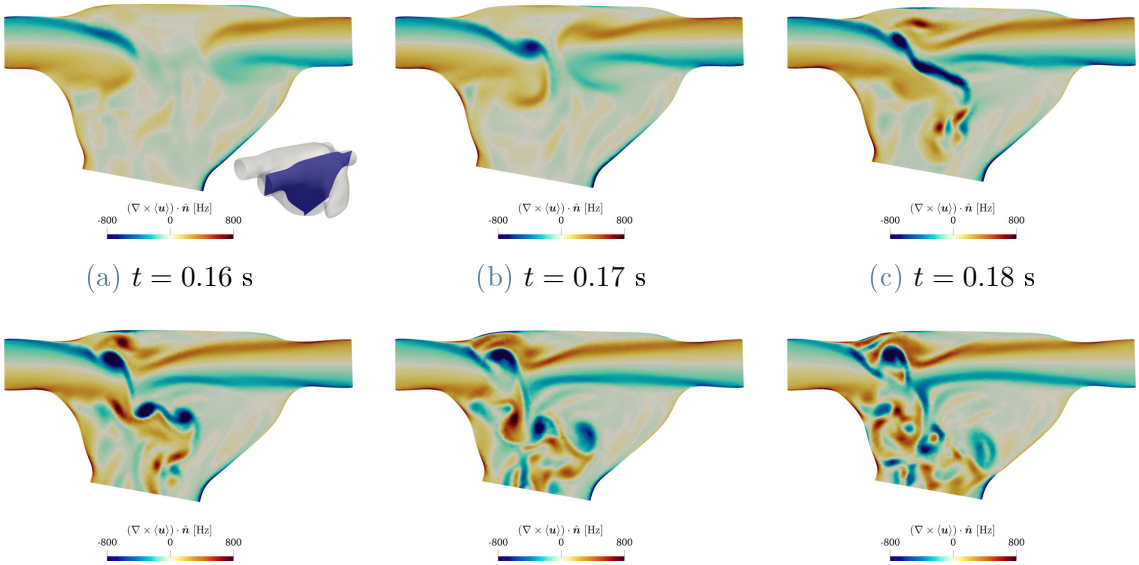

(a) $t = 0.16$ s (b) $t = 0.17$ s (c) $t = 0.18$ s

(d) $t = 0.20$ s (e) $t = 0.21$ s (f) $t = 0.22$ s

Figure 5.12: Reference solution: projection of the phase-averaged vorticity on the normal direction of a slice cutting two pulmonary veins (top-left) $(\nabla \times \langle \boldsymbol{u} \rangle) \cdot \boldsymbol{n}$. Results at different time instants in the proximity of the E-wave ($t = 0.20$ s).

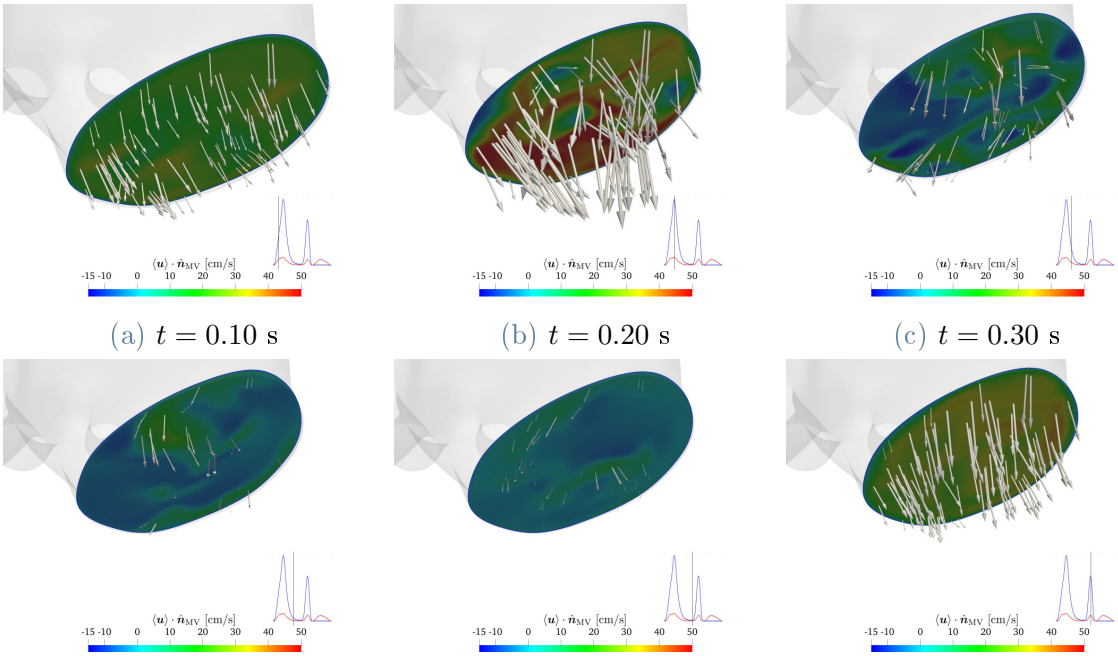

(a) $t = 0.10$ s (b) $t = 0.20$ s (c) $t = 0.30$ s

(d) $t = 0.40$ s (e) $t = 0.50$ s (f) $t = 0.60$ s

Figure 5.13: Reference solution: glyphs of velocity vector at the MV section during diastole on a slice coloured with $\langle \boldsymbol{u} \rangle \cdot \boldsymbol{n}_{\mathrm{MV}}$, i.e. the scalar product among the phase-averaged velocity and the outward pointing unit vector normal to the MV section.

spots reaching negative values of $\langle \boldsymbol{u} \rangle \cdot \boldsymbol{n}_{\mathrm{MV}} = -15$ cm/s. In Figure 5.14, we also report the MV velocity profile at different instants during diastole, which we remark being an output of our numerical simulations. The velocity profiles obtained significantly differ from a flat profile, a Pouiseuille profile, or, more generally, from those analytical profiles generally prescribed as inlet BCs during diastole for hemodynamic simulations of the LV (i.e. on the MV section) [74, 75, 163]. We made these profiles publicly available at the repository [9]: they can be used, after a suitable fitting in space and time, to prescribe an inflow BC at MV section during diastole for the LV simulation. This boundary treatment better accounts for the effect of the flow coming from the LA, which may considerably affects the hemodynamics of the LV.

Hemodynamic indicators

In view of calculating hemodynamic indicators, we define the viscous stress tensor related to the phase-averaged velocity field as

$$\boldsymbol{\tau}(\langle \boldsymbol{u} \rangle) = 2\mu \boldsymbol{\varepsilon}(\langle \boldsymbol{u} \rangle). \tag{5.12}$$

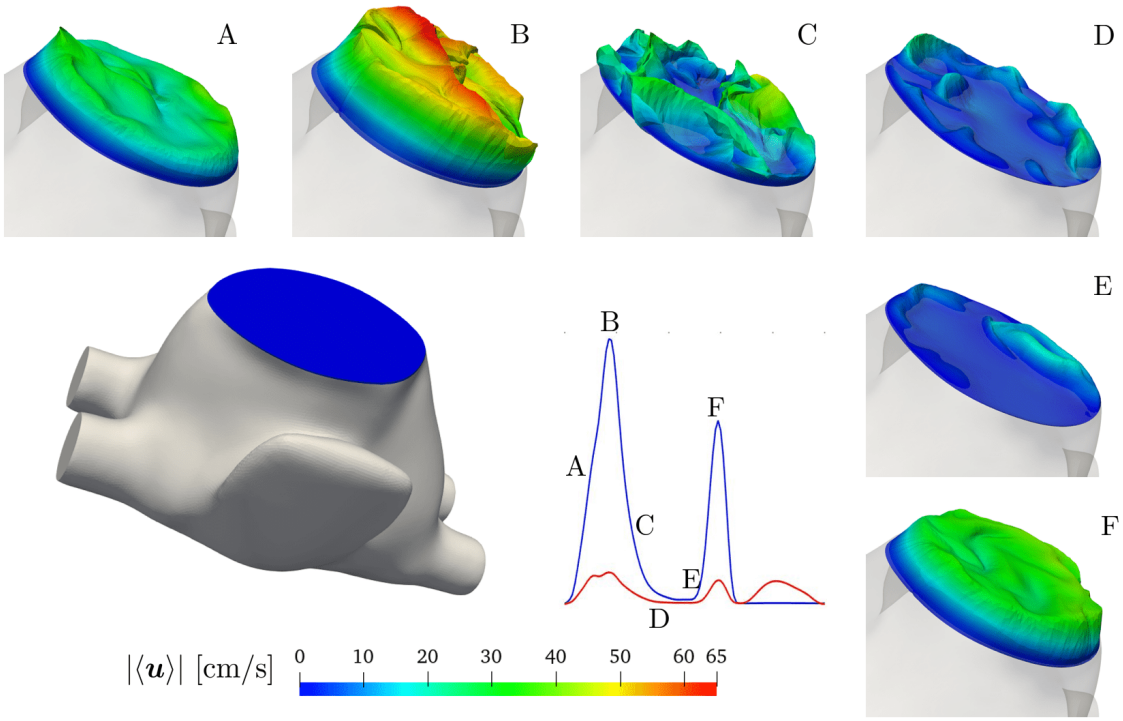

Figure 5.14: Reference solution: velocity profile at the MV section at different time during diastole.

We compute the vector wall shear stress (**WSS**) on the boundary of the reference configuration $\widehat{\Omega}$ (i.e. the LA at the beginning of diastole: $\widehat{\Omega} = \Omega_0$) as

$$\mathbf{WSS}(\langle \boldsymbol{u} \rangle) = \boldsymbol{\tau}(\langle \boldsymbol{u} \rangle)\boldsymbol{n} - (\boldsymbol{\tau}(\langle \boldsymbol{u} \rangle)\boldsymbol{n} \cdot \boldsymbol{n})\,\boldsymbol{n} \quad \text{on } \widehat{\Gamma}, \tag{5.13}$$

and the scalar fields time-averaged wall shear stress (TAWSS), oscillatory shear index (OSI) and relative residence time (RRT) (see [121, 147, 152]). These indicators can help shedding light on long-term response of endothelial cells since they are affected by both the magnitude of the WSS and its evolution in time. For this reason, they can be used to identify formation of new tissues, plaques and the promoting of neointimal hyperplasia [152]. With the WSS, we compute the TAWSS as the integral over the time period of the magnitude of the **WSS**,

$$\mathrm{TAWSS}(\langle \boldsymbol{u} \rangle) = \frac{1}{T_{\mathrm{HB}}} \int_0^{T_{\mathrm{HB}}} |\mathbf{WSS}(\langle \boldsymbol{u} \rangle)|_2 \, \mathrm{d}t \quad \text{on } \widehat{\Gamma}, \tag{5.14}$$

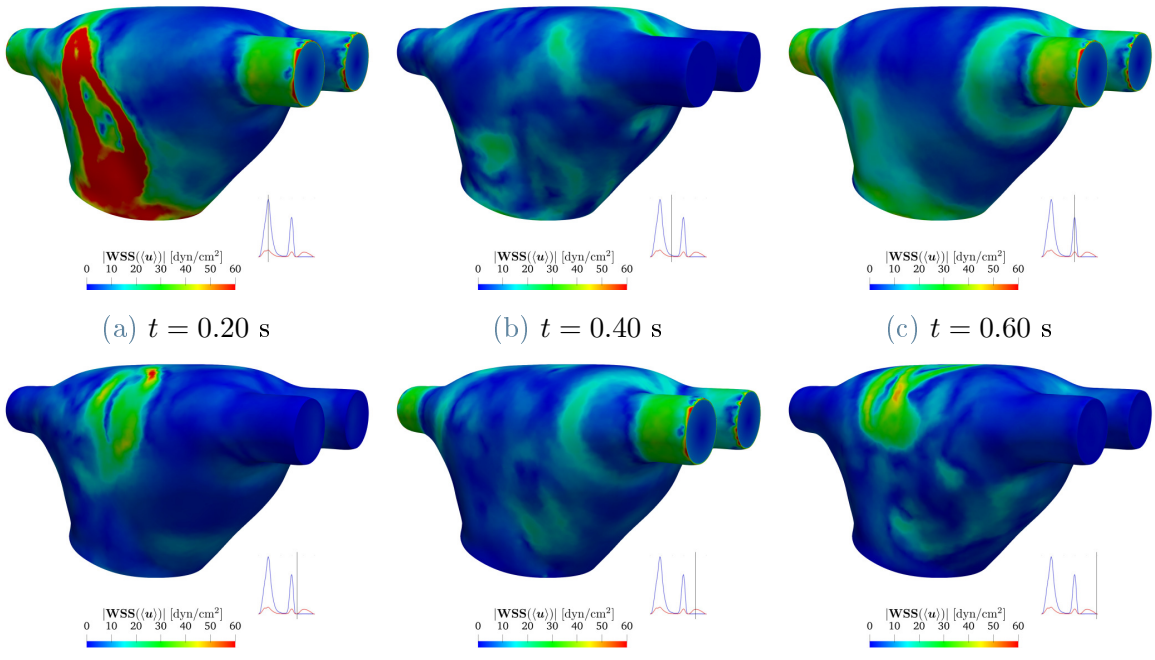

(a) $t = 0.20$ s (b) $t = 0.40$ s (c) $t = 0.60$ s

(d) $t = 0.68$ s (e) $t = 0.80$ s (f) $t = 1.00$ s

Figure 5.15: Reference solution: wall shear stress (WSS) magnitude at different time instants.

where $|\cdot|_2$ denotes the Euclidean norm of a vector. The OSI is defined as [152]:

$$\mathrm{OSI}(\langle \boldsymbol{u} \rangle) = \frac{1}{2}\left(1 - \frac{\left|\int_0^{T_{\mathrm{HB}}} \mathbf{WSS}(\langle \boldsymbol{u} \rangle)\,\mathrm{d}t\right|_2}{\int_0^{T_{\mathrm{HB}}} |\mathbf{WSS}(\langle \boldsymbol{u} \rangle)|_2\,\mathrm{d}t}\right) \quad \text{on } \widehat{\Gamma}, \tag{5.15}$$

and it is higher in regions where the WSS changes much during a heart cycle. Finally, we compute the RRT as in [121]

$$\mathrm{RRT}(\langle \boldsymbol{u} \rangle) = \left((1 - 2\,\mathrm{OSI}(\langle \boldsymbol{u} \rangle))\,\frac{1}{T_{\mathrm{HB}}}\int_0^{T_{\mathrm{HB}}} |\mathbf{WSS}(\langle \boldsymbol{u} \rangle)|_2\,\mathrm{d}t\right)^{-1} \quad \text{on } \widehat{\Gamma}. \tag{5.16}$$

The RRT is proportional to the residence time of blood particles in the proximity of the wall, and it can be regarded as a convenient fluid dynamics indicator to identify regions where WSS is both low and oscillatory [73].

In Figure 5.15, we report the WSS magnitude as computed on the surface of the LA at different time instants by using the phase averaged velocity. The largest values are attained during the E-wave in the middle of the surface of the LA, towards the MV. This region corresponds to areas where vortices interact and are pushed towards the LA wall. During the rest of the cycle, the WSS values remain quite small; large values

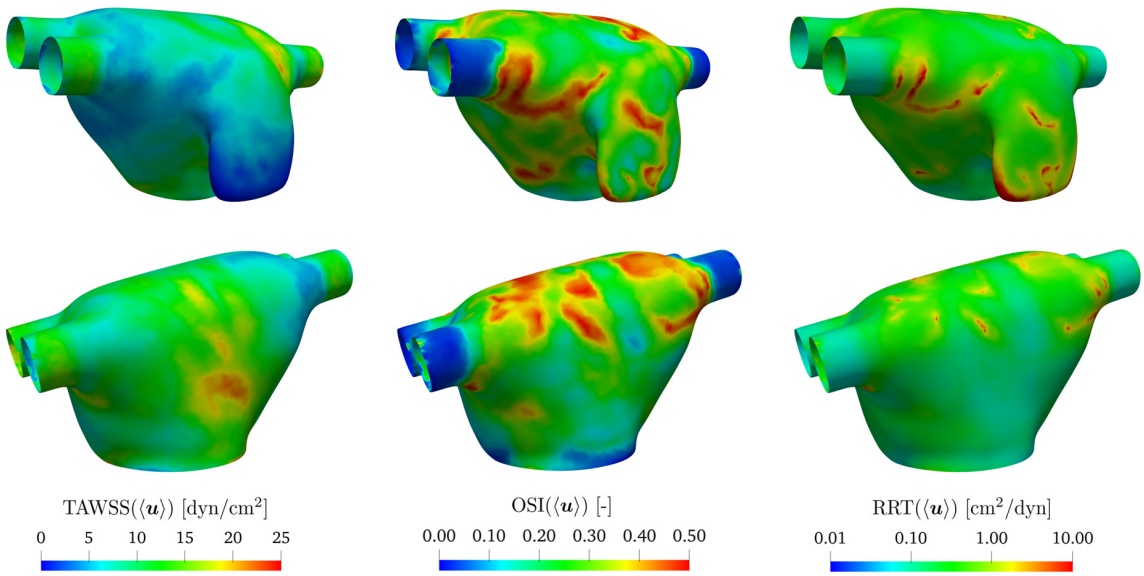

(a) TAWSS (b) OSI (c) RRT

Figure 5.16: Reference solution, hemodynamic indicators from two different perspectives: (a) TAWSS, (b) OSI, (c) RRT.

are attained only in the pulmonary veins and in the lower part of the LA.

Figure 5.16a shows the TAWSS on the reference configuration from two different perspectives: low values of the TAWSS are achieved in the LAA, while some peaks can be appreciated in the opposite side of the chamber, in accordance with the large values of $|\mathbf{WSS}|$ previously observed due to the interaction among the vortices and the endocardium.

In Figure 5.16b we report the OSI computed in the same settings of Figure 5.16a. The OSI is large on the top of the LA where a large recirculation is present and on the bottom of the LAA, revealing hence a significant variation of the wall shear stress.

As a qualitative indication of the time that a fluid particle spends in the vicinity of the wall, we report in Figure 5.16c the RRT: as expected, the largest values are attained in the bottom of the LAA. We suggest it could be related to the shape and position of the LAA, where the blood reaches very low velocities and recirculation effects are observed. Interestingly, analogous considerations in terms of all the analysed hemodynamic indicators are found in healthy patient-specific studies as highlighted in [147], both in terms of magnitude and their distribution on the LA surface.

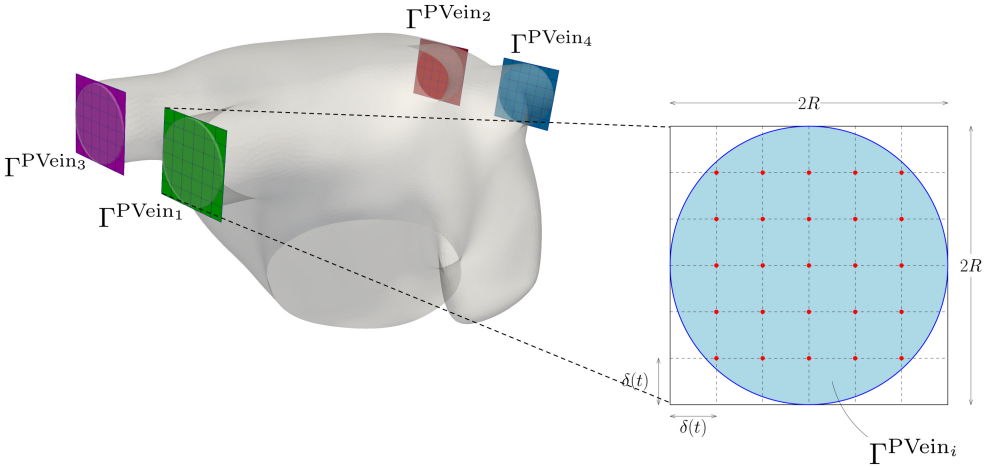

(a)

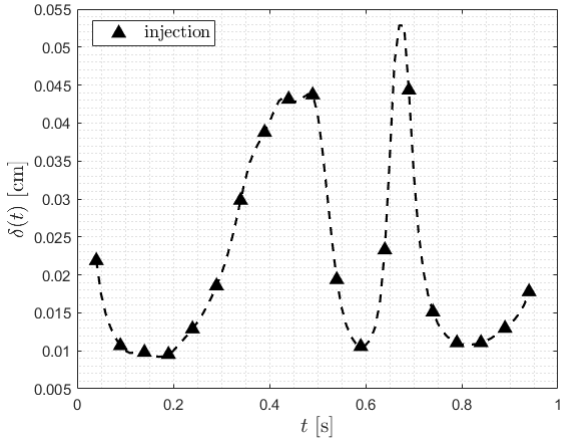

(b)

Figure 5.17: Details on the methodology adopted to estimate number of particles. Four grids built around the pulmonary veins of the LA with a focus on the grid (in red the $n(t)/4$ particles entering in each vein) (left). The behaviour of the grid element size $\delta(t)$ in time, with triangles, we denote the particles injection instants (every 0.05 s) (right).

5.1.5. Particles counting in the left atrium

Large values of RRT in the LAA suggest the stasis of blood particles, i.e. the coagulation of blood in low velocity regions, which may result in the formation of blood clots [70, 115]. For this reason, we want to count the number of blood particles remaining in the LA at the end of each heart-cycle. We inject in the chamber a number of particles

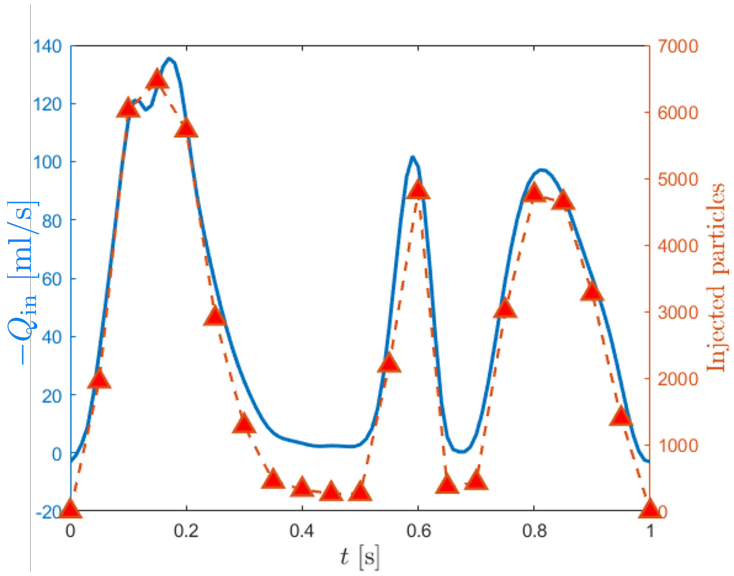

(a)

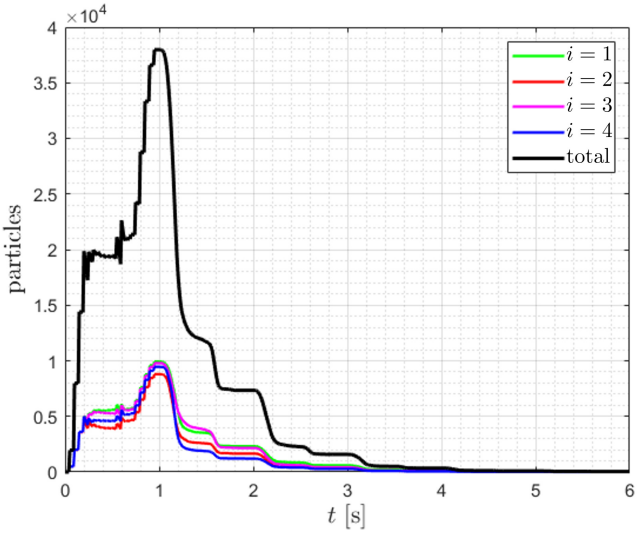

(b)

Figure 5.18: Reference solution. Particles injected every 0.05 s (in red) are proportional to the inlet flowrate (in blue) (left). Number of particles inside the LA during 6 cardiac cycles, introducing particles in the first cycle only. With different colours: the number of particles in the chamber coming from different pulmonary veins (right).

$n(t)$ that is proportional to the inlet flux $Q_{\text{in}}(t) = \sum_{i=1}^{4} Q_{\text{PVein}_i}(t)$ as:

$$n(t) = N_p \frac{Q_{\text{in}}(t)}{\max\limits_{t \in [0, T_{\text{HB}}]} Q_{\text{in}}(t)}, \tag{5.17}$$

time [s]	$t = 1.00$	$t = 2.00$	$t = 3.00$	$t = 4.00$	$t = 5.00$	$t = 6.00$
particles	37'971	7'336	1'583	344	91	42
% on total injected	75.23	14.53	3.14	0.68	0.18	0.08

Table 5.2: Reference solution: particles remaining in the LA at the end of each cardiac cycle and percentage of particles on total injected.

being N_p the maximum number particles injected at a specific time. In particular, we populate the LA with $n(t)$ particles only during the first heartbeat, and, at the end of each heart-cycle, we count how many particles are left inside the LA. As shown in Figure 5.17a, particles injection in the pulmonary veins is achieved by considering four squares of edge $2R$ (inlet sections diameter) discretized with a cartesian grid with element size $\delta(t)$. In a single vein, at time t, the number of particles entering in the LA is $\frac{n(t)}{4}$, which can be approximated as

$$\frac{n(t)}{4} \approx \left(\frac{2R}{\delta(t)} - 1 \right)^2 . \tag{5.18}$$

Using Eq. (5.17), the following expression of time-varying grid element size holds:

$$\delta(t) = R \left(\sqrt{N_p \frac{Q_{\text{in}}(t)}{\max\limits_{t \in [0, T_{\text{HB}}]} Q_{\text{in}}(t)}} + 2 \right)^{-1} , \tag{5.19}$$

which suggests that high flowrates correspond to small grid elements and therefore more particles are introduced. In Figure 5.17b, we report the behaviour of the grid element size in time. We inject particles in the four pulmonary veins every 0.05 s, proportionally to the inlet flowrate. In Figure 5.18a we plot the number of particles injected. In Figure 5.19 we report snapshots of the blood particles during six heartbeats, injecting in the first heart cycle only and leaving particles in the chamber for the following five cycles. We studied the contribution of particles coming from different veins representing with different colours particles from different inlets. We can observe the formation of four vortex rings coming from the pulmonary veins, with four jets impacting in the middle of the chamber and producing hence a mixing of particles. Particles remain inside the LAA, as also confirmed by large values of RRT previously found. In order to quantify wash-out effects, we stop particles introduction at $t = 1.00$ s, counting the number of particles at the end of each cycle. This result is then visualized in Figure 5.18b and quantified in Table 5.2. The overall number of particles introduced in the chamber during the first heartbeat is 50'471 and, at the end of each cardiac cycle, we report the percentage of particles still inside, showing that, after 5 cycles, in the LA there are the 0.08% of the total injected particles.

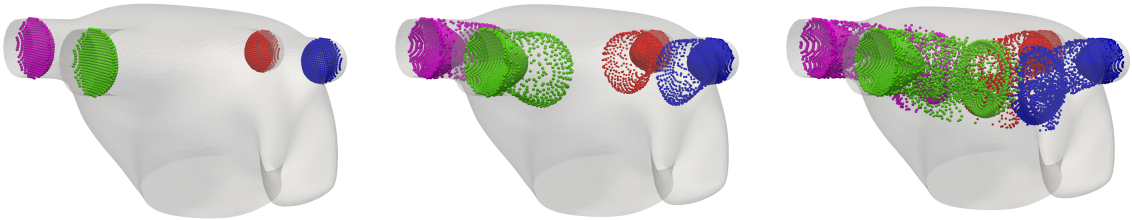

(a) $t = 0.05$ s (b) $t = 0.10$ s (c) $t = 0.15$ s

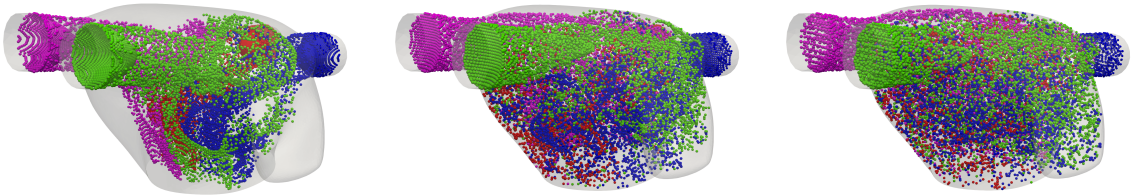

(d) $t = 0.20$ s (e) $t = 0.30$ s (f) $t = 0.40$ s

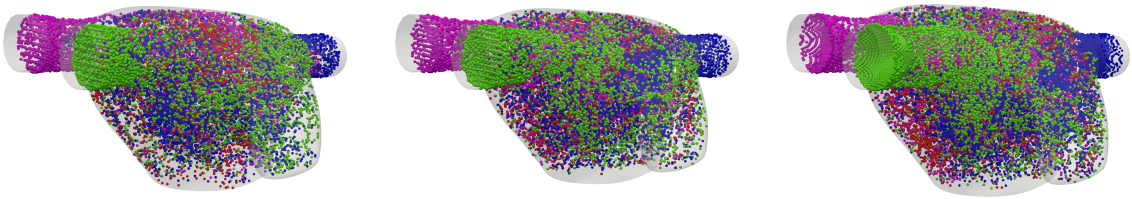

(g) $t = 0.50$ s (h) $t = 0.70$ s (i) $t = 0.80$ s

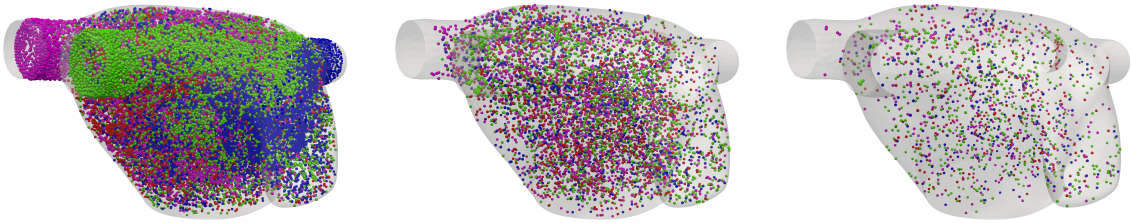

(j) $t = 1.00$ s (k) $t = 2.00$ s (l) $t = 3.00$ s

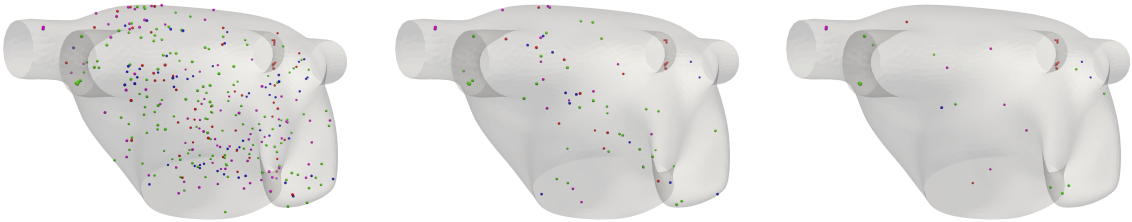

(m) $t = 4.00$ s (n) $t = 5.00$ s (o) $t = 6.00$ s

Figure 5.19: Reference solution: blood particles in the LA during six heartbeats, injecting particles for the first heartbeat only in a number proportional to the inlet flowrate. From (a) to (j) injection during the first cycle, from (k) to (o) particles remained inside the chamber at the end of each heart-cycle.

Mesh level	Δt [s]	Method	Courant numbers
$\mathcal{T}_{h_1}$	$1.00 \cdot 10^{-3}$	SUPG	0.8281
$\mathcal{T}_{h_1}$	$1.00 \cdot 10^{-3}$	VMS-LES	0.7666
$\mathcal{T}_{h_2}$	$2.50 \cdot 10^{-4}$	SUPG	0.3425
$\mathcal{T}_{h_2}$	$2.50 \cdot 10^{-4}$	VMS-LES	0.3871
$\mathcal{T}_{h_3}$ (reference)	$6.25 \cdot 10^{-5}$	SUPG	0.1560

Table 5.3: Details on the numerical simulations used to compare SUPG and VMS-LES stabilization methods in transitional regime. In all the simulations, we use $\mathbb{P}1 - \mathbb{P}1$ FE spaces, Backward Euler Method as time discretization scheme, and a semi-implicit treatment of the non linear terms.

5.2. On the role of VMS–LES in transitional cardiac flows

We present a comparison between VMS-LES and SUPG stabilization methods using the meshes $\mathcal{T}_{h_1}$ and $\mathcal{T}_{h_2}$. The results are compared with the reference solution of Section 5.1.4, which we remark has being obtained performing numerical simulation on the mesh $\mathcal{T}_{h_3}$ with the SUPG method. In Table 5.3, we summarize details of the five numerical simulations performed along with the Courant numbers computed as in [206] using the average mesh element size and the maximum (in space and time) velocity magnitude obtained in the numerical simulations. When the same mesh and the same time step are adopted, different Courant numbers are achieved due to different velocities obtained by the two methods. Further features on the meshes adopted are given in Table 5.1.

We define some turbulent indicators obtained integrating suitable variables over the whole domain that are then compared with reference data in order to validate the results of the numerical simulations. Specifically, we compute the total kinetic energy of the flow, by using the phase-averaged velocity (defined in Equation (5.11)), as

$$E_k(t) = \frac{1}{2}\rho \int_{\Omega_t} |\langle \boldsymbol{u} \rangle(\boldsymbol{x}, t)|_2^2 \, \mathrm{d}\boldsymbol{x}. \tag{5.20}$$

Moreover, we define the enstrophy of the flow as [158, 262]

$$S(t) = \frac{1}{2}\rho \int_{\Omega_t} |\nabla \times \langle \boldsymbol{u} \rangle(\boldsymbol{x}, t)|_2^2 \, \mathrm{d}\boldsymbol{x}. \tag{5.21}$$

The latter is a fluid dynamics indicator that can be used to identify a transitional flow [158, 262]. In Figure 5.20, we report E_k computed on the reference solution and for the meshes $\mathcal{T}_{h_1}$ and $\mathcal{T}_{h_2}$ with SUPG and VMS-LES methods. The total kinetic

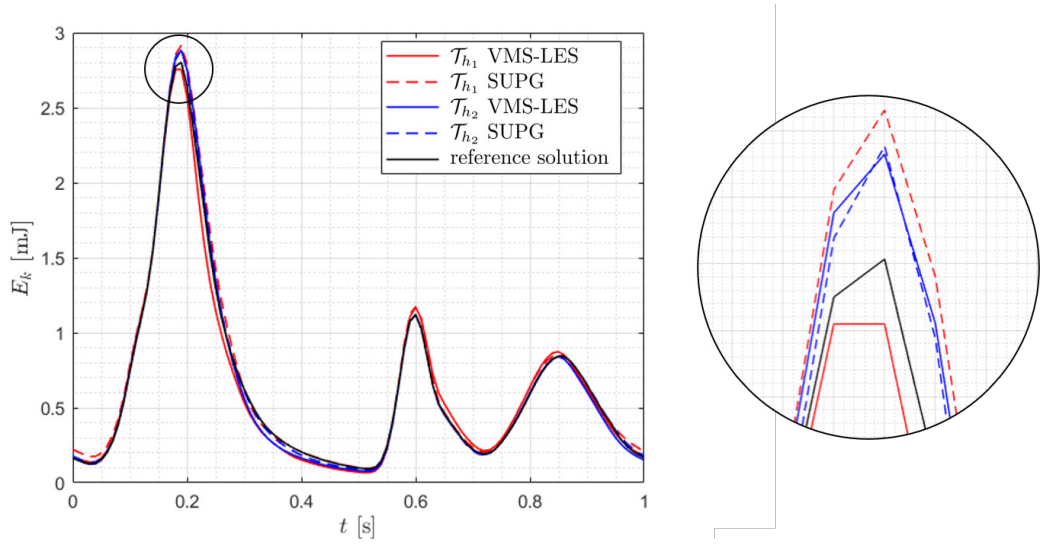

Figure 5.20: Total kinetic energy $E_k(\langle \boldsymbol{u} \rangle)$ using SUPG and VMS-LES methods on meshes $\mathcal{T}_{h_1}$ and $\mathcal{T}_{h_2}$ compared to the reference solution; zoom on the first peak.

energy presents three peaks in correspondence of E-wave, A-wave and systolic filling phase. Energy production is observed when high-speed blood flows arrive from the pulmonary veins. As the jets impact in the middle of the cardiac chamber, dissipation of the kinetic energy can be appreciated. All the methods and meshes share the same overall behaviour and coherent with the reference solution result. For the mesh $\mathcal{T}_{h_2}$, the results are almost always comparable, whereas small differences can be appreciated in correspondence of the first peak among VMS-LES and SUPG on the mesh $\mathcal{T}_{h_1}$: with a coarse level, we see how the VMS-LES method represents more accurately our reference solution, whereas SUPG overestimates it.

In Figure 5.21, we show the enstrophy S computed on the reference solution and for the meshes $\mathcal{T}_{h_1}$ and $\mathcal{T}_{h_2}$ with both SUPG and VMS-LES methods. As for the total kinetic energy E_k, we observe three main peaks during the hearbeat in correspondence of the production and consequent dissipation of vorticity. The solution largely depends on the underlying mesh and, as it is refined, the solution becomes more accurate and no remarkable differences among the methods can be appreciated.

In Figure 5.22, we report $E_k(\boldsymbol{u})$ and $S(\boldsymbol{u})$ computed on the reference solution during four heartbeats with the instantaneous velocity (not phase-averaged). The plot shows a high variability of the solution among heartbeats in terms of integral quantities: for instance, with respect to the last heartbeat, the E-wave peak shows a relative variation of about 6% for E_k and 12% for S. Thus, to quantify the large variation of the solution during different heart cycles, we introduce the fluctuating kinetic energy of the flow as

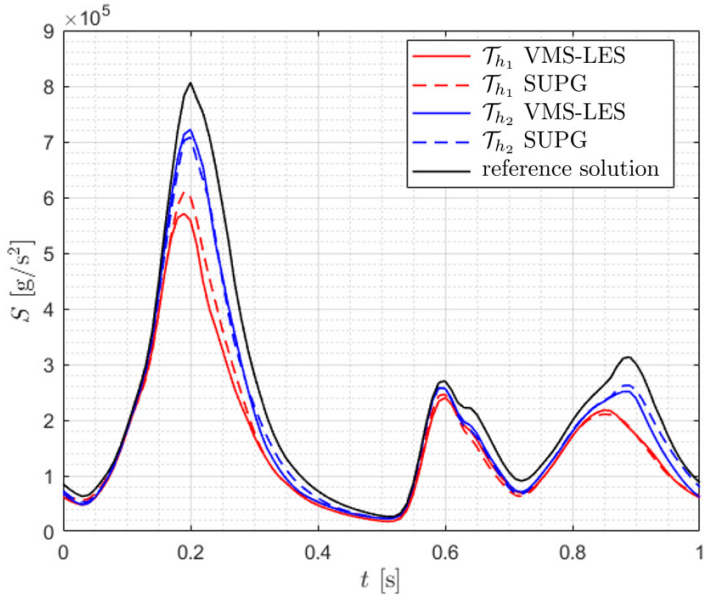

Figure 5.21: Enstrophy $S(\langle \boldsymbol{u} \rangle)$ using SUPG and VMS-LES methods on meshes $\mathcal{T}_{h_1}$ and $\mathcal{T}_{h_2}$ compared to the reference solution.

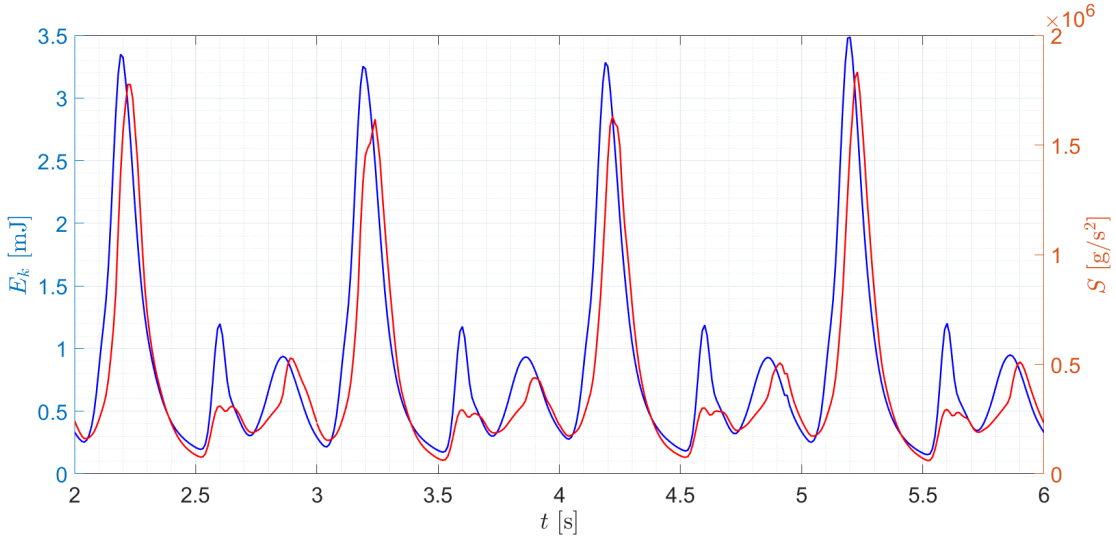

Figure 5.22: Total kinetic energy $E_k(\boldsymbol{u})$ and enstrophy $S(\boldsymbol{u})$ of the reference solution during four heartbeats.

[51, 249]

$$E_{kf}(t) = \frac{1}{2}\rho \int_{\Omega_t} |\boldsymbol{\sigma}_{\boldsymbol{u}}(\boldsymbol{x}, t)|_2^2 \mathrm{d}\boldsymbol{x}, \tag{5.22}$$

being $\boldsymbol{\sigma}_{\boldsymbol{u}} = (\sigma_{u_1}, \sigma_{u_2}, \sigma_{u_3})^T$ a vector containing the standard deviation (i.e. the fluc-

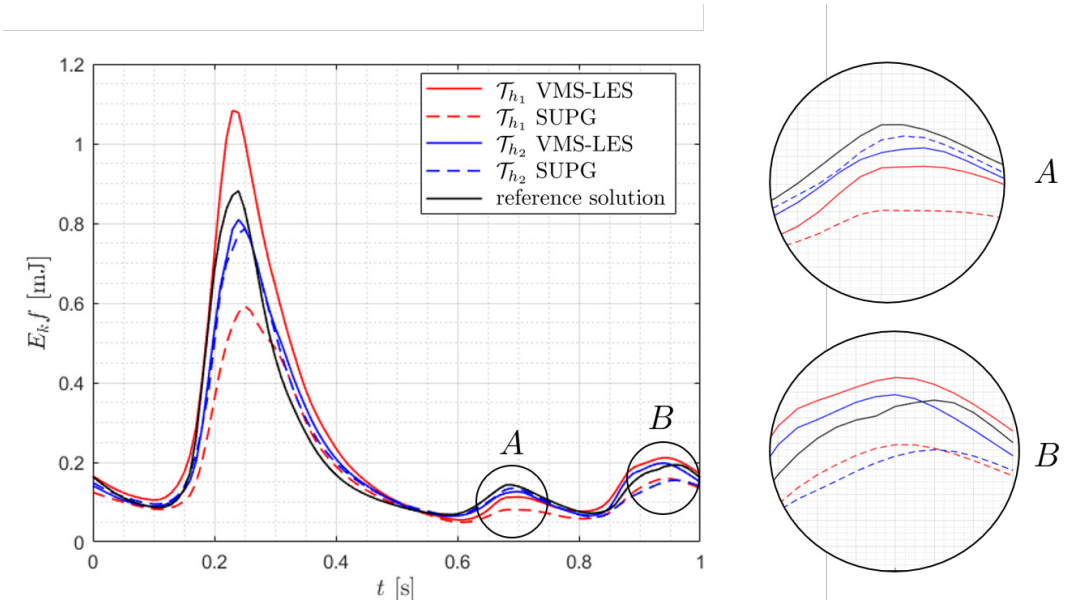

Figure 5.23: Fluctuating kinetic energy $E_{kf}(\boldsymbol{\sigma_u})$ using SUPG and VMS-LES methods on meshes $\mathcal{T}_{h_1}$ and $\mathcal{T}_{h_2}$ compared to the reference solution; zooms on the second and third peak.

tuations) of each component k of the velocity field with respect to the phase-averaged velocity. Its k–th component is defined as

$$\sigma_{u_k}(\boldsymbol{x},t) = \sqrt{\mathrm{var}(u_k(\boldsymbol{x},t))} = \sqrt{\langle {u_k}^2(\boldsymbol{x},t)\rangle - \langle u_k(\boldsymbol{x},t)\rangle^2}, \quad k=1,2,3. \tag{5.23}$$

The fluctuating kinetic energy is an important indicator of transition to turbulence but also provides informations on cycle-to-cycle variations. For this reason, it can be seen as one of the most characteristic indicators of transitional flow for hemodynamic applications [51, 249].

In Figure 5.23, we observe that the E_{kf} shows a peak with a large amplitude immediately after the E-wave. This result suggests that velocity fluctuations $\boldsymbol{\sigma_u}$ are higher during the first peak mainly due to small differences in the location of the shear layer and the vortical structures (where velocity gradients are high), as observed also in [51]. We show this by reporting in Figure 5.24 the specific fluctuating kinetic energy ($\frac{1}{2}\rho|\boldsymbol{\sigma_u}|^2$) on a slice passing through the four pulmonary veins at time $t = 0.25$ s. It can be observed in fact that the largest values are obtained in the area where jets and vortical structures impact. Large values of E_{kf} also confirm the large variability among heartbeats previously observed in Figure 5.22. In terms of meshes and methods, differently from the total kinetic energy E_k and the enstrophy S, we found more noticeable differences in the fluctuating kinetic energy E_{kf} as can be seen in Figure 5.23.

On the one hand, analysing the results related to the mesh $\mathcal{T}_{h_2}$, we observe that the

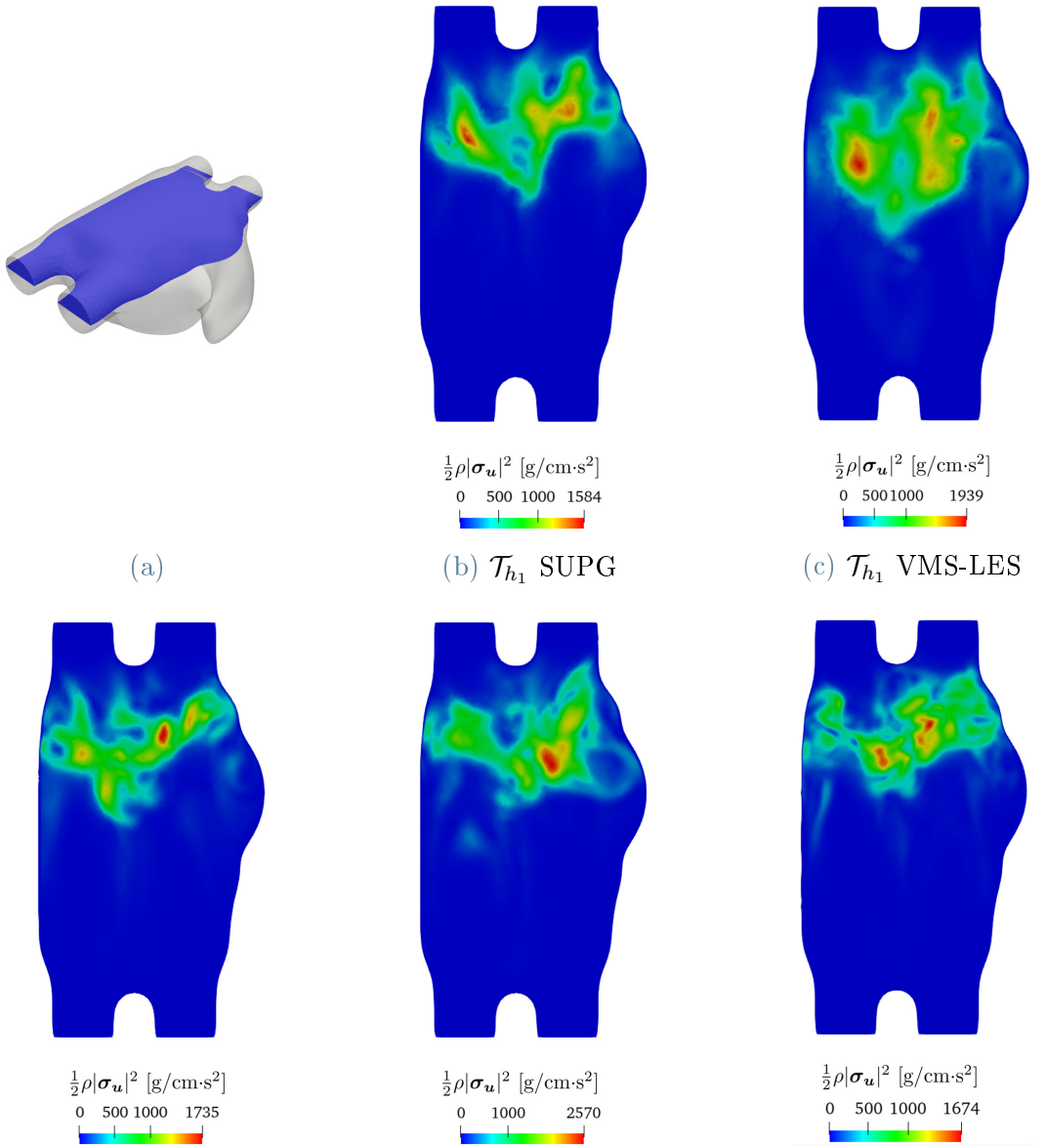

(a) (b) $\mathcal{T}_{h_1}$ SUPG (c) $\mathcal{T}_{h_1}$ VMS-LES

(d) $\mathcal{T}_{h_2}$ SUPG (e) $\mathcal{T}_{h_2}$ VMS-LES (f) Reference solution

Figure 5.24: Specific fluctuating kinetic energy $\frac{1}{2}\rho|\boldsymbol{\sigma_u}|$ on a slice passing through the four pulmonary veins (see (a)) at time $t = 0.25$ s using different meshes and methods. Large values of fluctuating velocities are observed in the region of impact among jets.

solutions obtained with SUPG and VMS-LES methods are very similar and both are close to the reference solution, except from the third peak (zoom B) when the VMS-LES method better predicts the reference solution. Moreover, to better quantify these differences, we report in Table 5.4 the minimum, maximum and average discrepancy

Mesh level	Method	$\min_t(e(t))$ [mJ]	$\max_t(e(t))$ [mJ]	$\overline{e(t)}$ [mJ]
$\mathcal{T}_{h_1}$	SUPG	0.0001	0.3408	0.0492
$\mathcal{T}_{h_1}$	VMS-LES	0.0009	0.2130	0.0438
$\mathcal{T}_{h_2}$	SUPG	0.0003	0.1826	0.0266
$\mathcal{T}_{h_2}$	VMS-LES	0.0002	0.1490	0.0256

Table 5.4: Minimum, maximum and average discrepancy of fluctuating kinetic energy with respect to the reference solution $e(t) = |E_{kf}(t) - E_{kf}^{\text{REF}}(t)|$.

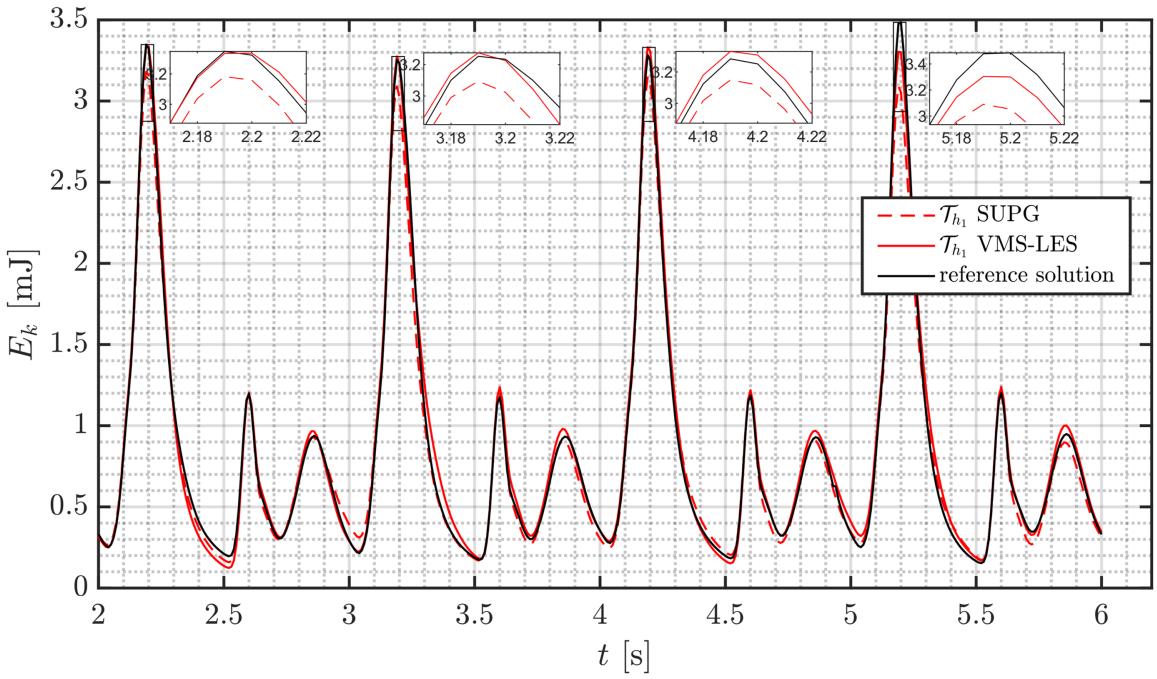

Figure 5.25: Total kinetic energy $E_k(\boldsymbol{u})$ during four heart-cycles with SUPG and VMS-LES on $\mathcal{T}_{h_1}$ compared with reference solution.

$e(t)$ achieved in terms of the fluctuating kinetic energy with respect to the reference solution $E_{kf}^{\text{REF}}(t)$, which shows that for the mesh $\mathcal{T}_{h_2}$, the VMS-LES method has a lower average and maximum discrepancy than SUPG. On the other hand, we found more remarkable differences for the mesh $\mathcal{T}_{h_1}$: as shown in Figure 5.23, the amplitude of the first peak is highly dependent on the stabilization method adopted; in particular, the VMS-LES solution produces a lower maximum error (that in this case coincides with the E-wave peak) than the one achieved with SUPG, as also confirmed in Table 5.4 in terms of maximum discrepancy. Moreover, the VMS-LES solution on $\mathcal{T}_{h_1}$ better predicts the reference solution than the SUPG on the same mesh (as confirmed also by zooms A and B and then better quantified in Table 5.4 in terms of mean discrepancy).

We investigated how the result obtained in terms of difference among fluctuating kinetic

energy with coarse meshes ($\mathcal{T}_{h_1}$) may affect the actual flow field: in Figure 5.25 we report the total kinetic energy computed with the instantaneous velocity $\boldsymbol{u}$ on four heartbeats obtained with the reference solution and with the SUPG and VMS-LES methods on $\mathcal{T}_{h_1}$. We observe that both methods correctly represent $E_k(\boldsymbol{u})$, but they both loose accuracy during energy dissipation stages, not revealing a clear trend among the two methods during these phases. On the contrary, the main difference between the two methods - and explained also by previous outcomes - is observed during the E-wave energy peak, which always shows that VMS-LES gives more accurate results, while SUPG method underestimates the peaks, revealing also how VMS-LES better predicts E-wave peaks variation from a cycle to another. This result shows that role of the VMS-LES method is more evident in the solution when larger Reynolds numbers are achieved, as during the E-wave, where at the MV section we measured a Reynolds number $Re_{\mathrm{MV}} \approx 3800$ and turbulence phenomena are more evident, as thoroughly detailed in Section 5.1.4. We believe this justifies the use of additional stabilization terms in Equation (2.44) modelling also Reynolds stresses [31, 93] in a LES fashion.

In the literature, we found few works that compare the SUPG and VMS-LES methods, and their conclusions go along different directions. In [118], the stabilized formulations for the fully-implicit log-morphology equation is adopted and applied to the centrifugal ventricular assist device: it is shown that the VMS stabilized formulation has better convergence behaviour and superior stabilization properties compared to the SUPG one. On the other hand, in [17] the numerical tests carried out revealed that both SUPG and VMS-LES methods exhibit comparable accuracy and they conclude that for their case the SUPG stabilization method is accurate enough. However, in our experience, we found that, as the mesh is refined, comparable results are achieved with SUPG and VMS-LES methods: the role of the turbulence model hence vanishes as the mesh becomes finer, which is coherent with the standard definition of a LES model. Thus, if sufficiently fine meshes are adopted, the SUPG method is accurate enough to predict transitional flows, and the use of the additional terms modelled by the VMS-LES do not yield additional benefits in terms of accuracy. On the contrary, the two methods show significant differences with coarser meshes in terms of fluctuating kinetic energy: VMS-LES produces a lower discrepancy with respect to the reference solution than with SUPG stabilization method; we also found that VMS-LES better predicts the E-wave kinetic energy peaks and their variations from a heartbeat to another. Thus, the VMS-LES method plays a significant role allowing to better catch transitional effects usually occurring in cardiac hemodynamics and cycle-to-cycle flow variations, fluid properties well described by the fluctuating kinetic energy. For this reason, when relatively coarse meshes are adopted, the use of a standard SUPG stabilization method might be not sufficient to correctly model cardiac hemodynamics.

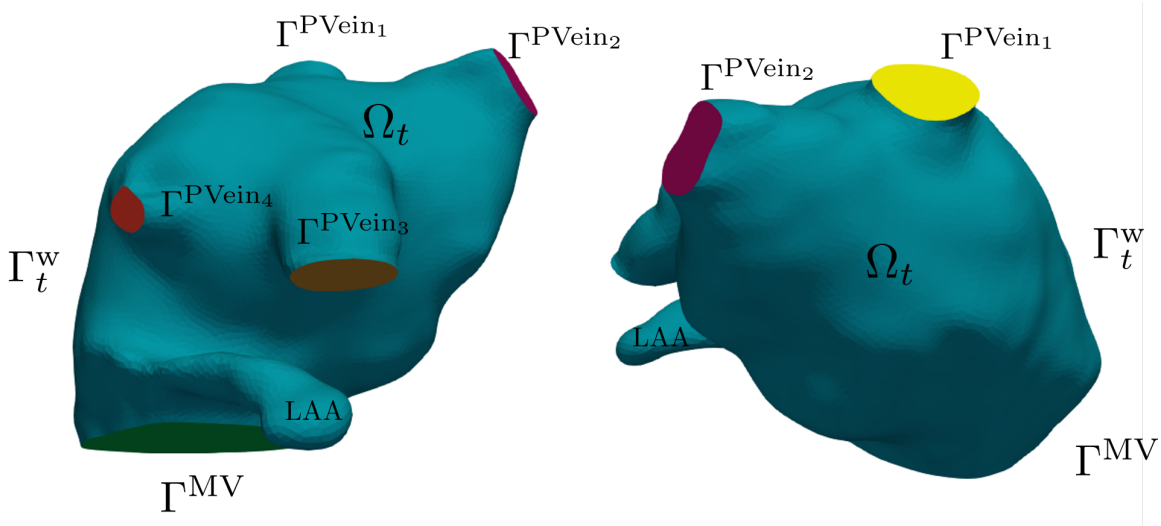

Figure 5.26: Example of patient-specific LA fluid domain Ω^t in two different perspectives. The fluid domain is bounded by $\Gamma_t = \left(\bigcup_{i=1}^{4} \Gamma^{\text{PVein}_i}\right) \cup \Gamma^{\text{MV}} \cup \Gamma_t^{\text{w}}$ and is built from the outer surface derived by [225].

5.3. Effects of atrial fibrillation on hemodynamics

In this section we present a computational model to simulate the LA hemodynamics subjected to atrial fibrillation (AF) and we perform a comparative study between the hemodynamics of patient-specifics LA in physiological (PH) conditions and under AF.

The AF pathology is one of the most common sustained cardiac arrhythmia and it is caused by an irregular atrial discharge which may result in an irregular motion of the chamber. Specifically, from a mechanical point of view, AF decreases the LA contractility yielding a reduced LA ejection fraction (LAEF):

$$\text{LAEF} = \frac{V_{\text{LA}}^{\max} - V_{\text{LA}}^{\min}}{V_{\text{LA}}^{\max}}, \tag{5.24}$$

being $V_{\text{LA}}^{\max}$ and $V_{\text{LA}}^{\min}$ the minimum and maximum LA volumes during a representative heart cycle respectively. AF is also the cause of atria remodeling due to pressure and volume overload, especially in the LA (compared to the right one). Specifically, remodeling effects are mainly manifested in the LAA, being the part of the LA that more suffers from reduced contractility. The latter produces also a smaller ejection fraction of the auricle (LAAEF) which may result in thrombus formation and blood stasis.

In this study, we consider patient-specific LA geometries acquired through Diffusion Tensor Magnetic Resonance Imaging (DTMRI) by [192] and made publicly accessible

in the supplementary material of [225]. In Figure 5.26, we display an example of a patient-specific LA fluid domain built from the endocardium geometry provided by [225]. As for the idealized case in Section 5.1, the domain Ω_t is bounded by $\Gamma_t = \left(\bigcup_{i=1}^{4} \Gamma^{\mathrm{PVein}_i}\right) \cup \Gamma^{\mathrm{MV}} \cup \Gamma_t^{\mathrm{w}}$.

5.3.1. Boundary conditions

Since we do not have pressure or flow measurements to be set at the pulmonary veins and MV sections, we rely on the flow properties computed in the 0D closed-loop model of the circulation introduced in Section 4.4 that we calibrate to match the original volumes of the LA and RA of the geometries considered. Further details on the calibration of the 0D model are given in Section 5.3.6 and can be also found in [61]. Specifically, we prescribe the pulmonary veins pressure $p_{\mathrm{VEN}}^{\mathrm{PUL}}(t)$ and pulmonary veins flowrates $Q_{\mathrm{VEN}}^{\mathrm{PUL}}(t)$ on the inlet sections of our domain and the LV pressure $p_{\mathrm{LV}}(t)$ on the outlet, corresponding to the MV section. The problem consists in solving Equation (4.17) with the following set of boundary and initial conditions:

$$
\begin{aligned}
&\boldsymbol{u} = \frac{2Q_{\mathrm{VEN}}^{\mathrm{PUL}}}{|\Gamma^{\mathrm{PVein}_i}|}\zeta_i\left(1-\frac{r^2}{R_i^2}\right)\boldsymbol{n}_i && \text{on } \Gamma^{\mathrm{PVein}_i}\times(0,T_{\mathrm{dias}}],\ i=1,\dots,4,\\
&\boldsymbol{\sigma}(\boldsymbol{u},p)\boldsymbol{n} = -p_{\mathrm{LV}}\boldsymbol{n} && \text{on } \Gamma^{\mathrm{MV}}\times(0,T_{\mathrm{HB}}),\\
&\boldsymbol{u} = \frac{2Q_{\mathrm{VEN}}^{\mathrm{PUL}}}{|\Gamma^{\mathrm{PVein}_i}|}\zeta_i\left(1-\frac{r^2}{R_i^2}\right)\boldsymbol{n}_i && \text{on } \Gamma^{\mathrm{PVein}_i}\times(T_{\mathrm{dias}},T_{\mathrm{HB}}),\ i=1,2\\
&\boldsymbol{\sigma}(\boldsymbol{u},p)\boldsymbol{n} = -p_{\mathrm{VEN}}^{\mathrm{PUL}}\boldsymbol{n} && \text{on } \Gamma^{\mathrm{PVein}_i}\times(T_{\mathrm{dias}},T_{\mathrm{HB}}),\ i=3,4\\
&\boldsymbol{u} = \boldsymbol{g}^{\mathrm{ALE}} && \text{on } \Gamma_t^{\mathrm{w}}\times(T_{\mathrm{dias}},T_{\mathrm{HB}}),\\
&\boldsymbol{u} = \boldsymbol{0} && \text{in } \Omega_0\times\{0\}.
\end{aligned}
\tag{5.25}
$$

As for the idealized case, we backflow-stabilized Neumann type BCs as reported in Equation (5.9). Furthermore, since the pulmonary veins are not characterized by the same cross-section area, in the Dirichlet BCs we have introduced ζ_i: the flow-repartition factor which expresses the amount of flow rate for each inlet section. We computed it as

$$
\zeta_i = \frac{|\Gamma^{\mathrm{PVein}_i}|}{\sum_{i=1}^{4}|\Gamma^{\mathrm{PVein}_i}|}. \tag{5.26}
$$

5.3.2. Displacement model

To define the ALE boundary velocity $\boldsymbol{g}^{\mathrm{ALE}}(\boldsymbol{x},t)$ we use the same model introduced in Section 5.1.1. However, differently from the idealized case, we define the space-dependent vectorial function $\widehat{\boldsymbol{f}}^{\mathrm{ALE}}$ as:

$$
\widehat{\boldsymbol{f}}^{\mathrm{ALE}}(\widehat{\boldsymbol{x}}) = \widehat{\boldsymbol{f}}_1^{\mathrm{ALE}}(\widehat{\boldsymbol{x}}) + \widehat{\boldsymbol{f}}_2^{\mathrm{ALE}}(\widehat{\boldsymbol{x}}) \text{ on } \widehat{\Gamma}. \tag{5.27}
$$

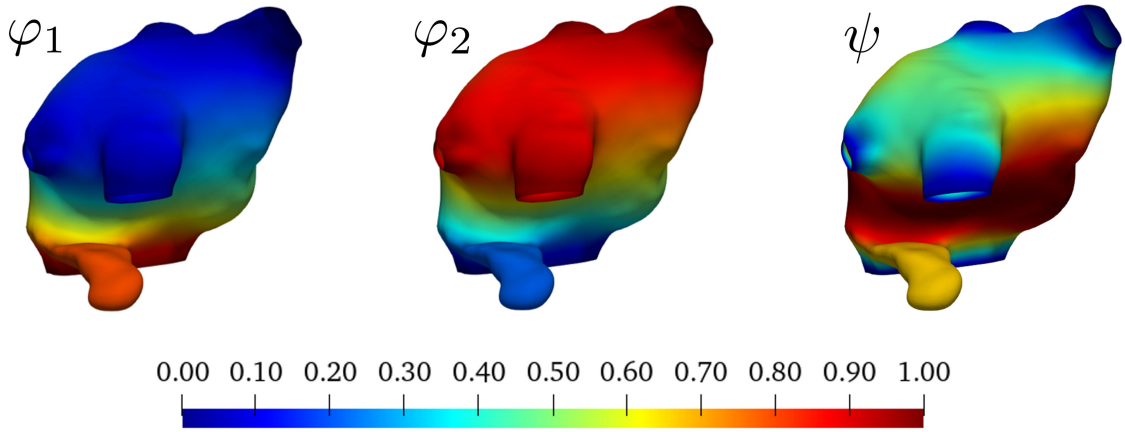

Figure 5.27: Functions φ_1, φ_2 and ψ on Γ_t^{w}. Image adapted from [61].

Since the focus of this work is the LA in AF, the motion of the LAA is a central aspect that may strongly influences the LA hemodynamics. For this reason, we have defined $\widehat{\boldsymbol{f}}^{\mathrm{ALE}}$ as in Equation (5.27) to have a better control on the contraction of the LAA from the contraction of the remaining chamber. Specifically, $\widehat{\boldsymbol{f}}_1^{\mathrm{ALE}}$ models the displacement of main chamber and $\widehat{\boldsymbol{f}}_2^{\mathrm{ALE}}$ accounts for the motion of the LAA.

Let $\boldsymbol{x}_{\mathrm{G}}$ be the LA center of mass, we define $\widehat{\boldsymbol{f}}_1^{\mathrm{ALE}}$ as

$$\widehat{\boldsymbol{f}}_1^{\mathrm{ALE}}(\widehat{\boldsymbol{x}}) = \widehat{\psi}(\widehat{\boldsymbol{x}})(\widehat{\boldsymbol{x}} - \boldsymbol{x}_{\mathrm{G}}) \text{ on } \widehat{\Gamma}, \tag{5.28}$$

being

$$\widehat{\psi}(\widehat{\boldsymbol{x}}) = \frac{\widehat{\varphi}_1(\widehat{\boldsymbol{x}})\widehat{\varphi}_2(\widehat{\boldsymbol{x}})}{\max_{\widehat{\boldsymbol{x}}\in\widehat{\Gamma}}(\widehat{\varphi}_1(\widehat{\boldsymbol{x}})\widehat{\varphi}_2(\widehat{\boldsymbol{x}}))} \text{ on } \widehat{\Gamma}, \tag{5.29}$$

and $\widehat{\varphi}_1$, $\widehat{\varphi}_2$ solutions of the following Laplace–Beltrami problems:

$$\begin{cases} -\Delta_{\widehat{\Gamma}}\widehat{\varphi}_1 = 0 & \text{on } \widehat{\Gamma}^{\mathrm{w}}, \\ \widehat{\varphi}_1 = 0 & \text{on } \bigcup_{i=1}^4 \partial\widehat{\Gamma}^{\mathrm{PVein}_i}, , \\ \widehat{\varphi}_1 = 1 & \text{on } \partial\widehat{\Gamma}^{\mathrm{MV}}, \end{cases} \quad \begin{cases} -\Delta_{\widehat{\Gamma}}\widehat{\varphi}_2 = 0 & \text{on } \widehat{\Gamma}^{\mathrm{w}}, \\ \widehat{\varphi}_2 = 1 & \text{on } \bigcup_{i=1}^4 \partial\widehat{\Gamma}^{\mathrm{PVein}_i}, \\ \widehat{\varphi}_2 = 0 & \text{on } \partial\widehat{\Gamma}^{\mathrm{MV}}. \end{cases} \tag{5.30}$$

In Figure 5.28 we display the computed scalar functions on Γ^{w}. Clearly, $\widehat{\psi} = 0$ also on $\bigcup_{i=1}^4 \widehat{\Gamma}^{\mathrm{PVein}_i}$ and $\widehat{\Gamma}^{\mathrm{MV}}$. Analogously, we define $\widehat{\boldsymbol{f}}_2^{\mathrm{ALE}}(\widehat{\boldsymbol{x}})$ as

$$\widehat{\boldsymbol{f}}_2^{\mathrm{ALE}} = k_{\mathrm{LAA}}\widehat{\psi}(\widehat{\boldsymbol{x}})\widehat{\varepsilon}_{\mathrm{LAA}}(\widehat{\boldsymbol{x}})(\widehat{\boldsymbol{x}} - \boldsymbol{x}_{\mathrm{G}}^{\mathrm{LAA}}) \text{ on } \widehat{\Gamma}, \tag{5.31}$$

being $\boldsymbol{x}_{\mathrm{G}}^{\mathrm{LAA}}$ the LAA center of mass and $\widehat{\varepsilon}_{\mathrm{LAA}}$ a function specifically designed to make $\widehat{\boldsymbol{f}}_2^{\mathrm{ALE}}$ having support on the LAA only. To define $\widehat{\varepsilon}_{\mathrm{LAA}}$, we do not use identity functions

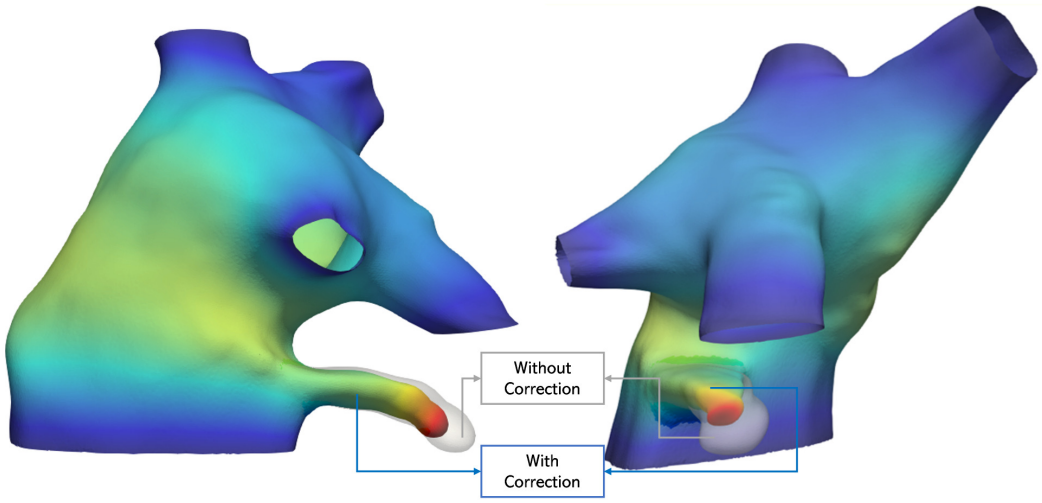

Figure 5.28: Difference between the maximum displacement with the correction $\widehat{\boldsymbol{f}}_2^{\mathrm{ALE}}$ (colored) and without it (transparent). Image from [61].

on the LAA, but we conveniently adopt a mollifier to avoid discontinuities among the LAA and the remaining chamber. Furthermore, in Equation (5.31) we have introduce a multiplicative constant k_{LAA} to penalize the LAA displacement: we tune this parameter to match clinical physiological and pathological values of the LAAEF.

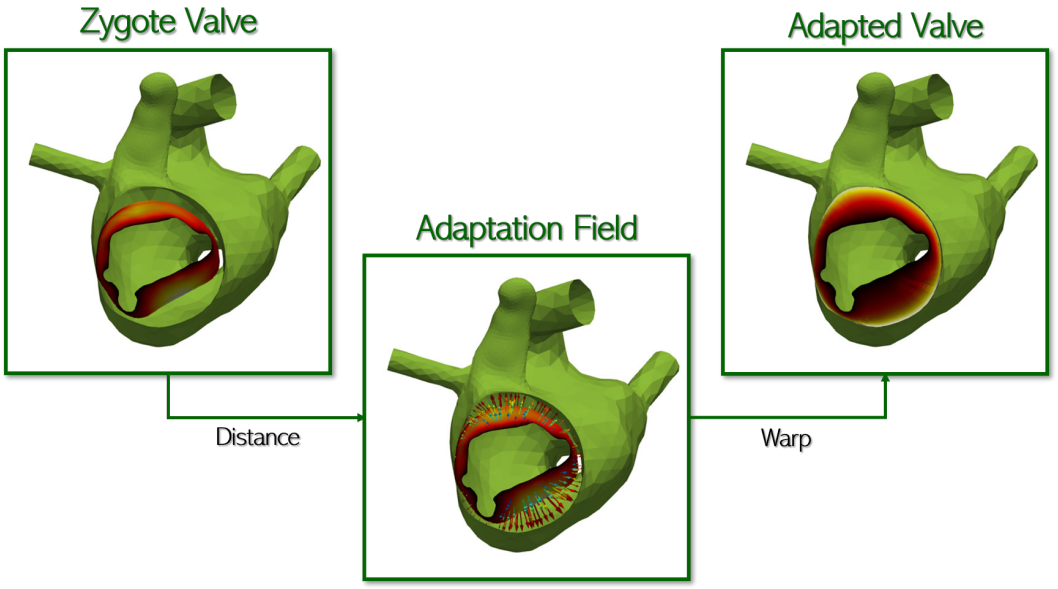

Figure 5.29: Example of Zygote MV adaptation process to the patient-specific LA geometries. Image from [61].

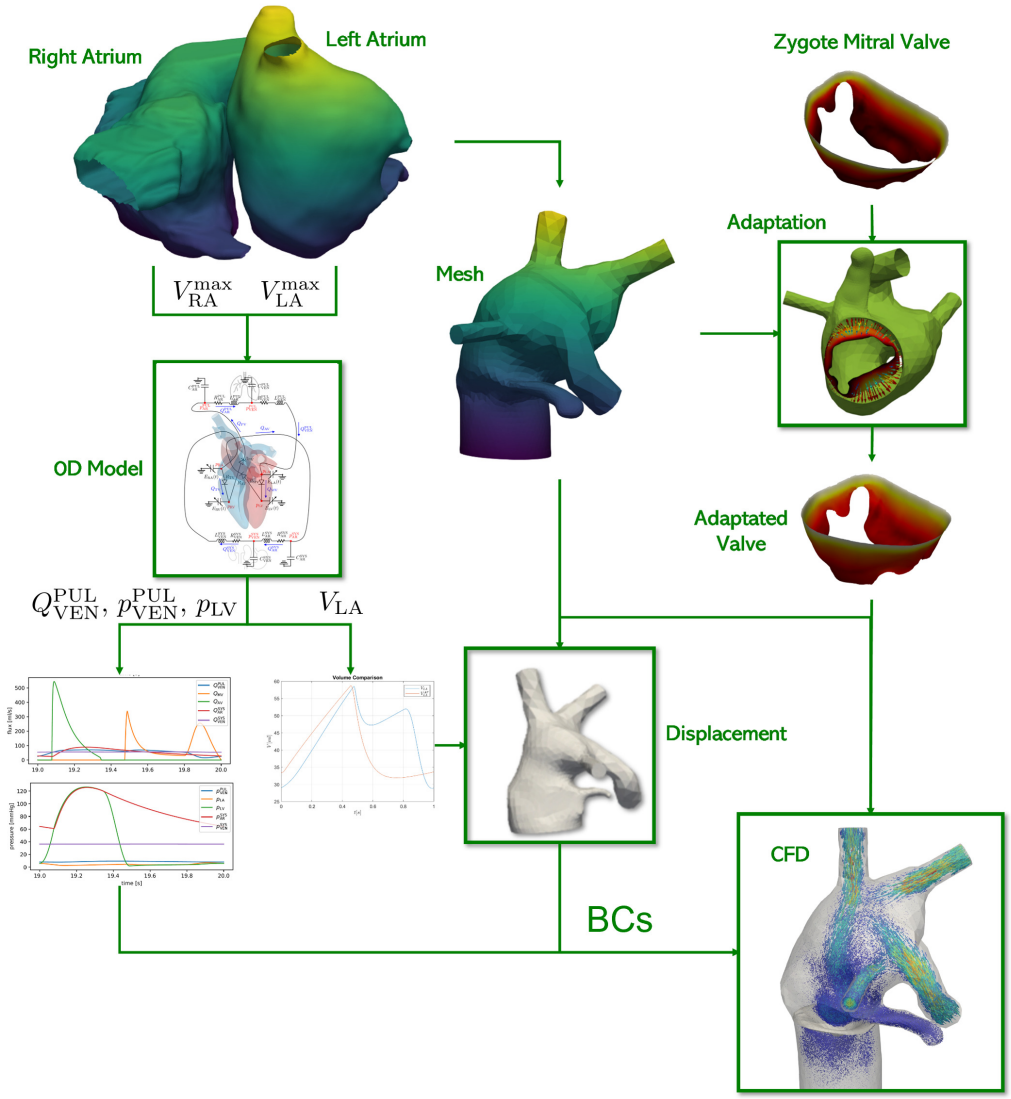

Figure 5.30: Complete schematic representation of the preprocessing procedure to simulate the patient-specific LA hemodynamics. Image from [61].

5.3.3. Valves modeling

We model the presence of the MV in the fluid domain by means of the RIIS model introduced in Section 4.2. Specifically, since the LA geometries repository [192, 225] does not provide patient-specific valves, we use the MV provided by Zygote [133], an accurate 3D model of the heart obtained with CT scan data. We will extensively use the Zygote's heart geometry in Chapters 6 and 7. Since the MV is referred to the Zygote's heart geometry, we conveniently adapt the MV geometry to our patient-specific geometry, as displayed in Figure 5.29. For details on the adaption process, we refer to [61, 100]. Following arguments of [259], the MV closes when a condition of reversed flow across the MV section is detected; the MV opens when the pressure jump across the surface becomes positive, i.e. when $p_{\mathrm{LA}}(t) > p_{\mathrm{LV}}(t)$. We prescribe characteristic times to open and close the valve: 20 ms for the opening and 60 ms for the closing stage. Additional details on the way we open and close valves are given in Chapter 6 when we deal with an hemodynamic model of the left part of the heart.

5.3.4. The complete preprocessing procedure

In Figure 5.30, we report a schematic representation of the complete preprocessing procedure required to carry out patient-specific LA CFD simulations with the parametrized displacement. We can observe the central role played by the 0D circulation model: it serves as input for the BCs – in terms of flowrates and pressures to be set at the inlet and outlet sections as reported in Equation (5.25) – and it also drives the LA motion since we use the LA volume $V_{\mathrm{LA}}(t)$ to define the ALE velocity on the boundary (see Equation (5.5)).

5.3.5. Modelling AF by means of the 0D circulation model

We mimic the effect of AF on the mechanical response of the cardiac tissues by conveniently tuning the 0D circulation model. The elastances of the cardiac chambers vary in the range

$$E_j(t) \in \left[E_j^{\mathrm{pass}}, E_j^{\mathrm{pass}} + E_j^{\mathrm{act,max}}\right], \text{ with } j = \mathrm{RA}, \mathrm{LA}, \mathrm{RV}, \mathrm{LV} \tag{5.32}$$

being E_j^{pass} and $E_j^{\mathrm{act,\,max}}$ the passive and maximum active elastances of the chamber respectively. We enforce the absence of the *atrial kick* – corresponding to the A-wave – by setting the active elastances of the atria equal to zero [230]:

$$E_{\mathrm{LA}}^{\mathrm{act,max}} = E_{\mathrm{RA}}^{\mathrm{act,max}} = 0, \tag{5.33}$$

thus, the time-varying elastances of the atria become constant and equal to

$$E_{\mathrm{LA}}(t) = E_{\mathrm{LA}}^{\mathrm{pass}}, \quad E_{\mathrm{RA}}(t) = E_{\mathrm{RA}}^{\mathrm{pass}}, \quad \text{for all } t \in (0, T_f). \tag{5.34}$$

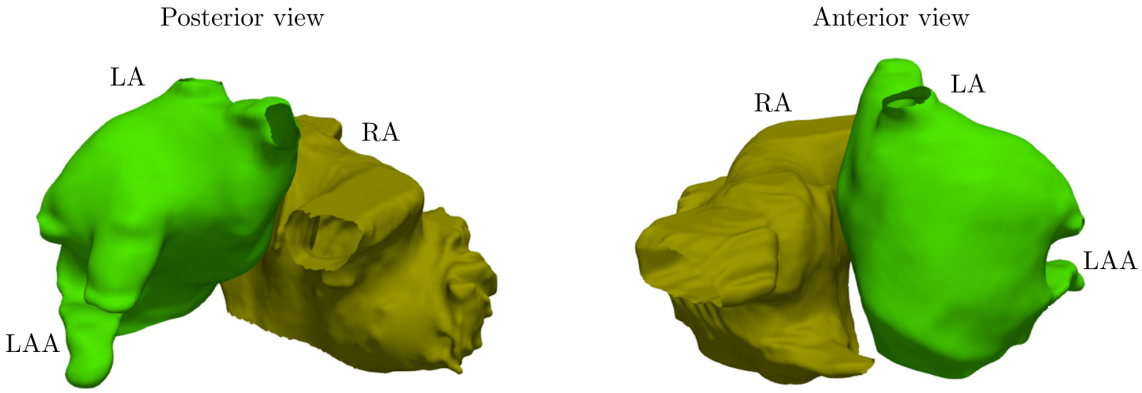

Figure 5.31: Patient-specific LA and RA geometries provided by [225]. Figure adapted from [61].

Moreover, as a consequence of the AF, we also reduce the contractility of the ventricles by decreasing the active elastances ($E_{\mathrm{LV}}^{\mathrm{act,max}}$ and $E_{\mathrm{RV}}^{\mathrm{act,max}}$). However, for the patients whose atria are not affected from the remodelling, we found that the corrections above do not bring to clinically meaningful results. As a matter of fact, the calibration of the circulation model is always constrained by the maximum volumes of the atria (see Figure 5.30) and, to recover the correct volumes, we increase the passive elastances of the heart chambers ($E_{\mathrm{LV}}^{\mathrm{pass}}$, $E_{\mathrm{RV}}^{\mathrm{pass}}$, $E_{\mathrm{LA}}^{\mathrm{pass}}$, and $E_{\mathrm{RA}}^{\mathrm{pass}}$). This choice is also fundamental to control $p_{\mathrm{VEN}}^{\mathrm{PUL}}$ which otherwise would assume very large values. We highlight that a consequence of the AF indeed is the increasing of $p_{\mathrm{VEN}}^{\mathrm{PUL}}$ [72, 186, 285], but the correction in terms of passive elastances is still needed to avoid too large and unphysical values.

5.3.6. Hemodynamics in physiologic and paroxysmal AF

In the following, we compare the LA hemodynamics in PH and AF conditions. For the pathological simulation, we are assuming *paroxysmal* AF, i.e. we consider an initial state of the AF which did not yet cause remodelling. Thus, for both scenarios, we carry out our numerical simulations on the same LA geometry corresponding to a 55 years old male with no known heart diseases. Considering the same LA domain allows to to perform a comparison not influenced by geometric details, which may strongly affect the hemodynamic results.

In Figure 5.31 we display the patient-specific LA and RA geometries provided by [225]. We calibrate the lumped parameter model to match the end systolic volumes provided by medical images [192, 225]: $V_{\mathrm{LA}}^{\mathrm{max}} = 58.06$ ml and $V_{\mathrm{RA}}^{\mathrm{max}} = 69.39$ ml. In Table 5.5a we summarize the resistance, inductance and capacitance of different compartments of the circulation model; in Table 5.5b the elastance values that we use to differentiate the PH and AF conditions, as explained in Section 5.3.5. Specifically, following for

Parameter	Value	
$R_{\text{AR}}^{\text{SYS}}$	1.00	$\text{mmHg} \cdot \text{s/mL}$
$C_{\text{AR}}^{\text{SYS}}$	2.00	mL/mmHg
$L_{\text{AR}}^{\text{SYS}}$	1.00	$\text{mmHg} \cdot \text{s}^2\text{/mL}$
$R_{\text{VEN}}^{\text{SYS}}$	0.50	$\text{mmHg} \cdot \text{s/mL}$
$C_{\text{VEN}}^{\text{SYS}}$	140.00	mL/mmHg
$L_{\text{VEN}}^{\text{SYS}}$	5×10^{-4}	$\text{mmHg} \cdot \text{s}^2\text{/mL}$
$R_{\text{AR}}^{\text{PUL}}$	0.04	$\text{mmHg} \cdot \text{s/mL}$
$C_{\text{AR}}^{\text{PUL}}$	15.00	mL/mmHg
$L_{\text{AR}}^{\text{PUL}}$	5×10^{-4}	$\text{mmHg} \cdot \text{s}^2\text{/mL}$
$R_{\text{VEN}}^{\text{PUL}}$	0.60	$\text{mmHg} \cdot \text{s/mL}$
$C_{\text{VEN}}^{\text{PUL}}$	10.00	mL/mmHg
$L_{\text{VEN}}^{\text{PUL}}$	1×10^{-4}	$\text{mmHg} \cdot \text{s}^2\text{/mL}$

(a) Parameter values common to PH and AF.

	Value [mmHg/mL]	
Parameter	PH	AF
$E_{\text{RA}}^{\text{act,max}}$	0.04	0.00
$E_{\text{RA}}^{\text{pass}}$	0.06	0.60
$E_{\text{RV}}^{\text{act,max}}$	1.20	1.20
$E_{\text{RV}}^{\text{pass}}$	0.05	0.80
$E_{\text{LA}}^{\text{act,max}}$	0.20	0.00
$E_{\text{LA}}^{\text{pass}}$	0.09	0.30
$E_{\text{LV}}^{\text{act,max}}$	6.00	4.00
$E_{\text{LV}}^{\text{pass}}$	0.08	0.20

(b) Elastances values (different from PH and AF)

Table 5.5: Values employed in the 0D model to simulate PH and AF cases. Table from [61].

instance arguments of [230], since we are simulating paroxysmal AF, we do not change the active elastance of the RV. On the contrary, this changing is fundamental in the case of persistent AF.

In Figure 5.32a we compare the LA volume in the PH and AF cases after calibration of the 0D model as explained. In the AF case, we con observe the absence of the atrial kick and a reduced LAEF (see Equation (5.24)):

$$\text{LAEF}^{\text{PH}} = 50.5\%, \quad \text{LAEF}^{\text{AF}} = 30.7\%. \tag{5.35}$$

The values obtained are coherent with medical estimates and measures for both PH [22, 196] and the AF case [141]. Moreover, by computing the displacement as explained, and by setting $k_{\text{LAA}} = 2$ and $k_{\text{LAA}} = 4/3$ in Equation (5.31) for the PH and AF cases respectively, we get the following values of left auricle ejection fraction:

$$\text{LAAEF}^{\text{PH}} = 77.8\%, \quad \text{LAAEF}^{\text{AF}} = 62.7\%, \tag{5.36}$$

which are coherent with clinical data [102].

In Figure 5.32b we show the inlet flow rate $Q_{\text{VEN}}^{\text{PUL}}$: a reduced variation of the flowrate is observed in the pathological case also as a consequence of a reduced LAEF. In Figures 5.32c and 5.32d we report pressures $p_{\text{VEN}}^{\text{PUL}}$ and p_{LV} respectively that we prescribe on the inlet and outlet sections of the LA domain. They result from the calibrated 0D model in the PH and AF conditions. We can observe a lower LV pressure during the

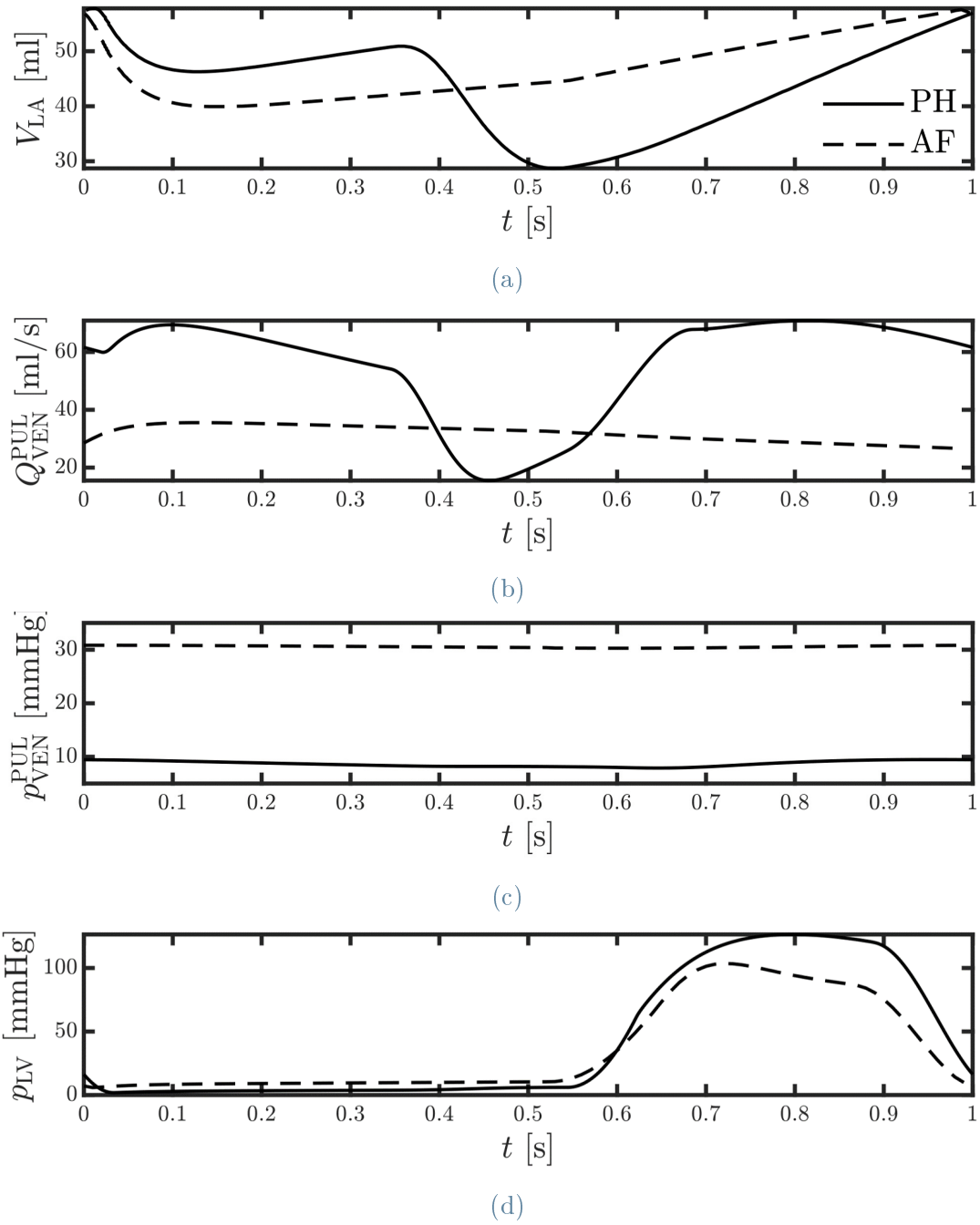

Figure 5.32: Comparison between PH and AF cases: (a) $V_{\mathrm{LA}}(t)$; (b) $Q^{\mathrm{PUL}}_{\mathrm{VEN}}(t)$; (c) $p^{\mathrm{PUL}}_{\mathrm{VEN}}(t)$; (d) $p_{\mathrm{LV}}(t)$.

LV ejection phase (systole) and a larger pulmonary venous pressures. Both results are known to be realistic pathological effects of AF [18, 72, 186].

Given the outer surface of the LA displayed in Figures 5.26 and 5.31, we use flow

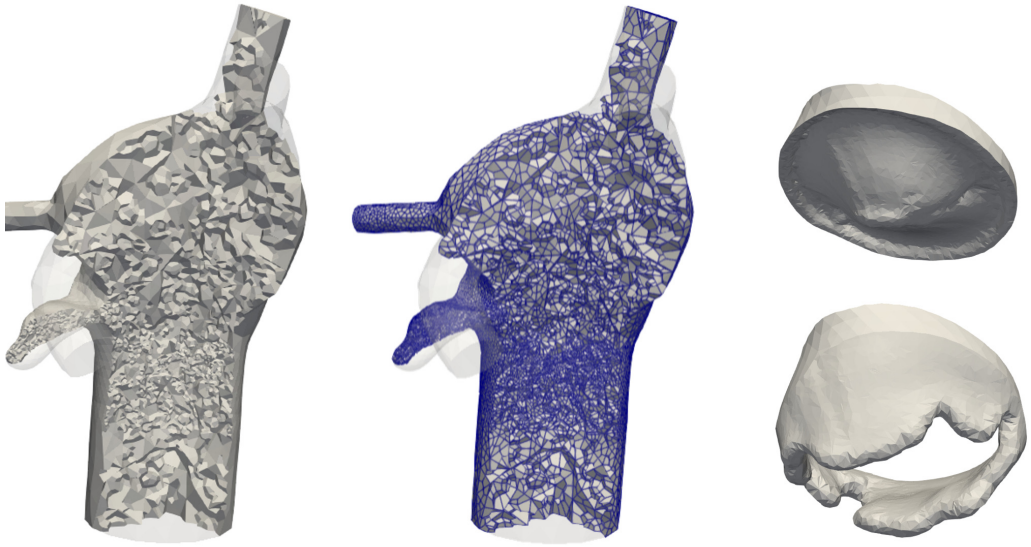

Figure 5.33: LA mesh used for the CFD simulations and representation of the immersed MV in open and closed configurations. Image from [61].

R_{MV}	ε_{MV}	h			cells	DOFs ($\mathbb{Q}_1 - \mathbb{Q}_1$)			Δt
[kg/(m^2·s)]	[10^{-3} m]	[10^{-3} m]			[10^3]	[10^3]			[s]
		min	avg	max		$\boldsymbol{u}$	p	total	
10^4	1.3	0.43	1.76	5.95	120.86	412	137	549	$2 \cdot 10^{-4}$

Table 5.6: Parameters for the setup of the numerical simulations.

extension in inlet and outlets 1) to avoid instability issues where Neumann BCs are set [268]; 2) to conveniently immerse the MV in the fluid domain, considering the absence of the LV in our computational domain. For the mesh, we use a varying mesh size h. Specifically, we refine the mesh in the LAA and in the pulmonary veins to correctly catch the geometrical details of the geometry; furthermore, we also use a smaller mesh size in correspondence of the MV to correctly represent the MV by means of the RIIS model. In Figure 5.33 we display the final LA mesh and we also represent the MV in its open and closed configurations. In Table 5.6 we summarize the parameters adopted for the setup of our numerical simulations. The value of ε_{MV} allows to have a physiologic representation of the MV leaflets and, with our choice of R_{MV} we avoid flow penetration across the immersed surfaces [86].

As for the idealized case, for both the PH and AF cases, we simulate 6 heartbeats, we discard the first two in order to remove the influence of a null initial condition and we phase-averaged the flow properties on the remaining 4 beats (see Equation (5.11)). We carry out numerical simulations in life$^{\text{x}}$ [6] and we use the VMS-LES method with semi–implicit treatment of non–linearities. As time advancing scheme, we use BDF1

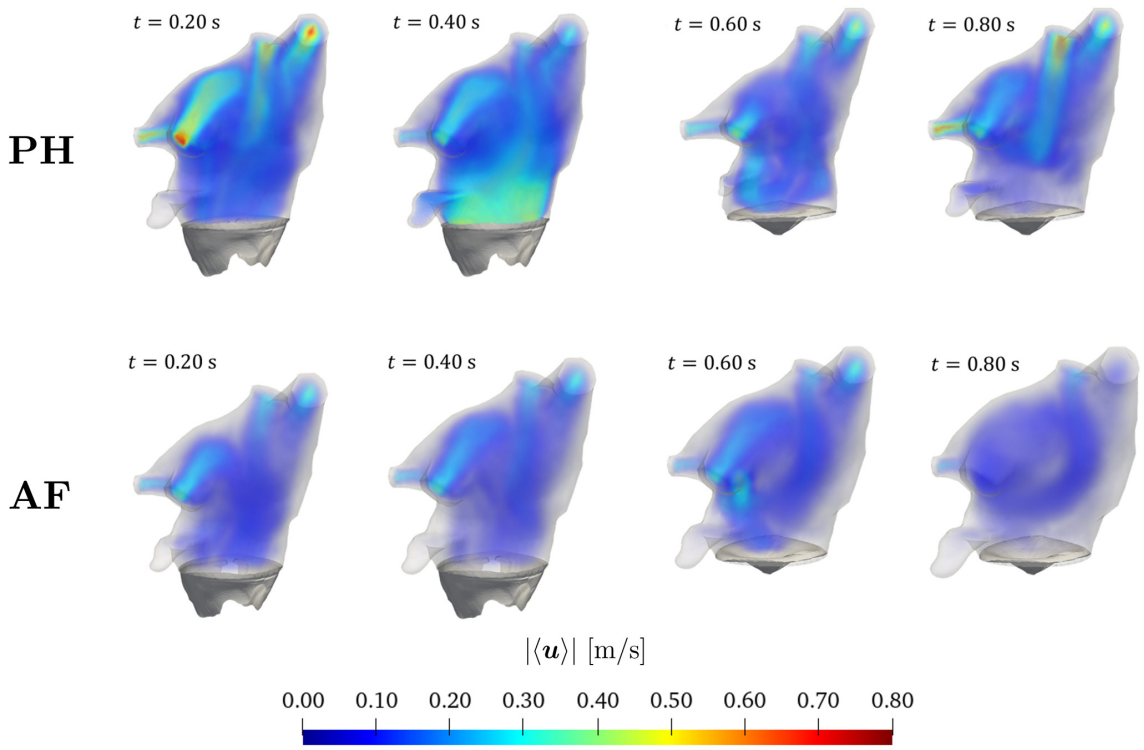

Figure 5.34: Volume rendering of phase-averaged velocity magnitude at different time instants. Comparison between PH (top) and AF (bottom) cases. Figure adapted from [61].

with $\Delta t = 2 \cdot 10^{-4}$ s.

In Figure 5.34 we show the volume rendering of phase-averaged velocity magnitude at different time instants during the heart cycle and we compare the PH and the AF cases. In both cases, the maximum velocities are obtained in the pulmonary veins, with a peak of 0.8 m/s in the PH case and about 0.4 m/s in AF ($t = 0.20$ s). Furthermore, the presence of the active contraction (atrial kick) in the PH cases produces a stronger jet in the MV section than the AF one ($t = 0.40$ s). Another relevant differences among the normal and pathological cases are the motion and the blood exchange of the LAA: in the AF case, very low velocities are measured throughout the heartbeat, whereas during the atrial kick of the PH case we can observe blood ejecting from the LAA and flowing towards the main chamber. We better visualize the ejection from the LAA to the LA in Figure 5.35 where we report the phase-averaged velocity magnitude on a section of the LA and the corresponding glyphs directed and scaled as $\langle \boldsymbol{u} \rangle$.

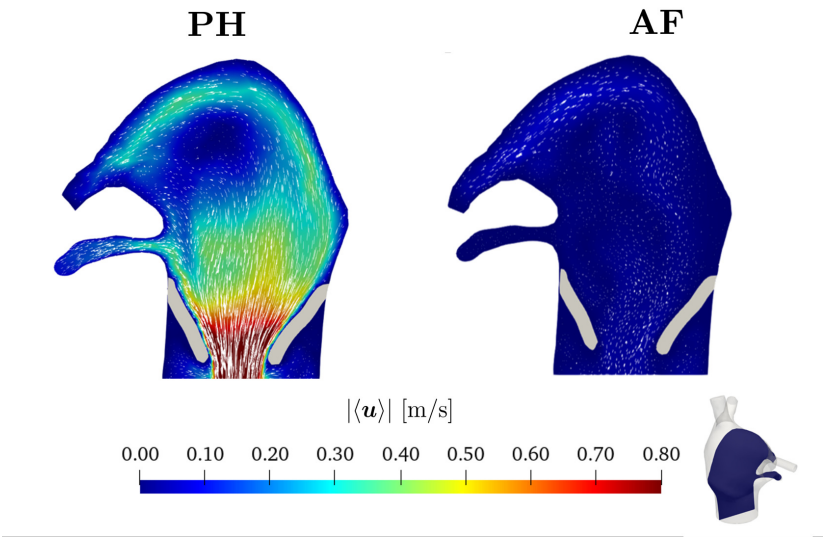

Figure 5.35: Phase-averaged velocity magnitude on a slice through the LA at $t = 0.40$ s (corresponding to the atrial kick in the PH case) with corresponding glyphs directed and scaled as $\langle \boldsymbol{u} \rangle$: comparison between PH and AF cases. Figure adapted from [61].

To quantify the blood stasis, we introduce the *flow stasis* indicator as

$$f_s(\widehat{\boldsymbol{x}}) = \frac{1}{T_{\text{HB}}} \int_0^{T_{\text{HB}}} \chi_{\{|\langle \boldsymbol{u} \rangle| < \bar{u}\}}(\widehat{\boldsymbol{x}}, t) \mathrm{d}t, \quad \text{for all } \widehat{\boldsymbol{x}} \in \widehat{\Omega}. \tag{5.37}$$

f_s represents the fraction of time of the heartbeat in which the magnitude of the phase-averaged velocity is smaller than a certain threshold values. Specifically, following [165], we choose $\bar{u} = 0.1$ m/s. In Figure 5.36 we display the volume rendering of the flow stasis in the PH and AF cases. Higher values of f_s are achieved in the AF case, coherently with the lower velocities previously observed and with the findings of [164, 165, 240] whereas studies based on 4D flow MRI acquisitions are performed. Moreover, to better investigate the reliability of our findings, we compute FS, the mean values of f_s, as

$$\text{FS} = \frac{1}{|\widehat{\Omega}|} \int_{\widehat{\Omega}} f_s(\widehat{\boldsymbol{x}}) \mathrm{d}\widehat{\boldsymbol{x}}, \tag{5.38}$$

and we get $\text{FS}^{\text{PH}} = 0.3326$, $\text{FS}^{\text{AF}} = 0.7815$, consistent with the findings of [165].

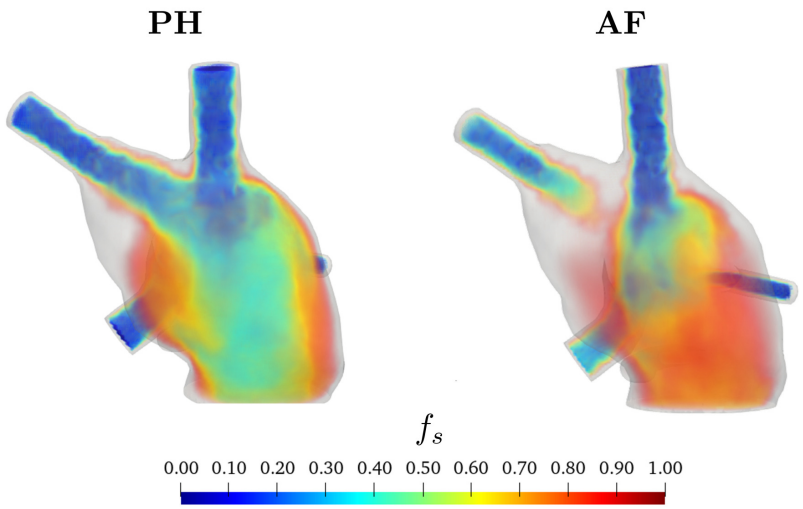

Figure 5.36: Volume rendering of flow stasis: comparison between PH (left) and AF (right) cases. Figure adapted from [61].

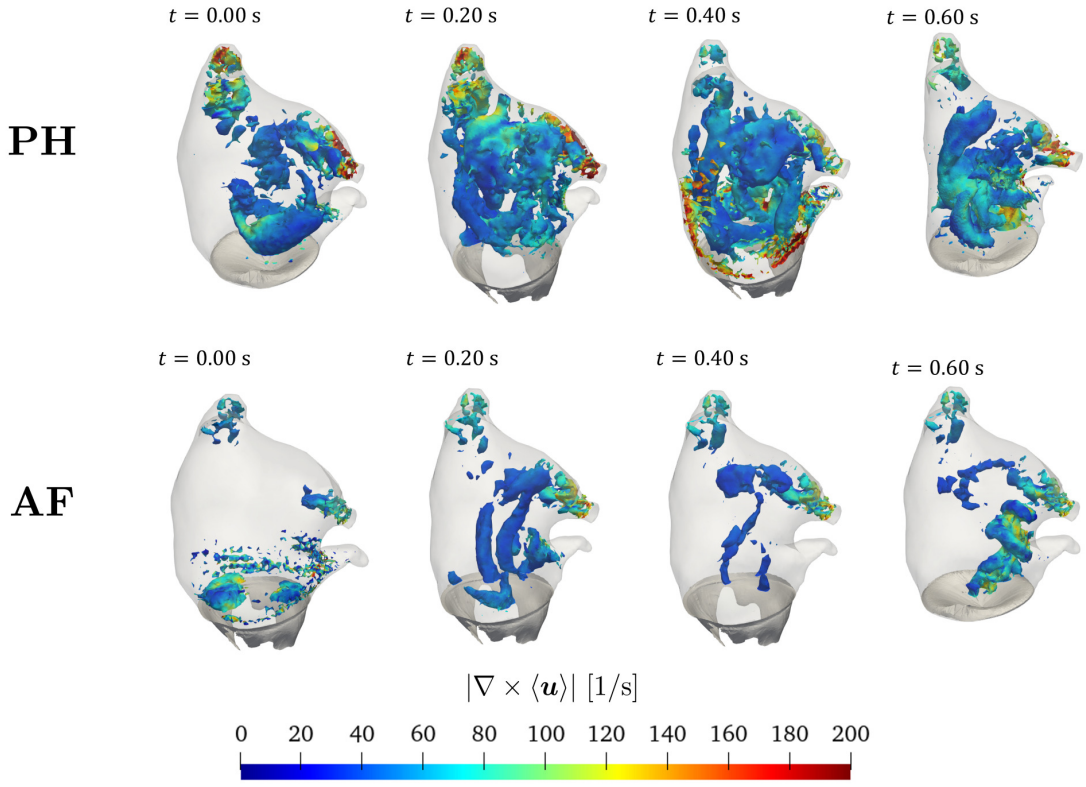

Figure 5.37: Isosurfaces of Q-criterion $\mathrm{Q} = 250\,\mathrm{Hz}^2$ coloured with phase-averaged vorticity magnitude at different time instants. Comparison between PH (top) and AF (bottom) cases. Figure adapted from [61].

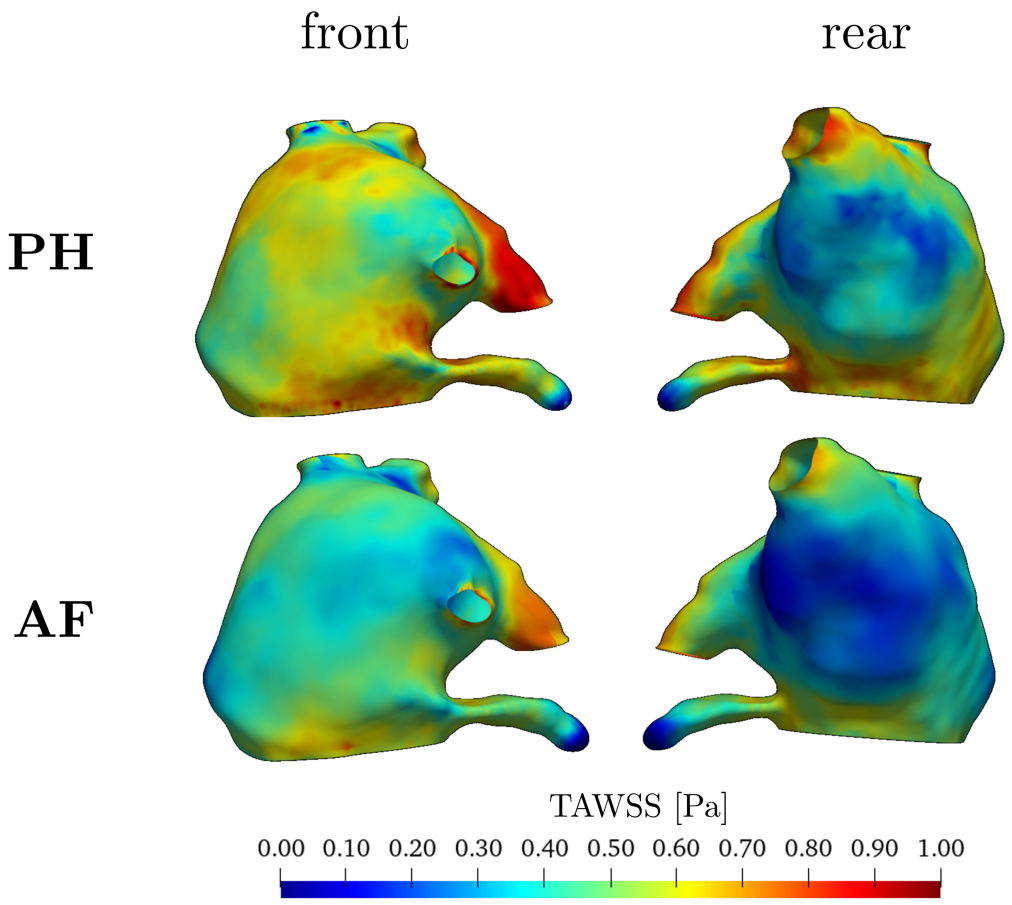

Figure 5.38: TAWSS on $\widehat{\Omega}$ in different perspectives: comparison between PH (top) and AF (bottom) cases. Figure adapted from [61].

In Figure 5.37 we compare the isosurfaces of Q-criterion between the PH and AF cases. In the PH case, as described in Section 5.1.4 for the case of a healthy idealized LA, the main feature is the formation of vortices coming from the pulmonary veins and their interaction in the middle of the LA, which produces a dissipation of kinetic energy. Differently from the PH case, with AF we can observe less eddies with the associated value of Q and the overall fluid motion is less chaotic than the normal case. The eddies formed are characterized by a lower vorticity magnitude than the one of PH case. Furthermore, in the LAA we cannot detect any vortex structure: neither in PH, nor in AF. This might be related to the thin geometrical morphology of this patient and the lower velocities that typically characterize the auricle.

In Figure 5.38 we display the TAWSS defined in Equation (5.14) in PH and AF conditions. The TAWSS is higher in normal conditions than in the pathological cases, coherently with the findings of [227, 276]. Moreover, in both scenarios, we can observe

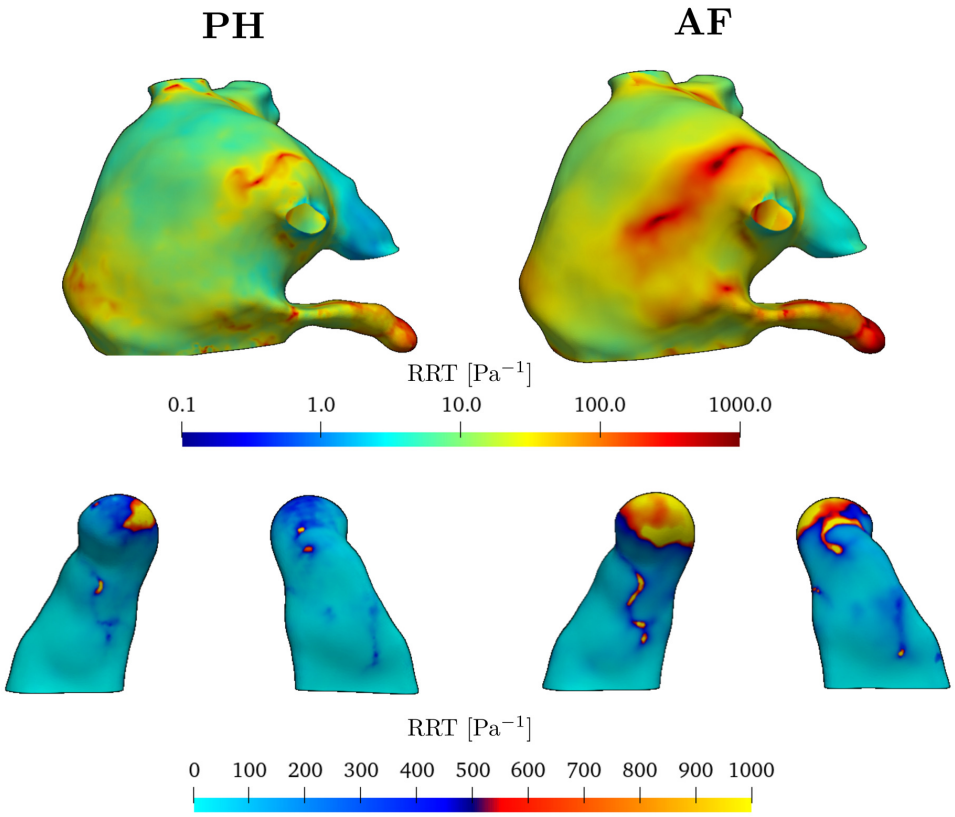

Figure 5.39: RRT on $\widehat{\Omega}$: comparison between PH (left) and AF (right) cases. On the bottom we report the RRT in the LAA in two different perspectives for both PH and AF cases. Figure adapted from [61].

higher values of the stress on the top of the LA in correspondence of the vein Γ^{PVein_3} (see Figure 5.26 for the veins numbering). This might be related to blood jet through Γ^{PVein_3} that impinges the LA upper wall increasing hence the TAWSS values. On the contrary, smallest TAWSS values are obtained in the rear part of the LA.

In Figure 5.39 we report the RRT defined in Equation (5.16) in PH and AF conditions. In both cases, higher values of RRT are reached in the LAA and on some spots on the upper part of the LA. However, comparing the two scenarios, we can observe that AF causes an increase of RRT due to slower velocities and recirculation effects. Thus, blood stagnation becomes more prominent in the pathological case especially in the LAA, as shown in the bottom part of Figure 5.39. We recall that RRT is directly related to the estimation of thrombogenic risks, and hence the quantification of this indicator is of primary importance especially in presence of AF.

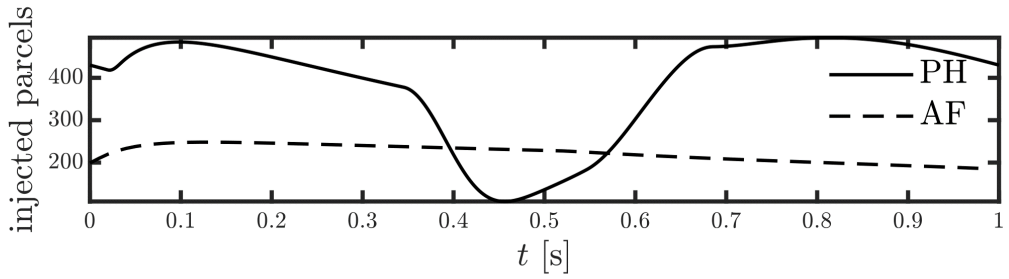

Figure 5.40: Number of parcels injected in a single heartbeat in PH and AF cases.

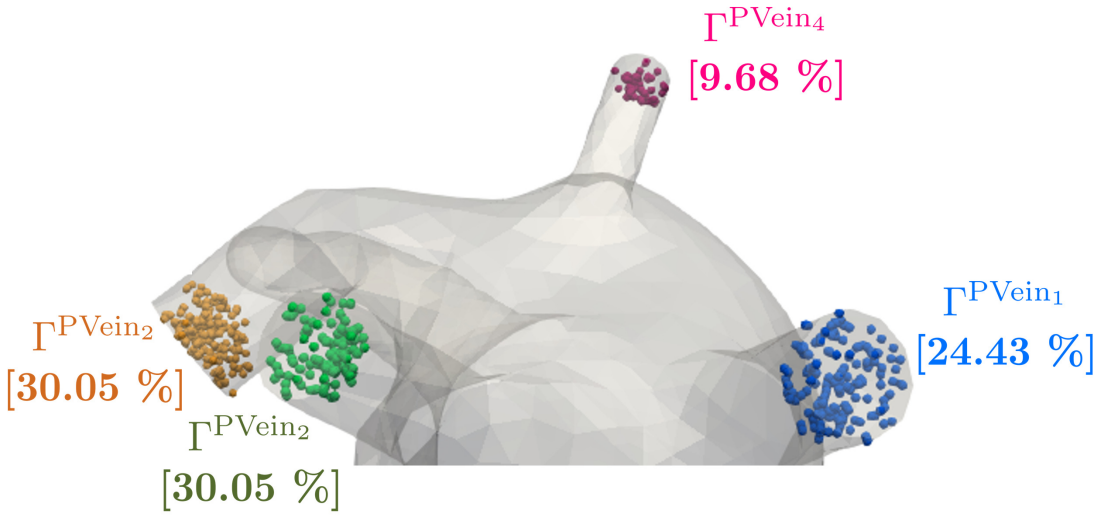

Figure 5.41: Position of the injected parcels in the inlet sections. Figure adapted from [61].

5.3.7. Particles counting: comparison between PH and AF

In the following, we perform a Lagrangian analysis by comparing the particles motion in the LA in PH and AF conditions. We follow the same strategy presented in Section 5.1.5 and the theoretical background developed in [61]. In a heartbeat, we inject a volume of blood estimated as

$$V_{\text{inj}} = \int_0^{T_{\text{HB}}} Q_{\text{VEN}}^{\text{PUL}}(t)\mathrm{d}t, \tag{5.39}$$

bringing to $V_{\text{inj}}^{\text{PH}} = 55.58$ ml and $V_{\text{inj}}^{\text{AF}} = 31.82$ ml for the PH and AF cases respectively. Considering that there areabout 5 millions of red blood cells per blood milliliter [66], we can estimate the number of particles entering in a single heartbeat as $N_{\text{particles}}^{\text{PH}} = 277'881'911$ and $N_{\text{particles}}^{\text{AF}} = 159'108'500$ for the PH and AF cases respectively. Considering the huge number of particles, to reduce the computational burden

of the simulation, we use the *Discrete Parcel Method* (DPM) [63] in which, instead of simulating all the particles, we consider group of particles called *parcels*. Specifically, we consider each parcel made of 1409 particles. Thus, the number of parcels N_p that we inject in a single heartbeat is

$$N_p^{\mathrm{PH}} = 197'064, \quad N_p^{\mathrm{AF}} = 112'950. \tag{5.40}$$

In Figure 5.40 we display the number of parcels injected in a single heartbeat. As expected, they are proportional to the inlet flow rate $Q_{\mathrm{VEN}}^{\mathrm{PUL}}(t)$ reported in Figure 5.32b. Specifically, we inject parcels in the LA every 0.001 s and we distribute them in an hemisphere centered in the center of the the cross-sections of the pulmonary veins, as displayed in Figure 5.41. Due to different measures of the cross–sections, we split the parcels proportionally to the flow repartition factor ζ_i introduced in Equation (5.26). The percentage of parcels injected in each vein is reported in Figure 5.41.

As for the idealized case in Section 5.1.5, we inject parcels during the first heartbeat, and we count the number of parcels left at the end of each heartbeat: this allows to estimate wash–out effects and hence the consequences of the pathology on atrial blood exchange.

In Figures 5.42 and 5.43 we display parcels in the LA in PH and AF conditions respectively. In both the cases, we can observe blood particles coming from the pulmonary veins and mixing in the middle of the chamber. Interestingly, in the PH case, particles start to leave the main chamber through the MV between $t = 0.20$ s and $t = 0.30$ s and, at the end of the first heartbeat, in the LA there are the 88.53% of the total injected particles. On the contrary, in the AF case, due to a reduced contraction of the LA, almost all the particles (99.41%) remain inside the chamber for all the duration of diastole, and only a very small portion manages to leave the chamber at the very end of diastole.

In Tables 5.7 and 5.8 we report the parcels remaining in the LA at the end of each cardiac cycle in PH and AF conditions respectively. Specifically, we report the percentages by distinguishing the contribution of each pulmonary vein. As previously discussed, during the first heartbeat, in the PH case the 11.47% of particles is able to leave the atrium; on the contrary, in the AF case, the 0.59% only. Furthermore, at the end of the last heartbeat simulated, in the LA remain the 2.92% and 6.85% of particles in the LA in the PH and AF cases with a slower decay of particles in AF conditions. Thus, wash–out properties are dramatically reduced even in the case of paroxysmal AF. Regarding how particles split in different veins, we observe that, due to the particular morphology of the vein labelled as $\Gamma^{\mathrm{PVein}_1}$, particles coming from this vein are characterized by a faster exit from the atrium comparing to particles coming from the remaining veins. This behavior is met in both PH and AF conditions; however, in the normal case, after many heartbeats this difference is mitigated, probably due to better contraction properties of the chamber.

Total parcels (PH)	197 064 (100.00%)	62 385 (100.00%)	47 069 (100.00%)	68 587 (100.00%)	19 023 (100.00%)
Time	**Parcels**	Γ^{PVein_1}	Γ^{PVein_2}	Γ^{PVein_3}	Γ^{PVein_4}
$t = 1.00\,\text{s}$	174 470 (88.53%)	49 477 (79.31%)	42 838 (91.01%)	64 479 (94.01%)	17 676 (92.91%)
$t = 2.00\,\text{s}$	70 097 (35.57%)	11 094 (17.78%)	18 698 (39.72%)	32 681 (47.64%)	7 624 (40.08%)
$t = 3.00\,\text{s}$	35 231 (17.87%)	5 633 (9.03%)	9 456 (20.09%)	16 094 (23.46%)	4 048 (21.28%)
$t = 4.00\,\text{s}$	19 458 (9.87%)	3 269 (5.24%)	4 868 (6.94%)	9 155 (13.34%)	2 166 (11.39%)
$t = 5.00\,\text{s}$	9 650 (4.89%)	1 658 (2.65%)	2 409 (5.11%)	4 492 (6.55%)	1 091 (5.73%)
$t = 6.00\,\text{s}$	5 761 (2.92%)	1 087 (1.74%)	1 368 (2.91%)	2 672 (3.89%)	634 (3.33%)

Table 5.7: Parcels remaining in the LA at the end of each cardiac cycle and relative percentage in PH conditions. Table from [61]

Total parcels (AF)	112 950 (100.00%)	35 759 (100.00%)	26 707 (100.00%)	39 536 (100.00%)	10 948 (100.00%)
Time	**Parcels**	Γ^{PVein_1}	Γ^{PVein_2}	Γ^{PVein_3}	Γ^{PVein_4}
$t = 1.00\,\text{s}$	112 282 (99.41%)	35 096 (98.15%)	26 705 (99.99%)	39 534 (99.99%)	10 947 (99.99%)
$t = 2.00\,\text{s}$	80 787 (71.52%)	20 298 (56.76%)	20 515 (76.82%)	31 039 (78.51%)	8 935 (81.61%)
$t = 3.00\,\text{s}$	40 071 (35.48%)	8 102 (22.66%)	11 624 (43.52%)	15 147 (38.31%)	5 198 (47.48%)
$t = 4.00\,\text{s}$	22 749 (20.14%)	4 031 (11.27%)	7 186 (26.91%)	8 588 (21.72%)	2 944 (26.89%)
$t = 5.00\,\text{s}$	13 055 (11.56%)	2 203 (6.16%)	4 915 (16.24%)	4 338 (12.43%)	1 599 (14.61%)
$t = 6.00\,\text{s}$	7 742 (6.85%)	1 333 (3.73%)	2 515 (9.42%)	2 960 (7.49%)	934 (8.53%)

Table 5.8: Particles remaining in the LA at the end of each cardiac cycle and relative percentage in AF conditions. Table from [61].

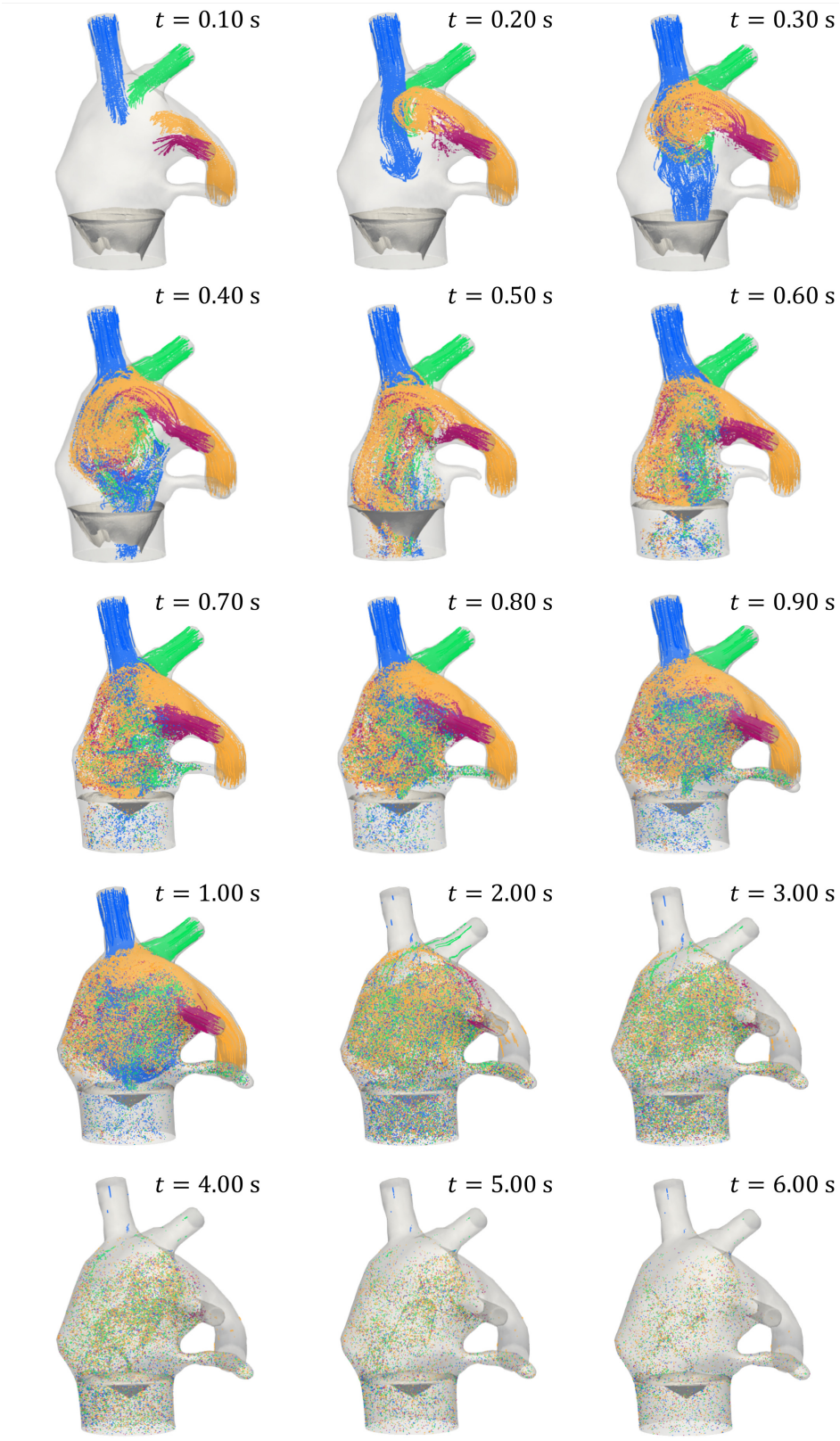

Figure 5.42: Parcels in the LA in PH condition during six heartbeats injecting parcels for the first heartbeat only (from $t = 0$ s to $t = 1$ s) in a number proportional to the inlet flowrate. Image from [61].

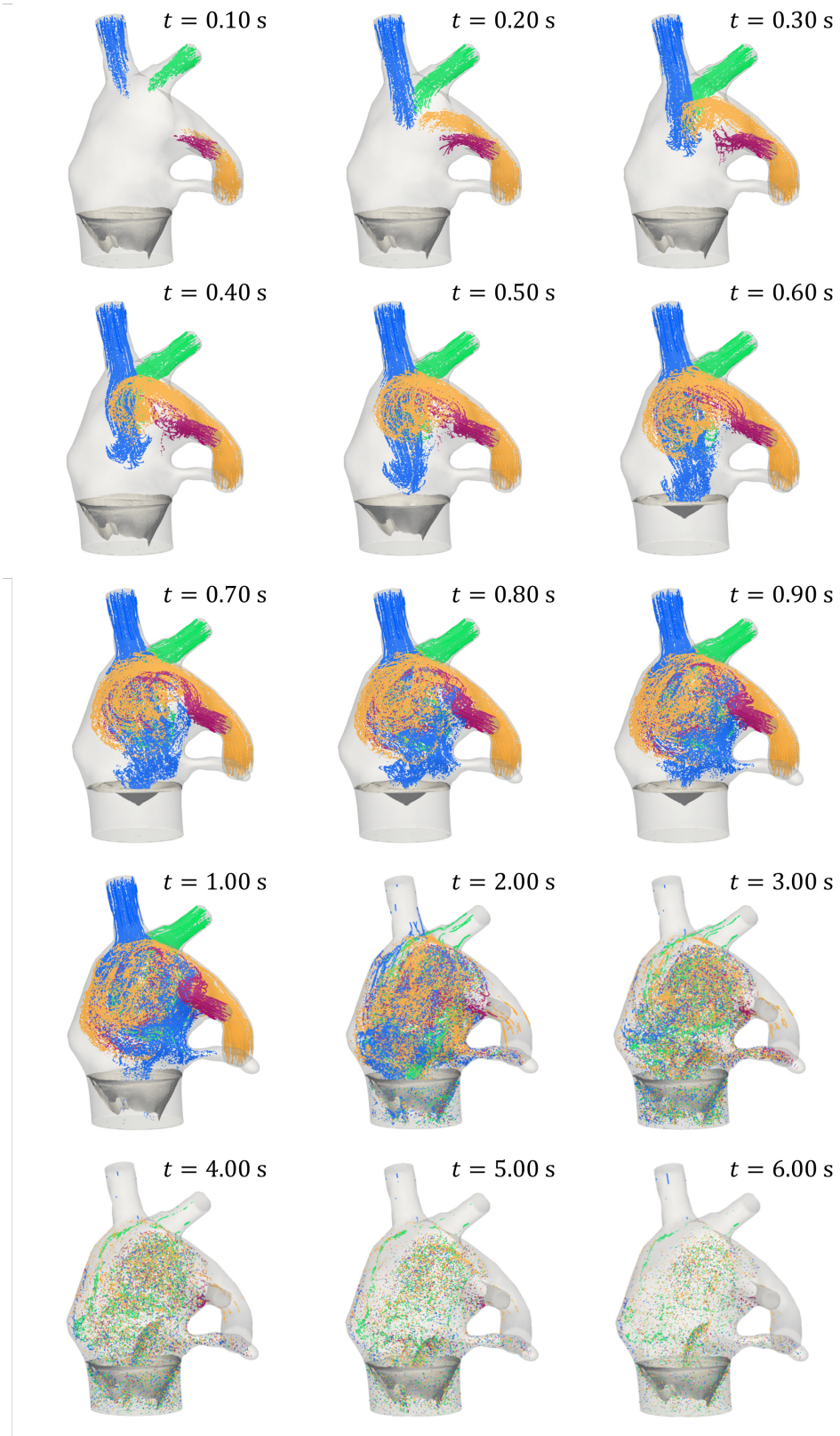

Figure 5.43: Parcels in the LA in AF condition during six heartbeats injecting parcels for the first heartbeat only (from $t = 0$ s to $t = 1$ s) in a number proportional to the inlet flowrate. Image from [61].

5.4. Concluding remarks

In this chapter, we introduced computational model of the LA; we carried out numerical simulations on an idealized geometry in healthy conditions and in patient specific geometries by considering either the PH and the AF case. We assessed the atrial hemodynamics in terms of flow patterns, kinetic energy and several clinical indicators, and we studied the effects of AF on LA hemodynamics. The pathology has been mimicked by conveniently tuning the 0D circulation model. We found that the reduced atrial contractility causes a slowing of the blood flow, vorticity reduction and an increasing blood stasis, especially in the auricle, where a dramatic washout reduction is measured.

Moreover, we used the simulation of the LA on the idealized geometry to investigate the role played by the VMS-LES method on transitional cardiac flows. Specifically, we simulated the LA hemodynamics on a fine mesh which served as our reference solution and we compared the VMS-LES and SUPG solutions on two coarser grid levels. We found that if sufficiently fine meshes are employed, the effects of the additional stabilization terms introduced by the VMS-LES are negligible, since both the SUPG and VMS-LES gave comparable and accurate results. However, if coarser meshes are used, the VMS-LES better predicts cycle-to-cyle blood flow variations and transition to turbulence indicators.

Once we have assessed the role of the VMS-LES method and designed a realistic computational model for the LA, we consider in Chapter 6 a computational model of the LH.

6 | Multiscale CFD modeling of the left heart

In this chapter, we present a novel multiscale computational model for the numerical simulation of the blood flow in the human LH. We employ a 3D cardiac EM model of the LV coupled to 0D circulation model [224] to impose a physiological displacement on the domain boundary, and we introduce a preprocessing procedure to extend the EM displacement on the whole LH boundary, accounting also for the motion of the LA. We couple the 3D CFD model of the LH with the 0D closed-loop model of the remaining circulation and we solve the coupled multiscale problem by means of a segregated numerical scheme.

This chapter is organized as follows: in Section 6.1 we present the LH geometry model and the BCs we set for the 3D CFD model; in Section 6.2 we introduce the preprocessing procedure to reconstruct the displacement on the whole domain boundary based on an EM simulation of the LV, while in Section 6.3 we present the reduced valve dynamics model employed. The coupling strategy between the 0D circulation model and the 3D CFD model is described in Section 6.4. Section 6.5 is devoted to the description of the numerical approximation of each component of the model and the segregated scheme for their coupling. Numerical results are reported in Section 6.6: specifically, we consider the case of a healthy LH in Section 6.6.1 and that of mitral valve regurgitation in Section 6.6.2. Eventually, in Section 6.7 we draw our conclusions.

The content of this chapter is reported in [292].

6.1. The left heart geometry model and boundary conditions

We consider a realistic LH geometry provided by Zygote [133], an accurate 3D model of the heart obtained with CT scan data. The LH is constituted by the LA, LV and a portion of the ascending aorta (AA). The two cardiac chambers (LA, LV) are divided by the MV whereas the AV separates the LV from the AA. The oxygenated blood is

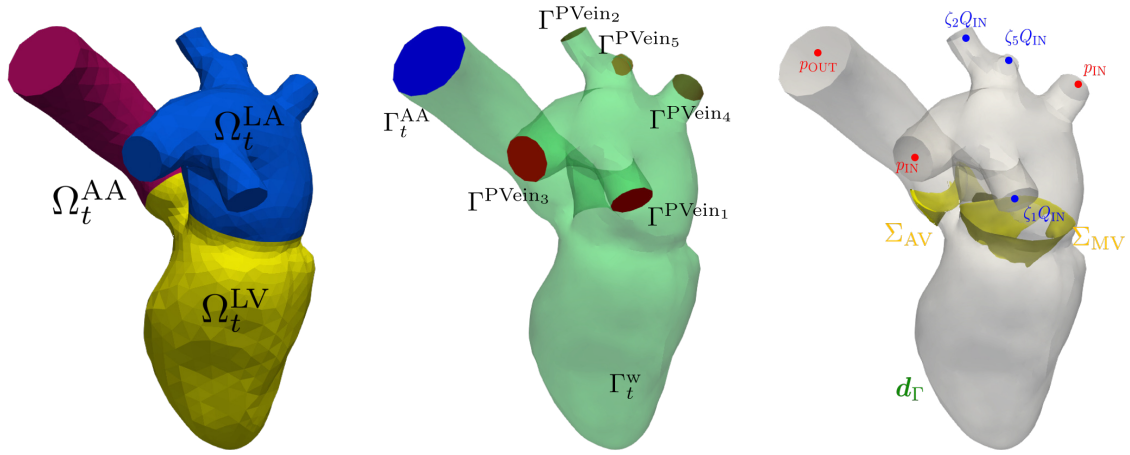

(a) (b) (c)

Figure 6.1: The LH geometry: (a) the three subdomains $\Omega_t = \Omega_t^{\mathrm{LA}} \cup \Omega_t^{\mathrm{LV}} \cup \Omega_t^{\mathrm{AA}}$; (b) the boundary portions of the LH geometry $\Gamma_t = \left(\bigcup_{i=1}^{5} \Gamma^{\mathrm{PVein}_i}\right) \cup \Gamma_t^{\mathrm{AA}} \cup \Gamma_t^{\mathrm{w}}$; (c) the immersed surfaces Σ_{MV} and Σ_{AV} (respectively in their open and closed configurations), in blue the inlet Dirichlet BCs, in red the Neumann BCs (for both inlet and outlet sections) and in green the Dirichlet condition at wall.

collected from the pulmonary veins, the inlets of our domain. The four pulmonary veins are connected to the upper part of the LA. In the geometry considered there are four pulmonary veins, but one of them is splitted into two inlets, thus, our LH geometry is characterized by five inlet sections as displayed in Figure 6.1. The blood is then pushed into the systemic circulation through the outlet section of the AA.

As shown in Figure 6.1a, we decompose the geometry into three subdomains: $\Omega_t = \Omega_t^{\mathrm{LA}} \cup \Omega_t^{\mathrm{LV}} \cup \Omega_t^{\mathrm{AA}}$, namely the LA Ω_t^{LA}, the LV Ω_t^{LV} and the AA Ω_t^{AA}. The boundary is split into

$$\Gamma_t = \left(\bigcup_{i=1}^{5} \Gamma^{\mathrm{PVein}_i}\right) \cup \Gamma_t^{\mathrm{AA}} \cup \Gamma_t^{\mathrm{w}},$$

where we denote with $\Gamma^{\mathrm{PVein}_i}$, $i = 1, \ldots, 5$ the five inlet sections of the four pulmonary veins; with Γ_t^{AA} the outlet section of the ascending aorta and with Γ_t^{w} the endocardium (see Figure 6.1b). The boundary portions $\Gamma^{\mathrm{PVein}_i}$, $i = 1, \ldots, 5$ are fixed. As displayed in Figure 6.1c, we immerse in the LH domain two surfaces Σ_{MV} and Σ_{AV}, namely the MV and the AV. Specifics on valves dynamics are given in Section 6.3.

To set pressures and flowrates in the LH, we prescribe Dirichlet BCs on three out of five inlet sections, and Neumann BCs on the remaining two. For the Dirichlet inlet sections, we have at our disposal the inlet flowrate $Q_{\mathrm{IN}}(t)$ only . Thus, the inlet BC is in principle a defective BC because the datum is provided only as averaged scalar quantity [267].

Since a laminar flow regime is reasonably expected in the pulmonary veins throughout the heart cycle [119, 231], we choose a priori a parabolic velocity profile in space, in the direction of the outward unit normal $\boldsymbol{n}_i$ to the i–th inlet section. Specifically, consistently with the BCs we used in Chapter 5, on the three Dirichlet sections, we set:

$$\boldsymbol{u} = 2Q_{\text{IN}} \frac{\zeta_i}{|\Gamma^{\text{PVein}_i}|} \left(1 - \frac{r^2}{R_i^2}\right) \boldsymbol{n}_i, \qquad \text{on } \Gamma^{\text{PVein}_i} \times (0, T_f), \quad i = 1, 2, 5, \tag{6.1}$$

being $r(\boldsymbol{x}) = |\boldsymbol{x}|$ the radial coordinate, R_i the radius of the i–th inlet section, $|\Gamma^{\text{PVein}_i}|$ its measure and ζ_i the flow-repartition factor which expresses the amount of flowrate for each inlet section and computed as

$$\zeta_i = \frac{|\Gamma^{\text{PVein}_i}|}{\sum_{i=1}^{5} |\Gamma^{\text{PVein}_i}|}.$$

We prescribe the pressure in the pulmonary veins $p_{\text{IN}}(t)$ with a Neumann BC on the two remaining inlet sections as:

$$\boldsymbol{\sigma}(\boldsymbol{u}, p)\boldsymbol{n} = -p_{\text{IN}} \boldsymbol{n}_i, \qquad \text{on } \Gamma^{\text{PVein}_i} \times (0, T_f), \quad i = 3, 4. \tag{6.2}$$

On the outlet section Γ_t^{AA} we prescribe a Neumann BC by setting the outlet pressure $p_{\text{OUT}}(t)$:

$$\boldsymbol{\sigma}\left(\boldsymbol{u}, p\right) \boldsymbol{n} = -p_{\text{OUT}} \boldsymbol{n}, \qquad \text{on } \Gamma_t^{\text{AA}} \times (0, T_f). \tag{6.3}$$

Details on the way we compute inlet flowrate $Q_{\text{IN}}(t)$, inlet and outlet pressures $p_{\text{IN}}(t)$, $p_{\text{OUT}}(t)$ are given in Section 6.4. Finally, on the endocardium (wall) we prescribe the boundary ALE velocity, by time differentiating the wall displacement $\boldsymbol{d}_\Gamma$ (that will be introduced in Section 6.2) in the current configuration:

$$\boldsymbol{u} = \boldsymbol{u}_\Gamma = \frac{\partial \boldsymbol{d}_\Gamma}{\partial t}, \qquad \text{on } \Gamma_t^{\text{w}} \times (0, T_f). \tag{6.4}$$

A graphical sketch of the whole set of BCs is given in Figure 6.1c.

6.2. Displacement modeling

The mathematical problem describing the hemodynamics of the LH is solved by prescribing a given displacement field denoted as $\widehat{\boldsymbol{d}}_\Gamma$ on the endocardium. In particular, the latter is used as Dirichlet BC on Γ_t^{w} for the NS-ALE-RIIS problem in Equation (6.4) and for the geometric problem in Equation (4.4b) on the whole boundary $\widehat{\Gamma}$. In the following, we present a procedure aimed at computing a physiological LH displacement $\widehat{\boldsymbol{d}}_\Gamma$ on $\widehat{\Gamma}$ starting from an EM simulation of the LV.

We split the wall into $\widehat{\Gamma}^{\text{w}} = \widehat{\Gamma}^{\text{w, LA}} \cup \widehat{\Gamma}^{\text{w, LV}} \cup \widehat{\Gamma}^{\text{w, AA}}$, being the walls of LA, LV and AA

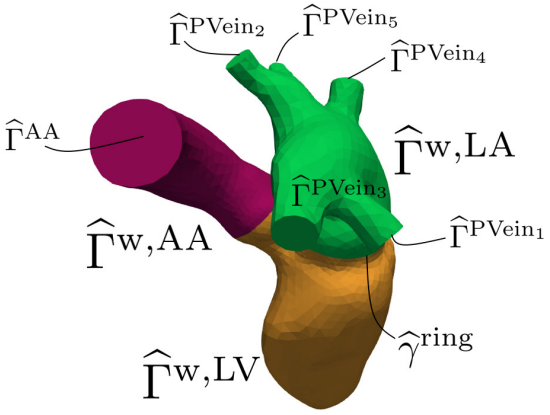

Figure 6.2: Boundary portions of the LH geometry in reference configuration to model displacement: $\widehat{\Gamma} = \widehat{\Gamma}^{\mathrm{w}} \cup \left(\bigcup_{i=1}^{5} \widehat{\Gamma}^{\mathrm{PVein}_i}\right) \cup \widehat{\Gamma}^{\mathrm{AA}}$, with $\widehat{\Gamma}^{\mathrm{w}} = \widehat{\Gamma}^{\mathrm{w,\,LA}} \cup \widehat{\Gamma}^{\mathrm{w,\,LV}} \cup \widehat{\Gamma}^{\mathrm{w,\,AA}}$ and $\widehat{\gamma}^{\mathrm{ring}} = \overline{\widehat{\Gamma}^{\mathrm{w,\,LV}}} \cap \left(\widehat{\Gamma} \setminus \widehat{\Gamma}^{\mathrm{w,\,LV}}\right)$

respectively, as displayed in Figure 6.2. Let $\widehat{\psi_1}$ and $\widehat{\psi_2}$ be two characteristic functions, $\widehat{\boldsymbol{d}}_{\mathrm{LV}}$ and $\widehat{\boldsymbol{d}}_{\mathrm{LA}}$ two displacement fields acting on the whole LH which account respectively for the motion of the LV and the LA. We define the displacement on the whole LH as

$$\widehat{\boldsymbol{d}}_{\Gamma}(\widehat{\boldsymbol{x}},t) = \underbrace{\widehat{\psi_1}(\widehat{\boldsymbol{x}})\widehat{\boldsymbol{d}}_{\mathrm{LV}}(\widehat{\boldsymbol{x}},t)}_{\text{(I)}} + \underbrace{\widehat{\psi_2}(\widehat{\boldsymbol{x}})\widehat{\boldsymbol{d}}_{\mathrm{LA}}(\widehat{\boldsymbol{x}},t)}_{\text{(II)}}, \quad \text{on } \widehat{\Gamma} \times (0,T_f). \tag{6.5}$$

Thus, we model the LH displacement as the sum of two contributions: (I) a displacement coming from an EM simulation of the LV that we extend to the whole LH domain; (II) an ad-hoc designed displacement for the LA. In the following, we describe how we compute all the quantities involved in Equation (6.5), namely the characteristic functions $\widehat{\psi_1}$, $\widehat{\psi_2}$ and the displacement fields $\widehat{\boldsymbol{d}}_{\mathrm{LV}}$, $\widehat{\boldsymbol{d}}_{\mathrm{LA}}$. In Algorithm 6.1 we summarize the main steps required in the preprocessing procedure; in Figure 6.3, we represent these steps with boxes numbered as the lines in Algorithm 6.1. We wish to point out that, since the displacement at the LV is computed through an EM simulation, and we prescribe this datum at walls of the fluid domain, we are enforcing in the LV a kinematic one-way coupling condition between EM and CFD.

6.2.1. Electromechanics of the left ventricle and harmonic extension on the left heart geometry

We describe how we compute the LV displacement through an EM simulation and then its extension on the whole LH geometry. The steps here introduced correspond to boxes 1-5 in Figure 6.3 and, analogously, to lines 1-5 of Algorithm 6.1.

Algorithm 6.1 Preprocessing procedure to compute LH displacement

Input $\widehat{\Omega}$, $\widehat{\Gamma}$
Output $\widehat{\boldsymbol{d}}_{\Gamma}$

1: LV-EM simulation $\rightarrow \widehat{\boldsymbol{d}}_{\text{LV}}^{\text{EM}}$ on $\widehat{\Omega}^{\text{LV, s}} \times (0, T_f)$
2: Extract solution on LV endocardium $\rightarrow \widehat{\boldsymbol{d}}_{\text{LV, endo}}^{\text{EM}}$ on $\widehat{\Gamma}^{\text{w, LV}} \times (0, T_f)$
3: $\widehat{\boldsymbol{d}}_{\text{LV, endo}}^{\text{EM}} \rightarrow$ Laplace - Beltrami (Equation (6.6) $\rightarrow \widehat{\boldsymbol{d}}_{*}$ on $\widehat{\Gamma} \setminus \widehat{\Gamma}^{\text{w, LV}} \times (0, T_f)$
4: Compute $\widehat{\boldsymbol{d}}_{\text{LV}}$ on $\widehat{\Gamma} \times (0, T_f)$ (Equation (6.7))
5: Compute characteristic functions $\widehat{\psi}_1$, $\widehat{\psi}_2$ on $\widehat{\Gamma}$
6: Solve the geometric problem (4.4) with Dirichlet datum: $\widehat{\boldsymbol{d}}_{\Gamma}^{\text{PRE}} = \widehat{\psi_1 \boldsymbol{d}}_{\text{LV}}$ on $\widehat{\Gamma} \times (0, T_f)$
7: Compute $V_{\text{LV}}(t)$, $V_{\text{AA}}(t)$, $\forall t \in (0, T_f)$
8: Compute $\mathcal{A}(t)$, $\forall t \in (0, T_f)$ (Equation (6.11))
9: Solve the 0D circulation model $\rightarrow V_{\text{LA}}(t) = V_{\text{LA}}^{\text{0D}}(t)$
10: Compute $\Phi(t)$, $\forall t \in (0, T_f)$
11: Compute $\widehat{\boldsymbol{e}}_{\text{G}}^{\text{LA}}$ on $\widehat{\Gamma}$
12: Compute $\mathcal{B}(t)$, $\forall t \in (0, T_f)$
13: Solve the ODE in Equation (6.13) $\forall t \in (0, T_f) \rightarrow g_{\text{LA}}(t)$
14: $\widehat{\boldsymbol{d}}_{\text{LA}} = \widehat{\boldsymbol{e}}_{\text{G}}^{\text{LA}} g_{\text{LA}}$ on $\widehat{\Gamma} \times (0, T_f)$
15: $\widehat{\boldsymbol{d}}_{\Gamma} = \widehat{\psi}_1 \widehat{\boldsymbol{d}}_{\text{LV}} + \widehat{\psi}_2 \widehat{\boldsymbol{d}}_{\text{LA}}$, on $\widehat{\Gamma} \times (0, T_f)$

We use the 3D EM model of the LV developed in [223, 224]. Electrophysiology is modelled through the Monodomain equation [95] coupled with the ten Tusscher-Panfilov ionic model [255]. Subcellular generation of active force is modelled by means of ANNs through the RDQ20-MF model [221]. The passive behaviour of the tissue is modelled through the Guccione strain energy density function [112]. At the epicardium we set generalized Robin-type BCs; on the rings of the AV and MV we impose energy-consistent BCs [222]. Fibers distribution is considered through rule based Bayer-Blake-Plank-Trayanova algorithm [30, 203]. The 3D EM model of the LV is coupled to the 0D closed-loop circulation model of the whole cardiovascular system introduced in Section 4.4. For the numerical approximation of the problem, we use linear FE for the space discretization. Specifically, in the EM model an intergrid transfer operator [229] is adopted to employ a coarser grid for the elastodynamic and a finer one for the electrophysiology, due to the higher resolution required by the latter. The coupled EM problem is solved by means of the staggered numerical scheme presented in [223]. For additional details on this model and for the numerical methods adopted to solve it, we refer respectively to [224] and [223].

Since the one-way coupling ignores the dynamic balance among CFD and EM, the pressure in the LV during the isovolumetric phases (i.e. when both valves are closed) would not be well defined [208, 259]. To overcome this issue, that would however regard

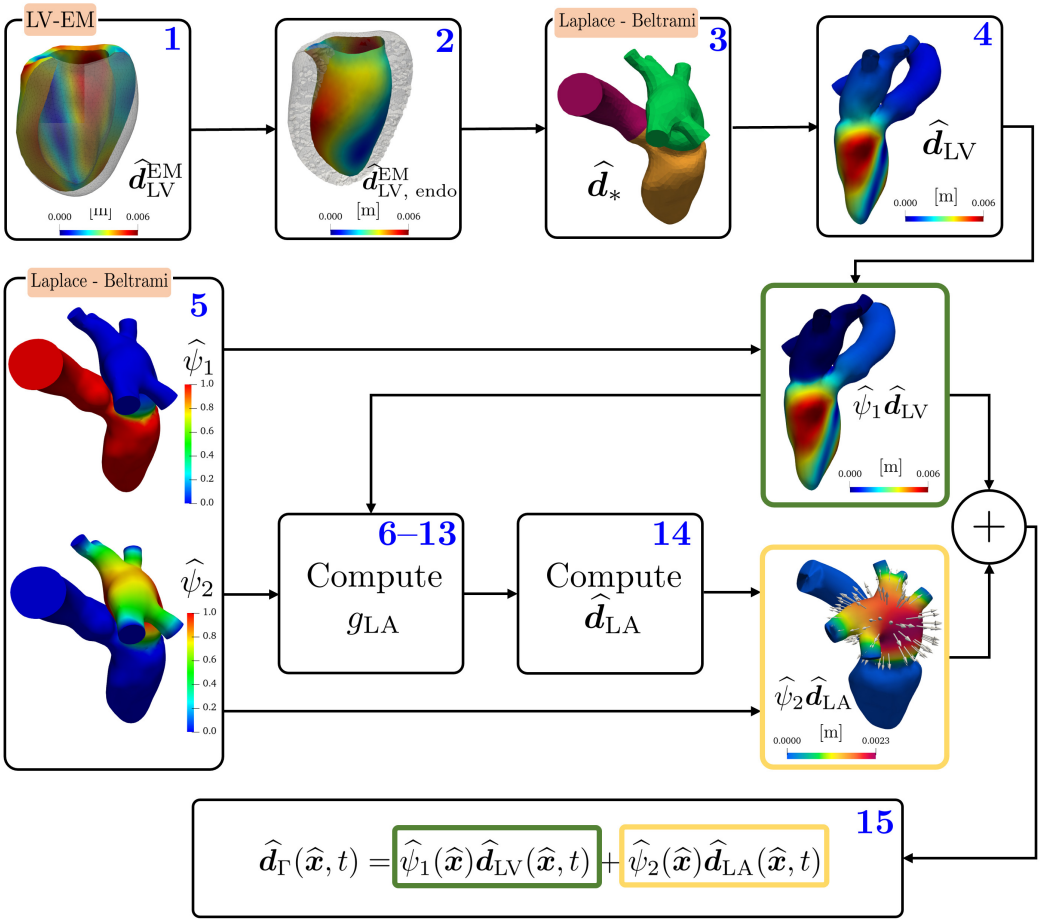

Figure 6.3: Displacement procedure. Boxes numbers are referred to lines in Algorithm 6.1.

only a short portion of the hearbeat, we neglect the isovolumetric phases obtained in the EM simulation for our CFD simulation.

Let $\widehat{\boldsymbol{d}}^{\mathrm{EM}}_{\mathrm{LV}}(\widehat{\boldsymbol{x}},t)$ in $\widehat{\Omega}^{\mathrm{LV,\,s}} \times (0,T_f)$ be the displacement of the LV, solution of the EM model and defined in the LV structure ("s", i.e. LV myocardium). In Figure 6.4a we show the LV in its reference configuration ($\widehat{\Omega}^{\mathrm{LV,\,s}}$); in Figures 6.4b and 6.4c we display snapshots of the numerical solution during systole and diastole respectively. Moreover, we also report the solution in Figure 6.3, box 1.

Let then $\widehat{\boldsymbol{d}}^{\mathrm{EM}}_{\mathrm{LV,\,endo}}(\widehat{\boldsymbol{x}},t)$ on $\widehat{\Gamma}^{\mathrm{w,\,LV}} \times (0,T_f)$ be the displacement field restricted to the LV endocardium – wall of the LV fluid domain – and shown in Figure 6.3, box 2.

We compute a displacement $\widehat{\boldsymbol{d}}_*$ acting on LA and AA only. We compute it as the solution of a vectorial Laplace-Beltrami problem. Specifically, we extend on LA and AA the LV displacement $\widehat{\boldsymbol{d}}^{\mathrm{EM}}_{\mathrm{LV,\,endo}}(\widehat{\boldsymbol{x}},t)$ by keeping the pulmonary veins fixed as (see

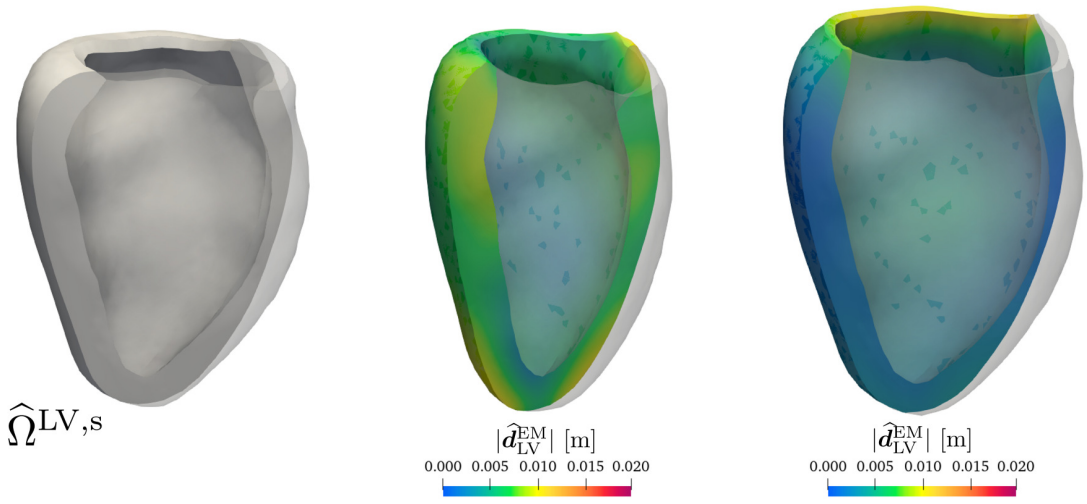

(a) Reference configuration (b) Systole (c) Diastole

Figure 6.4: EM simulation of the LV: (a) LV in its reference configuration; (b), (c) LV during systole and diastole colored with displacement magnitude.

Figure 6.3, box 3):

$$-\Delta_{\widehat{\Gamma}}\widehat{\boldsymbol{d}}_* = \boldsymbol{0} \qquad \text{on } \widehat{\Gamma} \setminus \left(\widehat{\Gamma}^{\text{w, LV}} \cup \left(\bigcup_{i=1}^{5} \widehat{\Gamma}^{\text{PVein}_i}\right)\right) \times (0, T_f), \tag{6.6a}$$

$$\widehat{\boldsymbol{d}}_* = \widehat{\boldsymbol{d}}^{\text{EM}}_{\text{LV, endo}} \qquad \text{on } \widehat{\gamma}^{\text{ring}} \times (0, T_f), \tag{6.6b}$$

$$\widehat{\boldsymbol{d}}_* = \boldsymbol{0} \qquad \text{on } \partial\widehat{\Gamma}^{\text{PVein}_i} \times (0, T_f), \quad i = 1, \dots, 5, \tag{6.6c}$$

being $\widehat{\gamma}^{\text{ring}} = \overline{\widehat{\Gamma}^{\text{w, LV}}} \cap \left(\widehat{\Gamma} \setminus \widehat{\Gamma}^{\text{w, LV}}\right)$. We define the displacement $\widehat{\boldsymbol{d}}_{\text{LV}}(\widehat{\boldsymbol{x}}, t)$ on $\widehat{\Gamma} \times (0, T_f)$ as:

$$\widehat{\boldsymbol{d}}_{\text{LV}}(\widehat{\boldsymbol{x}}, t) = \begin{cases} \widehat{\boldsymbol{d}}^{\text{EM}}_{\text{LV, endo}}(\widehat{\boldsymbol{x}}, t) & \text{on } \widehat{\Gamma}^{\text{w, LV}} \times (0, T_f), \\ \widehat{\boldsymbol{d}}_*(\widehat{\boldsymbol{x}}, t) & \text{on } \widehat{\Gamma} \setminus \widehat{\Gamma}^{\text{w, LV}} \times (0, T_f). \end{cases} \tag{6.7}$$

By combining $\widehat{\boldsymbol{d}}_*$ and $\widehat{\boldsymbol{d}}^{\text{EM}}_{\text{LV, endo}}$ as in Equation (6.7), the resulting $\widehat{\boldsymbol{d}}_{\text{LV}}$ is hence defined on the whole LH boundary $\widehat{\Gamma}$, as shown in Figure 6.3, box 4. Thus, $\widehat{\boldsymbol{d}}_{\text{LV}}$ is obtained by extending the EM-based LV displacement on the LH. As a consequence, at this stage, we are still not accounting for any contribution coming from the LA motion. As a matter of fact, a simple extension of the LV displacement would bring to a non physiological LA volume behavior, having then a direct impact on the fluid dynamics simulation, for instance in terms of non-physiological flowrates and pressures. In Section 6.2.2, we propose a simplified model to account for a physiological LA motion.

We define two scalar characteristic functions $\widehat{\psi}_1(\widehat{\boldsymbol{x}})$ and $\widehat{\psi}_2(\widehat{\boldsymbol{x}})$ on $\widehat{\Gamma}$ (reported in Fig-

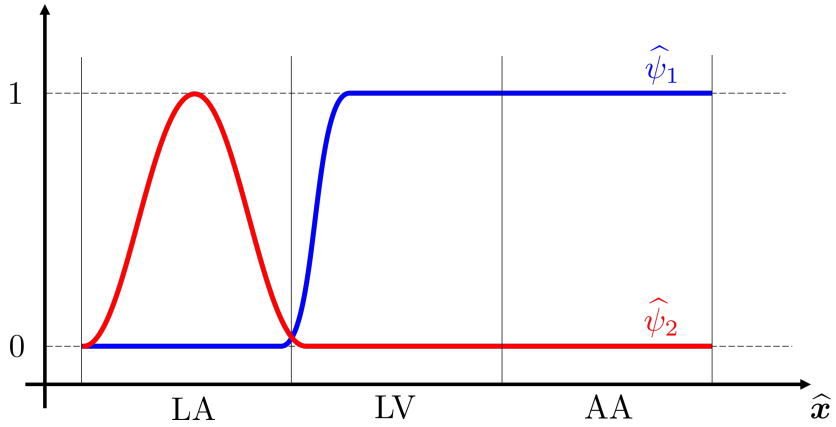

Figure 6.5: 1D representation of the functions $\widehat{\psi}_1$ and $\widehat{\psi}_2$.

ure 6.3, box 5) by solving additional scalar Laplace-Beltrami problems. We introduce them to isolate the effects of LA and LV displacements, while still guaranteeing an overall smooth solution over the whole LH. In particular,

1. $\widehat{\psi}_1(\widehat{\boldsymbol{x}})$ is equal to 1 on $\widehat{\Gamma}^{\text{w, LV}} \cup \widehat{\Gamma}^{\text{w, AA}} \cup \widehat{\Gamma}^{\text{AA}}$ and smoothly vanishes in a subregion of $\widehat{\Gamma}^{\text{w, LA}}$ and it is zero on $\bigcup_{i=1}^{5} \widehat{\Gamma}^{\text{PVein}_i}$;
2. $\widehat{\psi}_2(\widehat{\boldsymbol{x}})$ is equal to 0 on $\widehat{\Gamma}^{\text{w, LV}} \cup \widehat{\Gamma}^{\text{w, AA}} \cup \widehat{\Gamma}^{\text{AA}}$, positive on $\widehat{\Gamma}^{\text{w, LA}}$, and vanishes on $\bigcup_{i=1}^{5} \widehat{\Gamma}^{\text{PVein}_i}$.

We give a 1D representation of the functions $\widehat{\psi}_1$ and $\widehat{\psi}_2$ in Figure 6.5.

In the green box of Figure 6.3, we report the displacement field $\widehat{\psi}_1 \widehat{\boldsymbol{d}}_{\text{LV}}$ arising from the aforementioned steps: on the LV it is equal to to the displacement computed in the EM simulation; it is harmonically extended on the AA and it smoothly vanishes on the LA.

6.2.2. Modeling the atrial motion

As the EM model of the whole LH (or of the isolated LA) is lacking (currently being developed by [202]), we propose a simplified model to compute the displacement of the whole LH, also considering the LA physiological motion.

Let $\widehat{\boldsymbol{d}}_{\text{LA}}(\widehat{\boldsymbol{x}}, t)$ be the (unknown) displacement of the LA introduced in Equation (6.5); we assume that the LA displacement can be modelled by separation of variables. Moreover, as we do in Chapter 5, we assume that the LA displacement is directed towards its center of volume $\widehat{\boldsymbol{x}}_{\text{G}}^{\text{LA}}$. We introduce $\widehat{\boldsymbol{e}}_{\text{G}}^{\text{LA}}$ as the unit vector directed towards $\widehat{\boldsymbol{x}}_{\text{G}}^{\text{LA}}$ as $\widehat{\boldsymbol{e}}_{\text{G}}^{\text{LA}}(\widehat{\boldsymbol{x}}) = \frac{\widehat{\boldsymbol{x}} - \widehat{\boldsymbol{x}}_{\text{G}}^{\text{LA}}}{|\widehat{\boldsymbol{x}} - \widehat{\boldsymbol{x}}_{\text{G}}^{\text{LA}}|}$, where $|\cdot|$ is the Euclidean norm. Thus, we define $\widehat{\boldsymbol{d}}_{\text{LA}}$ as

$$\widehat{\boldsymbol{d}}_{\text{LA}}(\widehat{\boldsymbol{x}}, t) = \widehat{\boldsymbol{e}}_{\text{G}}^{\text{LA}}(\widehat{\boldsymbol{x}}) g_{\text{LA}}(t), \text{ on } \widehat{\Gamma} \times (0, T_f), \tag{6.8}$$

being $g_{\mathrm{LA}}(t)$ a time-dependent function.

To compute $g_{\mathrm{LA}}(t)$, we consider the LH volume time-derivative and we express it through the RTT [153] as

$$\frac{\mathrm{d}V_{\mathrm{LH}}(t)}{\mathrm{d}t} = \frac{\mathrm{d}}{\mathrm{d}t}\int_{\Omega_t} \mathrm{d}\boldsymbol{x} \overset{\mathrm{RTT}}{=} \oint_{\Gamma_t} \boldsymbol{u}_\Gamma \cdot \boldsymbol{n}\mathrm{d}\boldsymbol{x} = \oint_{\Gamma_t} \frac{\partial}{\partial t}\boldsymbol{d}_\Gamma \cdot \boldsymbol{n}\mathrm{d}\boldsymbol{x}, \tag{6.9}$$

being V_{LH} the LH volume. By defining $\boldsymbol{u}_\Gamma(\boldsymbol{x},t) = \frac{\partial}{\partial t}\widehat{\boldsymbol{d}}_\Gamma(\mathcal{A}_t^{-1}(x),t)$ and by recalling that for a generic function w holds that $w = \widehat{w}\circ\mathcal{A}_t^{-1}$, we use Equation (6.5) and (6.8) mapped to the current configuration Γ_t in Equation (6.9) to get:

$$\frac{\mathrm{d}V_{\mathrm{LH}}(t)}{\mathrm{d}t} = \oint_{\Gamma_t} \frac{\partial}{\partial t}\left(\psi_1(\boldsymbol{x})\boldsymbol{d}_{\mathrm{LV}}(\boldsymbol{x},t)\right)\cdot\boldsymbol{n}\mathrm{d}\boldsymbol{x} + \frac{\mathrm{d}g_{\mathrm{LA}}(t)}{\mathrm{d}t}\oint_{\Gamma_t}\psi_2(\boldsymbol{x})\boldsymbol{e}_{\mathrm{G}}^{\mathrm{LA}}(\boldsymbol{x})\cdot\boldsymbol{n}\mathrm{d}\boldsymbol{x}, \tag{6.10}$$

Let V_{LA}, V_{LV} and V_{AA} be the volumes of LA, LV and AA, with $V_{\mathrm{LH}}(t) = V_{\mathrm{LA}}(t) + V_{\mathrm{LV}}(t) + V_{\mathrm{AA}}(t)$; we define the fluxes in (6.10) as

$$\mathcal{A}(t) = \oint_{\Gamma_t} \frac{\partial}{\partial t}\left(\psi_1(\boldsymbol{x})\boldsymbol{d}_{\mathrm{LV}}(\boldsymbol{x},t)\right)\cdot\boldsymbol{n}\mathrm{d}\boldsymbol{x}, \quad \mathcal{B}(t) = \oint_{\Gamma_t}\psi_2(\boldsymbol{x})\boldsymbol{e}_{\mathrm{G}}^{\mathrm{LA}}(\boldsymbol{x})\cdot\boldsymbol{n}\mathrm{d}\boldsymbol{x}, \tag{6.11}$$

$$\Phi(t) = \frac{\mathrm{d}V_{\mathrm{LH}}(t)}{\mathrm{d}t} - \mathcal{A}(t) = \frac{\mathrm{d}V_{\mathrm{LA}}(t)}{\mathrm{d}t} + \frac{\mathrm{d}V_{\mathrm{LV}}(t)}{\mathrm{d}t} + \frac{\mathrm{d}V_{\mathrm{AA}}(t)}{\mathrm{d}t} - \mathcal{A}(t). \tag{6.12}$$

Solving Equation (6.10) for $\frac{\mathrm{d}g_{\mathrm{LA}}(t)}{\mathrm{d}t}$, yields the following Cauchy problem:

$$\begin{cases} \dfrac{\mathrm{d}g_{\mathrm{LA}}(t)}{\mathrm{d}t} &= \dfrac{\Phi(t)}{\mathcal{B}(t)}, \quad t\in(0,T_f), \\ g_{\mathrm{LA}}(0) &= g_{\mathrm{LA}_0}. \end{cases} \tag{6.13}$$

Since the Zygote's geometry is scanned at 70 % of diastole [133], we consider such instant as initial time $t=0$ such that $\widehat{\Omega} = \Omega_0$, thus $g_{\mathrm{LA}_0} = 0$. To compute $V_{\mathrm{LA}}(t)$ in Equation (6.12), we solve the 0D closed-loop circulation model - tuned on the basis of the EM simulation[1]- and we denote the LA volume computed as $V_{\mathrm{LA}}^{\mathrm{0D}}(t)$. Thus, we set:

$$V_{\mathrm{LA}}(t) = V_{\mathrm{LA}}^{\mathrm{0D}}(t).$$

To compute the remaining terms in $\Phi(t)$, we define a preliminary displacement field which accounts for the LV motion only (i.e. the one appearing in the definition of $\mathcal{A}(t)$ in Equation (6.11)):

$$\widehat{\boldsymbol{d}}_\Gamma^{\mathrm{PRE}}(\widehat{\boldsymbol{x}},t) = \widehat{\psi}_1(\widehat{\boldsymbol{x}})\widehat{\boldsymbol{d}}_{\mathrm{LV}}(\widehat{\boldsymbol{x}},t), \text{ on } \widehat{\Gamma}\times(0,T_f). \tag{6.14}$$

[1]In principle, one could directly adopt the LA volume obtained with the 3D-0D EM model [223, 224]. However, as previously explained, since we remove in post-processing the isovolumetric phases, we calibrate the 0D model to be consistent with the LV volume achieved.

Algorithm 6.2 Numerically compute g_{LA}

Input $\widehat{\Gamma}$, $\widehat{\psi}_2$, $\widehat{\boldsymbol{d}}^{\mathrm{PRE}}_{\Gamma_n,n}$, $n = 0, \dots N_t$
Output g_{LA_n}, $n = 0, \dots N_t$.

1: Initialize $g_{\mathrm{LA}_0} = 0$, $n = 0$, $\Gamma_0 = \widehat{\Gamma}$
2: **while** $n < N_t$ **do**
3: Set $\widehat{\boldsymbol{d}}_{\Gamma_n}(\boldsymbol{x}) = \widehat{\boldsymbol{d}}^{\mathrm{PRE}}_{\Gamma_n}(\widehat{\boldsymbol{x}}) + \widehat{\psi}_2(\widehat{\boldsymbol{x}}) g_{\mathrm{LA}_n} \widehat{\boldsymbol{e}}^{\mathrm{LA}}_{\mathrm{G}}$ on $\widehat{\Gamma}$
4: Move the domain $\rightarrow \Gamma_n$
5: Compute $\boldsymbol{e}^{\mathrm{LA}}_{\mathrm{G}}$ and $\boldsymbol{n}$ on Γ_n
6: $\mathcal{B}_n = \oint_{\Gamma_n} \psi_2(\boldsymbol{x}) \boldsymbol{e}^{\mathrm{LA}}_{\mathrm{G}} \cdot \boldsymbol{n} \mathrm{d}\boldsymbol{x}$
7: $g_{\mathrm{LA},n+1} = g_{\mathrm{LA},n} + \Delta t \, \mathcal{B}_n^{-1} \, \Phi_{n+1}$
8: $n \leftarrow n + 1$
9: **end while**

As reported in Algorithm 6.1, in order to compute $g_{\mathrm{LA}}(t)$, we first solve a preliminary geometric problem, as the one in Equation (4.4) but using $\widehat{\boldsymbol{d}}^{\mathrm{PRE}}_{\Gamma}$ as Dirichlet BC on $\widehat{\Gamma} \times (0, T_f)$. By introducing $\widehat{\boldsymbol{d}}^{\mathrm{PRE}}_{\Gamma}$, we can compute once and for all the volumes $V_{\mathrm{LV}}(t)$, $V_{\mathrm{AA}}(t)$ and the flux $\mathcal{A}(t)$. We solve the 0D circulation model to get $V_{\mathrm{LA}}(t)$ and we compute the flux $\Phi(t)$. Once we compute $\widehat{\boldsymbol{e}}^{\mathrm{LA}}_{\mathrm{G}}$, we calculate the flux $\mathcal{B}(t)$ to finally get $g_{\mathrm{LA}}(t)$ as solution of the Cauchy problem (6.13). The steps here mentioned are aimed at computing $g_{\mathrm{LA}}(t)$: they are shown in lines 6-13 of Algorithm 6.1 and gathered in a single box in Figure 6.3.

Once we get $g_{\mathrm{LA}}(t)$, we can compute $\widehat{\boldsymbol{d}}_{\mathrm{LA}}$ as in Equation (6.8) and displayed in box 14 in Figure 6.3. The magnitude of the displacement $\widehat{\psi}_2 \widehat{\boldsymbol{d}}_{\mathrm{LA}}$ is shown in the yellow box in Figure 6.3: it is non-null on the LA only, smoothly vanishing towards the pulmonary veins and on the LV and the AA. We also report glyphs of $\widehat{\psi}_2 \widehat{\boldsymbol{d}}_{\mathrm{LA}}$: the LA displacement direction coincides with $\widehat{\boldsymbol{e}}^{\mathrm{LA}}_{\mathrm{G}}$.

The displacement $\boldsymbol{d}_{\Gamma}$ can be eventually computed as in Equation (6.5) and as reported in Figure 6.3, box 15.

6.2.3. Algorithms, numerical methods for the displacement model and displacement results

We implemented the procedure in PvPython [8]. To compute $\widehat{\boldsymbol{d}}^{\mathrm{EM}}_{\mathrm{LV}}$ and $\widehat{\boldsymbol{d}}^{\mathrm{PRE}}_{\Gamma}$, solving respectively the EM model of the LV [223, 224] and the geometric problem (4.4), we carry out numerical simulations using life$^{\times}$ [6]. We solved the Laplace-Beltrami problems to get $\widehat{\boldsymbol{d}}_*$, $\widehat{\psi}_1$ and $\widehat{\psi}_2$ using vmtk [14, 20] and the pre-processing tools for cardiac numerical simulations [85].

Specifically, referring to Algorithm 6.1, the computation of g_{LA} in step 13 would involve

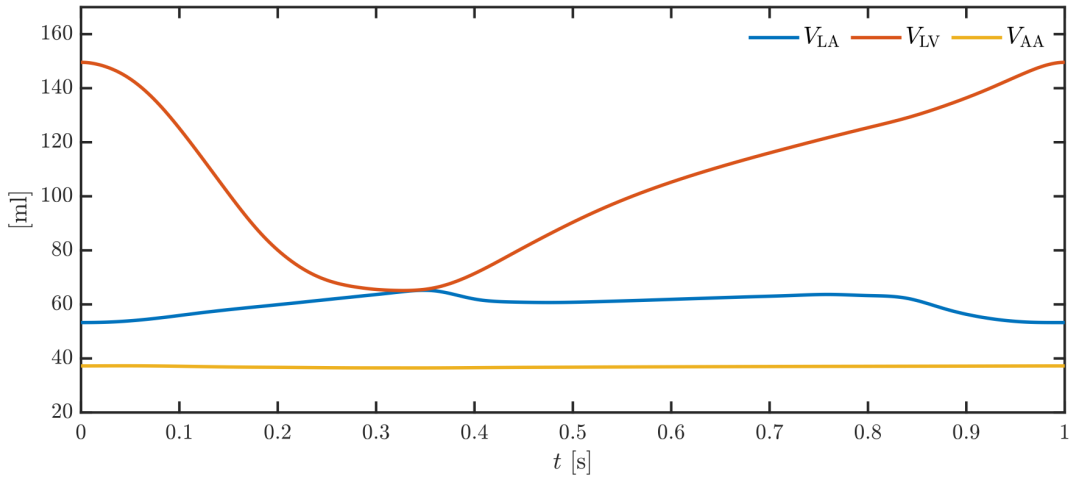

Figure 6.6: Volumes of LA, LV and AA achieved applying to $\widehat{\Gamma}$ the displacement $\widehat{\boldsymbol{d}}_{\Gamma}$ defined in Equation (6.5).

a non-linear problem. As a matter of fact, the definition of the flux $\mathcal{B}(t)$ (specified in step 12 and required in step 13) entails an integral acting on LA and computed on Γ_t, which is still unknown. Hence, differently from $\mathcal{A}(t)$ – where we already know the geometry since $\psi_1 = 0$ on the LA – we cannot evaluate this flux once and for all. We address the non linearity by considering the flux $\mathcal{B}$ at the previous time step, as reported in Algorithm 6.2. We denote with n the quantities evaluated at time step t_n, with $n = 0, \ldots, N_t$ and let Δt be the time step size. At each time step, we compute the displacement $\widehat{\boldsymbol{d}}_{\Gamma_n}(\widehat{\boldsymbol{x}}) = \widehat{\boldsymbol{d}}_{\Gamma}(\widehat{\boldsymbol{x}}, t_n)$, we move the domain boundary to recover the geometry Γ_n (computing also $\boldsymbol{e}_{\mathrm{G}}^{\mathrm{LA}}$ and $\boldsymbol{n}$ on Γ_n), we evaluate the flux $\mathcal{B}_n$. The ODE (6.13) is then numerically integrated with the backward Euler method: given g_{LA_n}, for $n = 0, \ldots, N_t - 1$, find $g_{\mathrm{LA}_{n+1}}$ such that

$$g_{\mathrm{LA}_{n+1}} = g_{\mathrm{LA}_n} + \Delta t \, \frac{\Phi_{n+1}}{\mathcal{B}_n}. \tag{6.15}$$

Finally, in Figure 6.7, we report the LH geometry warped by $\widehat{\boldsymbol{d}}_{\Gamma}$ at different time steps during the heart cycle starting from the time of end diastole. Moreover, in Figure 6.6 we show the volumes of LA, LV and AA obtained with our preprocessing procedure.

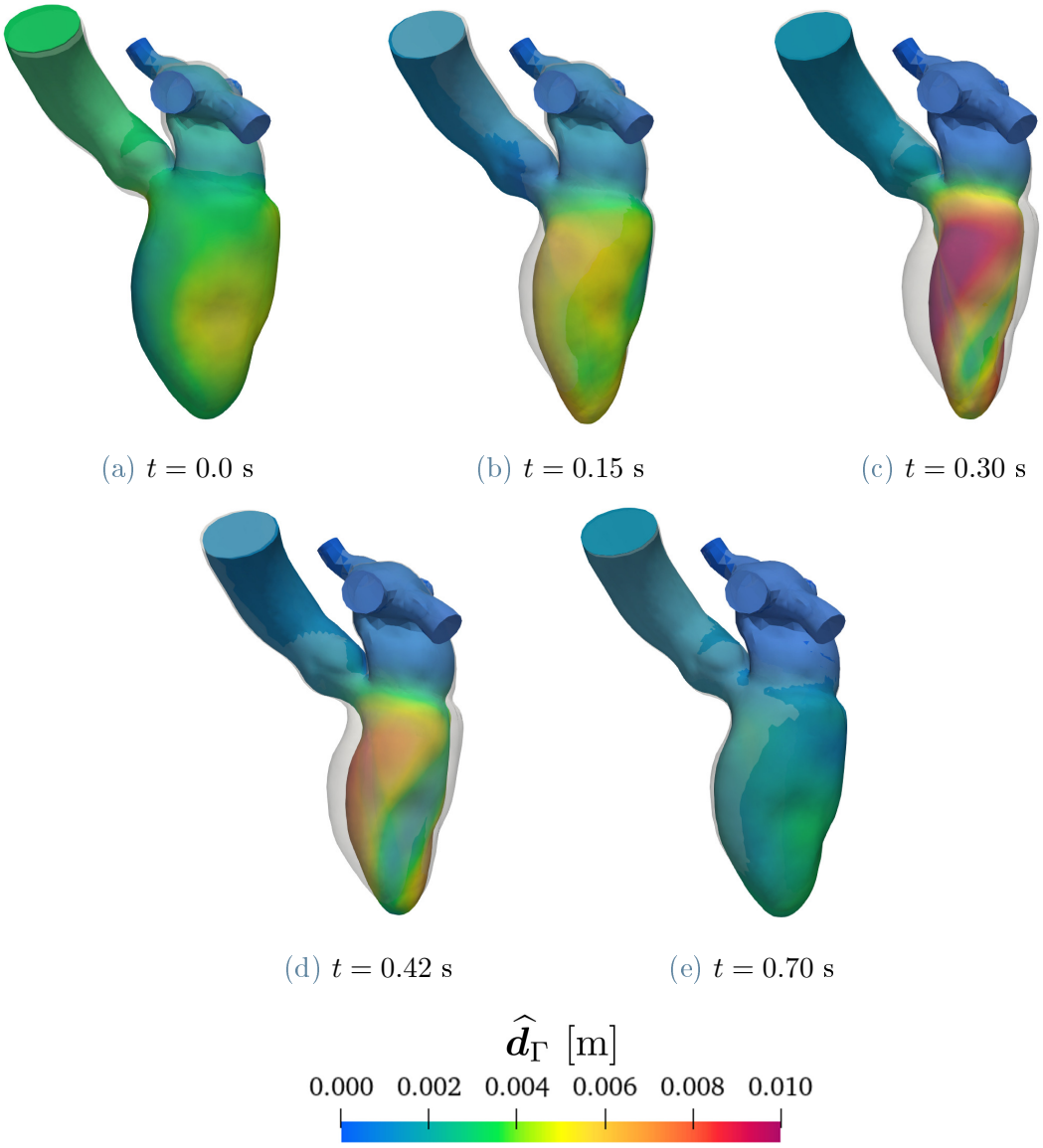

(a) $t = 0.0$ s (b) $t = 0.15$ s (c) $t = 0.30$ s

(d) $t = 0.42$ s (e) $t = 0.70$ s

Figure 6.7: LH geometry warped by $\widehat{\boldsymbol{d}}_\Gamma$ at different time step.

6.3. Valves dynamics

As described in Section 4.2, the effect of MV and AV on the fluid is modelled by means of the RIIS method [86, 100]. In addition, we developed preprocessing pipelines to define a displacement to move the leaflets of the cardiac valves and hence to bring the immersed surfaces from the open to the closed configuration and vice versa. The MV and AV are given by Zygote [133] respectively in their closed and open configuration. In Figure 6.9, we show the cardiac valves from their fully closed to fully open configurations and we

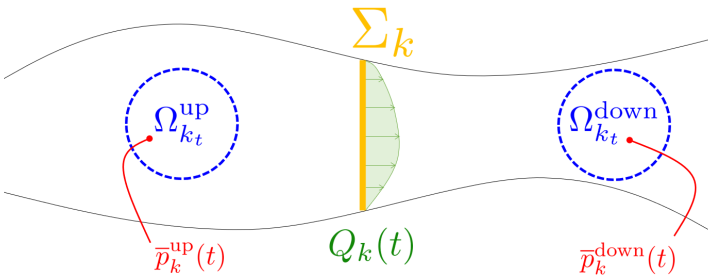

Figure 6.8: Immersed valve Σ_k with upwind and downwind control volumes where average pressures are computed. Q_k is the flowrate across Σ_k.

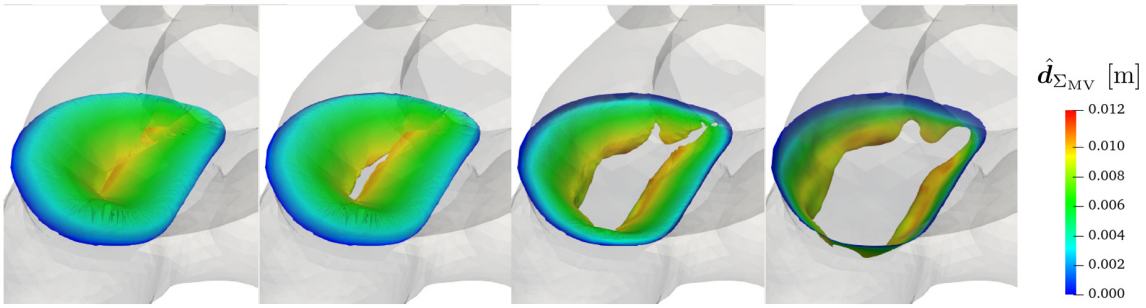

(a) MV

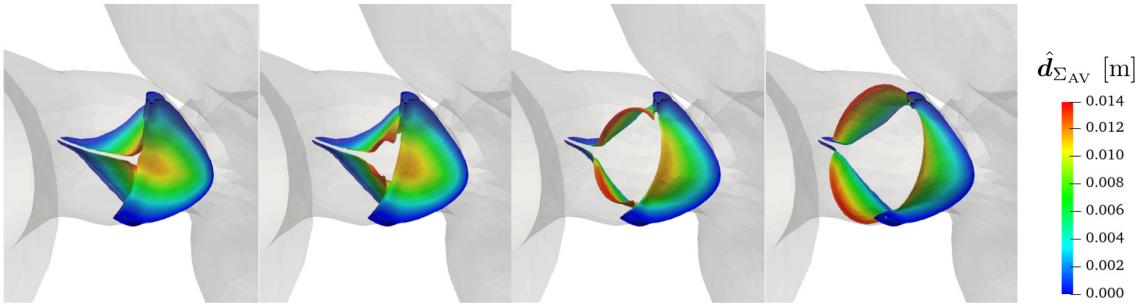

(b) AV

Figure 6.9: Cardiac valves from their fully closed to their fully open configuration. Leaflets are deformed with the displacement $\widehat{\boldsymbol{d}}_{\Sigma_{\text{MV}}}$ and $\widehat{\boldsymbol{d}}_{\Sigma_{\text{AV}}}$.

denote the valves leaflets' displacements as $\widehat{\boldsymbol{d}}_{\Sigma_{\text{MV}}}(\widehat{\boldsymbol{x}})$ and $\widehat{\boldsymbol{d}}_{\Sigma_{\text{AV}}}(\widehat{\boldsymbol{x}})$.

We do not prescribe a priori the time at which valves open and close as this is the result of our numerical simulations. If a valve is closed, its leaflets start to open when the pressure jump across it becomes positive; viceversa, the valve closes when a

condition of reversed flow across the orifice area is detected [259]. The condition on the pressure jump across the valve k, with $k = \text{MV}, \text{AV}$ is checked by considering two control volumes inside the upwind and downwind chambers, namely $\Omega_{k_t}^{\text{up}}$ and $\Omega_{k_t}^{\text{down}}$, as shown in Figure 6.8. Let $\overline{p}_k^{\text{up}}(t)$ and $\overline{p}_k^{\text{down}}(t)$ be the average pressure inside each control volume:

$$\overline{p}_k^{\text{up}}(t) = \frac{1}{|\Omega_{k_t}^{\text{up}}|}\int_{\Omega_{k_t}^{\text{up}}} p(\boldsymbol{x},t)d\boldsymbol{x}, \quad \overline{p}_k^{\text{down}}(t) = \frac{1}{|\Omega_{k_t}^{\text{down}}|}\int_{\Omega_{k_t}^{\text{down}}} p(\boldsymbol{x},t)d\boldsymbol{x}, \tag{6.16}$$

respectively. Then, the pressure jump across the valve k is computed as

$$\delta\overline{p}_k(t) = \overline{p}_k^{\text{up}}(t) - \overline{p}_k^{\text{down}}(t). \tag{6.17}$$

The valve k will thus open when $\delta\overline{p}_k(t) > 0$.

The closure condition at time t of reversed flow is checked when $Q_k(t) < 0$, Q_k being the flowrate through the valve k. Hinging upon a mass balance, the sign of $Q_k(t)$ is directly related to that of $\dot{V}_{\text{LV}}(t)$. Therefore, the MV will close when $\dot{V}_{\text{LV}}(t) < 0$, while the AV when $\dot{V}_{\text{LV}}(t) > 0$

Hence, during a heart cycle, to each cardiac valve two times will be associated: a closing (superscript '$\emptyset$') and an opening (superscript '0') times that we assemble in

$$\boldsymbol{\tau} = \left(\tau_{\text{MV}}^{\emptyset}, \tau_{\text{MV}}^{0}, \tau_{\text{AV}}^{\emptyset}, \tau_{\text{AV}}^{0}\right)^T. \tag{6.18}$$

Opening and closure stages of valves are not instantaneous: we prescribe a given ramp time to fully open/close the valve. For instance, the MV starts opening at $t = \tau_{\text{MV}}^0$ and its opening stage ends at $t = \tau_{\text{MV}}^0 + \Delta\tau_{\text{MV}}^0$, with $\Delta\tau_{\text{MV}}^0$ given. More details on the role played by the displacement fields $\widehat{\boldsymbol{d}}_{\Sigma_{\text{MV}}}$ and $\widehat{\boldsymbol{d}}_{\Sigma_{\text{AV}}}$ and the opening and closing times $\boldsymbol{\tau}$ will be given in Section 6.5.1.

6.4. Coupling the 3D CFD model to the 0D circulation model

In order to couple the 3D CFD model of the LH with the 0D circulation model of the whole cardiovascular system, we first remove from the 0D model Equation (4.31a), (4.31b), (4.32a), (4.32b), (4.33a), (4.33b) and we replace them with the 3D model of the LH. The coupling between che 3D and 0D models consists of the enforcement of the continuity of flowrates and pressures on the "artificially chopped" boundaries, i.e. inlet and outlet sections of the 3D domain: Γ^{PVein_i}, $i = 1, \ldots, 5$ and Γ_t^{AA}. Thus, by denoting with Q_{IN}, Q_{OUT} and p_{IN}, p_{OUT} the flowrates and averaged pressure at the inlet and outlet sections of our computational domain, the continuity among the 3D

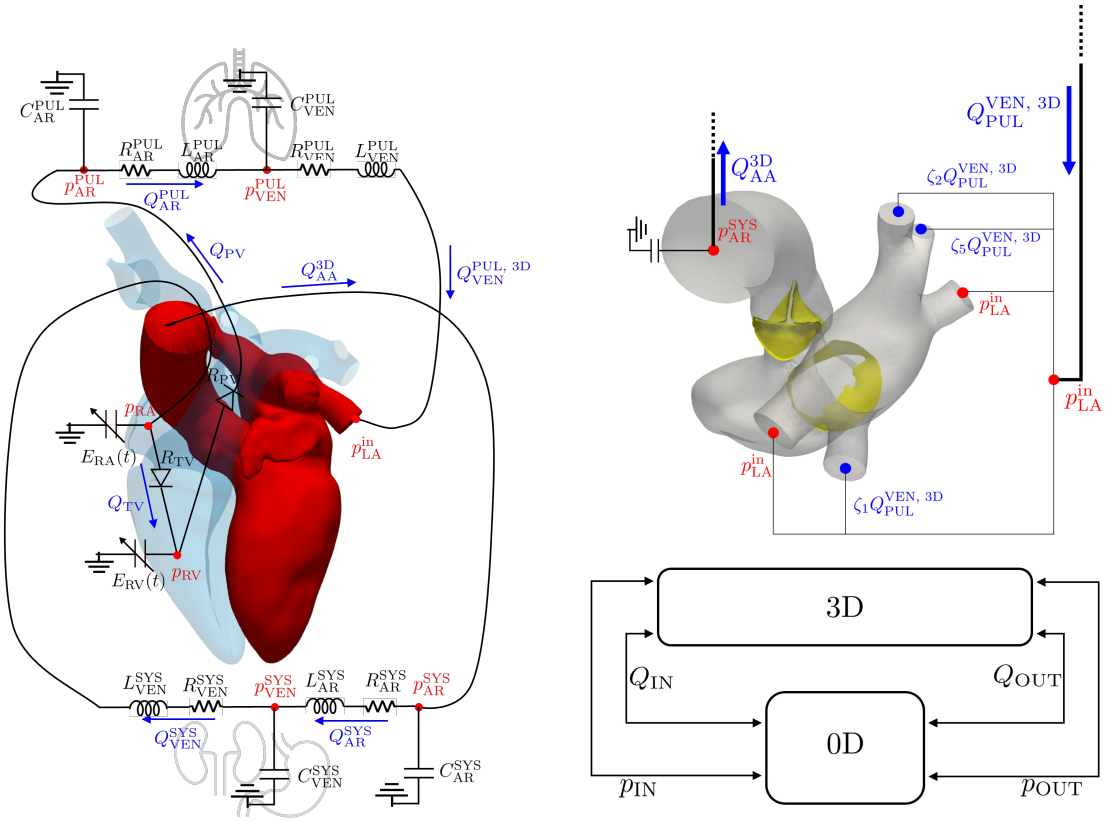

(a) 3D-0D coupling

(b) zoom on LH and continuity of flowrates and pressures among 3D and 0D models.

Figure 6.10: 3D-0D coupling among the 3D fluid-dynamics model of the LH and the 0D circulation model of the whole cardiovascular system with a zoom on the LH and a scheme explaining the adopted coupled strategy.

and 0D models read:

$$Q_{IN}^{0D}(t) = Q_{IN}^{3D}(t), \tag{6.19a}$$
$$Q_{OUT}^{0D}(t) = Q_{OUT}^{3D}(t), \tag{6.19b}$$
$$p_{IN}^{0D}(t) = p_{IN}^{3D}(t), \tag{6.19c}$$
$$p_{OUT}^{0D}(t) = p_{OUT}^{3D}(t). \tag{6.19d}$$

Specifically, referring to Figure 6.10, the arterial systemic pressure $p_{AR}^{SYS}(t)$, appearing in Equation (4.31e) and (4.31i) acts as the outlet pressure used in the Neumann BC on the AA outlet section Γ_t^{AA} in Equation (6.3), formerly denoted as $p_{OUT}(t)$. The outlet

BC hence becomes:

$$\boldsymbol{\sigma}(\boldsymbol{u},p)\boldsymbol{n} = -p_{\mathrm{AR}}^{\mathrm{SYS}}\boldsymbol{n}, \qquad \text{on } \Gamma_t^{\mathrm{AA}} \times (0,T_f). \tag{6.20}$$

Conversely, the LA pressure $p_{\mathrm{LA}}(t)$ appearing in Equation (4.31l) represents the pressure downwind the "PUL VEN" RLC system, i.e. the one to be prescribed on the inlet sections of our 3D domain. We rename the latter as $p_{\mathrm{LA}}^{\mathrm{in}}(t)$ and it replaces $p_{\mathrm{IN}}(t)$ in the inlet BC (6.2):

$$\boldsymbol{\sigma}(\boldsymbol{u},p)\boldsymbol{n} = -p_{\mathrm{LA}}^{\mathrm{in}}\boldsymbol{n}_i, \qquad \text{on } \Gamma^{\mathrm{PVein}_i} \times (0,T_f), \quad i=3,4. \tag{6.21}$$

The flowrate $Q_{\mathrm{VEN}}^{\mathrm{PUL}}(t)$, appearing in Equation (4.31h) and (4.31l), is the inlet flowrate $Q_{\mathrm{IN}}(t)$ used as inlet BC for the 3D problem (see Equation (6.1)). Since in all the parts of the heartbeat mass conservation must be ensured, the inlet flowrate should match the volume time derivative of LA and LV in diastole (when the MV is open) and of the sole LA in systole (MV closed):

$$Q_{\mathrm{IN}}(t) = \begin{cases} -\dfrac{\mathrm{d}\left(V_{\mathrm{LV}}(t)+V_{\mathrm{LA}}(t)\right)}{\mathrm{d}t} & \text{if MV is open,} \\ -\dfrac{\mathrm{d}V_{\mathrm{LA}}(t)}{\mathrm{d}t} & \text{if MV is closed.} \end{cases} \tag{6.22}$$

Since $Q_{\mathrm{IN}}(t)$ is computed in the 3D simulation and represents the flowrate in the pulmonary veins, we replace it with $Q_{\mathrm{VEN}}^{\mathrm{PUL,\ 3D}}(t)$ and the inlet BC becomes:

$$\boldsymbol{u} = 2Q_{\mathrm{VEN}}^{\mathrm{PUL,\ 3D}}\frac{\zeta_i}{|\Gamma^{\mathrm{PVein}_i}|}\left(1-\frac{r^2}{R_i^2}\right)\boldsymbol{n}_i, \qquad \text{on } \Gamma^{\mathrm{PVein}_i} \times (0,T_f), \quad i=1,2,5. \tag{6.23}$$

In an analogous fashion, the flowrate $Q_{\mathrm{AV}}(t)$ in the 0D model represents in our 3D model the outlet flowrate at the AA section Γ_t^{AA}. Hence, we replaced it as $Q_{\mathrm{AA}}^{\mathrm{3D}}(t)$ and we compute it – exploiting mass balance – as

$$Q_{\mathrm{AA}}^{\mathrm{3D}}(t) = \begin{cases} -\dfrac{\mathrm{d}V_{\mathrm{AA}}(t)}{\mathrm{d}t} & \text{if AV is closed,} \\ -\dfrac{\mathrm{d}\left(V_{\mathrm{LV}}(t)+V_{\mathrm{AA}}(t)\right)}{\mathrm{d}t} & \text{if AV is open.} \end{cases} \tag{6.24}$$

Equation (6.22) and (6.24) are valid for healthy valves motion. In Section 6.6.2, we consider the case of a regurgitant MV and the flowrates definitions will properly consider the amount of regurgitant flow. In particular, by considering the valves characteristic times introduced in Section 6.3, Equation (6.22) and (6.24) are conveniently rewritten

as:

$$Q_{\mathrm{VEN}}^{\mathrm{PUL,\ 3D}}(t) = \begin{cases} -\dfrac{\mathrm{d}\left(V_{\mathrm{LV}}(t) + V_{\mathrm{LA}}(t)\right)}{\mathrm{d}t} & \text{if } t < \tau_{\mathrm{MV}}^{\emptyset} \text{ or } t \geq \tau_{\mathrm{MV}}^{0}, \\ -\dfrac{\mathrm{d}V_{\mathrm{LA}}(t)}{\mathrm{d}t} & \text{if } \tau_{\mathrm{MV}}^{\emptyset} \leq t < \tau_{\mathrm{MV}}^{0}, \end{cases} \tag{6.25}$$

$$Q_{\mathrm{AA}}^{\mathrm{3D}}(t) = \begin{cases} -\dfrac{\mathrm{d}V_{\mathrm{AA}}(t)}{\mathrm{d}t} & \text{if } t \leq \tau_{\mathrm{AV}}^{0} \text{ or } t > \tau_{\mathrm{AV}}^{\emptyset}, \\ -\dfrac{\mathrm{d}\left(V_{\mathrm{LV}}(t) + V_{\mathrm{AA}}(t)\right)}{\mathrm{d}t} & \text{if } \tau_{\mathrm{AV}}^{0} < t \leq \tau_{\mathrm{AV}}^{\emptyset}. \end{cases} \tag{6.26}$$

Finally, note that, in Equation (4.31l), the variable $Q_{\mathrm{VEN}}^{\mathrm{PUL}}(t)$ can be computed from the 3D model using Equation (6.22), while $p_{\mathrm{LA}}(t)$ is replaced by $p_{\mathrm{LA}}^{\mathrm{in}}(t)$ and it is an unknown. Hence, we can solve (4.31l) in terms of the pressure to be prescribed at the inlet sections $p_{\mathrm{LA}}^{\mathrm{in}}(t)$ (see Equation (6.28a)). The reduced 0D model arising from these observations is the following: for any $t \in (0, T_f)$:

$$\frac{\mathrm{d}V_{\mathrm{RA}}(t)}{\mathrm{d}t} = Q_{\mathrm{VEN}}^{\mathrm{SYS}}(t) - Q_{\mathrm{TV}}(t), \tag{6.27a}$$

$$\frac{\mathrm{d}V_{\mathrm{RV}}(t)}{\mathrm{d}t} = Q_{\mathrm{TV}}(t) - Q_{\mathrm{PV}}(t), \tag{6.27b}$$

$$\frac{\mathrm{d}p_{\mathrm{AR}}^{\mathrm{SYS}}(t)}{\mathrm{d}t} = \frac{1}{C_{\mathrm{AR}}^{\mathrm{SYS}}}\left(Q_{\mathrm{AA}}^{\mathrm{3D}}(t) - Q_{\mathrm{AR}}^{\mathrm{SYS}}(t)\right), \tag{6.27c}$$

$$\frac{\mathrm{d}p_{\mathrm{VEN}}^{\mathrm{SYS}}(t)}{\mathrm{d}t} = \frac{1}{C_{\mathrm{VEN}}^{\mathrm{SYS}}}\left(Q_{\mathrm{AR}}^{\mathrm{SYS}}(t) - Q_{\mathrm{VEN}}^{\mathrm{SYS}}(t)\right), \tag{6.27d}$$

$$\frac{\mathrm{d}p_{\mathrm{AR}}^{\mathrm{PUL}}(t)}{\mathrm{d}t} = \frac{1}{C_{\mathrm{AR}}^{\mathrm{PUL}}}\left(Q_{\mathrm{PV}}(t) - Q_{\mathrm{AR}}^{\mathrm{PUL}}(t)\right), \tag{6.27e}$$

$$\frac{\mathrm{d}p_{\mathrm{VEN}}^{\mathrm{PUL}}(t)}{\mathrm{d}t} = \frac{1}{C_{\mathrm{VEN}}^{\mathrm{PUL}}}\left(Q_{\mathrm{AR}}^{\mathrm{PUL}}(t) - Q_{\mathrm{PUL}}^{\mathrm{VEN,\ 3D}}(t)\right), \tag{6.27f}$$

$$\frac{\mathrm{d}Q_{\mathrm{AR}}^{\mathrm{SYS}}(t)}{\mathrm{d}t} = \frac{R_{\mathrm{AR}}^{\mathrm{SYS}}}{L_{\mathrm{AR}}^{\mathrm{SYS}}}\left(-Q_{\mathrm{AR}}^{\mathrm{SYS}}(t) - \frac{p_{\mathrm{VEN}}^{\mathrm{SYS}}(t) - p_{\mathrm{AR}}^{\mathrm{SYS}}(t)}{R_{\mathrm{AR}}^{\mathrm{SYS}}}\right), \tag{6.27g}$$

$$\frac{\mathrm{d}Q_{\mathrm{VEN}}^{\mathrm{SYS}}(t)}{\mathrm{d}t} = \frac{R_{\mathrm{VEN}}^{\mathrm{SYS}}}{L_{\mathrm{VEN}}^{\mathrm{SYS}}}\left(-Q_{\mathrm{VEN}}^{\mathrm{SYS}}(t) - \frac{p_{\mathrm{RA}}(t) - p_{\mathrm{VEN}}^{\mathrm{SYS}}(t)}{R_{\mathrm{VEN}}^{\mathrm{SYS}}}\right), \tag{6.27h}$$

$$\frac{\mathrm{d}Q_{\mathrm{AR}}^{\mathrm{PUL}}(t)}{\mathrm{d}t} = \frac{R_{\mathrm{AR}}^{\mathrm{PUL}}}{L_{\mathrm{AR}}^{\mathrm{PUL}}}\left(-Q_{\mathrm{AR}}^{\mathrm{PUL}}(t) - \frac{p_{\mathrm{VEN}}^{\mathrm{PUL}}(t) - p_{\mathrm{AR}}^{\mathrm{PUL}}(t)}{R_{\mathrm{AR}}^{\mathrm{PUL}}}\right), \tag{6.27i}$$

being

$$p_{\mathrm{LA}}^{\mathrm{in}}(t) = p_{\mathrm{VEN}}^{\mathrm{PUL}}(t) - R_{\mathrm{VEN}}^{\mathrm{PUL}} Q_{\mathrm{VEN}}^{\mathrm{PUL,\ 3D}}(t) - L_{\mathrm{VEN}}^{\mathrm{PUL}} \frac{\mathrm{d}Q_{\mathrm{VEN}}^{\mathrm{PUL,\ 3D}}(t)}{\mathrm{d}t}, \tag{6.28a}$$

$$p_{\mathrm{RA}}(t) = p_{\mathrm{EX}}(t) + E_{\mathrm{RA}}(t)\left(V_{\mathrm{RA}}(t) - V_{0,\mathrm{RA}}\right), \tag{6.28b}$$

$$p_{\mathrm{RV}}(t) = p_{\mathrm{EX}}(t) + E_{\mathrm{RV}}(t)\left(V_{\mathrm{RV}}(t) - V_{0,\mathrm{RV}}\right), \tag{6.28c}$$

$$Q_{\mathrm{TV}}(t) = \frac{p_{\mathrm{RA}}(t) - p_{\mathrm{RV}}(t)}{R_{\mathrm{TV}}(p_{\mathrm{RA}}(t), p_{\mathrm{RV}}(t))}, \tag{6.28d}$$

$$Q_{\mathrm{PV}}(t) = \frac{p_{\mathrm{RV}}(t) - p_{\mathrm{AR}}^{\mathrm{PUL}}(t)}{R_{\mathrm{PV}}(p_{\mathrm{RV}}(t), p_{\mathrm{AR}}^{\mathrm{PUL}}(t))}. \tag{6.28e}$$

We gather the unknown variables of Equations (6.27) in a vector $\boldsymbol{c}(t) = (V_{\mathrm{RA}}(t),\, V_{\mathrm{RV}}(t),\, p_{\mathrm{AR}}^{\mathrm{SYS}}(t),\, p_{\mathrm{VEN}}^{\mathrm{SYS}}(t),\, p_{\mathrm{AR}}^{\mathrm{PUL}}(t),\, p_{\mathrm{VEN}}^{\mathrm{PUL}}(t),\, Q_{\mathrm{AR}}^{\mathrm{SYS}}(t),\, Q_{\mathrm{VEN}}^{\mathrm{SYS}}(t),\, Q_{\mathrm{AR}}^{\mathrm{PUL}}(t))^T$ and the left-hand side of Equation (6.28) in a vector $\widetilde{\boldsymbol{c}}(t) = (p_{\mathrm{LA}}^{\mathrm{in}}(t),\, p_{\mathrm{RA}}(t),\, p_{\mathrm{RV}}(t),\, Q_{\mathrm{TV}}(t),\, Q_{\mathrm{PV}}(t))^T$. We then collect the right-hand sides of Equation (6.27) and (6.28) respectively in the vectors $\boldsymbol{r}(t, \boldsymbol{c}(t), \widetilde{\boldsymbol{c}}(t))$ and $\widetilde{\boldsymbol{r}}(t, \boldsymbol{c}(t))$. Hence, the reduced 0D model, enriched with suitable initial conditions, is expressed in a compact form as

$$\frac{\mathrm{d}\boldsymbol{c}(t)}{\mathrm{d}t} = \boldsymbol{r}(t, \boldsymbol{c}(t), \widetilde{\boldsymbol{c}}(t)) \qquad t \in (0, T_f), \tag{6.29a}$$

$$\widetilde{\boldsymbol{c}}(t) = \widetilde{\boldsymbol{r}}(t, \boldsymbol{c}(t)) \qquad t \in (0, T_f), \tag{6.29b}$$

$$\boldsymbol{c}(0) = \boldsymbol{c}_0. \tag{6.29c}$$

Finally, a graphical representation of the 3D-0D coupling scheme is given in Figure 6.10 and the overall set of 3D-0D coupled equations is expressed as

$$\begin{aligned}
&\rho\frac{\widehat{\partial}\boldsymbol{u}}{\widehat{\partial t}} + \rho\left(\left(\boldsymbol{u} - \boldsymbol{u}^{\mathrm{ALE}}\right)\cdot\nabla\right)\boldsymbol{u} \\
&-\nabla\cdot\boldsymbol{\sigma}(\boldsymbol{u}, p) \\
&+\frac{R_{\mathrm{AV}}}{\varepsilon_{\mathrm{AV}}}\delta_{\Sigma_{\mathrm{AV}},\varepsilon_{\mathrm{AV}}}\boldsymbol{u} + \frac{R_{\mathrm{MV}}}{\varepsilon_{\mathrm{MV}}}\delta_{\Sigma_{\mathrm{MV}},\varepsilon_{\mathrm{MV}}}\boldsymbol{u} = \boldsymbol{0} && \text{in } \Omega_t \times (0, T_f), && (6.30a)\\
&\nabla\cdot\boldsymbol{u} = 0 && \text{in } \Omega_t \times (0, T_f), && (6.30b)\\
&\boldsymbol{u} = 2Q_{\mathrm{VEN}}^{\mathrm{PUL,\ 3D}}\frac{\zeta_i}{|\Gamma^{\mathrm{PVein}_i}|}\left(1 - \frac{r^2}{R_i^2}\right)\boldsymbol{n}_i && \text{on } \Gamma^{\mathrm{PVein}_i} \times (0, T_f),\ i = 1, 2, 5, && (6.30c)\\
&\boldsymbol{\sigma}(\boldsymbol{u}, p)\boldsymbol{n} = -p_{\mathrm{LA}}^{\mathrm{in}}\boldsymbol{n}_i && \text{on } \Gamma^{\mathrm{PVein}_i} \times (0, T_f),\ i = 3, 4, && (6.30d)\\
&\boldsymbol{\sigma}(\boldsymbol{u}, p)\boldsymbol{n} = -p_{\mathrm{AR}}^{\mathrm{SYS}}\boldsymbol{n} && \text{on } \Gamma_t^{\mathrm{AA}} \times (0, T_f), && (6.30e)\\
&\boldsymbol{u} = \boldsymbol{u}_\Gamma = \partial_t\boldsymbol{d}_\Gamma && \text{on } \Gamma_t^{\mathrm{w}} \times (0, T_f), && (6.30f)\\
&\boldsymbol{u} = \boldsymbol{0} && \text{in } \Omega_0 \times \{0\}, && (6.30g)\\
&\boldsymbol{x} = \widehat{\boldsymbol{x}} + \widehat{\boldsymbol{d}} = \mathcal{A}_t(\widehat{\boldsymbol{x}}) && && (6.30h)\\
&-\nabla\cdot\left(\boldsymbol{K}\nabla\widehat{\boldsymbol{d}}\right) = \boldsymbol{0} && \text{in } \widehat{\Omega}, && (6.30i)\\
&\widehat{\boldsymbol{d}} = \widehat{\boldsymbol{d}}_\Gamma && \text{on } \widehat{\Gamma}, && (6.30j)\\
&\boldsymbol{u}^{\mathrm{ALE}} = \left(\frac{\partial\widehat{\boldsymbol{d}}}{\partial t}\right)\circ\widehat{\boldsymbol{d}}^{-1}, && && (6.30k)
\end{aligned}$$

Algorithm 6.3 Geometric problem

Input $\widehat{\boldsymbol{d}}_{\Gamma_n}, \widehat{\Omega}, \widehat{\mathcal{T}}^h$
Output $\boldsymbol{u}_n^{\mathrm{ALE},h}$, Ω_n, $\mathcal{T}_n^h$

Solve lifting problem in Equation (4.28) $\rightarrow \widehat{\boldsymbol{d}}_n^h$
Compute ALE velocity through Equation (4.29) $\rightarrow \widehat{\boldsymbol{u}}_n^{\mathrm{ALE},h} \rightarrow \boldsymbol{u}_n^{\mathrm{ALE},h}$
Move the domain and the mesh through Equation (4.30) $\rightarrow \Omega_n$, $\mathcal{T}_n^h$

Algorithm 6.4 Opening and closing times of the valves

Input $\delta\overline{p}_n^{\mathrm{MV},h}$, $\delta\overline{p}_n^{\mathrm{AV},h}$, $\dot{V}_{\mathrm{LV},n}$
Output $\boldsymbol{\tau} = \left(\tau_{\mathrm{MV}}^0, \tau_{\mathrm{MV}}^{\emptyset}, \tau_{\mathrm{AV}}^0, \tau_{\mathrm{AV}}^{\emptyset}\right)^T$

if $t_n = jT_{\mathrm{HB}}$, $j = 0, 1, 2, \ldots$ **then**
  $\boldsymbol{\tau} = \boldsymbol{0}$
end if
if $\delta\overline{p}_{n-1}^{\mathrm{MV},h} \leq 0$ and $\delta\overline{p}_n^{\mathrm{MV},h} > 0$ **then**
  $\tau_{\mathrm{MV}}^0 = t_n$
else if $\dot{V}_{\mathrm{LV},n-1} \geq 0$ and $\dot{V}_{\mathrm{LV},n} < 0$ **then**
  $\tau_{\mathrm{MV}}^{\emptyset} = t_n$
end if
if $\delta\overline{p}_{n-1}^{\mathrm{AV},h} \leq 0$ and $\delta\overline{p}_n^{\mathrm{AV},h} > 0$ **then**
  $\tau_{\mathrm{AV}}^0 = t_n$
else if $\dot{V}_{\mathrm{LV},n-1} \leq 0$ and $\dot{V}_{\mathrm{LV},n} > 0$ **then**
  $\tau_{\mathrm{AV}}^{\emptyset} = t_n$
end if

$$\frac{\mathrm{d}\boldsymbol{c}(t)}{\mathrm{d}t} = \boldsymbol{r}(t, \boldsymbol{c}(t), \widetilde{\boldsymbol{c}}(t)) \qquad \text{for } t \in (0, T_f), \tag{6.30l}$$

$$\widetilde{\boldsymbol{c}}(t) = \widetilde{\boldsymbol{r}}(t, \boldsymbol{c}(t)) \qquad \text{for } t \in (0, T_f), \tag{6.30m}$$

$$\boldsymbol{c} = \boldsymbol{c}_0 \qquad \text{for } t = 0. \tag{6.30n}$$

6.5. Numerical schemes

In this section we present the numerical strategies to solve the multiscale problem (6.30).

We discretize the geometric problem as reported in Section 4.3.2 and in Algorithm 6.3 we summarize the the main steps. We denote the discretization of the geometric

Algorithm 6.5 Valves' leaflets position

Input $\widehat{\boldsymbol{x}}, \widehat{\Sigma}_{\mathrm{MV}}, \widehat{\Sigma}_{\mathrm{AV}}, \widehat{\boldsymbol{d}}_{\Sigma_{\mathrm{MV}}}, \widehat{\boldsymbol{d}}_{\Sigma_{\mathrm{AV}}}, \boldsymbol{\tau}, \Delta\tau^0_{\mathrm{MV}}, \Delta\tau^{\emptyset}_{\mathrm{MV}}, \Delta\tau^0_{\mathrm{AV}}, \Delta\tau^{\emptyset}_{\mathrm{AV}}$
Output $\Sigma_{\mathrm{MV},n}, \Sigma_{\mathrm{AV},n}$
$\eta_{\mathrm{MV},n}, \eta_{\mathrm{AV},n} \in \mathbb{R}$

if $t_n < \tau^0_{\mathrm{MV}}$ **then**
$\eta_{\mathrm{MV},n} = 0$
else if $\tau^0_{\mathrm{MV}} \le t_n < \tau^0_{\mathrm{MV}} + \Delta\tau^0_{\mathrm{MV}}$ **then**
$\eta_{\mathrm{MV},n} = \dfrac{t_n - \tau^0_{\mathrm{MV}}}{\Delta\tau^0_{\mathrm{MV}}}$
else if $\tau^0_{\mathrm{MV}} + \Delta\tau^0_{\mathrm{MV}} \le t_n < \tau^{\emptyset}_{\mathrm{MV}}$ **then**
$\eta_{\mathrm{MV},n} = 1$
else if $\tau^{\emptyset}_{\mathrm{MV}} \le t_n < \tau^{\emptyset}_{\mathrm{MV}} + \Delta\tau^{\emptyset}_{\mathrm{MV}}$ **then**
$\eta_{\mathrm{MV},n} = -\dfrac{t_n - \tau^{\emptyset}_{\mathrm{MV}}}{\Delta\tau^{\emptyset}_{\mathrm{MV}}}$
else
$\eta_{\mathrm{MV},n} = 0$
end if

if $t_n < \tau^{\emptyset}_{\mathrm{AV}}$ **then**
$\eta_{\mathrm{AV},n} = 0$
else if $\tau^{\emptyset}_{\mathrm{AV}} \le t_n < \tau^{\emptyset}_{\mathrm{AV}} + \Delta\tau^{\emptyset}_{\mathrm{AV}}$ **then**
$\eta_{\mathrm{AV},n} = \dfrac{t_n - \tau^{\emptyset}_{\mathrm{AV}}}{\Delta\tau^{\emptyset}_{\mathrm{AV}}}$
else if $\tau^{\emptyset}_{\mathrm{AV}} + \Delta\tau^{\emptyset}_{\mathrm{AV}} \le t_n < \tau^0_{\mathrm{AV}}$ **then**
$\eta_{\mathrm{AV},n} = 1$
else if $\tau^0_{\mathrm{AV}} \le t_n < \tau^0_{\mathrm{AV}} + \Delta\tau^0_{\mathrm{AV}}$ **then**
$\eta_{\mathrm{AV},n} = -\dfrac{t_n - \tau^0_{\mathrm{AV}}}{\Delta\tau^0_{\mathrm{AV}}}$
else
$\eta_{\mathrm{AV},n} = 0$
end if

$$\Sigma_{\mathrm{MV},n} = \left\{ \widehat{\boldsymbol{x}} + \eta_{\mathrm{MV},n}\widehat{\boldsymbol{d}}_{\Sigma_{\mathrm{MV}}} \ : \ \varphi_{\mathrm{MV}}(\widehat{\boldsymbol{x}} + \eta_{\mathrm{MV},n}\widehat{\boldsymbol{d}}_{\Sigma_{\mathrm{MV}}}) = 0 \right\}$$
$$\Sigma_{\mathrm{AV},n} = \left\{ \widehat{\boldsymbol{x}} + \eta_{\mathrm{AV},n}\widehat{\boldsymbol{d}}_{\Sigma_{\mathrm{AV}}} \ : \ \varphi_{\mathrm{AV}}(\widehat{\boldsymbol{x}} + \eta_{\mathrm{AV},n}\widehat{\boldsymbol{d}}_{\Sigma_{\mathrm{AV}}}) = 0 \right\}$$

problem in short as

$$\left(\boldsymbol{u}_n^{\mathrm{ALE},h},\, \Omega_n,\, \mathcal{T}_n^h\right)^T = \textsc{Geometric}\left(\widehat{\boldsymbol{d}}_{\Gamma_n}, \widehat{\Omega}, \widehat{\mathcal{T}}^h\right). \tag{6.31}$$

The geometric problem – taking as input the prescribed displacement, the domain and the mesh in its reference configuration – computes the ALE fluid velocity, the domain and the mesh at the current time step.

6.5.1. Valves: algorithms to update opening and closing times and leaflets position

In the following, we show the algorithms adopted to find the opening and closing times of the valves and to determine the valves' leaflets position based on the displacements $\widehat{\boldsymbol{d}}_{\Sigma_{\mathrm{MV}}}$ and $\widehat{\boldsymbol{d}}_{\Sigma_{\mathrm{AV}}}$ introduced in Section 6.3 and the opening and closing times.

In Algorithm 6.4 the opening and closing times of the valves are obtained by checking whether the pressure jump across an immersed surface changes signs (valve opens) and if a condition of reverse flow across the valve is detected (valve closes). At the beginning of each heart cycle of period T_{HB}, the opening and closing times are set to

Algorithm 6.6 Compute volumes and flowrates

Input $\Omega_n, \mathcal{T}_n^h, \boldsymbol{\tau}$
Output $Q_{\mathrm{VEN},n}^{\mathrm{PUL,\,3D}}, Q_{\mathrm{AA},n}^{\mathrm{3D}}, \dot{V}_{\mathrm{LV},n}$

Compute volumes: $V_{\mathrm{LV},n} = \int_{\Omega_n^{\mathrm{LV}}} d\boldsymbol{x}, \quad V_{\mathrm{LA},n} = \int_{\Omega_n^{\mathrm{LA}}} d\boldsymbol{x}, \quad V_{\mathrm{AA},n} = \int_{\Omega_n^{\mathrm{AA}}} d\boldsymbol{x}$
Compute flowrates:

$$Q_{\mathrm{VEN},n}^{\mathrm{PUL,\,3D}} = \begin{cases} -\dfrac{(V_{\mathrm{LV},n} + V_{\mathrm{LA},n}) - (V_{\mathrm{LV},n-1} + V_{\mathrm{LA},n-1})}{\Delta t} & \text{if } t^n < \tau_{\mathrm{MV}}^{\emptyset} \text{ or } t^n \geq \tau_{\mathrm{MV}}^{0} \\ -\dfrac{V_{\mathrm{LA},n} - V_{\mathrm{LA},n-1}}{\Delta t} & \text{if } \tau_{\mathrm{MV}}^{\emptyset} \leq t^n < \tau_{\mathrm{MV}}^{0}. \end{cases}$$

$$Q_{\mathrm{AA},n}^{\mathrm{3D}} = \begin{cases} -\dfrac{V_{\mathrm{AA},n} - V_{\mathrm{AA},n-1}}{\Delta t} & \text{if } t^n < \tau_{\mathrm{AV}}^{0} \text{ or } t^n \geq \tau_{\mathrm{AV}}^{\emptyset} \\ -\dfrac{(V_{\mathrm{LV},n} + V_{\mathrm{AA},n}) - (V_{\mathrm{LV},n-1} - V_{\mathrm{AA},n-1})}{\Delta t} & \text{if } \tau_{\mathrm{AV}}^{0} \leq t^n < \tau_{\mathrm{AV}}^{\emptyset}. \end{cases}$$

Compute LV volume derivative: $\dot{V}_{\mathrm{LV},n} = \frac{V_{\mathrm{LV},n} - V_{\mathrm{LV},n-1}}{\Delta t}$

zero. The algorithm is invoked at every time step of the numerical simulation as

$$\boldsymbol{\tau} = \textsc{ValvesOpeningClosingTimes}(\delta\overline{p}_n^{\mathrm{MV},h},\ \delta\overline{p}_n^{\mathrm{AV},h}, \dot{V}_{\mathrm{LV},n}). \tag{6.32}$$

In Algorithm 6.5, we report the procedure to determine the position of the valves' leaflets $\Sigma_{\mathrm{MV},n}, \Sigma_{\mathrm{AV},n}$ on the basis of the heartbeat phases (vector $\boldsymbol{\tau}$ determined in Algorithm 6.4), the space-dependent displacement fields $\widehat{\boldsymbol{d}}_{\Sigma_{\mathrm{MV}}}, \widehat{\boldsymbol{d}}_{\Sigma_{\mathrm{AV}}}$ introduced in Section 6.3. In the algorithm we introduce the scalars $\eta_{\mathrm{MV},n}, \eta_{\mathrm{AV},n} \in \mathbb{R}$ to define fully and partially applied displacement fields. Since our simulation starts at the end-diastole time, the valves reference configuration $\widehat{\Sigma}_{\mathrm{MV}}, \widehat{\Sigma}_{\mathrm{AV}}$ corresponds to the fully opened configuration for MV and the fully closed one for the AV. During the opening and closing stages, the displacement increases (decreases) linearly. We will refer to this algorithm as

$$(\Sigma_{\mathrm{MV},n}, \Sigma_{\mathrm{AV},n})^T = \textsc{ValvesLeafletsPosition}(\widehat{\boldsymbol{x}}, \widehat{\Sigma}_{\mathrm{MV}}, \widehat{\Sigma}_{\mathrm{AV}}, \widehat{\boldsymbol{d}}_{\Sigma_{\mathrm{MV}}}, \widehat{\boldsymbol{d}}_{\Sigma_{\mathrm{AV}}}, \tag{6.33}$$

$$\boldsymbol{\tau}, \Delta\tau_{\mathrm{MV}}^{0}, \Delta\tau_{\mathrm{MV}}^{\emptyset}, \Delta\tau_{\mathrm{AV}}^{0}, \Delta\tau_{\mathrm{AV}}^{\emptyset}). \tag{6.34}$$

6.5.2. A segregated scheme for the 3D-0D coupling

In Algorithm 6.6, we show how we numerically compute $Q_{\mathrm{VEN},n}^{\mathrm{PUL,\,3D}}, Q_{\mathrm{AA},n}^{\mathrm{3D}}$ and $\dot{V}_{\mathrm{LV},n}$ given Ω_n, $\mathcal{T}_n^h$ and the valves status described by $\boldsymbol{\tau}$. We denote it in short as:

$$\left(Q_{\mathrm{VEN},n}^{\mathrm{PUL,\,3D}}, Q_{\mathrm{AA},n}^{\mathrm{3D}}, \dot{V}_{\mathrm{LV},n}\right)^T = \textsc{Flowrates}\left(\Omega_n,\ \mathcal{T}_n^h, \boldsymbol{\tau}\right). \tag{6.35}$$

Algorithm 6.7 Fluid dynamics problem

Input $\boldsymbol{u}_n^{\mathrm{ALE},h}, p_{\mathrm{LA},n}^{\mathrm{in}}, Q_{\mathrm{VEN},n}^{\mathrm{PUL,\,3D}}, p_{\mathrm{AR},n}^{\mathrm{SYS}}, \boldsymbol{d}_{\Gamma_n}; R_{\mathrm{MV}},\ R_{\mathrm{AV}},\ \varepsilon_{\mathrm{MV}},\ \varepsilon_{\mathrm{AV}}, \Sigma_{\mathrm{MV},n}, \Sigma_{\mathrm{AV},n};\ \Omega_n,\ \mathcal{T}_n^h$
Output $\boldsymbol{u}_n^h,\ p_n^h,\ \delta\overline{p}_n^{\mathrm{MV},h},\ \delta\overline{p}_n^{\mathrm{AV},h}$

Solve NS-ALE-RIIS equations with VMS-LES modeling in Equation (2.43):

$$\begin{aligned}\mathcal{P}_{\text{NS-ALE-RIIS-VMS-LES}}(&\boldsymbol{u}_n^h, p_n^h; \boldsymbol{u}_n^{\mathrm{ALE},h}; p_{\mathrm{LA},n}^{\mathrm{in}}, Q_{\mathrm{VEN},n}^{\mathrm{PUL,\,3D}}, p_{\mathrm{AR},n}^{\mathrm{SYS}}, \boldsymbol{d}_{\Gamma_n};\\ &\Sigma_{\mathrm{MV},n}, \Sigma_{\mathrm{AV},n},\ R_{\mathrm{MV}},\ R_{\mathrm{AV}},\ \varepsilon_{\mathrm{MV}},\ \varepsilon_{\mathrm{AV}};\\ &\Omega_n,\ \mathcal{T}_n^h) = 0\end{aligned}$$

Compute pressure jumps as in Equation (6.17) $\rightarrow \delta\overline{p}_n^{\mathrm{MV},h},\ \delta\overline{p}_n^{\mathrm{AV},h}$

Algorithm 6.8 Segregated scheme for the 3D-0D coupled problem

Initialize $\boldsymbol{u}_0^h,\ \boldsymbol{c}_0, \delta\overline{p}_0^{\mathrm{MV},h},\ \delta\overline{p}_0^{\mathrm{AV},h},\ \dot{V}_0^{\mathrm{LV}}, n = 1$
Set $R_{\mathrm{MV}},\ R_{\mathrm{AV}},\ \varepsilon_{\mathrm{MV}},\ \varepsilon_{\mathrm{AV}},\ \Delta\tau_{\mathrm{MV}}^0,\ \Delta\tau_{\mathrm{MV}}^{\emptyset},\ \Delta\tau_{\mathrm{AV}}^0,\ \Delta\tau_{\mathrm{AV}}^{\emptyset}$
Compute $\widehat{\boldsymbol{d}}_{\Gamma_n}$ for $n = 0, \ldots, N_t$
Compute $\widehat{\boldsymbol{d}}_{\Sigma_{\mathrm{MV}}}, \widehat{\boldsymbol{d}}_{\Sigma_{\mathrm{AV}}}$
while $n \leq N_t$ **do**

$$\left(\boldsymbol{u}_n^{\mathrm{ALE},h},\ \Omega_n,\ \mathcal{T}_n^h\right)^T = \textsc{Geometric}\left(\widehat{\boldsymbol{d}}_{\Gamma_n}, \widehat{\Omega}, \widehat{\mathcal{T}}^h\right)$$

$$\boldsymbol{\tau} = \textsc{ValvesOpeningClosingTimes}(\delta\overline{p}_n^{\mathrm{MV},h},\ \delta\overline{p}_n^{\mathrm{AV},h}, \dot{V}_{\mathrm{LV},n})$$

$$\left(Q_{\mathrm{VEN},n}^{\mathrm{PUL,\,3D}}, Q_{\mathrm{AA},n}^{\mathrm{3D}}, \dot{V}_{\mathrm{LV},n}\right)^T = \textsc{Flowrates}\left(\Omega_n,\ \mathcal{T}_n^h, \boldsymbol{\tau}\right)$$

$$\begin{aligned}(\Sigma_{\mathrm{MV},n}, \Sigma_{\mathrm{AV},n})^T = \textsc{ValvesLeafletPosition}(&\widehat{\boldsymbol{x}}, \widehat{\Sigma}_{\mathrm{MV}}, \widehat{\Sigma}_{\mathrm{AV}}, \widehat{\boldsymbol{d}}_{\Sigma_{\mathrm{MV}}}, \widehat{\boldsymbol{d}}_{\Sigma_{\mathrm{AV}}},\\ &\boldsymbol{\tau}, \Delta\tau_{\mathrm{MV}}^0, \Delta\tau_{\mathrm{MV}}^{\emptyset}, \Delta\tau_{\mathrm{AV}}^0, \Delta\tau_{\mathrm{AV}}^{\emptyset})\end{aligned}$$

$$(\boldsymbol{c}_n, \widetilde{\boldsymbol{c}}_n)^T = \textsc{Circulation}(Q_{\mathrm{VEN},n}^{\mathrm{PUL,\,3D}}, Q_{\mathrm{AA},n}^{\mathrm{3D}})$$

$$\begin{aligned}\left(\boldsymbol{u}_n^h,\ p_n^h,\ \delta\overline{p}_n^{\mathrm{MV},h},\ \delta\overline{p}_n^{\mathrm{AV},h}\right)^T = \textsc{FluidDynamics}(&\boldsymbol{u}_n^{\mathrm{ALE},h}; p_{\mathrm{LA},n}^{\mathrm{in}}, Q_{\mathrm{VEN},n}^{\mathrm{PUL,\,3D}}, p_{\mathrm{AR},n}^{\mathrm{SYS}}, \boldsymbol{d}_{\Gamma_n};\\ &R_{\mathrm{MV}},\ R_{\mathrm{AV}},\ \varepsilon_{\mathrm{MV}},\ \varepsilon_{\mathrm{AV}}, \Sigma_{\mathrm{MV},n}, \Sigma_{\mathrm{AV},n}; \Omega_n,\ \mathcal{T}_n^h)\end{aligned}$$

$n \leftarrow n + 1$

end while

Flowrates are computed hinging upon mass balance and volumes time derivatives are discretized with backward finite differences.

We gather the problems in Equation (6.30l)-(6.30n), discretized as in Section 4.4, as

$$(\boldsymbol{c}_n, \widetilde{\boldsymbol{c}}_n)^T = \textsc{Circulation}(Q_{\mathrm{VEN},n}^{\mathrm{PUL,\,3D}}, Q_{\mathrm{AA},n}^{\mathrm{3D}}), \tag{6.36}$$

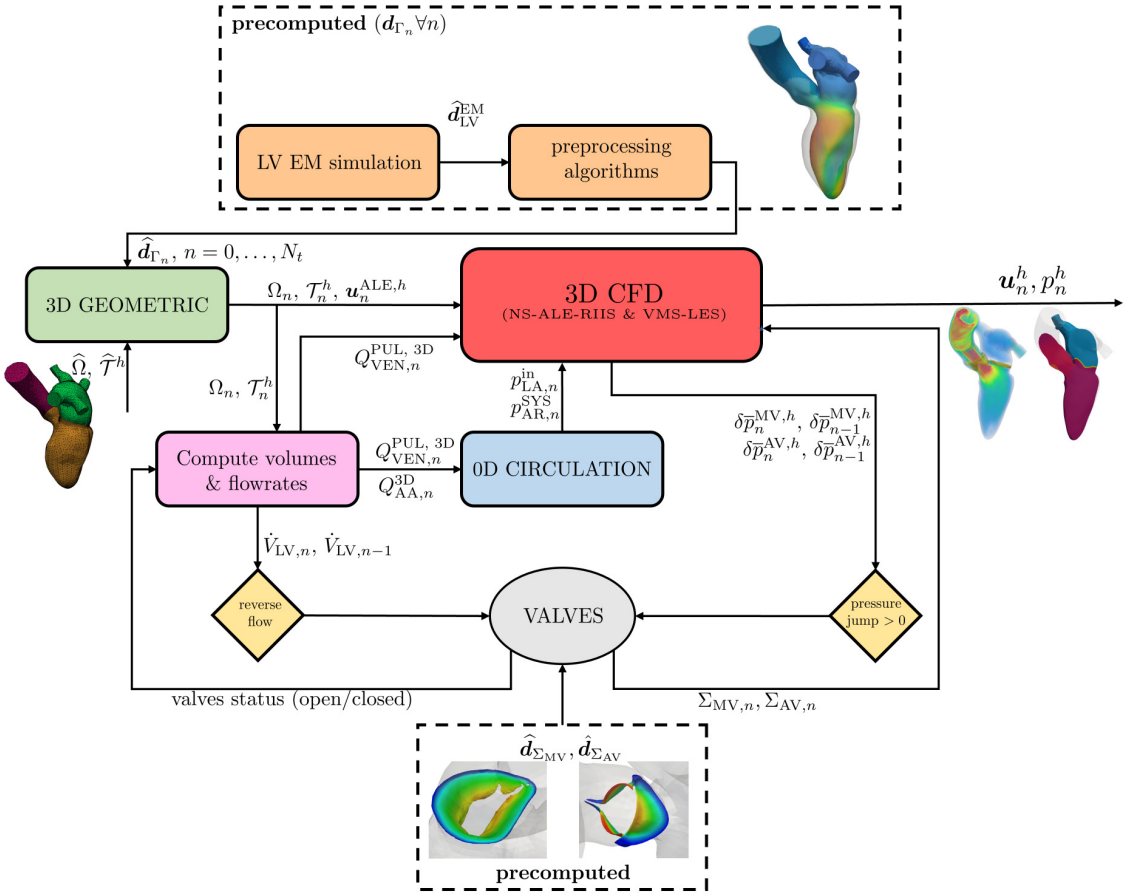

Figure 6.11: Coupling scheme among 3D geometric, 0D circulation and 3D CFD problems for the LH model at time step n (segregated scheme).

where we highlight the dependency of the circulation problem on the fluxes $Q^{\text{PUL, 3D}}_{\text{VEN},n}$, $Q^{\text{3D}}_{\text{AA},n}$ computed in Algorithm 6.6. To solve the system of ODEs in Equation (6.30l)-(6.30n), at every time step, the right-hand sides $\boldsymbol{r}(t_n, \boldsymbol{c}_n, \widetilde{\boldsymbol{c}}_n)$ and $\widetilde{\boldsymbol{r}}(t_n, \boldsymbol{c}_n)$ is fed with $Q^{\text{PUL, 3D}}_{\text{VEN},n}$ and $Q^{\text{3D}}_{\text{AA},n}$ as computed in Algorithm 6.6; in turn, the pressures $p^{\text{SYS}}_{\text{AR},n}$ and $p^{\text{in}}_{\text{LA},n}(t)$, computed in the 0D model, are used to prescribe BCs to the 3D CFD problem. We denote by $\mathcal{P}_{\text{NS-ALE-RIIS-VMS-LES}}$ the fluid-dynamics problem in Equation (4.21):

$$\begin{aligned}\mathcal{P}_{\text{NS-ALE-RIIS-VMS-LES}}(\boldsymbol{u}^h_n, p^h_n; \boldsymbol{u}^{\text{ALE},h}_n; p^{\text{in}}_{\text{LA},n}, Q^{\text{PUL, 3D}}_{\text{VEN},n}, p^{\text{SYS}}_{\text{AR},n}, \boldsymbol{d}_{\Gamma_n};\\ \Sigma_{\text{MV},n}, \Sigma_{\text{AV},n}, R_{\text{MV}}, R_{\text{AV}}, \varepsilon_{\text{MV}}, \varepsilon_{\text{AV}}; \Omega_n, \mathcal{T}^h_n) = 0,\end{aligned} \tag{6.37}$$

where we highlight the dependency of the problem on the ALE velocity $\boldsymbol{u}^{\text{ALE},h}_n$, on quantities required to set BCs ($p^{\text{in}}_{\text{LA},n}, Q^{\text{PUL, 3D}}_{\text{VEN},n}, p^{\text{SYS}}_{\text{AR},n}, \boldsymbol{d}_{\Gamma_n}$) as in Equation (6.30d), (6.30c), (6.30e) and (6.30f), on quantities required by the valves' RIIS modeling ($\Sigma_{\text{MV},n}, \Sigma_{\text{AV},n}$,

R_k		ε_k		h			cells	DOFs ($\mathbb{Q}_1 - \mathbb{Q}_1$)		
[kg/(m^2·s)]		[10^{-3} m]		[10^{-3} m]			[10^3]	[10^3]		
MV	AV	MV	AV	min	avg	max		$\boldsymbol{u}$	p	total
10^4	10^4	1	1	0.7	2.3	5.2	157	534	178	712

Table 6.1: Parameters for the setup of the numerical simulations.

R_{MV}, R_{AV}, ε_{MV}, ε_{AV}) as in Equation (6.30a) and on the domain and mesh at current time step (Ω_n, $\mathcal{T}_n^h$). $\mathcal{P}_{\text{NS-ALE-RIIS-VMS-LES}}$ denotes the numerical solution at time step n of the fluid dynamics problem made of the NS-ALE-RIIS equations with VMS-LES modeling, as explained in Section 4.3.1. The whole procedure to solve the fluid-dynamics problem is reported in Algorithm 6.7 and consists of solving Equation (6.37) and computing the pressure jumps across valves. The algorithm is in short called as

$$\begin{aligned}\left(\boldsymbol{u}_n^h,\, p_n^h,\, \delta\overline{p}_n^{\text{MV},h},\, \delta\overline{p}_n^{\text{AV},h}\right)^T = \textsc{FluidDynamics}(&\boldsymbol{u}_n^{\text{ALE},h}; p_{\text{LA},n}^{\text{in}}, Q_{\text{VEN},n}^{\text{PUL, 3D}}, p_{\text{AR},n}^{\text{SYS}}, \boldsymbol{d}_{\Gamma_n};\\ &R_{\text{MV}},\, R_{\text{AV}},\, \varepsilon_{\text{MV}},\, \varepsilon_{\text{AV}}, \Sigma_{\text{MV},n}, \Sigma_{\text{AV},n};\\ &\Omega_n,\, \mathcal{T}_n^h).\end{aligned} \tag{6.38}$$

We solve the 3D-0D model of Equation (6.30) by means of a segregated numerical scheme that we show in Algorithm 6.8. After initialization, at each time step we solve the geometric problem (Algorithm 6.3), we check the valves status through Algorithm 6.4, which – after checking positive pressure jumps and reversed flow conditions – returns the valves' opening and closing times $\boldsymbol{\tau}$. The latter is used to compute the flowrates (Algorithm 6.6). The flowrates $Q_{\text{VEN},n}^{\text{PUL, 3D}}, Q_{\text{AA},n}^{\text{3D}}$, computed in the latter, are then used to assemble the right-hand side of Equation (6.30l), (6.30m) (circulation problem). Finally, the pressures $p_{\text{LA},n}^{\text{in}}$, $p_{\text{AR},n}^{\text{SYS}}$ computed by the circulation problem and the flowrate $Q_{\text{VEN},n}^{\text{PUL, 3D}}$ provided by the flowrates computation are used to set BCs of the fluid dynamics problem as described in Section 6.4.

In Figure 6.11 we report a conceptual scheme of the whole problem: from the pre-computed quantities to the coupling among circulation and fluid dynamics problems. We highlight the central role played by the valves status determination and all the quantities shared among different the problems.

6.6. Numerical simulations

We perform numerical simulations on a LH mesh built from the Zygote Solid 3D heart model [133]. To preprocess the geometry and generate the mesh, we use vmtk [20] and the pre-processing tools recently developed in [85]. We mesh each portion of the domain (LA, LV and AA) separately with a non-uniform mesh size, refining the mesh

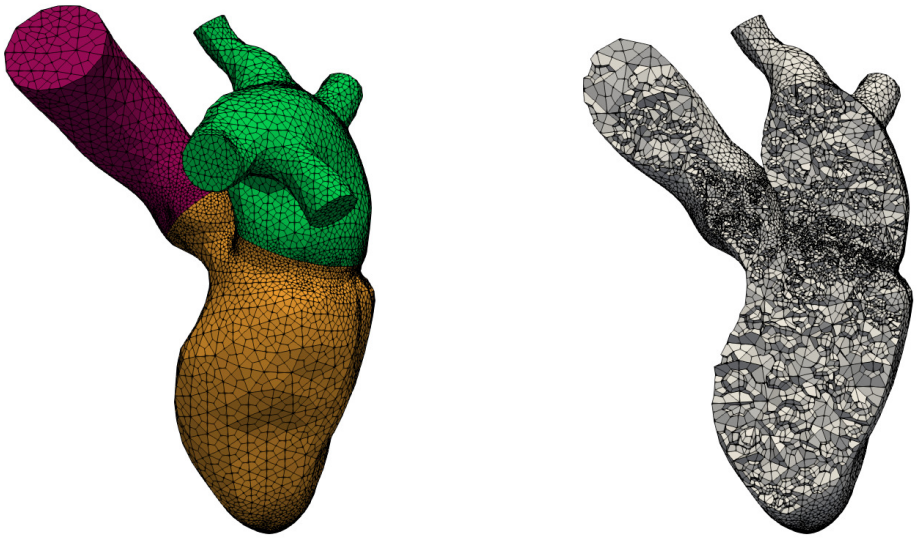

(a) (b)

Figure 6.12: The LH hexahedral mesh: (a) the mesh made of three conforming submeshes for LA, LV and AA; (b) a clip of the mesh showing the local mesh refinement near the MV and AV.

near the MV, AV and the LV apex, exploiting algorithms based on the closest-point distances [85]. The three submeshes are then connected in a conforming fashion to get the hexahedral mesh in Figure 6.12. Specifically, with vmtk we first generate a tetrahedral mesh, then we use mesh tethex [11, 85] to obtain an hexaedral mesh in which each tetrahedron is split into four hexaedra preserving the aspect ratio of the original element.

For the RIIS method, following arguments of [86, 100], we set $R_{\text{MV}} = R_{\text{AV}} = 10^4$ kg/(m^2·s) and $\varepsilon_{\text{MV}} = \varepsilon_{\text{AV}} = 10^{-3}$ m. This choice of ε_{MV} and ε_{AV} allows to have a physiologic representation of the valves' leaflets in a healthy subject and, with our setting of R_{MV} and R_{AV} to avoid flow penetration across the immersed surfaces [86]. As shown in Figure 6.12b, we have refined the mesh in the valves region in order to accurately represent the leaflets as described by the RIIS method with our choices of ε_{MV} and ε_{AV}. Since we neglect the isovolumetric phases, we cannot employ physiological opening and closing times of the valves, thus we open and close them instantaneously (i.e. in one time step). Thus, we set $\Delta\tau^0_{\text{MV}} = \Delta\tau^{\emptyset}_{\text{MV}} = \Delta\tau^0_{\text{AV}} = \Delta\tau^{\emptyset}_{\text{AV}} = \Delta t$, with $\Delta t = 2 \cdot 10^{-4}$ s.

We start our simulation from a zero velocity initial condition $\boldsymbol{u}_0 = \mathbf{0}$ and we set linear FE spaces for velocity and pressures ($\mathbb{Q}_1 - \mathbb{Q}_1$). In Table 6.1 we summarize the parameters adopted for the setup of our numerical simulations. Mathematical

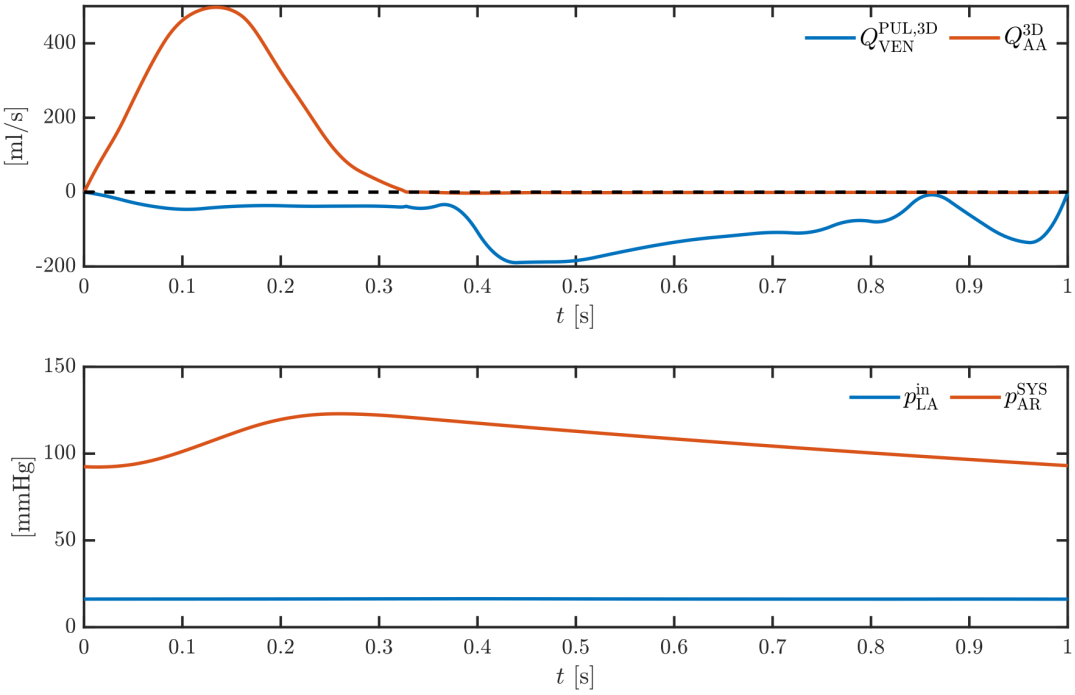

Figure 6.13: Flowrates (top) and pressures (bottom) at the interfaces of the 3D-0D model.

models and numerical methods described in Section 6.5 have been implemented in life^x [6] and numerical simulations are run in a parallel framework [2]. In the following, we first present our numerical results for the case of a healthy LH, then we apply our computational model to the pathological case of MV regurgitation.

6.6.1. Physiological simulation

We simulate 4 heartbeats ($T_f = 4$ s) of period $T_{HB} = 1$ s and we discard the first 3 cycles in order to remove the influence of a null initial condition. We show numerical results on the last heartbeat and we shift the temporal domain in $[0, T_{HB}]$. We start our simulation from the time of end diastole, with the MV open and the AV closed. In Figure 6.13 we report flowrates and pressure at the inlet and outlet sections of the 3D domain, which are the interfaces of the 3D-0D coupling. In Figure 6.14 we show the average pressure in LA, LV and AA computed by averaging the pressure field in control

[2]Numerical simulations were run either on the cluster iHEART (Lenovo SR950 8 x 24-Core Intel Xeon Platinum 8160, 2100 MHz and 1.7TB RAM) available at MOX, Dipartimento di Matematica, Politecnico di Milano and on the cluster GALILEO supercomputer (IBM NeXtScale cluster, 1022 nodes (Intel Broadwell), 2 x 18-Cores Intel Xeon E5-2697 v4 at 2.30 GHz, 36 cores/node, 26.572 cores in total with 128 GB/node) by CINECA.

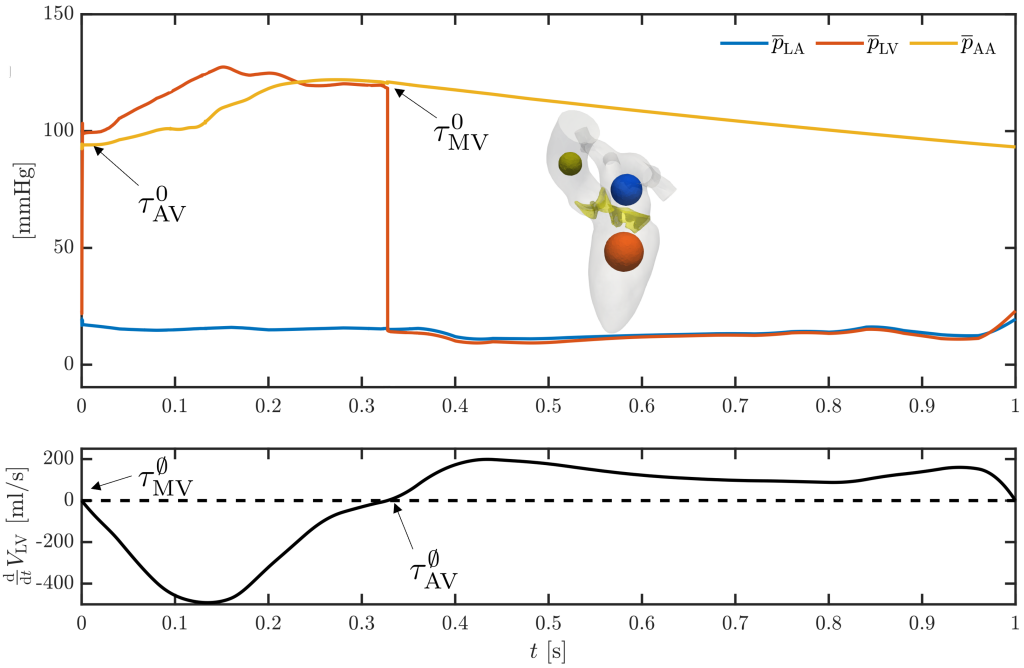

Figure 6.14: Flow properties to determine opening and closure of valves. Top: average pressure in LA, LV and AA; bottom: time derivative of LV volume. The pressure jumps among chambers determine the opening times of valves (τ^0_{MV}, τ^0_{AV}); the sign of LV volume time derivative determines a condition of reversed flow across the MV and the AV sections which defines valves closing times ($\tau^{\emptyset}_{\mathrm{MV}}$, $\tau^{\emptyset}_{\mathrm{AV}}$). Average pressures in the chambers are computed as in Equation (6.16) in the control volumes shown in the LH on the top box.

volumes in each chamber, as explained in Section 6.3. On the bottom box, we report the LV volume time-derivative, which is the indicator adopted to check for reversed flow across a valve and hence to determine the valves' closing times. The MV closes at the beginning of the heartbeat when the flow becomes reverse on its section ($t = \tau^{\emptyset}_{\mathrm{MV}}$, when $\dot{V}_{\mathrm{LV}}$ becomes negative). The pressure in the LV starts rising and the AV opens when the pressure in the LV becomes larger than the one in the AA ($t = \tau^0_{\mathrm{AV}}$, when $\overline{p}_{\mathrm{LV}}$ becomes larger than $\overline{p}_{\mathrm{AA}}$). This very time marks the beginning of the ejection phase in systole. In Figure 6.16 we report the volume rendering of the velocity magnitude and in 6.17 the pressure on a clip in the LV apico-basal direction. During the LV contraction, as shown in Figure 6.16, box 2, the blood flows from the LV to the AA, reaching large values of velocity at the systolic peak $t = 0.134$ s. In particular, we measured a maximum flowrate in the AV section equal to 489.5 ml/s and a maximum systemic arterial pressure equal to 121.1 mmHg. The numerical results achieved are

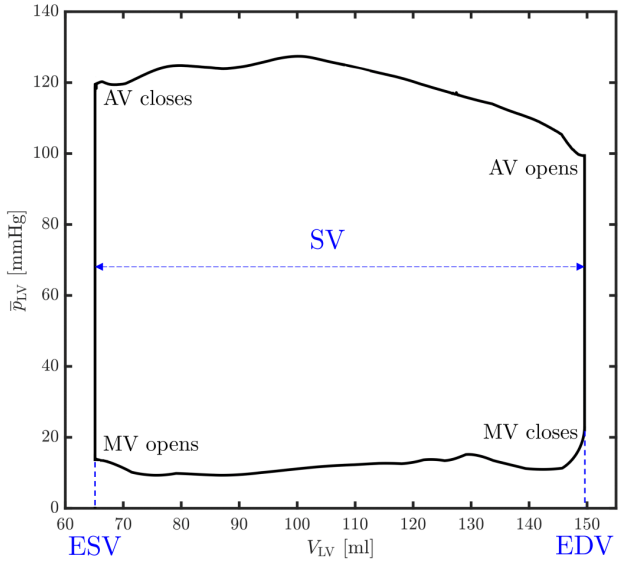

Figure 6.15: Computed LV pressure-volume loop.

consistent with standard physiological data [46, 113, 245]: a peak systolic pressure in the range 119 ± 13 mmHg [245]; a maximum flowrate of about 489 ml/s [113].

Specifically on the ejection phase, as shown in Figure 6.18, during the acceleration phase (Figure 6.18, boxes 1 and 2), the spatial profile of the velocity field is almost flat, suggesting the development of a turbulent flow inside the AA. However, as the systolic peak is reached, the blood continues to flow from the LV to the AA (Figure 6.16, box 3) but it decelerates; differently from the acceleration stage, the velocity profile is no longer flat but the flow is partially oriented towards the LV (Figure 6.18, boxes 3-6). The AV closes when the flow becomes completely reverse on its section ($t = \tau^{\emptyset}_{\mathrm{AV}}$, when $\dot{V}_{\mathrm{LV}}$ becomes positive). Once the AV is closed, the pressure in the LV suddenly decreases, until it becomes smaller than the one in the LA: this marks the beginning of diastole with the opening of the MV ($t = \tau^{0}_{\mathrm{MV}}$, when $\overline{p}_{\mathrm{LA}}$ becomes larger than $\overline{p}_{\mathrm{LV}}$). The diastole is characterized by two filling stages: the E-wave and the A-wave (Figure 6.16, boxes 4, 5). As the E-wave starts ($t \approx 0.43$ s), a high-speed flux coming from the LA is observed at the MV section: the LV volume increases and the LA volume decreases. During the A-wave (atrial kick, $t \in [0.87, 1]$ s), we observe a rapid contraction of the LA, as also observed in Figures 6.6 (V_{LA}) and 6.13 ($Q^{\mathrm{PUL,\ 3D}}_{\mathrm{VEN}}$), producing a second high speed flux through the MV section, but milder than the one characterizing the E-wave. Once the atrial kick is over and a reverse flow condition is detected on the MV section, the MV closes at the beginning of a new heartbeat.

Figure 6.15 shows the computed LV pressure-volume (pV) loop. We correctly capture the standard shape of the LV pV loop in physiological conditions, obtaining and end diastolic volume EDV = 149.6 ml, end systolic volume ESV = 65.1 ml, stroke volume

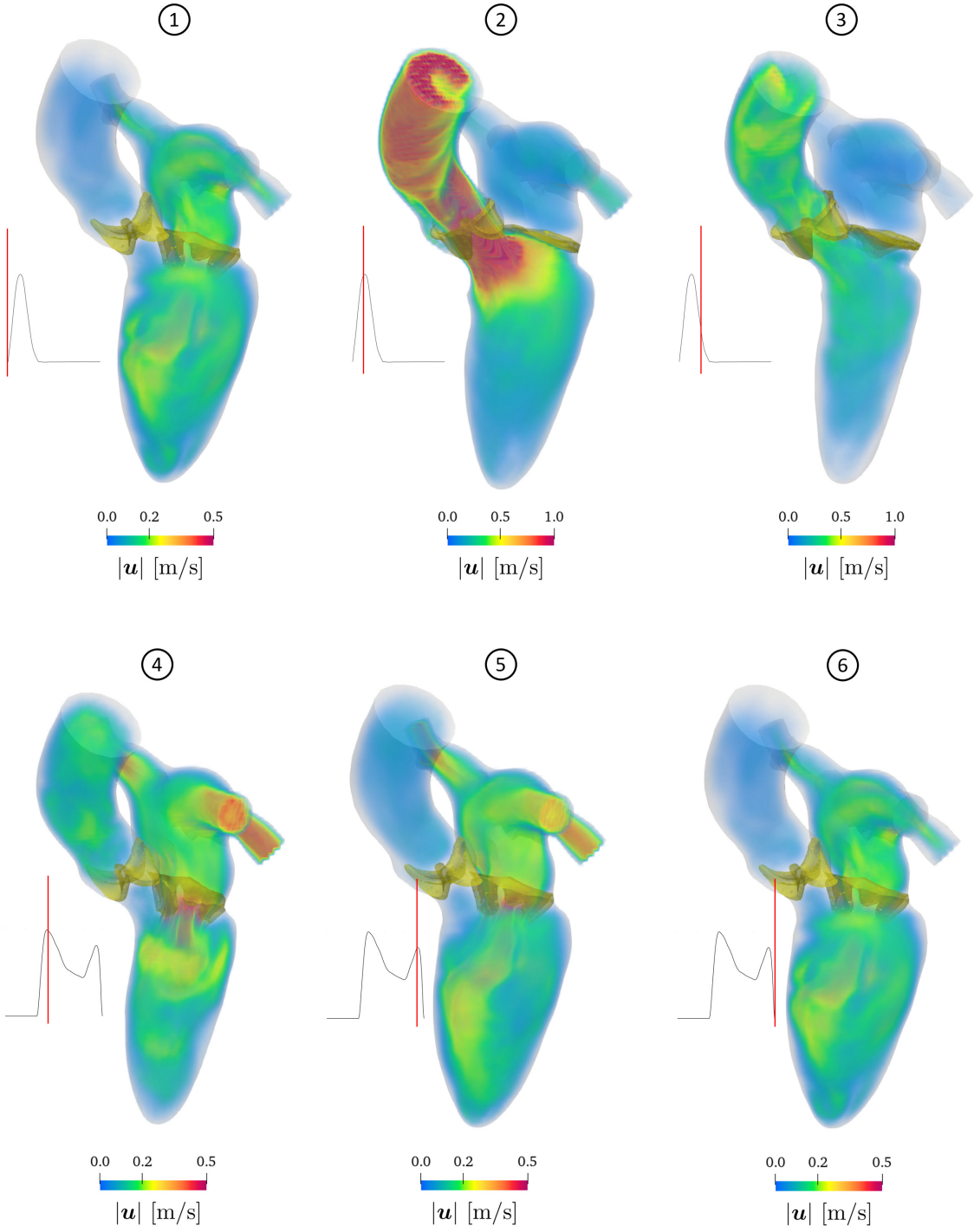

Figure 6.16: Volume rendering of velocity magnitude during a whole heartbeat. In boxes 1, 2, 3 the 1D plot shows Q_{AV}, in boxes 4, 5, 6 the MV flowrate Q_{MV}.

SV = EDV − ESV = 84.4 ml and ejection fraction EF = 100 SV/EDV = 56.5%. Our results are consistent with values routinely acquired in healthy subjects [160, 272].

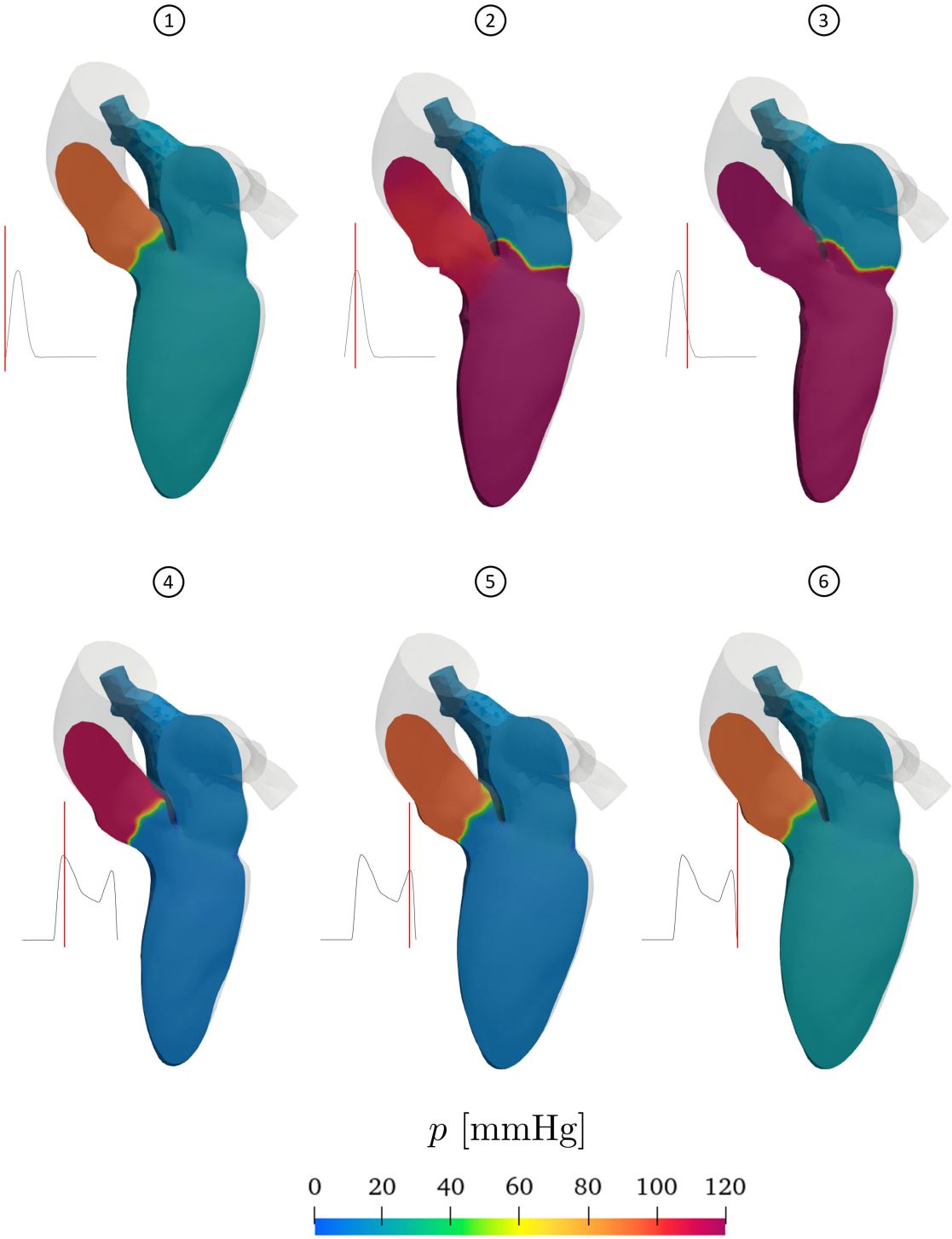

Figure 6.17: Pressure fields on a clip in the LV apico-basal direction during a whole heartbeat. In boxes 1, 2, 3 the 1D plot shows Q_{AV}, in boxes 4, 5, 6 the MV flowrate Q_{MV}.

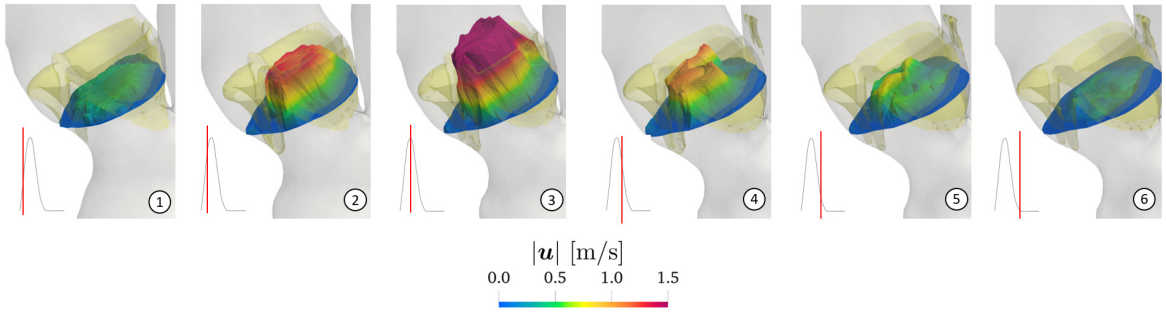

Figure 6.18: Snapshots of velocity profile at the AV section during systole. The 1D plot shows Q_{AV}.

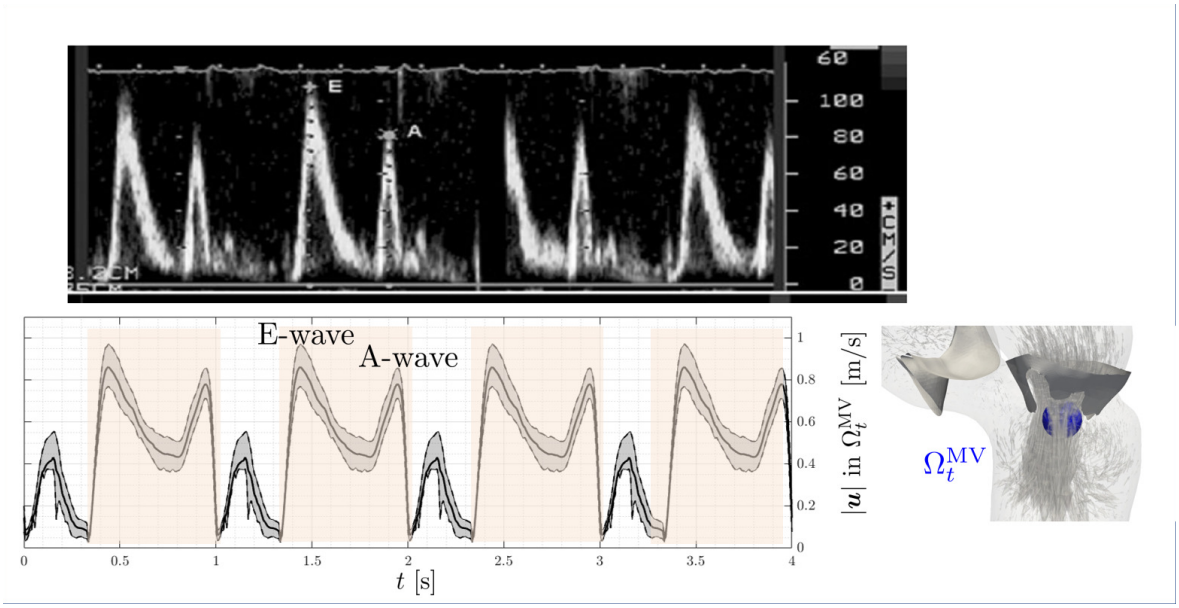

Figure 6.19: MV velocity: comparison between the velocity profile acquired through trans-mitral valve spectral Doppler in a normal subject (top) and the results obtained in the numerical simulation (bottom). The image on the top is taken from [261]; on the bottom we display the average, first and third quartile of velocity magnitude in a control volume under the MV section.

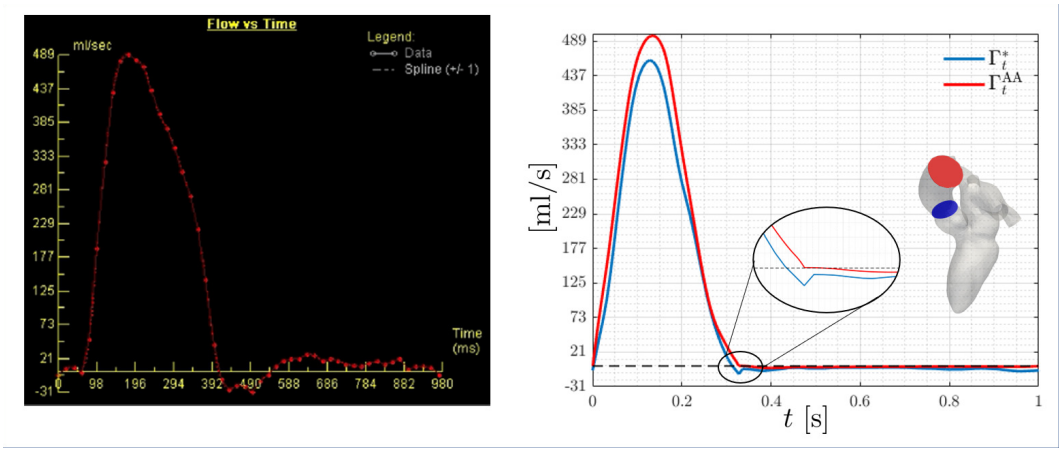

Figure 6.20: AA flowrate: comparison between a CMR result (left) and our numerical simulation (right). The image on the left is taken from [113]; on the right we compute the flowrate on a section downwind the AV ($\int_{\Gamma_t^*} \boldsymbol{u} \cdot \boldsymbol{n}$) and on the outlet section ($Q_{\mathrm{AA}}^{\mathrm{3D}}(t) = \int_{\Gamma_t^{\mathrm{AA}}} \boldsymbol{u} \cdot \boldsymbol{n}$)

Figure 6.19 shows a comparison between the velocity at MV section computed in our numerical simulations (bottom) and the one acquired in-vivo in a normal subject in [261] (top). Specifically, since the MV velocity is routinely measured in a sample volume between the mitral leaflet tips [21]), we report the in-silico velocity magnitude computed in a control volume immediately below the MV section because . We perform this comparison in diastole only (yellow boxes in Figure 6.19, bottom box), the peak obtained in systole is due to the blood flowing from the LV to the AA. We observe that our model is able to correctly reproduce the two characteristic waves in diastole, namely E-wave and A-wave: as for our reference data, the first wave shows a stronger peak than the second one. In the Doppler data, the E-wave and A-wave are characterized by amplitudes approximately equal to 1 m/s and 0.8 m/s; from the numerical results we get 0.97 m/s and 0.85 m/s respectively. We compute an EA ratio equal to 1.14 (ratio among E-wave and A-wave peak velocities), which lays within the physiological range of EA $\in [0.75, 1.5]$ and is typical of young healthy subjects (EA > 1) [13, 21].

In Figure 6.20, we compare the AA flowrate measured with CMR and with our numerical simulations. Specifically, the in-vivo data are acquired through CMR through-plane phase-contrast velocity mapping [113]. By computing the flowrate at a section Γ_t^* downwind the AV and at the outlet section Γ_t^{AA}, we match accurately the systolic peak, with amplitudes 460.2 ml/s and 489.5 ml/s respectively on Γ_t^* and Γ_t^{AA}, against a peak approximately equal to 490 ml/s in the reference data. As diastole begins, the flow becomes reverse on the section considered, with a maximum amplitude equal to -12.0 ml/s and -2.8 ml/s on Γ_t^* and Γ_t^{AA} respectively. This pattern is also observed in the MRI data even though with a larger amplitude: we believe that the usage of a FSI model would better predict the elastic return of the AA after the AV closure.

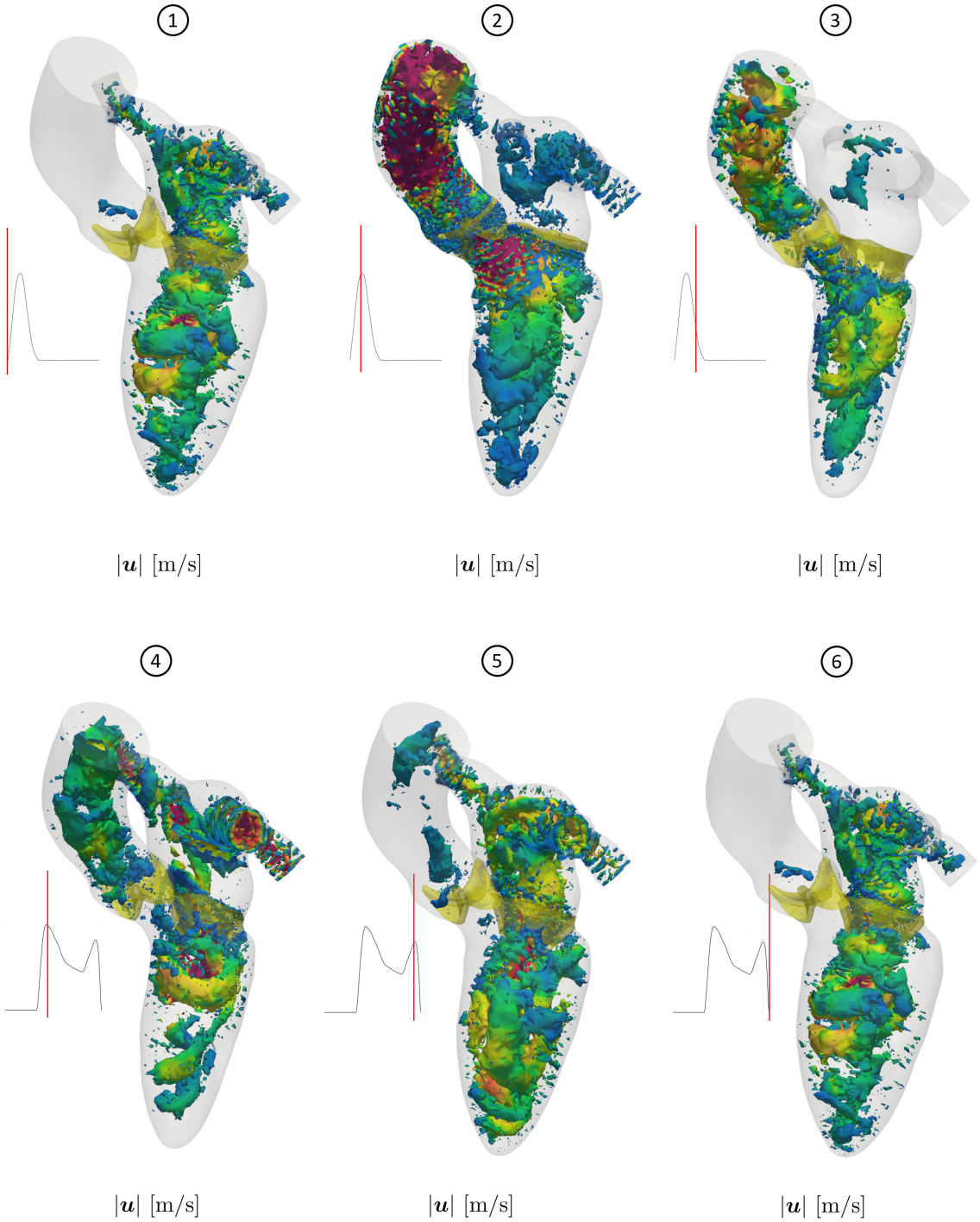

Figure 6.21: Iso-contours of Q-criterion ($\mathrm{Q}(\boldsymbol{u}) = 200\,\mathrm{s}^{-2}$) colored with velocity magnitude during a whole heartbeat. In boxes 1, 2, 3 the 1D plot shows Q_{AV}, in boxes 4 and 5 Q_{MV}.

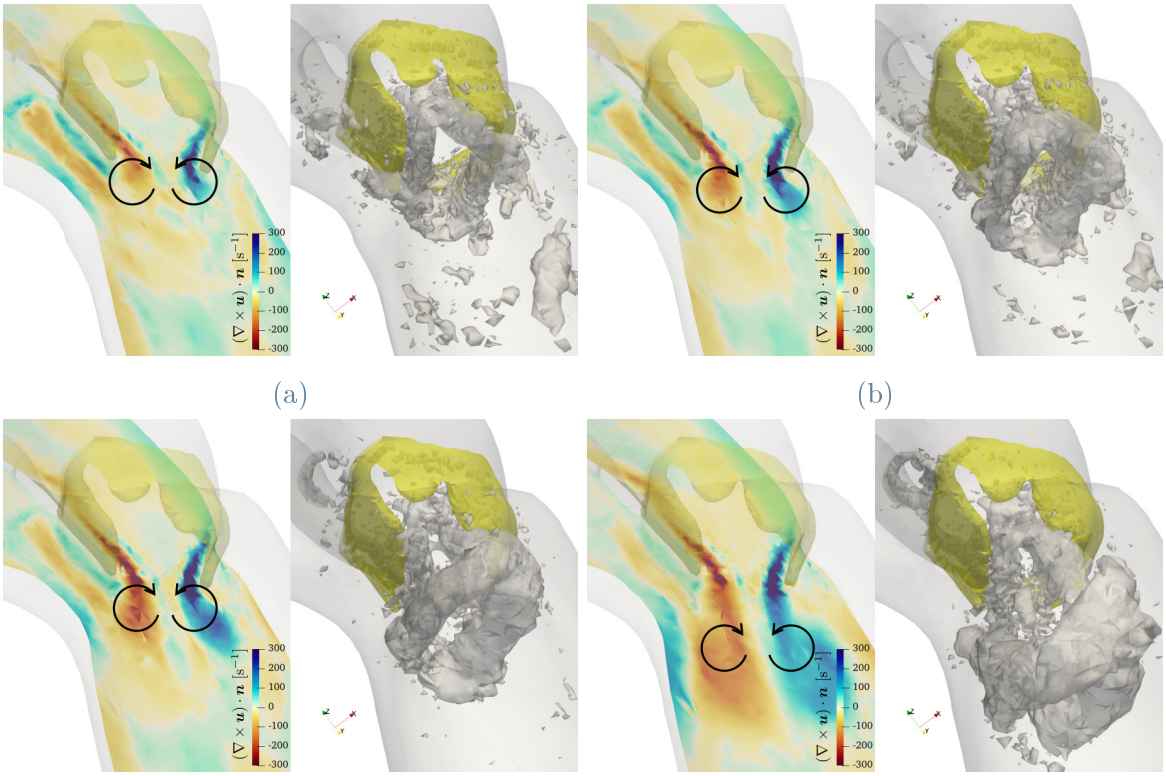

Figure 6.22: Formation of ring shaped vortex during early diastole. In each subfigure: on the left, projection of the vorticity on the normal direction (pointing towards the reader) of a slice in the LV apico-basal direction; on the right: the Q-criterion with $\mathsf{Q}(\boldsymbol{u}) = 1500\,\mathrm{s}^{-2}$ to identify the vortex.

We wish to point out that our numerical simulations are run on a template – even though realistic – geometry [133] and fed with data coming from EM simulations and 0D circulation model tuned for a generic healthy subject. Thus, from our analysis we conclude that a qualitative good agreement can be found with the in-vivo results available in literature, making hence the whole computational model significant and reliable from an hemodynamic view point.

In Figure 6.21 we show the iso-contours of Q-criterion with $\mathsf{Q}(\boldsymbol{u}) = 200\,\mathrm{s}^{-2}$ at different instants during the whole heartbeat. At the beginning of the heartbeat (box 1), we observe the residual vortical structures in the LH from late diastole. As the AV opens and the ejection phase starts, coherent structures are flushed out in the AA and the LV remains almost free. During systole, the LA is filled and coherent structures coming from the pulmonary veins impact in the middle of the LA, with still some visible structures at the end of systole (boxes 2-3). As the MV opens, in the LA we observe the formation of four vortex rings coming from the pulmonary veins. As in the systolic

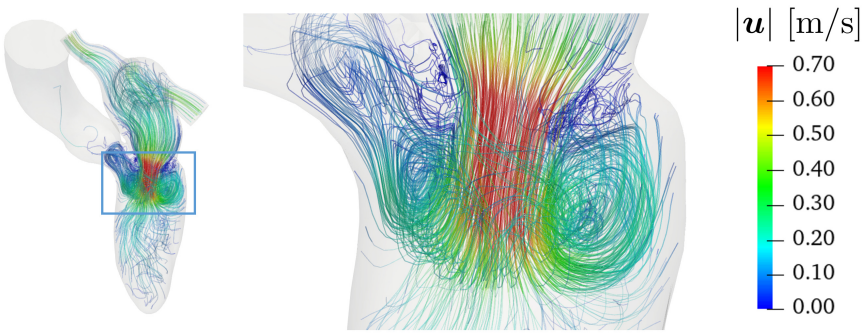

(a)

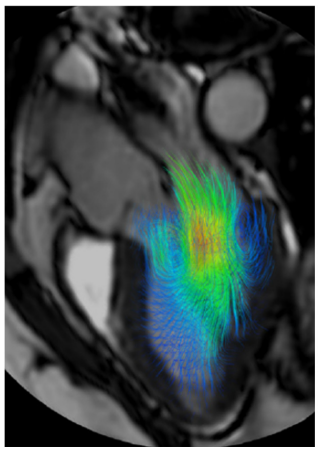

(b)

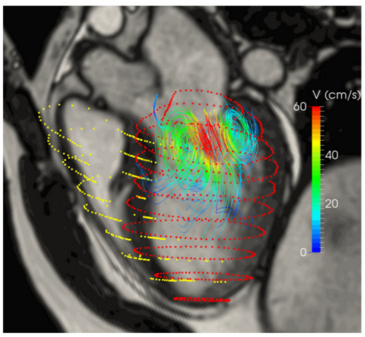

(c)

Figure 6.23: Streamlines colored according to velocity magnitude at early diastolic peak (E-wave): comparison between numerical results (a) and 4D flow MRI images taken from [80] and [264].

filling, they impact in the LA producing smaller and smaller coherent structures, during the E-wave and A-wave, as described in Chapter 5. At the same time, during E-wave, a big vortex ring rolls through the MV leaflets. The observed organized vortical pattern observed rapidly evolves into a chaotic complex flow that fills the whole LV reaching its apex (box 5). During the A-wave, a new vortex under the MV section is formed, but weaker than the one seen during the E-wave (boxes 5-6). A new cycle begins, the MV closes, the vortex under its section is suddenly broken and, with the opening of the AV, all the coherent structures are flushed out again.

In each subfigure of Figure 6.22, we show on the left the projection of the vorticity on the normal direction of a slice in the LV apico-basal direction; on the right the iso-contours of Q-criterion with $\mathsf{Q}(\boldsymbol{u}) = 1500\,\mathrm{s}^{-2}$. Each subfigure represents a snapshot

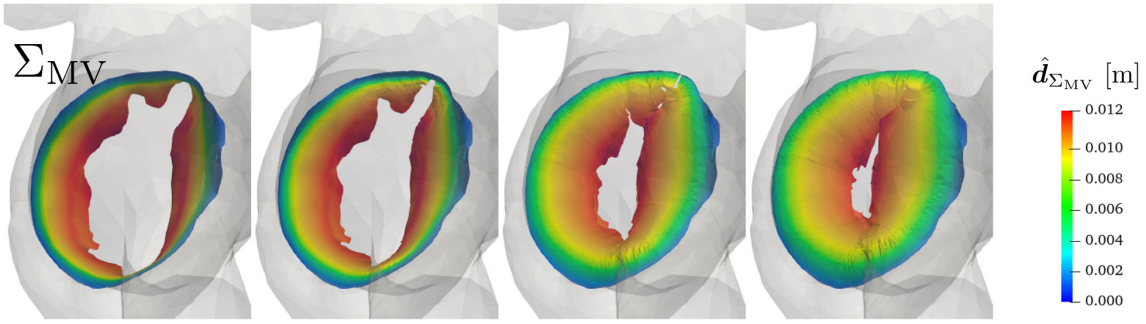

Figure 6.24: MV: from fully open to closed (regurgitant) configuration. Leaflets are deformed with the displacement $\widehat{\boldsymbol{d}}_{\Sigma_{\mathrm{MV}}}$.

during early diastole. We observe the formation of shear layers on the leaflets of the MV producing different velocities on the two sides of the leaflets. Shear layers roll on MV leaflets and enter in the main cavity producing low-pressure circulation regions. The flow rotates in clockwise direction under the anterior leaflet, counterclockwise under the posterior, as shown in the projection of the vorticity in the slice's normal direction. This process characterizes the formation of the vortex ring that rolls through the MV leaflets (also shown in Figure 6.21, box 4), with a higher velocity in the inner part with respect to the exterior part of the ring. Once the vortex is formed, it evolves towards the LV apex and it breaks into smaller coherent structures.

In Figure 6.23 we compare the streamlines at the MV section during the E-wave obtained with our numerical simulation and with 4D flow MRI data taken from [80] and [264]. The numerical simulation well predicts the high speed jet across the MV and the formation of vortical flow under its section described by the in-vivo data. Thus, our model captures the formation and the dynamic of the vortex ring (also referred to as "O vortex" [51, 67]) during diastole, a well studied cardiac hemodynamic feature whose characteristics and interactions with LV wall provide information about the diastolic function [23, 51, 145, 177].

6.6.2. Mitral valve regurgitation

We now employ our model to investigate primary mitral valve regurgitation. In particular, we mimic the presence of MV regurgitation by redefining $\widehat{\boldsymbol{d}}_{\Sigma_{\mathrm{MV}}}(\boldsymbol{x})$ to get the displacement field displayed in Figure 6.24. Due to the mitral regurgitant flow, an amount of blood flows from the LV to the LA during systole. Therefore, the flowrate at the aortic outlet can no longer be computed exploiting mass balance as in Equation (6.24). Thus, for the coupling with the 0D circulation model we compute the outlet flowrate as

$$Q^{\mathrm{3D}}_{\mathrm{AA}}(t) = \int_{\Gamma^{\mathrm{AA}}_t} \boldsymbol{u} \cdot \boldsymbol{n} \mathrm{d}\boldsymbol{x}. \tag{6.39}$$

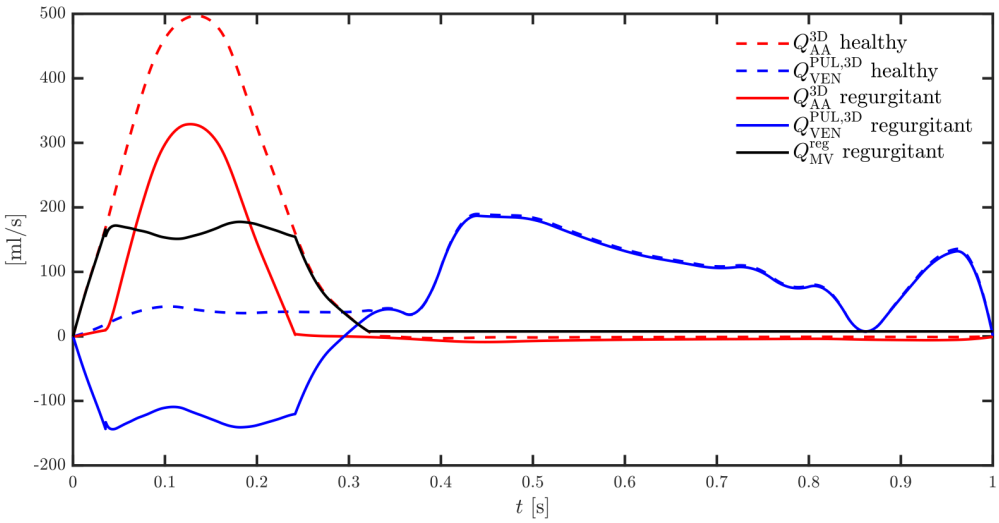

Figure 6.25: Flowrates at inlet and outlet sections: comparison between healthy and MV regurgitation case.

We introduce the mitral regurgitant flow $Q_{\mathrm{MV}}^{\mathrm{reg}}(t)$ as the amount of blood that flows from the LV into the LA during systole:

$$Q_{\mathrm{MV}}^{\mathrm{reg}}(t) = \begin{cases} 0 & \text{if MV in open configuration,} \\ -\dfrac{\mathrm{d}}{\mathrm{d}t}\left(V_{\mathrm{LV}}(t) + V_{\mathrm{AA}}(t)\right) - Q_{\mathrm{AA}}^{\mathrm{3D}}(t) & \text{if MV in closed (regurgitant) configuration.} \end{cases} \tag{6.40}$$

The inlet flowrate accounts for MV regurgitation by modifing its definition with respect to the physiological case as

$$Q_{\mathrm{VEN}}^{\mathrm{PUL,\ 3D}}(t) = \begin{cases} -\dfrac{\mathrm{d}\left(V_{\mathrm{LV}}(t) + V_{\mathrm{LA}}(t)\right)}{\mathrm{d}t} & \text{if MV in open configuration,} \\ -\dfrac{\mathrm{d}V_{\mathrm{LA}}(t)}{\mathrm{d}t} - Q_{\mathrm{MV}}^{\mathrm{reg}}(t) & \text{if MV in closed (regurgitant) configuration.} \end{cases} \tag{6.41}$$

The new definitions (6.39) and (6.41) replace the corresponding quantities in the coupling conditions and in the setting of BCs in Equation (6.22) and Equation (6.24). Moreover, the AV flow no longer matches the LV volume time derivative when the AV is open. Thus, a condition of reversed flow across the AV section – which marks the closure of the AV – is now detected by checking the sign of the AV flow computed as

$$Q_{\mathrm{AV}}(t) = -\left(\frac{\mathrm{d}V_{\mathrm{LV}}(t)}{\mathrm{d}t} + Q_{\mathrm{MV}}^{\mathrm{reg}}(t)\right). \tag{6.42}$$

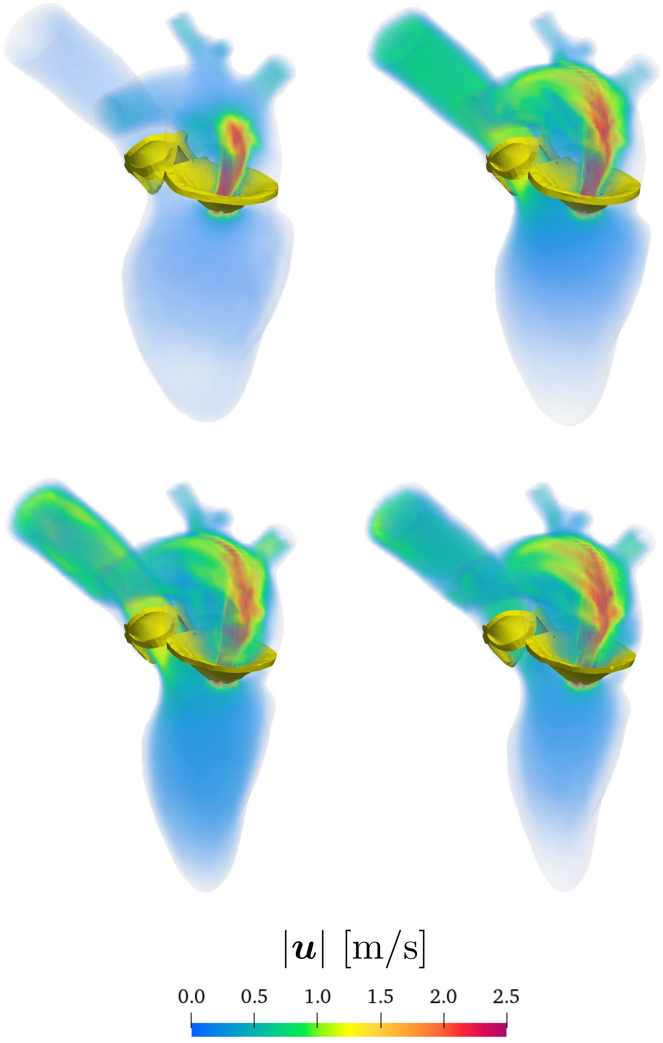

Figure 6.26: Volume rendering of velocity magnitude for the regurgitant mitral valve during systole.

Figure 6.26 shows the volume rendering of velocity magnitude during systole: a high-speed jet flows from the LV to the LA (reversed flow) and a weaker jet is observed in the AA with respect to the healthy case. To better focus on the strong systolic jets, in Figure 6.27 we report a contour surface of the velocity magnitude ($|\boldsymbol{u}| = 0.5$ m/s) colored according to pressure. As systole starts at $t = 0.036$ s, the blood flows from the LV to the LA, accelerates towards the LA endocardium and it impinges on the latter thus yielding higher pressure.

Figure 6.25 reports the flowrates at inlet and outlet sections for the healthy and the pathological cases along with the mitral regurgitant flow. Particularly, we measure a

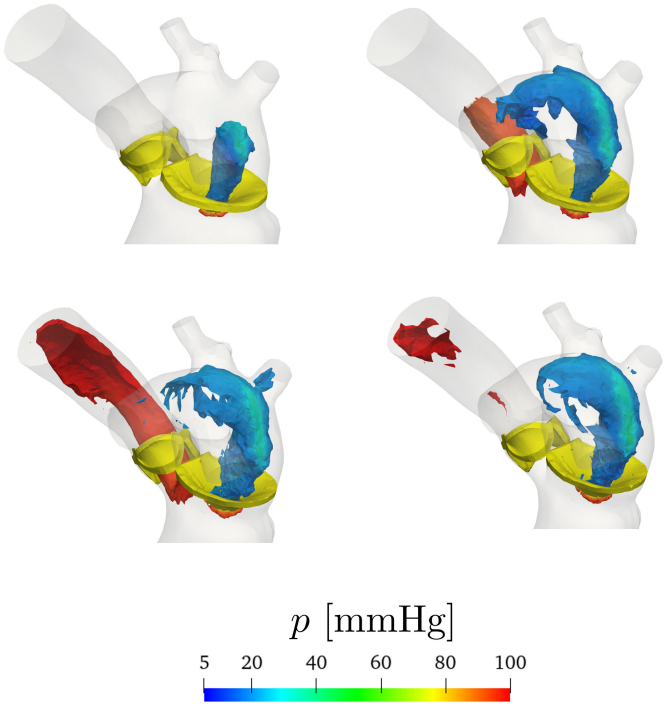

Figure 6.27: Contour surface of velocity magnitude ($|\boldsymbol{u}| = 0.5$ m/s) colored according to pressure for the regurgitant mitral valve during systole.

maximum $Q_{\mathrm{MV}}^{\mathrm{reg}}$ equal to 177.50 ml/s and a peak $Q_{\mathrm{AA}}^{\mathrm{3D}}$ of 328.94 ml/s, against the aortic flow of 489.54 ml/s measured in the healthy case. Furthermore, we observe that, due to the presence of the mitral regurgitant flow, the inlet flowrate $Q_{\mathrm{VEN}}^{\mathrm{PUL,\,3D}}$ becomes negative during systole, thus inducing a reversal pulmonary venous flow. This phenomenon is also observed by clinicians in the case of MV regurgitation and it is a routinely employed indicator to grade its severity [82].

Our numerical results allow to estimate additional hemodynamic indicators as the TAWSS. In Figure 6.28a we report the TAWSS on the LH geometry and we compare the healthy (left) and the MV regurgitation (right) scenarios. In the case of valvular insufficiency we observe large values of TAWSS (up to 2.54 Pa) on the top of the LA due to the high speed retrograde flow that impinges the LA endocardium. At the same time, as shown in Figure 6.28b, due to a lower amount of blood flowing from the LV to the systemic arterial system, a milder interaction between the jet and the wall of the AA is reported as shown by lower values of TAWSS in the AA.

We compute two mitral valve regurgitation indicators: the regurgitant volume (RVol) and the regurgitant fraction (RF). These indicators are routinely computed in the clinical practice via the Proximal Isovelocity Surface Area (PISA) method, an ecocar-

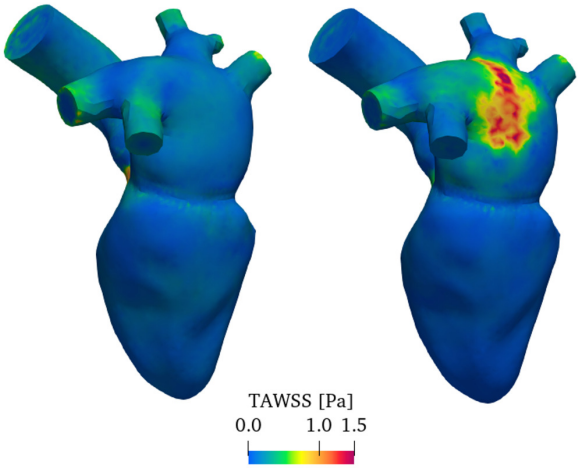

(a) Front view

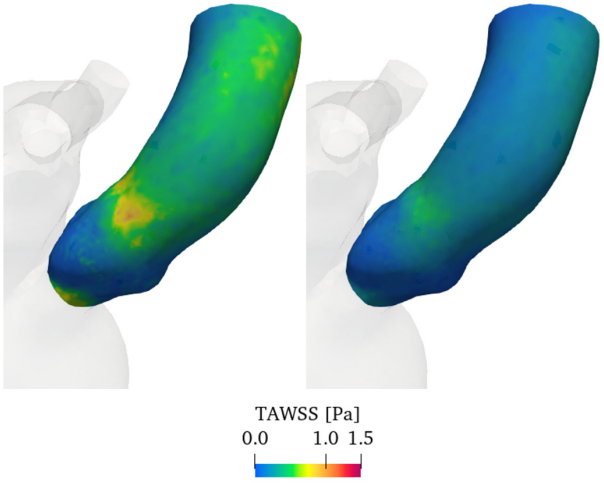

(b) Focus on the AA

Figure 6.28: Comparison of TAWSS in physiologic and mitral valve regurgitation case: (a) front view of the LH (b) focus on the AA. In each subfigure: on the left the healthy case, on the right the mitral valve regurgitation.

diographic technique based on conservation of mass which however relies on several limiting assumptions [258]. On the contrary, numerical simulations allow to accurately estimate these indicators without the need of hypotheses considered in the PISA method. We compute RVol as the amount of blood flowing from the LV to the LA in

a heartbeat by integrating in time the regurgitant flowrate, as

$$\mathrm{RVol} = \int_0^{T_{\mathrm{HB}}} Q_{\mathrm{MV}}^{\mathrm{reg}}(t)\mathrm{d}t. \tag{6.43}$$

The RF is defined as the ratio among the RVol and the SV [258]. For this proof of concept simulation, we get RVol = 47.07 ml/s and RF = 55.74 %, values which would indicate a severe mitral valve regurgitation [89].

6.7. Concluding remarks

In this chapter we proposed a computational model for the detailed analysis of the LH hemodynamics, accounting for the displacement of the domain boundary, the motion of the valves, the dynamics of the circulatory system, and transition to turbulence effects. In particular:

- We introduced a novel preprocessing procedure that combines i) an extension of a given left ventricular displacement on the whole LH by means of Laplace-Beltrami equations with physiological kinematic constraints; and ii) a reduced model for the motion of the atrium based on the volume variation dictated by a lumped-parameter circulation model. This yields an integrated system in which fluid dynamics is one-way coupled to EM in the LV. The extension procedure can also be employed to merge displacement fields coming from different sources, such as a reconstruction from diagnostic images, and may, thus, be applied also to patient-specific studies. As the imaging data routinely acquired in diagnostic exams is often focused on the ventricle, the extension procedure that we propose can be used to complete the missing data.
- We devised a coupled 3D-0D model consisting of of the 3D CFD model of the LH and the 0D circulation model of the whole cardiovascular system. We solve the coupled model with a segregated scheme and we develop computational strategies to solve the integrated system made of fluid dynamics, displacement, valves and circulation.
- We found that our numerical simulations yielded a qualitative and quantitative good agreement with clinical data from different sources, making the whole integrated multiscale model significant and realiable from an hemodynamics view point. Furthermore, the flexibility of the model also allowed to simulate pathological scenarios.

To conclude, the present chapter can be viewed as a significant step forward towards the final goal of this thesis: the CFD simulation of the whole human heart coupled to the external pulmonary and systemic circulation. This will be the focus of Chapter 7, and it represents a challenging task that can be reached with intermediate stages.

7 | Multiscale CFD modeling of the whole heart

In this chapter, we present a multiscale CFD model of the whole human heart coupled to the external systemic and pulmonary circulations. The simulation carried out in this chapter represents one of the few attempts in the literature to model the whole heart hemodynamics and, at the best of our knowledge, the first work in which the whole heart hemodynamics is coupled to the surrounding circulation. This chapter is organized as follows: in Section 7.1, we present the whole heart geometry; in Section 7.2, we describe how we compute the displacement by adapting the novel procedure introduced in Section 6.2. In Section 7.3, we couple the 3D model of the whole heart with the surrounding circulation described by the 0D closed-loop model. In Section 7.5 we present the numerical results and in Section 7.6 we draw our concluding remarks.

7.1. The whole heart geometry

We employ the whole heart geometry provided by Zygote [133] that we display in Figure 7.1. From a fluid dynamics view point, the whole heart fluid domain Ω_t is topologically disjoint and split into the left (Ω_t^{LH}) and right (Ω_t^{RH}) parts, as we display in Figure 7.1a, thus

$$\Omega_t = \Omega_t^{\mathrm{RH}} \cup \Omega_t^{\mathrm{LH}},$$

with $\overline{\Omega}_t^{\mathrm{RH}} \cap \overline{\Omega}_t^{\mathrm{LH}} = \emptyset$. Specifically,

$$\Omega_t^{\mathrm{RH}} = \Omega_t^{\mathrm{RA}} \cup \Omega_t^{\mathrm{RV}} \cup \Omega_t^{\mathrm{PT}} \text{ and } \Omega_t^{\mathrm{LH}} = \Omega_t^{\mathrm{LA}} \cup \Omega_t^{\mathrm{LV}} \cup \Omega_t^{\mathrm{AA}},$$

being Ω_t^{RA}, Ω_t^{RV}, Ω_t^{PT} the RA, RV and pulmonary trunk (PT) subdomains defining the RH, and Ω_t^{LA}, Ω_t^{LV}, Ω_t^{AA} the LA, LV and AA subdomains defining the LH.

Analogously, we split the boundary of the whole heart domain as $\partial\Omega_t \equiv \Gamma_t = \Gamma_t^{\mathrm{RH}} \cup \Gamma_t^{\mathrm{LH}}$.

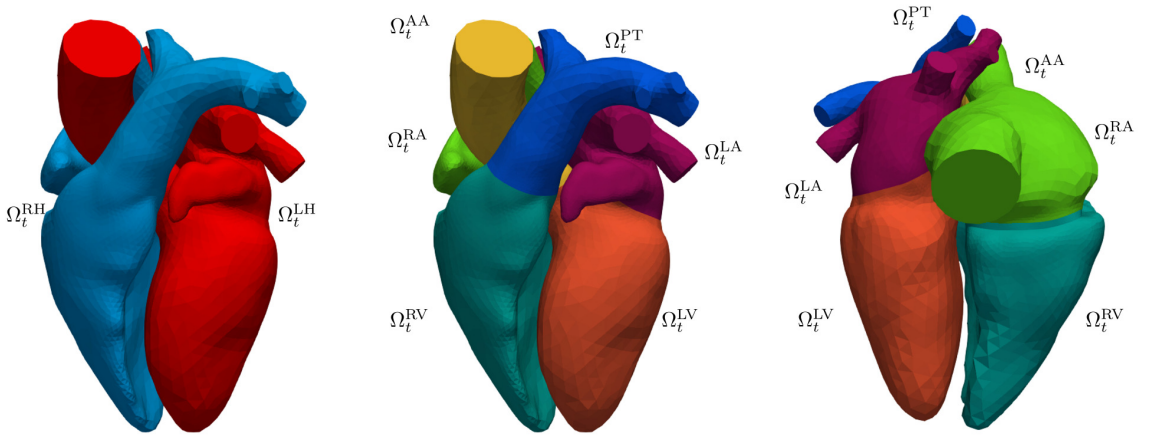

(a) (b) (c)

Figure 7.1: The whole heart domain: $\Omega_t = \Omega_t^{RH} \cup \Omega_t^{LH}$, with $\Omega_t^{RH} = \Omega_t^{RA} \cup \Omega_t^{RV} \cup \Omega_t^{PT}$ and $\Omega_t^{LH} = \Omega_t^{LA} \cup \Omega_t^{LV} \cup \Omega_t^{AA}$: (a) the left and right part; (b) whole heart subdomains from frontal view; (c) whole heart subdomains from posterior view.

In particular, as displayed in Figure 7.2a,

$$\Gamma_t^{RH} = \Gamma^{SupVC} \cup \Gamma^{InfVC} \cup \left(\bigcup_{i=1}^{5} \Gamma^{PArt_i} \right) \cup \Gamma_t^{w,RH},$$

being Γ^{SupVC}, Γ^{InfVC} the inlet section of the superior and inferior venae cavae (VC), Γ^{PArt_i} is the i–th outlet section of the pulmonary artery, with $i = 1, \dots, 5$ and $\Gamma_t^{w,RH}$ the endocardium (wall) of the RH.

On the left part, as reported in Figure 7.2b instead

$$\Gamma_t^{LH} = \left(\bigcup_{i=1}^{5} \Gamma^{PVein_i} \right) \cup \Gamma_t^{AA} \cup \Gamma_t^{w,LH},$$

with Γ^{PVein_i}, $i = 1, \dots, 5$ the five inlet sections of the four pulmonary veins; Γ_t^{AA} the outlet section of the AA and $\Gamma_t^{w,LH}$ the LH endocardium (wall). We denote by $\Gamma_t^{w} = \Gamma_t^{w,LH} \cup \Gamma_t^{RH}$. We display the four valves immersed in the fluid domain in Figure 7.3: we consider the valves geometry provided by Zygote [133]. In the right part, the TV (Σ_{TV}) separates the RA from the RV; the PV (Σ_{PV}) the RV from the PT. In the left part, the MV (Σ_{MV}) separates the LA from the LV, while the AV (Σ_{AV}) the LV from the AA. Zygote provides the cardiac valves in open (TV, MV) and closed (PV, AV) configuration. Thus, as for the left part in Chapter 6, we devise preprocessing procedures aimed at computing a displacement to open/close the valves given the input

configuration. These procedures are mainly based on Laplace-Beltrami problems and exploit algorithms based on closest-point distance.

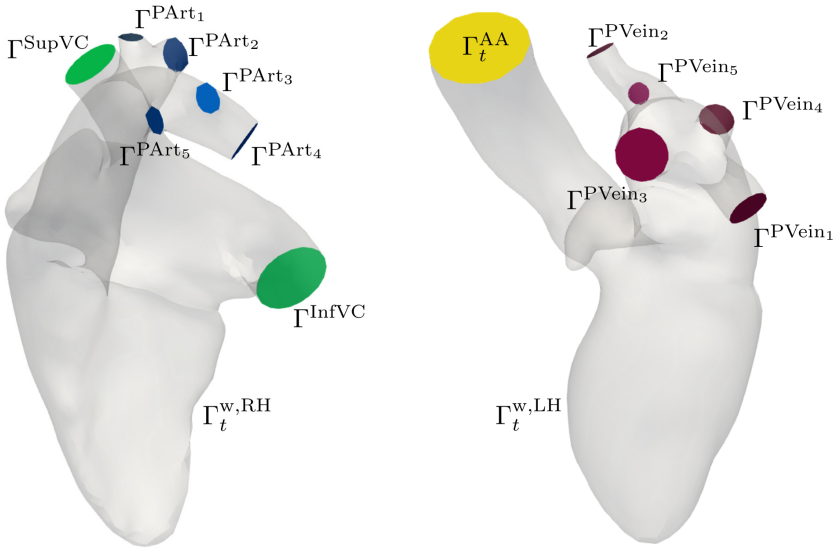

(a) Γ_t^{RH} (b) Γ_t^{LH}

Figure 7.2: Whole heart boundaries: $\partial\Omega_t \equiv \Gamma_t = \Gamma_t^{\text{RH}} \cup \Gamma_t^{\text{LH}}$: (a) $\Gamma_t^{\text{RH}} = \Gamma^{\text{SupVC}} \cup \Gamma^{\text{InfVC}} \cup \left(\bigcup_{i=1}^{5} \Gamma^{\text{PArt}_i}\right) \cup \Gamma_t^{\text{w,RH}}$; (b) $\Gamma_t^{\text{LH}} = \left(\bigcup_{i=1}^{5} \Gamma^{\text{PVein}_i}\right) \cup \Gamma_t^{\text{AA}} \cup \Gamma_t^{\text{w,LH}}$.

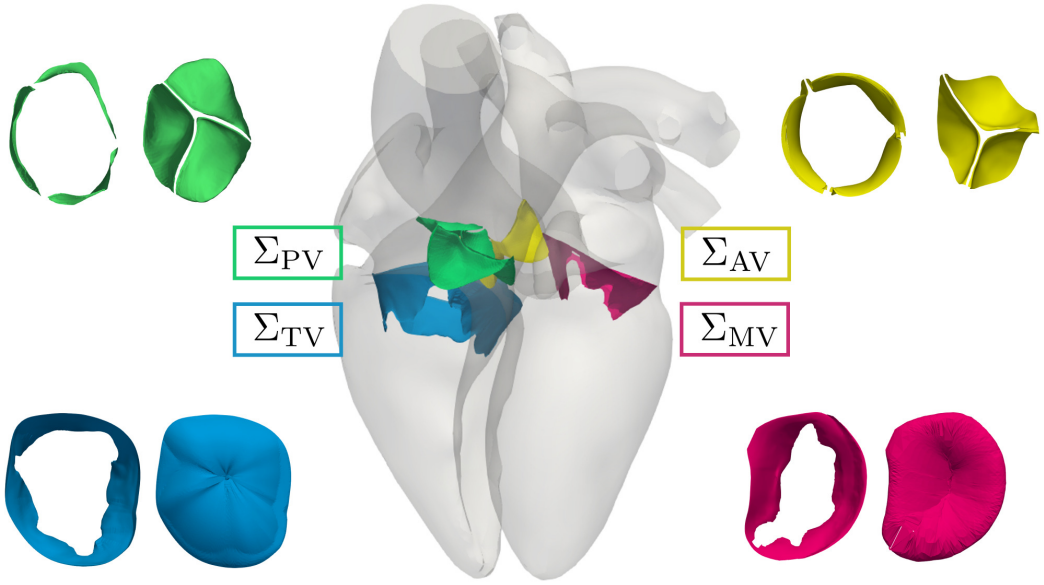

Figure 7.3: Immersed valves in the whole heart geometry: Σ_{TV}, Σ_{PV}, Σ_{MV}, Σ_{AV}.

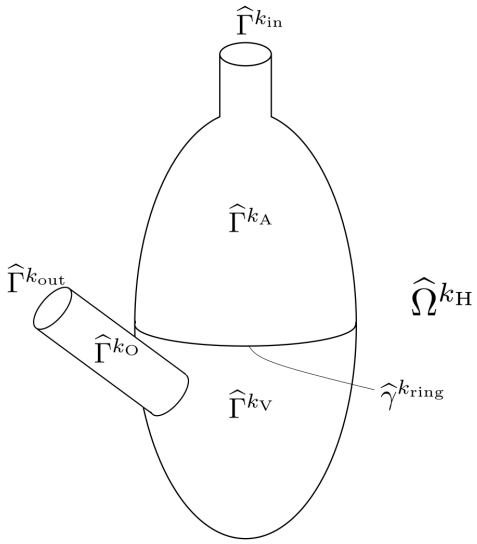

Figure 7.4: The generic idealized geometry that "mimics" a part (right or left) of the human heart.

7.2. Displacement modeling

We compute the displacement $\boldsymbol{d}_\Gamma$ to be prescribed on the whole heart endocardium Γ_t by employing a procedure analogous to the one introduced in Section 6.2. However, differently from the LH case, here we design a more physiological displacement field since we define it in a way that it does not vanish on the rings of the MV and TV, which was a limitation of the previous approach.

Considering that the RH and LH fluid domains are topologically disjoint, we can separately model the RH and LH displacements:

$$\widehat{\boldsymbol{d}}_\Gamma = \begin{cases} \widehat{\boldsymbol{d}}_\Gamma^{\text{RH}} & \text{on } \widehat{\Gamma}^{\text{RH}} \times (0, T_f), \\ \widehat{\boldsymbol{d}}_\Gamma^{\text{LH}} & \text{on } \widehat{\Gamma}^{\text{LH}} \times (0, T_f). \end{cases} \tag{7.1}$$

In the following, we explain how we compute the displacement $\widehat{\boldsymbol{d}}_\Gamma^{k_{\text{H}}}$ on a single part of the heart k_{H}, with $k_{\text{H}} = \text{RH}, \text{LH}$; the procedure is then extended on both sides (LH and RH). We thus consider a generic heart geometry $\widehat{\Omega}^{k_{\text{H}}}$ – as displayed in Figure 7.4 – whose boundary $\widehat{\Gamma}^{k_{\text{H}}}$ is made of an inlet section $\widehat{\Gamma}^{k_{\text{in}}}$, the atrium $\widehat{\Gamma}^{k_{\text{A}}}$, the ventricle $\widehat{\Gamma}^{k_{\text{V}}}$, the outflow tract $\widehat{\Gamma}^{k_{\text{O}}}$ and the outlet section $\widehat{\Gamma}^{k_{\text{out}}}$. We show the analogy between the boundaries of this idealized geometry and the boundaries of the real RH and LH in Table 7.1. In particular, the inlet sections represent the venae cavae in the RH and the pulmonary veins section in the LH; the outlet section represents the outlet sections of the pulmonary artery in the RH and the outlet section of the AA in the LH. The

Idealized geometry	RH	LH
$\widehat{\Gamma}^{k_{\mathrm{H}}}$	$\widehat{\Gamma}^{\mathrm{RH}}$	$\widehat{\Gamma}^{\mathrm{LH}}$
$\widehat{\Gamma}^{k_{\mathrm{A}}}$	$\widehat{\Gamma}^{\mathrm{RA}}$	$\widehat{\Gamma}^{\mathrm{LA}}$
$\widehat{\Gamma}^{k_{\mathrm{V}}}$	$\widehat{\Gamma}^{\mathrm{RV}}$	$\widehat{\Gamma}^{\mathrm{LV}}$
$\widehat{\Gamma}^{k_{\mathrm{O}}}$	$\widehat{\Gamma}^{\mathrm{PT}}$	$\widehat{\Gamma}^{\mathrm{AA}}$
$\widehat{\Gamma}^{k_{\mathrm{in}}}$	$\widehat{\Gamma}^{\mathrm{SupVC}} \cup \widehat{\Gamma}^{\mathrm{InfVC}}$	$\bigcup_{i=1}^{5} \widehat{\Gamma}^{\mathrm{PVein}_i}$
$\widehat{\Gamma}^{k_{\mathrm{out}}}$	$\bigcup_{i=1}^{5} \widehat{\Gamma}^{\mathrm{PArt}_i}$	$\widehat{\Gamma}^{\mathrm{AA}}$
$\widehat{\gamma}^{k_{\mathrm{ring}}}$	$(\widehat{\Gamma}^{\mathrm{RA}} \cap \widehat{\Gamma}^{\mathrm{RV}}) \cup (\widehat{\Gamma}^{\mathrm{RV}} \cap \widehat{\Gamma}^{\mathrm{PT}})$	$(\widehat{\Gamma}^{\mathrm{LA}} \cap \widehat{\Gamma}^{\mathrm{LV}}) \cup (\widehat{\Gamma}^{\mathrm{LV}} \cap \widehat{\Gamma}^{\mathrm{AA}})$

Table 7.1: Analogy between the domain boundaries in the idealized geometry and the boundaries of RH and LH.

atrium represents the RA and LA, the ventricle the RV and LV, the outflow tract the PT and the AA, in the RH and LH respectively.

We assume that a displacement defined on the ventricle $\widehat{\boldsymbol{d}}^{k_{\mathrm{V}}}_{\mathrm{datum}}$ on $\widehat{\Gamma}^{k_{\mathrm{V}}} \times (0, T_f)$ is available. It can be acquired via images data or computed from a ventricular EM simulation and restricted on its endocardium (as we do for instance in Section 6.2).

We define the overall displacement on the part k_{H} of the heart as

$$\widehat{\boldsymbol{d}}^{k_{\mathrm{H}}}_{\Gamma}(\widehat{\boldsymbol{x}}, t) = \widehat{\boldsymbol{d}}^{k_{\mathrm{V}}}(\widehat{\boldsymbol{x}}, t) + \widehat{\boldsymbol{d}}^{k_{\mathrm{A}}}(\widehat{\boldsymbol{x}}, t), \quad \text{on } \widehat{\Gamma}^{k_{\mathrm{H}}} \times (0, T_f), \tag{7.2}$$

being

- $\widehat{\boldsymbol{d}}^{k_{\mathrm{V}}}$ on $\widehat{\Gamma}^{k_{\mathrm{H}}} \times (0, T_f)$ the displacement of the ventricle extended on $\widehat{\Gamma}^{k_{\mathrm{H}}}$:

$$\widehat{\boldsymbol{d}}^{k_{\mathrm{V}}}(\widehat{\boldsymbol{x}}, t) = \begin{cases} \widehat{\boldsymbol{d}}^{k_{\mathrm{V}}}_{\mathrm{datum}}(\widehat{\boldsymbol{x}}, t) & \text{on } \widehat{\Gamma}^{k_{\mathrm{V}}} \times (0, T_f), \\ \widehat{\boldsymbol{d}}_{*}(\widehat{\boldsymbol{x}}, t) & \text{on } \widehat{\Gamma}^{k_{\mathrm{H}}} \setminus \widehat{\Gamma}^{k_{\mathrm{V}}} \times (0, T_f), \end{cases} \tag{7.3}$$

with $\widehat{\boldsymbol{d}}_*$ solution of the following Laplace-Beltrami problem:

$$-\Delta_{\widehat{\Gamma}}\widehat{\boldsymbol{d}}_* = \boldsymbol{0} \qquad \text{on } \widehat{\Gamma}^{k_{\mathrm{H}}} \setminus \left(\widehat{\Gamma}^{k_{\mathrm{V}}} \cup \widehat{\Gamma}^{k_{\mathrm{in}}}\right) \times (0, T_f), \tag{7.4a}$$

$$\widehat{\boldsymbol{d}}_* = \widehat{\boldsymbol{d}}^{k_{\mathrm{V}}}_{\mathrm{datum}} \qquad \text{on } \widehat{\gamma}^{k_{\mathrm{ring}}} \times (0, T_f), \tag{7.4b}$$

$$\widehat{\boldsymbol{d}}_* = \boldsymbol{0} \qquad \text{on } \partial\widehat{\Gamma}^{k_{\mathrm{in}}} \times (0, T_f), \tag{7.4c}$$

being $\widehat{\gamma}^{k_{\mathrm{ring}}} = \widehat{\Gamma}^{k_{\mathrm{V}}} \cap \widehat{\Gamma}^{k_{\mathrm{A}}}$, as displayed in Figure 7.4.

- $\widehat{\boldsymbol{d}}^{k_{\mathrm{A}}}$ on $\widehat{\Gamma}^{k_{\mathrm{H}}} \times (0, T_f)$ the displacement accounting for the atrial motion.

7.2.1. Modeling the atrial displacement

To model $\widehat{\boldsymbol{d}}^{k_{\mathrm{A}}}$, we assume separation of variables:

$$\widehat{\boldsymbol{d}}^{k_{\mathrm{A}}}(\widehat{\boldsymbol{x}}, t) = \widehat{\varphi}^{k_{\mathrm{A}}}(\widehat{\boldsymbol{x}})\widehat{\boldsymbol{e}}^{k_{\mathrm{A}}}_{\mathrm{G}}(\widehat{\boldsymbol{x}})g^{k_{\mathrm{A}}}(t) \quad \text{ on } \widehat{\Gamma}^{k_{\mathrm{H}}}, \tag{7.5}$$

being $\widehat{\varphi}^{k_{\mathrm{A}}}(\widehat{\boldsymbol{x}})$ a characteristic function equal to 1 on $\widehat{\Gamma}^{k_{\mathrm{A}}}$ and smoothly vanishing on $\widehat{\Gamma}^{k_{\mathrm{in}}} \cup \widehat{\Gamma}^{k_{\mathrm{V}}} \cup \widehat{\Gamma}^{k_{\mathrm{O}}} \cup \widehat{\Gamma}^{k_{\mathrm{out}}}$; $\widehat{\boldsymbol{e}}^{k_{\mathrm{A}}}_{\mathrm{G}}$ the unit vector directed towards the atrial center of mass and $g^{k_{\mathrm{A}}}(t)$ the time dependent function. Following the same steps introduced in Section 6.2.2, it can be shown that $g^{k_{\mathrm{A}}}$ is the solution of the following Cauchy's problem:

$$\begin{cases} \dfrac{\mathrm{d}g^{k_{\mathrm{A}}}(t)}{\mathrm{d}t} &= \dfrac{\Phi^{k_{\mathrm{A}}}(t)}{\mathcal{B}^{k_{\mathrm{A}}}(t)}, \quad t \in (0, T_f), \\ g^{k_{\mathrm{A}}}(0) &= g_0^{k_{\mathrm{A}}}, \end{cases} \tag{7.6}$$

being

$$\mathcal{B}^{k_{\mathrm{A}}}(t) = \oint_{\Gamma_t^{k_{\mathrm{H}}}} \varphi^{k_{\mathrm{A}}}(\boldsymbol{x})\boldsymbol{e}^{k_{\mathrm{A}}}_{\mathrm{G}}(\boldsymbol{x}) \cdot \boldsymbol{n}\,\mathrm{d}\boldsymbol{x}, \quad \mathcal{A}^{k_{\mathrm{A}}}(t) = \oint_{\Gamma_t^{k_{\mathrm{H}}}} \frac{\partial}{\partial t}\left(\boldsymbol{d}^{k_{\mathrm{V}}}(\boldsymbol{x}, t)\right) \cdot \boldsymbol{n}\,\mathrm{d}\boldsymbol{x}, \tag{7.7}$$

$$\Phi^{k_{\mathrm{A}}}(t) = \frac{\mathrm{d}V^{k_{\mathrm{H}}}(t)}{\mathrm{d}t} - \mathcal{A}^{k_{\mathrm{A}}}(t) = \frac{\mathrm{d}V^{k_{\mathrm{A}}}(t)}{\mathrm{d}t} + \frac{\mathrm{d}V^{k_{\mathrm{V}}}(t)}{\mathrm{d}t} + \frac{\mathrm{d}V^{k_{\mathrm{O}}}(t)}{\mathrm{d}t} - \mathcal{A}^{k_{\mathrm{A}}}(t). \tag{7.8}$$

In Equation (7.8), $V^{k_{\mathrm{H}}}(t) = |\Omega_t^{k_{\mathrm{H}}}|$ is the volume of the domain considered (LH or RH), with $V^{k_{\mathrm{H}}}(t) = V^{k_{\mathrm{A}}}(t) + V^{k_{\mathrm{V}}}(t) + V^{k_{\mathrm{O}}}(t)$, being the volumes of the atrium, ventricle and outflow tract. As for the LH (see Section 6.2.2), to compute $V^{k_{\mathrm{V}}}$ and $V^{k_{\mathrm{O}}}$ we solve a preliminary lifting problem in the fluid domain using as Dirichlet datum on the whole boundary $\widehat{\boldsymbol{d}}^{k_{\mathrm{V}}}$; for the atrial volume instead, we set

$$V^{k_{\mathrm{A}}}(t) = V^{k_{\mathrm{A}}}_{\mathrm{0D}}(t), \tag{7.9}$$

being $V^{k_{\mathrm{A}}}_{\mathrm{0D}}(t)$ the atrial volume computed through the 0D closed-loop model. We remark that by applying this method to the whole-heart geometry, penetration between the RA and LA may occur. In order to avoid this, one should account for a proper contact

model among atria's walls.

7.2.2. Biventricular EM simulation

To compute the ventricular displacement, we employ the EM model of the biventricular (BiV) geometry (i.e. RV and LV) developed in [204]. Electrophysiology is modelled through the Monodomain equation [95] and coupled with the ventricular ten Tusscher-Panfilov ionic model [255]. The mechanical response of the tissue is modelled via an active stress approach: the first Piola-Kirchhoff stress tensor is decomposed into passive mechanics and orthotropic active stress. In particular, the passive behaviour of the tissue is modelled through the Guccione strain energy density function [112]; subcellular generation of active force is modelled by means of ANNs through the RDQ20-MF model [221]. We set generalized Robin-type BCs at the epicardium and we impose energy-consistent BCs [222] on the rings of the TV, PV, MV and AV. Fibers distribution is considered through the rule-based method by Doste et al. [78, 203]. The 3D BiV EM model is coupled to the 0D closed-loop circulation model of the remaining cardiovascular system introduced in Section 4.4. For the numerical approximation of the problem, we use linear FE for the space discretization. Specifically, we use a coarser grid for the elastodynamic and a finer one for the electrophysiology, due to the higher resolution required by the latter, and we employ an intergrid transfer operator [229] between two nested grids. The coupled EM problem is solved by means of a segregated-intergrid-staggered numerical scheme presented in [223]. For additional details on this model we refer to [204, 223, 224].

We report our EM solution on the BiV geometry in Figure 7.7. Furthermore, in Figure 7.5, we display a clip on the apico-basal direction and the displacement field restricted on the endocardium of the ventricles: walls of the ventricles fluid domain ($\widehat{\Gamma}^{\mathrm{RV}}$, $\widehat{\Gamma}^{\mathrm{LV}}$). The displacement fields on $\widehat{\Gamma}^{\mathrm{RV}} \times (0, T_f)$ and $\widehat{\Gamma}^{\mathrm{LV}} \times (0, T_f)$ represent the the displacements we have available previously denoted as $\widehat{\boldsymbol{d}}^{k_{\mathrm{V}}}_{\mathrm{datum}}$.

We display the displacement obtained on the whole heart by means of the proposed methodology in different time instants of the heartcycle in Figure 7.8. On the ventricles, the displacement is the EM displacement restricted to the endocardium of the BiV geometry. On the atria and outflow tracts, it is the result of our novel preprocessing procedure. We highlight that, by defining the displacement as in Equation (7.2) instead of as in Equation (6.5), we get a more physiological motion of the valvular plane: we better capture the lowering of the plane of the TV and MV, differently from the result we achieve in the case of the sole LH (see Figure 6.7). Finally, we report in Figure 7.6 the volumes of RA, RV, PT, LA, LV and AA.

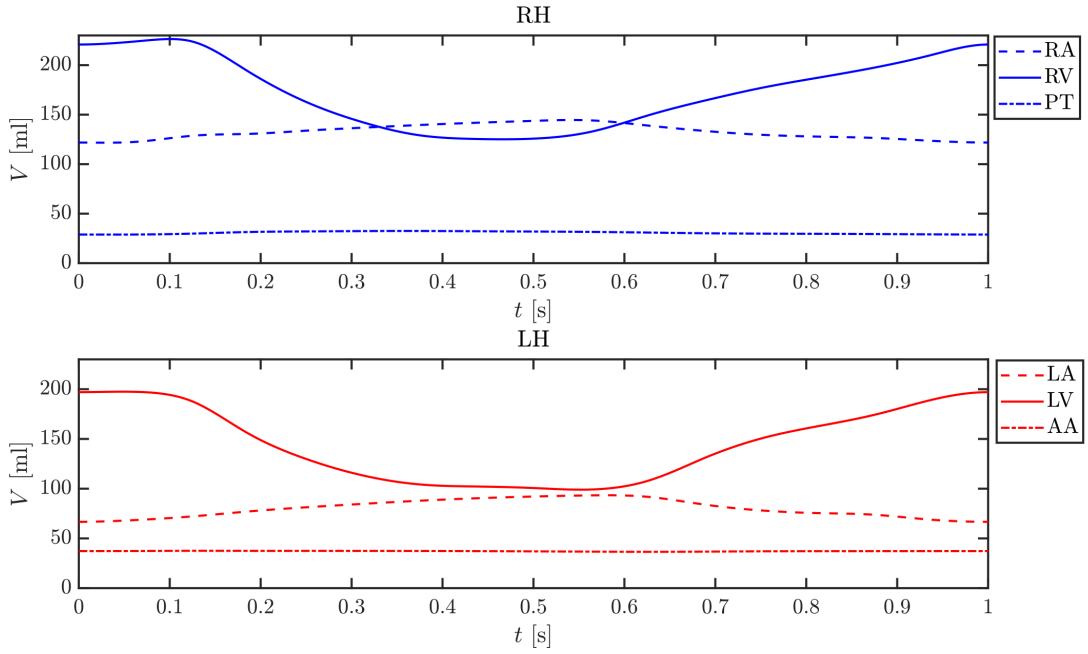

Figure 7.6: Volumes of RA, RV, PT (top), LA, RV, AA (bottom).

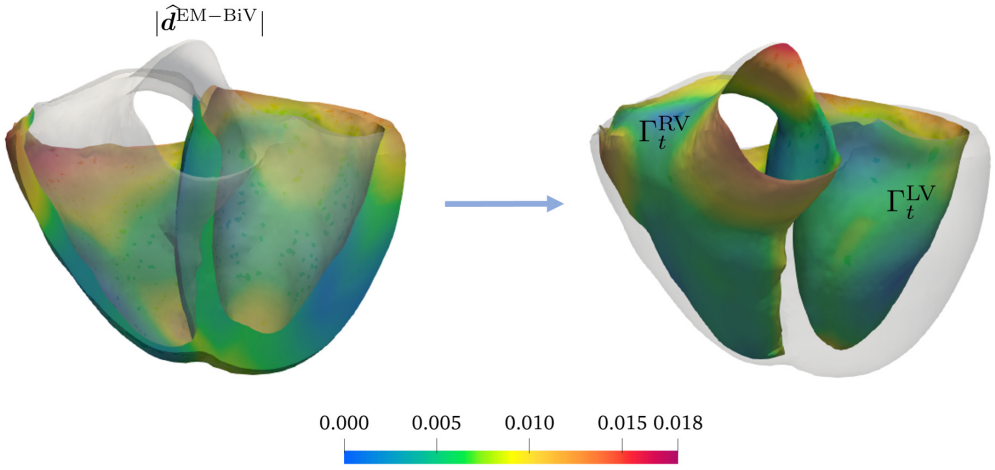

Figure 7.5: Displacement of the BiV geometry during systole (current configuration). On the left: a clip in the apico-basal direction; on the right: the EM displacement restricted on the BiV endocardium, i.e. on $\widehat{\Gamma}_t^{\mathrm{RV}}$ and $\widehat{\Gamma}_t^{\mathrm{RV}}$.

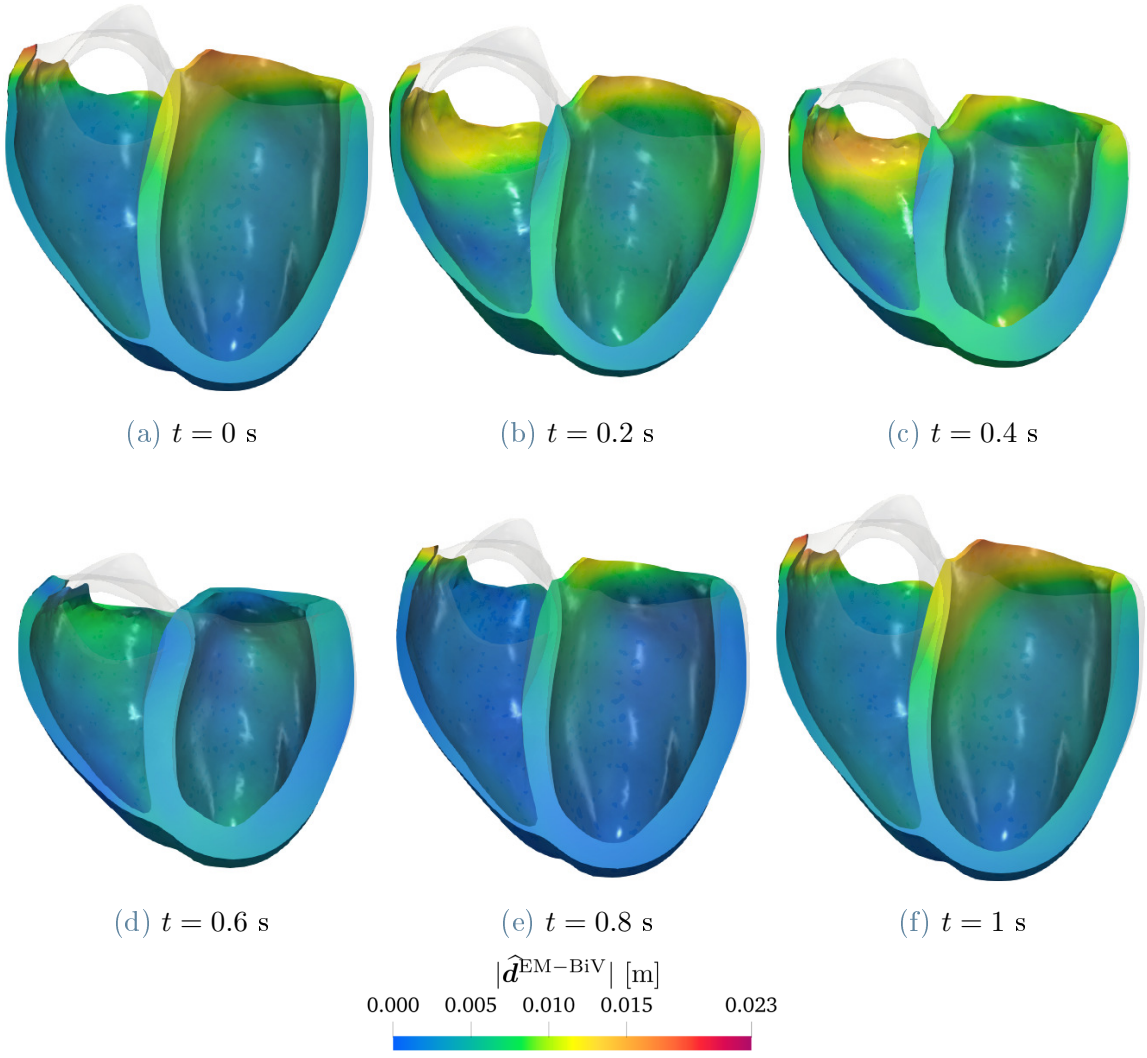

(a) $t = 0$ s (b) $t = 0.2$ s (c) $t = 0.4$ s

(d) $t = 0.6$ s (e) $t = 0.8$ s (f) $t = 1$ s

Figure 7.7: Displacement of the BiV geometry obtained via the EM simulation.

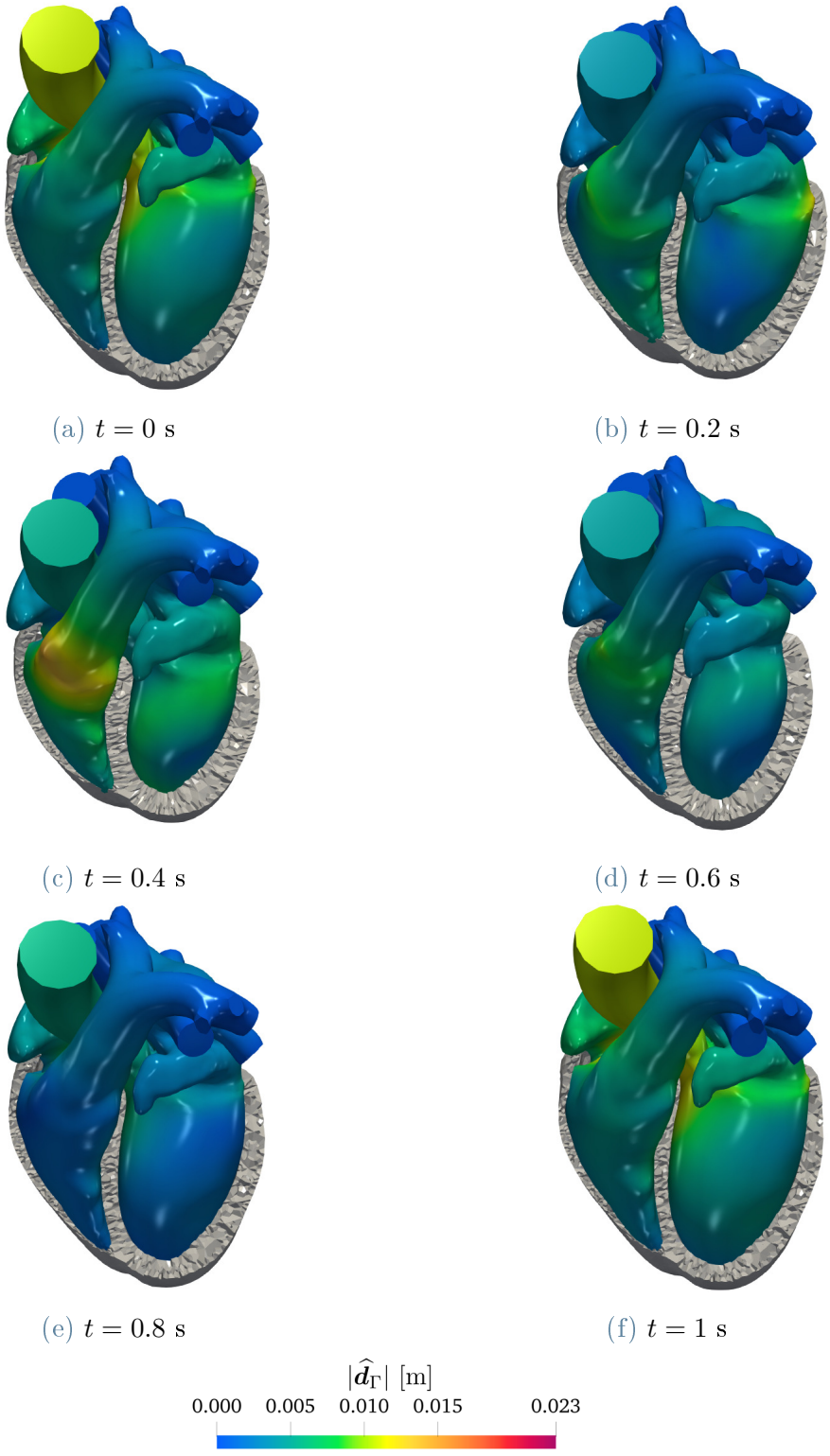

(a) $t = 0$ s (b) $t = 0.2$ s

(c) $t = 0.4$ s (d) $t = 0.6$ s

(e) $t = 0.8$ s (f) $t = 1$ s

Figure 7.8: Whole heart boundary displacement field at different instants of the heartbeat.

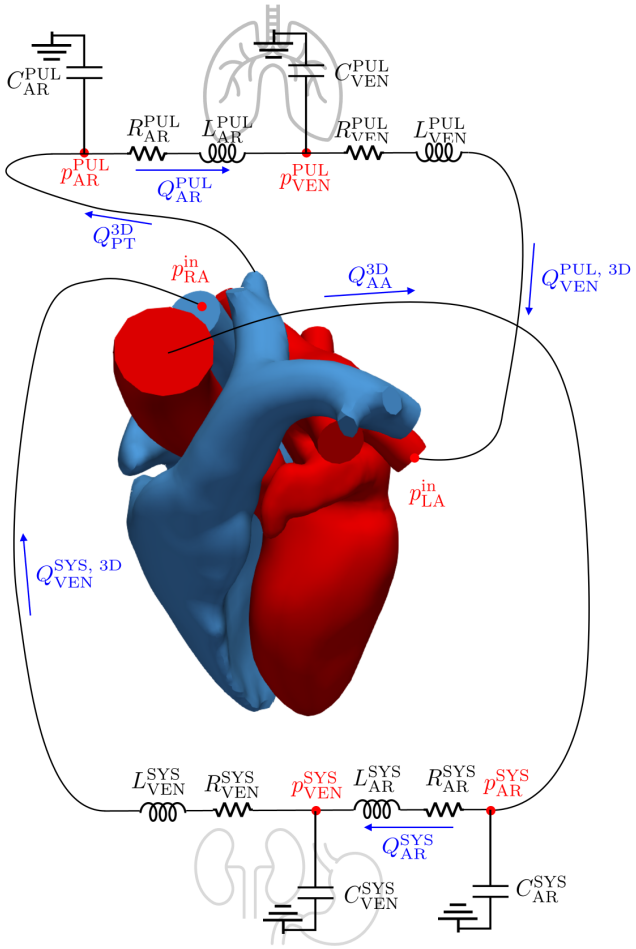

Figure 7.9: The 3D-0D multiscale CFD model of the whole heart coupled to the external systemic and pulmonary circulation.

7.3. The 3D-0D CFD model of the whole heart coupled with the external circulation

In the following, we present the 3D CFD model of the whole heart, the reduced 0D circulation model and the coupling conditions among the 3D and the 0D models. The 3D model consists of Equation (4.17) and we prescribe the following BCs on the inlet, outlet sections and wall of the whole heart domain:

$$\boldsymbol{\sigma}(\boldsymbol{u},p)\boldsymbol{n} = -p_{\mathrm{IN,RH}}\boldsymbol{n} \qquad \text{on } \left(\Gamma^{\mathrm{SupVC}} \cup \Gamma^{\mathrm{InfVC}}\right) \times (0,T_f), \tag{7.10a}$$

$$\boldsymbol{\sigma}(\boldsymbol{u},p)\boldsymbol{n} = -p_{\mathrm{OUT,RH}}\boldsymbol{n} \qquad \text{on } \Gamma^{\mathrm{PArt}_i} \times (0,T_f), \quad i = 1,\dots,5, \tag{7.10b}$$

$$\boldsymbol{\sigma}(\boldsymbol{u},p)\boldsymbol{n} = -p_{\mathrm{IN,LH}}\boldsymbol{n} \qquad \text{on } \Gamma^{\mathrm{PVein}_i}\times(0,T_f), \quad i=1,\dots,5, \tag{7.10c}$$

$$\boldsymbol{\sigma}(\boldsymbol{u},p)\boldsymbol{n} = -p_{\mathrm{OUT,LH}}\boldsymbol{n} \qquad \text{on } \Gamma_t^{\mathrm{AA}}\times(0,T_f), \tag{7.10d}$$

$$\boldsymbol{d} = \boldsymbol{d}_\Gamma \qquad \text{on } \Gamma_t^{\mathrm{w}}\times(0,T_f), \tag{7.10e}$$

being $p_{\mathrm{IN,RH}}(t)$, $p_{\mathrm{OUT,RH}}(t)$, $p_{\mathrm{IN,LH}}(t)$, $p_{\mathrm{OUT,LH}}(t)$ the averaged pressure to be prescribed at inlet and outlet sections of the RH and LH section boundaries. In particular, in all the Neumann BCs we introduce backflow stabilization to weakly penalize the reverse flow [32] and we treat the new non-linearity introduced as we consider the one in the NS equations [36], so in our specific case, in a semi-implicit fashion.

By referring to Figures 4.3 and 7.9, to couple the CFD model with the circulation, we remove from the 0D model all those equations that are already described by the 3D counterpart, namely Equations (4.31a), (4.31b), (4.31c), (4.31d), (4.32a), (4.32b), (4.32c), (4.32d), (4.33a), (4.33b), (4.33c) and (4.33d). The coupling between che 3D and 0D models consists of the enforcement of the continuity of flowrates and pressures on the "artificially chopped" boundaries, i.e. inlet and outlet sections of the 3D whole heart domain. Referring to Figure 7.10, the continuity of pressures yields:

$$p_{\mathrm{IN,RH}}(t) = p_{\mathrm{RA}}^{\mathrm{in}}(t), \tag{7.11a}$$

$$p_{\mathrm{OUT,RH}}(t) = p_{\mathrm{AR}}^{\mathrm{PUL}}(t), \tag{7.11b}$$

$$p_{\mathrm{IN,LH}}(t) = p_{\mathrm{LA}}^{\mathrm{in}}(t), \tag{7.11c}$$

$$p_{\mathrm{OUT,LH}}(t) = p_{\mathrm{AR}}^{\mathrm{SYS}}(t), \tag{7.11d}$$

and the continuity of flowrates:

$$Q_{\mathrm{VEN}}^{\mathrm{SYS}}(t) = -Q_{\mathrm{VEN}}^{\mathrm{SYS,\,3D}}(t) = \int_{\Gamma^{\mathrm{SupVC}}\cup\Gamma^{\mathrm{InfVC}}} \big(\boldsymbol{u}(\boldsymbol{x},t) - \boldsymbol{u}^{\mathrm{ALE}}(\boldsymbol{x},t)\big)\cdot\boldsymbol{n}(\boldsymbol{x},t)\,\mathrm{d}\boldsymbol{x}, \tag{7.12a}$$

$$Q_{\mathrm{PV}}(t) = Q_{\mathrm{PT}}^{\mathrm{3D}}(t) = \int_{\bigcup_{i=1}^{5}\Gamma^{\mathrm{PArt}_i}} \big(\boldsymbol{u}(\boldsymbol{x},t) - \boldsymbol{u}^{\mathrm{ALE}}(\boldsymbol{x},t)\big)\cdot\boldsymbol{n}(\boldsymbol{x},t)\,\mathrm{d}\boldsymbol{x}, \tag{7.12b}$$

$$Q_{\mathrm{VEN}}^{\mathrm{PUL}}(t) = -Q_{\mathrm{VEN}}^{\mathrm{PUL,\,3D}}(t) = \int_{\bigcup_{i=1}^{5}\Gamma_t^{\mathrm{PVein}_i}} \big(\boldsymbol{u}(\boldsymbol{x},t) - \boldsymbol{u}^{\mathrm{ALE}}(\boldsymbol{x},t)\big)\cdot\boldsymbol{n}(\boldsymbol{x},t)\,\mathrm{d}\boldsymbol{x}, \tag{7.12c}$$

$$Q_{\mathrm{AV}}(t) = Q_{\mathrm{AA}}^{\mathrm{3D}}(t) = \int_{\Gamma_t^{\mathrm{AA}}} \big(\boldsymbol{u}(\boldsymbol{x},t) - \boldsymbol{u}^{\mathrm{ALE}}(\boldsymbol{x},t)\big)\cdot\boldsymbol{n}(\boldsymbol{x},t)\,\mathrm{d}\boldsymbol{x}. \tag{7.12d}$$

In Equations (7.11a) and (7.11c), we set the continuity of pressure on the inlets section of the RH and LH with the inlet left and right atrial pressure. By considering Equations (4.31j) and (4.31l), the pressures downwind the "SYS-VEN" and "PUL-VEN" RLC systems were originally labelled as p_{RA} and p_{LA} (see Figure 4.3). However, in this context they represent the pressures to be prescribed at the inlet sections of our 3D domain, thus we rename them as $p_{\mathrm{RA}}^{\mathrm{in}}$ and $p_{\mathrm{LA}}^{\mathrm{in}}$. In particular, they can be computed

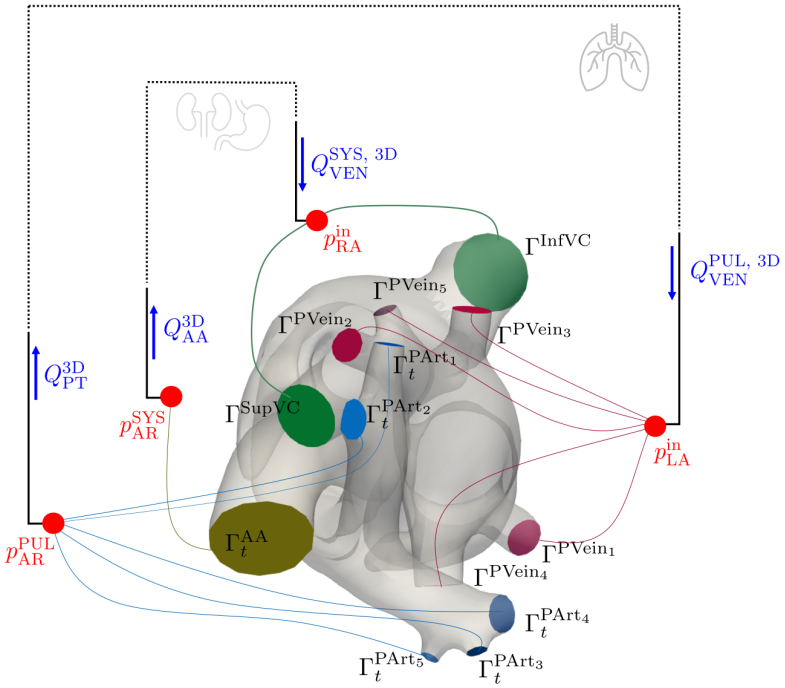

Figure 7.10: Interfaces conditions in the coupled problem.

by solving Equations (4.31j) and (4.31l) for p_{RA} and p_{LA} respectively, leading to

$$p_{\text{RA}}^{\text{in}}(t) = p_{\text{VEN}}^{\text{SYS}}(t) - R_{\text{VEN}}^{\text{SYS}} Q_{\text{VEN}}^{\text{SYS, 3D}}(t) - L_{\text{VEN}}^{\text{SYS}} \frac{\mathrm{d}Q_{\text{VEN}}^{\text{SYS, 3D}}(t)}{\mathrm{d}t}, \tag{7.13a}$$

$$p_{\text{LA}}^{\text{in}}(t) = p_{\text{VEN}}^{\text{PUL}}(t) - R_{\text{VEN}}^{\text{PUL}} Q_{\text{VEN}}^{\text{PUL, 3D}}(t) - L_{\text{VEN}}^{\text{PUL}} \frac{\mathrm{d}Q_{\text{VEN}}^{\text{PUL, 3D}}(t)}{\mathrm{d}t}. \tag{7.13b}$$

Conversely, in Equations (7.12b) and (7.12d), the flowrates $Q_{\text{PV}}(t)$ and $Q_{\text{AV}}(t)$ in the 0D model represent the outlet flowrate at the PT sections (on $\bigcup_{i=1}^{5} \Gamma_t^{\text{PArt}_i}$) and AA section (on Γ_t^{AA}) in our 3D model. Hence, we replace them by $Q_{\text{PT}}^{\text{3D}}(t)$ and $Q_{\text{AA}}^{\text{3D}}(t)$ respectively.

The reduced 0D model

The reduced 0D model that we obtain is the following: for any $t \in (0, T_f)$:

$$\frac{\mathrm{d}p_{\text{AR}}^{\text{SYS}}(t)}{\mathrm{d}t} = \frac{1}{C_{\text{AR}}^{\text{SYS}}} \left(Q_{\text{AA}}^{\text{3D}}(t) - Q_{\text{AR}}^{\text{SYS}}(t) \right), \tag{7.14a}$$

$$\frac{\mathrm{d}p_{\text{VEN}}^{\text{SYS}}(t)}{\mathrm{d}t} = \frac{1}{C_{\text{VEN}}^{\text{SYS}}} \left(Q_{\text{AR}}^{\text{SYS}}(t) - Q_{\text{VEN}}^{\text{SYS, 3D}}(t) \right), \tag{7.14b}$$

$$\frac{\mathrm{d}p_{\mathrm{AR}}^{\mathrm{PUL}}(t)}{\mathrm{d}t} = \frac{1}{C_{\mathrm{AR}}^{\mathrm{PUL}}}\left(Q_{\mathrm{PT}}^{\mathrm{3D}}(t) - Q_{\mathrm{AR}}^{\mathrm{PUL}}(t)\right), \tag{7.14c}$$

$$\frac{\mathrm{d}p_{\mathrm{VEN}}^{\mathrm{PUL}}(t)}{\mathrm{d}t} = \frac{1}{C_{\mathrm{VEN}}^{\mathrm{PUL}}}\left(Q_{\mathrm{AR}}^{\mathrm{PUL}}(t) - Q_{\mathrm{PUL}}^{\mathrm{VEN,\,3D}}(t)\right), \tag{7.14d}$$

$$\frac{\mathrm{d}Q_{\mathrm{AR}}^{\mathrm{SYS}}(t)}{\mathrm{d}t} = \frac{R_{\mathrm{AR}}^{\mathrm{SYS}}}{L_{\mathrm{AR}}^{\mathrm{SYS}}}\left(-Q_{\mathrm{AR}}^{\mathrm{SYS}}(t) - \frac{p_{\mathrm{VEN}}^{\mathrm{SYS}}(t) - p_{\mathrm{AR}}^{\mathrm{SYS}}(t)}{R_{\mathrm{AR}}^{\mathrm{SYS}}}\right), \tag{7.14e}$$

$$\frac{\mathrm{d}Q_{\mathrm{AR}}^{\mathrm{PUL}}(t)}{\mathrm{d}t} = \frac{R_{\mathrm{AR}}^{\mathrm{PUL}}}{L_{\mathrm{AR}}^{\mathrm{PUL}}}\left(-Q_{\mathrm{AR}}^{\mathrm{PUL}}(t) - \frac{p_{\mathrm{VEN}}^{\mathrm{PUL}}(t) - p_{\mathrm{AR}}^{\mathrm{PUL}}(t)}{R_{\mathrm{AR}}^{\mathrm{PUL}}}\right), \tag{7.14f}$$

solved with suitable initial conditions, and

$$p_{\mathrm{LA}}^{\mathrm{in}}(t) = p_{\mathrm{VEN}}^{\mathrm{PUL}}(t) - R_{\mathrm{VEN}}^{\mathrm{PUL}} Q_{\mathrm{VEN}}^{\mathrm{PUL,\,3D}}(t) - L_{\mathrm{VEN}}^{\mathrm{PUL}} \frac{\mathrm{d}Q_{\mathrm{VEN}}^{\mathrm{PUL,\,3D}}(t)}{\mathrm{d}t}, \tag{7.15a}$$

$$p_{\mathrm{RA}}^{\mathrm{in}}(t) = p_{\mathrm{VEN}}^{\mathrm{SYS}}(t) - R_{\mathrm{VEN}}^{\mathrm{SYS}} Q_{\mathrm{VEN}}^{\mathrm{SYS,\,3D}}(t) - L_{\mathrm{VEN}}^{\mathrm{SYS}} \frac{\mathrm{d}Q_{\mathrm{VEN}}^{\mathrm{SYS,\,3D}}(t)}{\mathrm{d}t}. \tag{7.15b}$$

We gather the unknown variables of Equations (7.14) in a vector $\boldsymbol{c}(t) = (p_{\mathrm{AR}}^{\mathrm{SYS}}(t),\, p_{\mathrm{VEN}}^{\mathrm{SYS}}(t),\, p_{\mathrm{AR}}^{\mathrm{PUL}}(t),\, p_{\mathrm{VEN}}^{\mathrm{PUL}}(t),\, Q_{\mathrm{AR}}^{\mathrm{SYS}}(t),\, Q_{\mathrm{AR}}^{\mathrm{PUL}}(t))^T$ and the left-hand side of Equation (7.15) in a vector $\widetilde{\boldsymbol{c}}(t) = (p_{\mathrm{LA}}^{\mathrm{in}}(t),\, p_{\mathrm{RA}}^{\mathrm{in}}(t))^T$. We then collect the right-hand sides of Equation (7.14) and (7.15) respectively in the vectors $\boldsymbol{r}(t, \boldsymbol{c}(t)(t))$ and $\widetilde{\boldsymbol{r}}(t, \boldsymbol{c}(t))$. Hence, the reduced 0D model, enriched with suitable initial conditions, is expressed in a compact form as

$$\frac{\mathrm{d}\boldsymbol{c}(t)}{\mathrm{d}t} = \boldsymbol{r}(t, \boldsymbol{c}(t)) \qquad t \in (0, T_f), \tag{7.16a}$$

$$\widetilde{\boldsymbol{c}}(t) = \widetilde{\boldsymbol{r}}(t, \boldsymbol{c}(t)) \qquad t \in (0, T_f), \tag{7.16b}$$

$$\boldsymbol{c}(0) = \boldsymbol{c}_0. \tag{7.16c}$$

Note that, differently from the coupling with the LH (see Equation (6.29)), the right hand side $\boldsymbol{r}$ does not depend anymore from $\widetilde{c}$ because all those variables are now substituted by the 3D model.

The multiscale 3D-0D problem

The overall set of 3D-0D coupled equations is expressed as

$$\begin{aligned}
&\rho \frac{\widehat{\partial}\boldsymbol{u}}{\widehat{\partial}t} + \rho\left(\left(\boldsymbol{u} - \boldsymbol{u}^{\mathrm{ALE}}\right)\cdot\nabla\right)\boldsymbol{u} \\
&- \nabla\cdot\boldsymbol{\sigma}(\boldsymbol{u}, p) \\
&+ \frac{R_{\mathrm{TV}}}{\varepsilon_{\mathrm{TV}}}\delta_{\Sigma_{\mathrm{TV}},\varepsilon_{\mathrm{TV}}}\boldsymbol{u} + \frac{R_{\mathrm{PV}}}{\varepsilon_{\mathrm{PV}}}\delta_{\Sigma_{\mathrm{PV}},\varepsilon_{\mathrm{PV}}}\boldsymbol{u} \\
&+ \frac{R_{\mathrm{MV}}}{\varepsilon_{\mathrm{MV}}}\delta_{\Sigma_{\mathrm{MV}},\varepsilon_{\mathrm{MV}}}\boldsymbol{u} + \frac{R_{\mathrm{AV}}}{\varepsilon_{\mathrm{AV}}}\delta_{\Sigma_{\mathrm{AV}},\varepsilon_{\mathrm{AV}}}\boldsymbol{u} = \boldsymbol{0} \qquad \text{in } \Omega_t \times (0, T_f),
\end{aligned} \tag{7.17a}$$

$$\nabla \cdot \boldsymbol{u} = 0 \qquad \text{in } \Omega_t \times (0, T_f), \tag{7.17b}$$

$$\boldsymbol{\sigma}(\boldsymbol{u}, p)\boldsymbol{n} = -p_{\mathrm{RA}}^{\mathrm{in}}\boldsymbol{n} \qquad \text{on } \left(\Gamma^{\mathrm{SupVC}} \cup \Gamma^{\mathrm{InfVC}}\right) \times (0, T_f), \tag{7.17c}$$

$$\boldsymbol{\sigma}(\boldsymbol{u}, p)\boldsymbol{n} = -p_{\mathrm{AR}}^{\mathrm{PUL}}\boldsymbol{n}_i \qquad \text{on } \Gamma^{\mathrm{PArt}_i} \times (0, T_f),\ i = 1, \dots, 5, \tag{7.17d}$$

$$\boldsymbol{\sigma}(\boldsymbol{u}, p)\boldsymbol{n} = -p_{\mathrm{LA}}^{\mathrm{in}}\boldsymbol{n}_i \qquad \text{on } \Gamma^{\mathrm{PVein}_i} \times (0, T_f),\ i = 1, \dots, 5, \tag{7.17e}$$

$$\boldsymbol{\sigma}(\boldsymbol{u}, p)\boldsymbol{n} = -p_{\mathrm{AR}}^{\mathrm{SYS}}\boldsymbol{n} \qquad \text{on } \Gamma_t^{\mathrm{AA}} \times (0, T_f), \tag{7.17f}$$

$$\boldsymbol{u} = \boldsymbol{u}_\Gamma = \partial_t \boldsymbol{d}_\Gamma \qquad \text{on } \Gamma_t^{\mathrm{w}} \times (0, T_f), \tag{7.17g}$$

$$\boldsymbol{u} = \boldsymbol{0} \qquad \text{in } \Omega_0 \times \{0\}, \tag{7.17h}$$

$$\boldsymbol{x} = \widehat{\boldsymbol{x}} + \widehat{\boldsymbol{d}} = \mathcal{A}_t(\widehat{\boldsymbol{x}}) \tag{7.17i}$$

$$-\nabla \cdot \left(\boldsymbol{K}\nabla\widehat{\boldsymbol{d}}\right) = \boldsymbol{0} \qquad \text{in } \widehat{\Omega}, \tag{7.17j}$$

$$\widehat{\boldsymbol{d}} = \widehat{\boldsymbol{d}}_\Gamma \qquad \text{on } \widehat{\Gamma}, \tag{7.17k}$$

$$\boldsymbol{u}^{\mathrm{ALE}} = \left(\frac{\partial \widehat{\boldsymbol{d}}}{\partial t}\right) \circ \widehat{\boldsymbol{d}}^{-1}, \tag{7.17l}$$

$$\frac{\mathrm{d}\boldsymbol{c}(t)}{\mathrm{d}t} = \boldsymbol{r}(t, \boldsymbol{c}(t)) \qquad \text{for } t \in (0, T_f), \tag{7.17m}$$

$$\widetilde{\boldsymbol{c}}(t) = \widetilde{\boldsymbol{r}}(t, \boldsymbol{c}(t)) \qquad \text{for } t \in (0, T_f), \tag{7.17n}$$

$$\boldsymbol{c} = \boldsymbol{c}_0 \qquad \text{for } t = 0. \tag{7.17o}$$

7.4. Numerical schemes

The numerical schemes employed to solve the coupled problem in Equation (7.17) are analogous to the ones presented in Section 6.5. However, differently from Chapter 6, we enforce in Equation (7.12) the flowrates coupling conditions by computing the flowrates in the 3D problem via integration of the normal relative velocity on the inlet/outlet sections. On the contrary, in Chapter 6, the flowrates are computed via volume derivatives hinging upon a mass balance (see Equations (6.22) and (6.24)).

By considering that in this model the displacement is known a-priori, and hence also the chambers volumes, the computation of the flowrates via volume derivatives allows to compute the flowrate at the current time step without introducing any discretization error. As a matter of fact, by denoting with $Q(t_n)$ a generic flowrate to be prescribed at a generic section Γ_n at the discrete time step n, and by $\dot{V}$ the time derivative of the volumes considered in a specific stage of the heartbeat, the computation via volume derivatives yields

$$Q(t_n) = -\dot{V}(t_n). \tag{7.18}$$

On the other hand, the flowrates are computed in Equation (7.12) via the normal relative velocity, which is, at current time step n, still an unknown. A possible way

is to use a monolithic approach in which $Q(t_n)$ becomes an unknown itself of the problem via the velocity $\boldsymbol{u}_n^h$. Another approach could be to sub-iterate between the 3D and 0D problems until a certain criterion is satisfied (for instance an error estimator based on the difference between the flowrates at two different subiterations $|Q^{(k)}(t_n) - Q^{(k-1)}(t_n)| < \text{TOL}$) [211]. The main disadvantage of these two approaches is the large computational cost to be added to the overall burden of the numerical simulation. As a matter of fact, two subiterations would require in practice to double the cost of the numerical simulation. On the contrary, to enhance the computational efficiency of the simulation, we decide to adopt an explicit treatment in which the flowrate at time step t_n is computed via the normal velocity at time step t_{n-1} as:

$$Q(t_n) \approx \int_{\Gamma_{n-1}} \left(\boldsymbol{u}_{n-1}^h - \boldsymbol{u}_{n-1}^{h,\text{ALE}} \right) \cdot \boldsymbol{n} \, \mathrm{d}\boldsymbol{x}. \tag{7.19}$$

We found that using an explicit approach in this context leads a numerical solution which is conditionally stable thanks to the small time step already required by the 3D fluid dynamics. We recall that, as $\Delta t \to 0$, the methods (7.18) and (7.19) become equivalent. Compared to the approach based on volume derivatives, we prefer now to rely on the flowrate computation via normal velocity in order to

- **make the model more flexible to address pathological scenarios**: the flowrate computation via the normal velocity allows to simulate valvular insufficiency without the need of changing the coupling conditions (see Section 6.6.2). As a matter of fact, we are feeding the 0D model with the *actual* flowrate already, and not the one computed relying on the mass balance (expressed for healthy valves);
- **make the model more flexible towards possible FSI simulation**: since in a FSI model the displacement represents an unknown of the problem (and thus also the ALE velocity), the volume derivatives (at current time step) cannot be computed to estimate the flowrate. Thus, the computation based on the normal velocity becomes the only viable alternative.

In Figure 7.11, we report a conceptual scheme for the coupling strategy among the 3D geometric, 0D circulation and 3D CFD problem for the whole heart. The valves open when the pressure jump across them becomes positive and close when the flow is reverse on their sections. Specifically, as explained in Section 6.3, the flowrate at the valve section is computed by time differentiating the ventricular volumes. Differently from the LH case, the flowrates are computed as in Equation (7.19) and the Algorithm "FLOWRATES" (Algorithm 6.6) reduces here to the computation of RV and LV volumes time derivatives to detect a condition of reversed flow across the immersed valves. Thus, the computation of the flowrates are embedded in the fluid dynamics problem (red box).

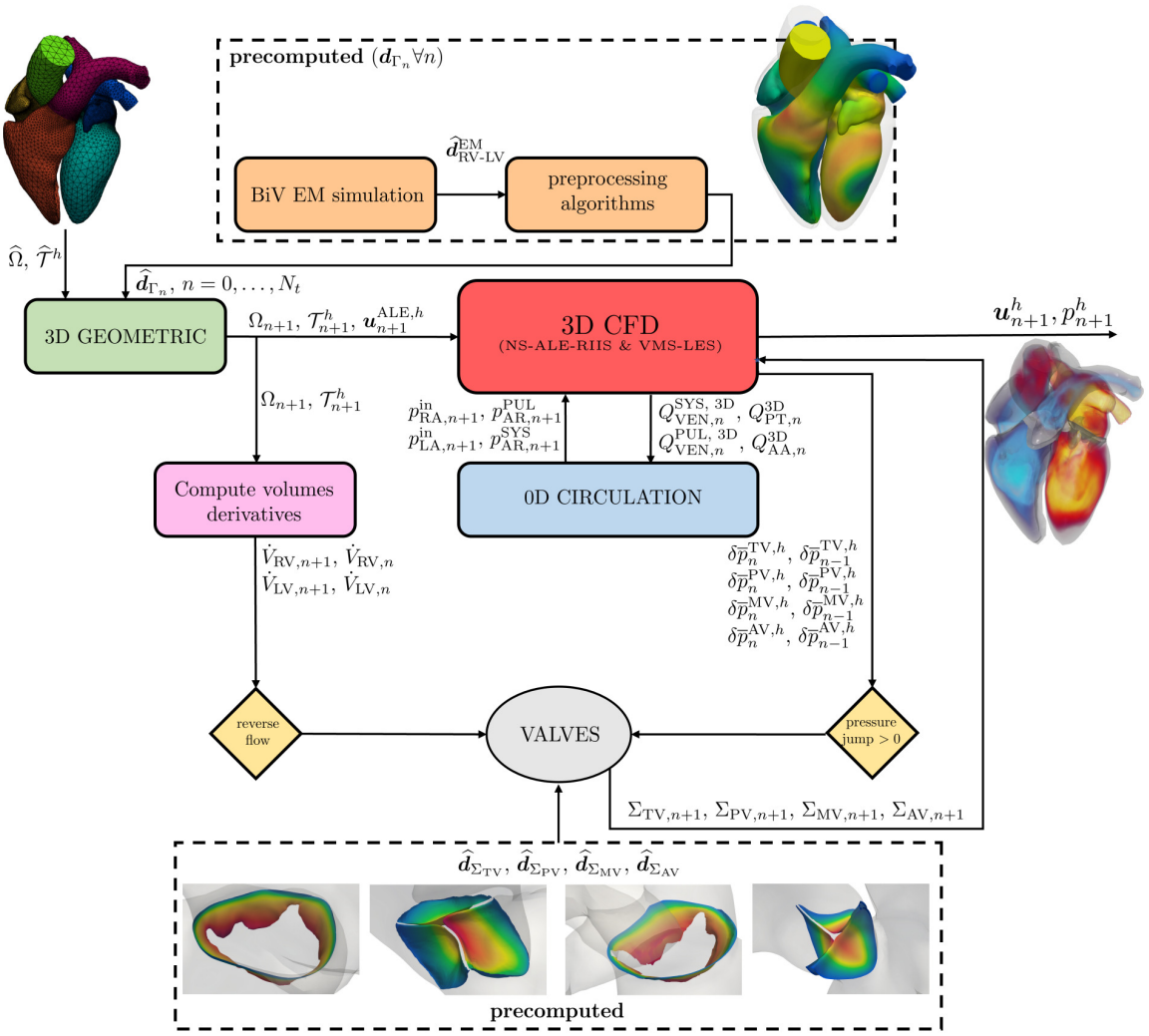

Figure 7.11: Coupling scheme among 3D geometric, 0D circulation and 3D CFD problems for the whole heart model at time step $n+1$ (segregated scheme).

R_k [kg/(m^2·s)]	ε_k [mm]	h [mm]			cells	DOFs ($\mathbb{P}_1 - \mathbb{P}_1$)		
		min	avg	max		$\boldsymbol{u}$	p	total
10^4	1	0.36	1.59	6.44	1'255'456	636'927	212'309	849'236

Table 7.2: Parameters for the setup of the whole heart CFD simulations.

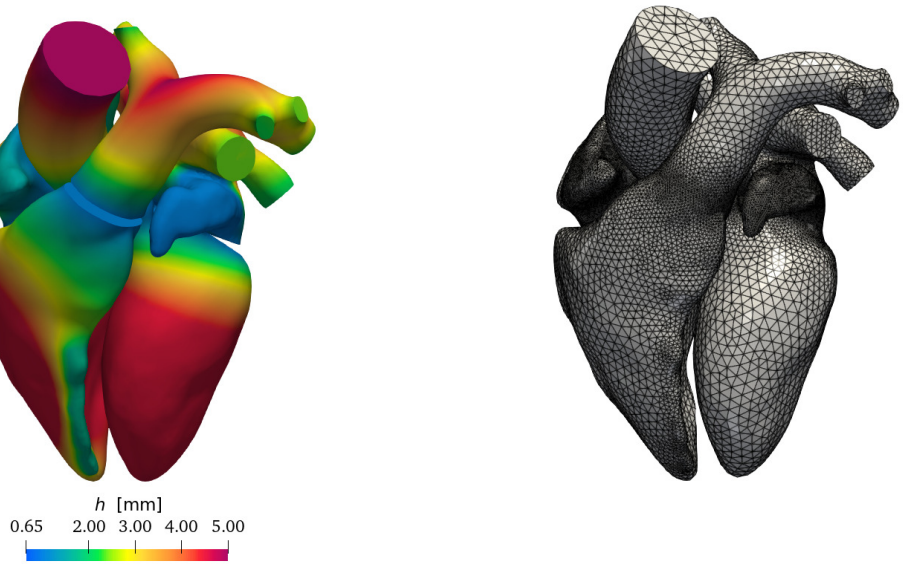

(a) (b)

Figure 7.12: Details on the mesh strategy: (a) subdomain boundaries colored with the prescribed mesh size h; (b) final tetrahedral mesh of the whole heart.

7.5. Numerical results

We carry out numerical simulations on a tetrahedral whole heart mesh built from the Zygote Solid 3D heart model [133]. To preprocess the geometry and generate the mesh, we use vmtk [20] and the tools recently developed in [85]. We generate surface meshes of each portion of the domain (RA, RV, PT, LA, LV and AA) separately with a non-uniform mesh size, refining the mesh near the valves and wherever the small curvature requires a better resolution the correctly describe the geometry (as for the auricles of the RA and LA and on the RV below the PT). We display in Figure 7.12a the six subdomains coloured with the boundary mesh size we set. We computed the mesh size by solving Laplace-Beltrami equations and by exploiting algorithms based on closest-point distances [85]. We generate volume meshes of each subdomain with a volume-element-factor equal to 0.9 and we connect the submeshes to get the final whole heart mesh displayed in Figure 7.12b. Eventually, we report clips of the internal mesh in Figure 7.13, where we also highlight the refinements near the valves.

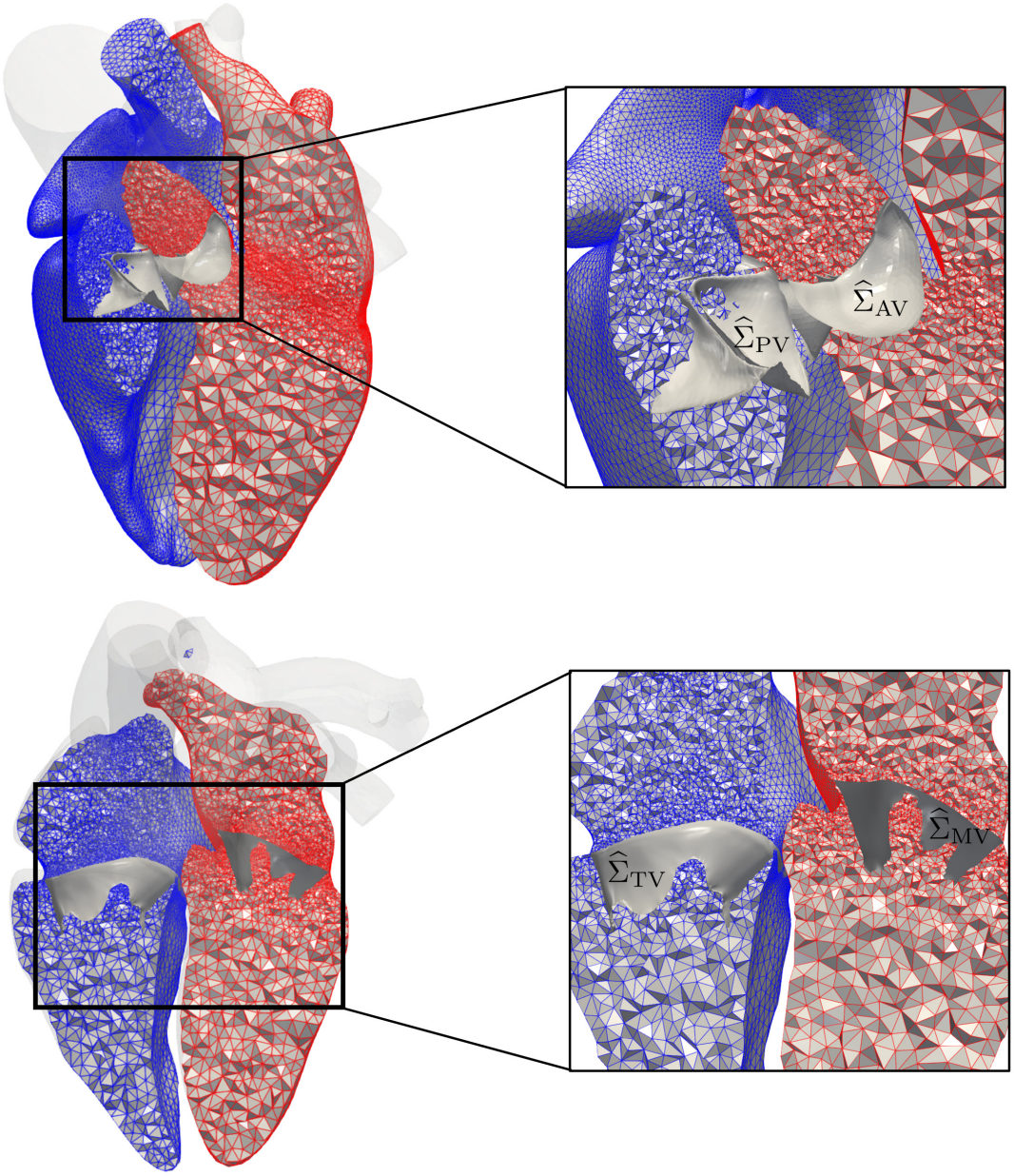

Figure 7.13: Clips of the internal mesh with a focus on the refinements near the cardiac valves.

For the RIIS method, following arguments of [86, 100], we set $R_k = 10^4$ kg/(m^2·s) and $\varepsilon_k = 10^{-3}$ m and with k = TV, PV, MV, AV. We use as time step size $\Delta t = 5 \cdot 10^{-4}$ s. We start our simulation from a zero velocity initial condition $\boldsymbol{u}_0 = \mathbf{0}$ and we set linear FE spaces for velocity and pressures ($\mathbb{P}_1 - \mathbb{P}_1$). In Table 7.2 we summarize the parameters employed for the setup of our numerical simulations along with cells and DOFs employing linear FEs. Numerical simulations are carried out in life^x in a parallel framework with 44 cores[1]. We carry out numerical simulations on two heartbeats of period $T_{\text{HB}} = 1$ s ($T_f = 2$ s) and we report the results on the second heartbeat to remove the influence of a zero initial condition. We shift the second heartbeat in the time domain $(0, T_{\text{HB}})$. The CPU time required to carry out this simulation is about 10 days.

We report the pressures and flowrates at the interfaces of the 3D and 0D models in Figure 7.14 computed at the inlet and outlet sections of the right (blue) and left (red) heart. Furthermore, we display the averaged pressure $\overline{p}$ computed in control volumes in each cardiac chamber in Figure 7.15a; the status of each cardiac valve is instead reported in Figure 7.15b: a valve is fully open when the opening coefficient is equal to one; viceversa it is fully closed when the coefficient is zero.

We display the volume rendering of velocity magnitude in the front and rear view of the whole heart in Figures 7.16 and 7.17 respectively. Analogously, we report the pressure on a clip in the apico basal direction and on the remain heart boundary in transparency in Figures 7.18 and 7.19. For the volume rendering of the velocity magnitude, we use two different colorbars to better distinguish the right from the left heart flows (blue right, red left). We start our simulation at the time corresponding to end diastole; the TV and MV closes when reverse flow is detected on their sections, i.e. when $\dot{V}_{\text{RV}} < 0$ and $\dot{V}_{\text{LV}} < 0$ respectively. The ejection phase starts with the opening of the PV and AV when the pressure upwind the valves overcomes the one measured downind ($\overline{p}_{\text{RV}} > \overline{p}_{\text{PT}}$ and $\overline{p}_{\text{LV}} > \overline{p}_{\text{AA}}$). As the ejection phase starts, we observe high speed jets from the RV to the PT and from the LV to the AA. We report the velocity at the valves in Figure 7.20 by computing the averaged velocity in control volumes Ω_t^k between the leaflets of the valve k:

$$\overline{\boldsymbol{u}}_k(t) = \frac{1}{|\Omega_t^k|} \int_{\Omega_t^k} \boldsymbol{u}(\boldsymbol{x}, t)\, \mathrm{d}\boldsymbol{x}, \text{ with } k = \text{TV}, \text{PV}, \text{MV}, \text{AV}. \tag{7.20}$$

We measure a peak velocity of the PV and AV respectively equal to 1.12 m/s and 1.48 m/s. Our results are consistent with the clinical data acquired in healthy subjects: in [10], it is reported a maximum PV velocity in the range $0.8 - 1.2$ m/s; in [15], it is reported the AV velocity measured in-vivo with Doppler echocardiograph in a normal subject and they measured a peak velocity of about 1.3 m/s; furthermore, in the computational study of [272] where FSI simulations of the LH are carried out, they

[1] Numerical simulations were run on the cluster iHEART (Lenovo SR950 8 x 24-Core Intel Xeon Platinum 8160, 2100 MHz and 1.7TB RAM) available at MOX, Dipartimento di Matematica, Politecnico di Milano

measure a velocity peak in AV of about 1.5 m/s. The intraventricular pressure increases during systole, and we observe larger pressure values on the LV with respect to the RV: specifically we measure 97 mmHg and 118 mHg at the systolic peak in the right and left ventricles respectively. For the left heart, the value obtained is consistent with clinical measurements [46, 245]; however, in the right heart we get too large pressure values. We believe that more physiological results might be achieved in terms of right ventricular pressure after a further calibration of the circulation model coefficients. Moreover, large values of pressures may be also caused by a too fast ejection phase obtained in the electromechanical simulation, thus a recalibration of the latter might be also required. The PV and AV closed when $\dot{V}_{\mathrm{RV}} > 0$ and $\dot{V}_{\mathrm{LV}} > 0$; the filling phase begins as $\overline{p}_{\mathrm{RA}} > \overline{p}_{\mathrm{RV}}$ and $\overline{p}_{\mathrm{LA}} > \overline{p}_{\mathrm{LV}}$, which determines the opening of the TV and MV respectively. During the filling phase, the RA receives blood from the venae cavae and it fills the RV though the TV orifice; at the same time, the oxygenated blood flows in the LA through the pulmonary veins filling the LV through the MV orifice. The intraventricular pressure decreases and, as for systole, the LH is subjected to higher pressure values with respect to the RH. The diastole is characterized on both sides of the heart by two waves, namely E-wave and A-wave. The amplitude of these waves is higher in the LH: specifically, as displayed in Figure 7.20, we measures amplitudes equal to 0.30 m/s (E) and 0.20 m/s (A) in the TV; 0.92 m/s (E) and 0.5 m/s (A) in the MV.

We compute the turbulent kinetic energy as in Equation (5.20) with the velocity field at the second heartbeat in each chamber of the heart. In Figure 7.21 we display $E_k(t)$ in the RA, RV (top) and LA, LV (bottom). The energy produced and dissipated in the ejection phase from the RV is comparable to the one of the LV. On the contrary, the main differences among the two part of the heart are observed in diastole, being the LV the part with larger values of E_k. Consistently with the velocity at the TV and MV, diastole is characterized by two energy peaks in the four chambers of the heart in correspondence of the E-wave and A-wave.

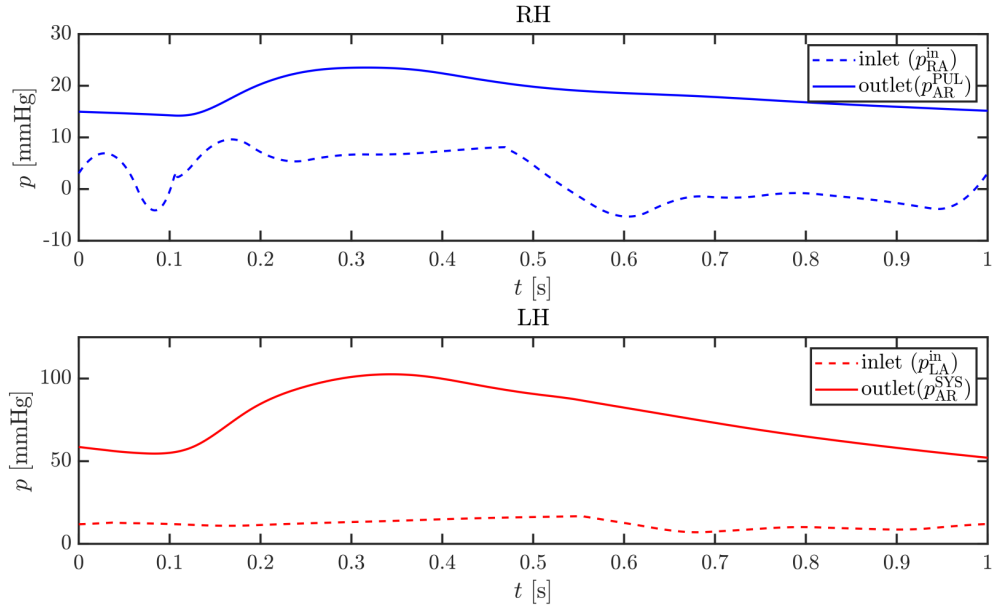

(a) Pressures

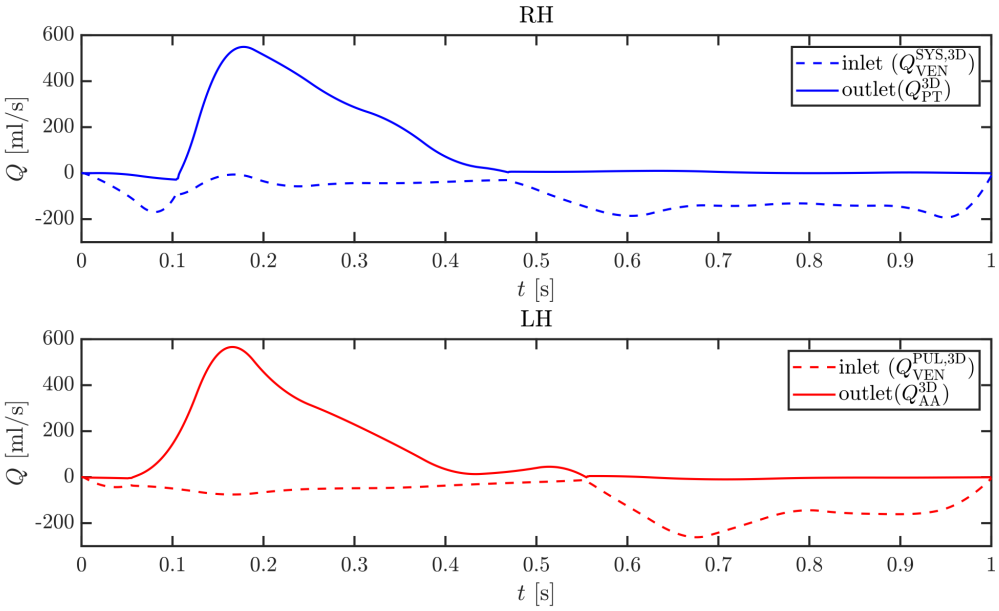

(b) Flowrates

Figure 7.14: Interfaces flow properties between the 3D and 0D models: (a) pressures; (b) flowrates.

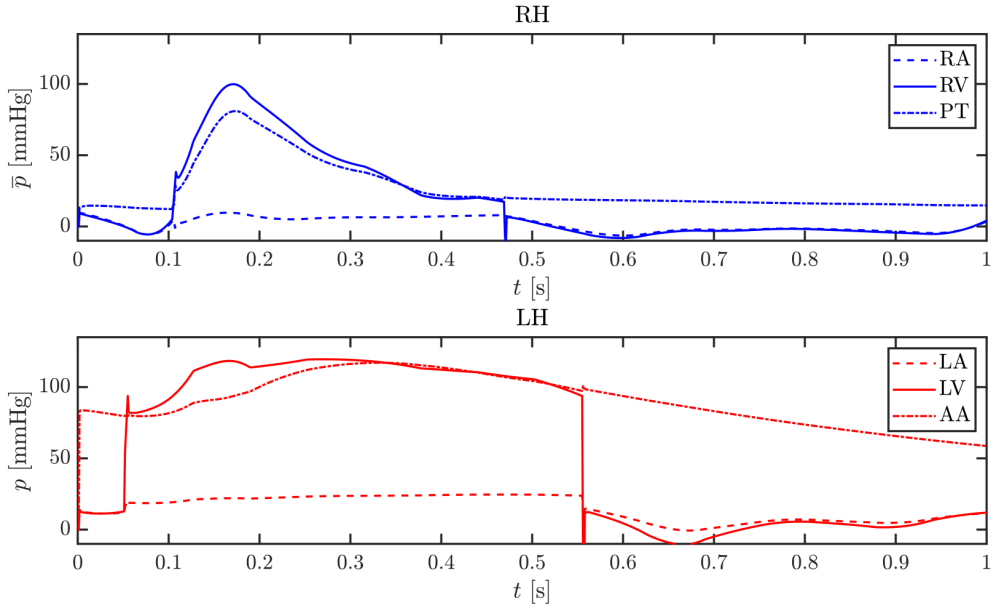

(a) Pressures

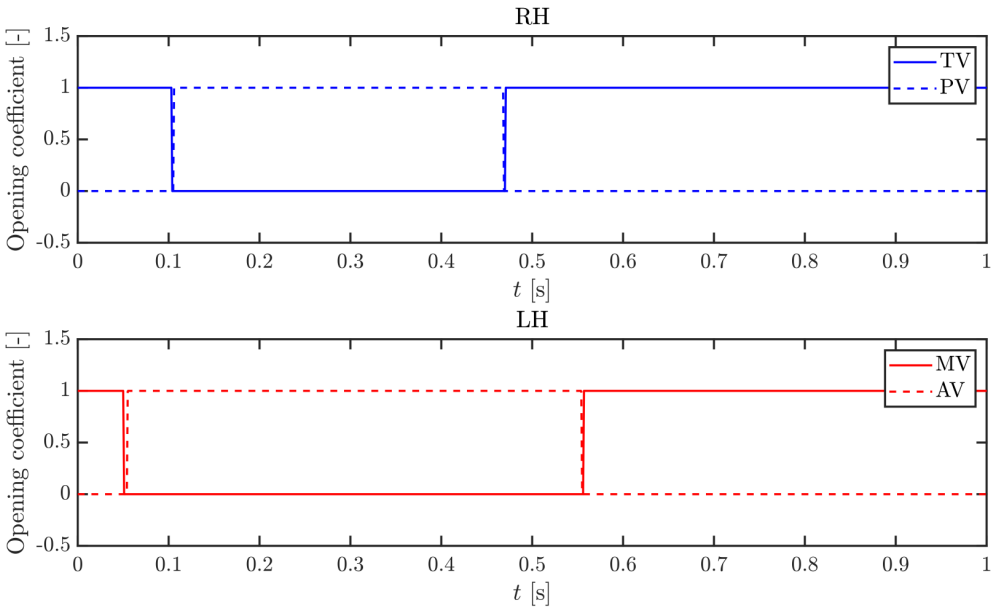

(b) Valves status

Figure 7.15: Averaged-pressures in control volumes in RA, RV, PT, LA, LV, AA and valves status.

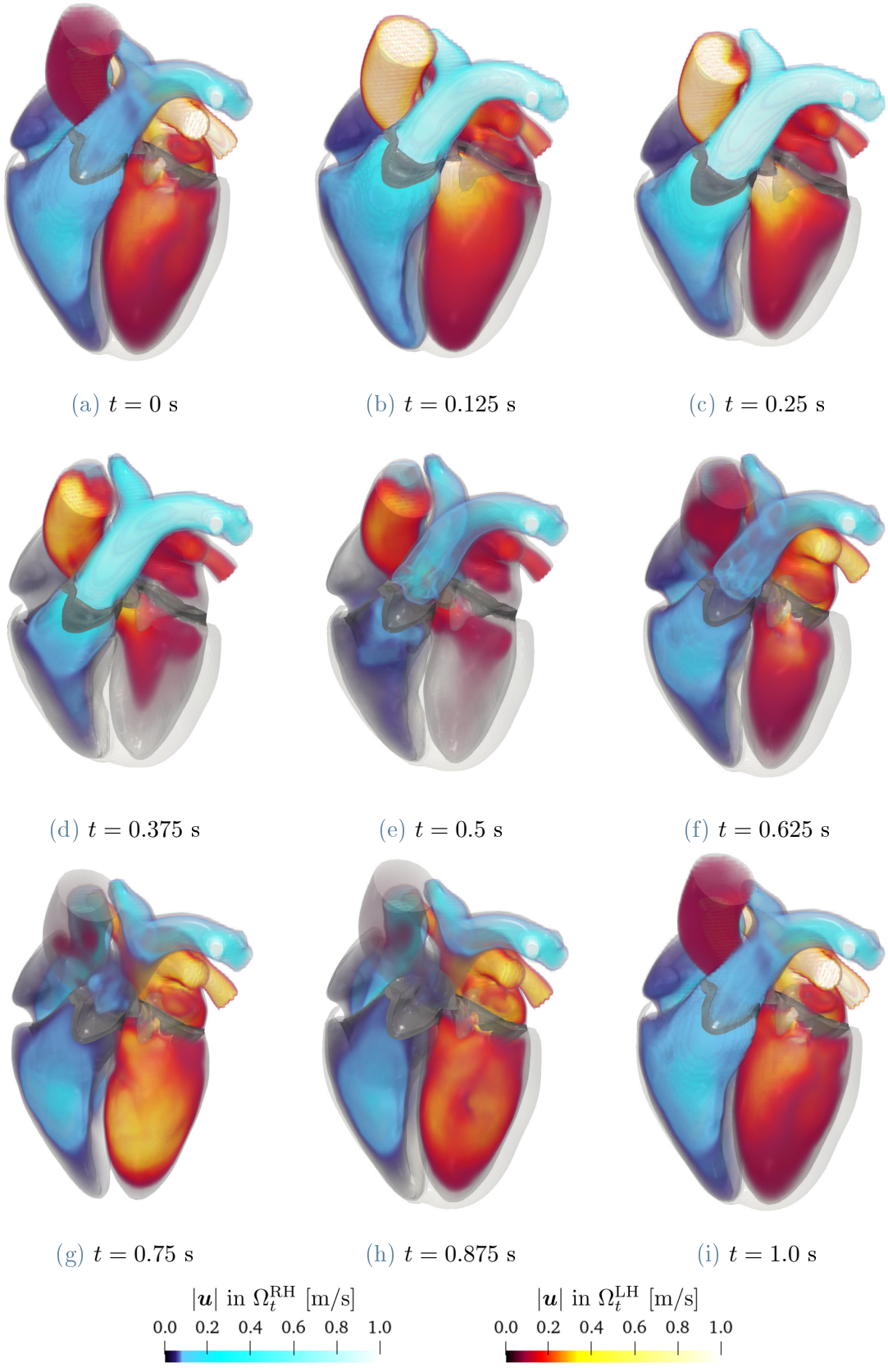

(a) $t = 0$ s (b) $t = 0.125$ s (c) $t = 0.25$ s

(d) $t = 0.375$ s (e) $t = 0.5$ s (f) $t = 0.625$ s

(g) $t = 0.75$ s (h) $t = 0.875$ s (i) $t = 1.0$ s

Figure 7.16: Volume rendering of velocity magnitude (front view).

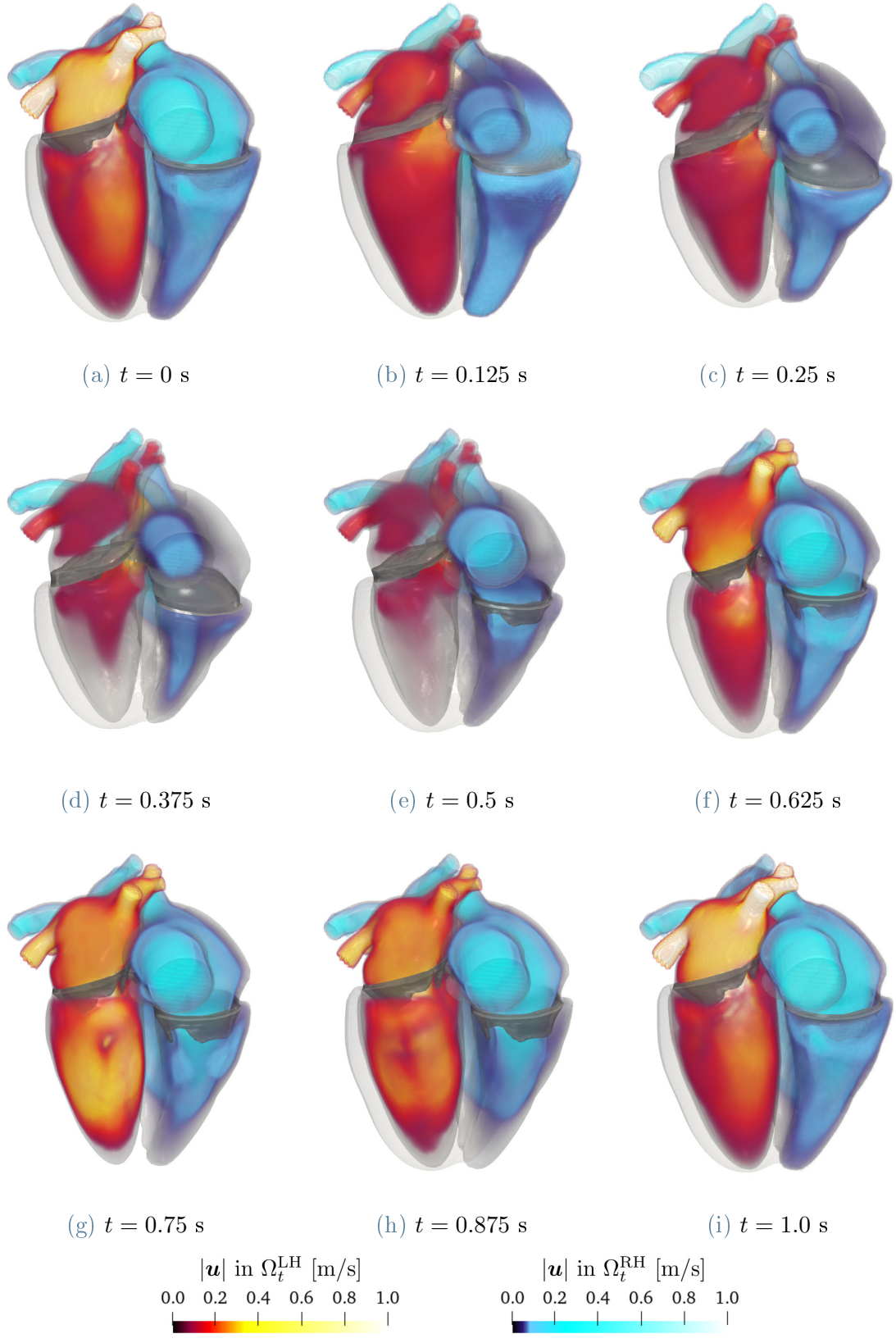

(a) $t = 0$ s (b) $t = 0.125$ s (c) $t = 0.25$ s

(d) $t = 0.375$ s (e) $t = 0.5$ s (f) $t = 0.625$ s

(g) $t = 0.75$ s (h) $t = 0.875$ s (i) $t = 1.0$ s

Figure 7.17: Volume rendering of velocity magnitude (rear view).

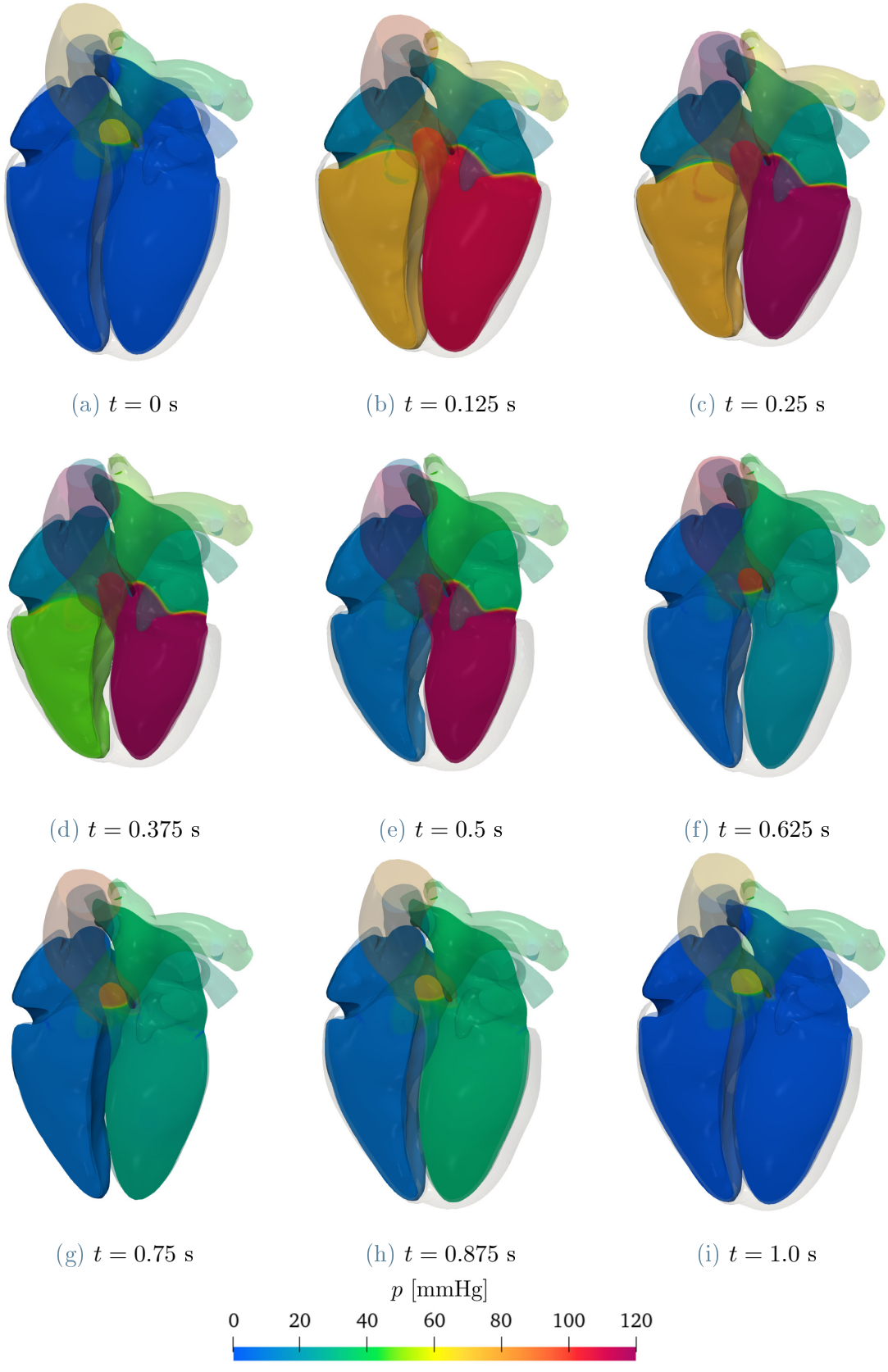

(a) $t = 0$ s (b) $t = 0.125$ s (c) $t = 0.25$ s

(d) $t = 0.375$ s (e) $t = 0.5$ s (f) $t = 0.625$ s

(g) $t = 0.75$ s (h) $t = 0.875$ s (i) $t = 1.0$ s

Figure 7.18: Pressure (front view).

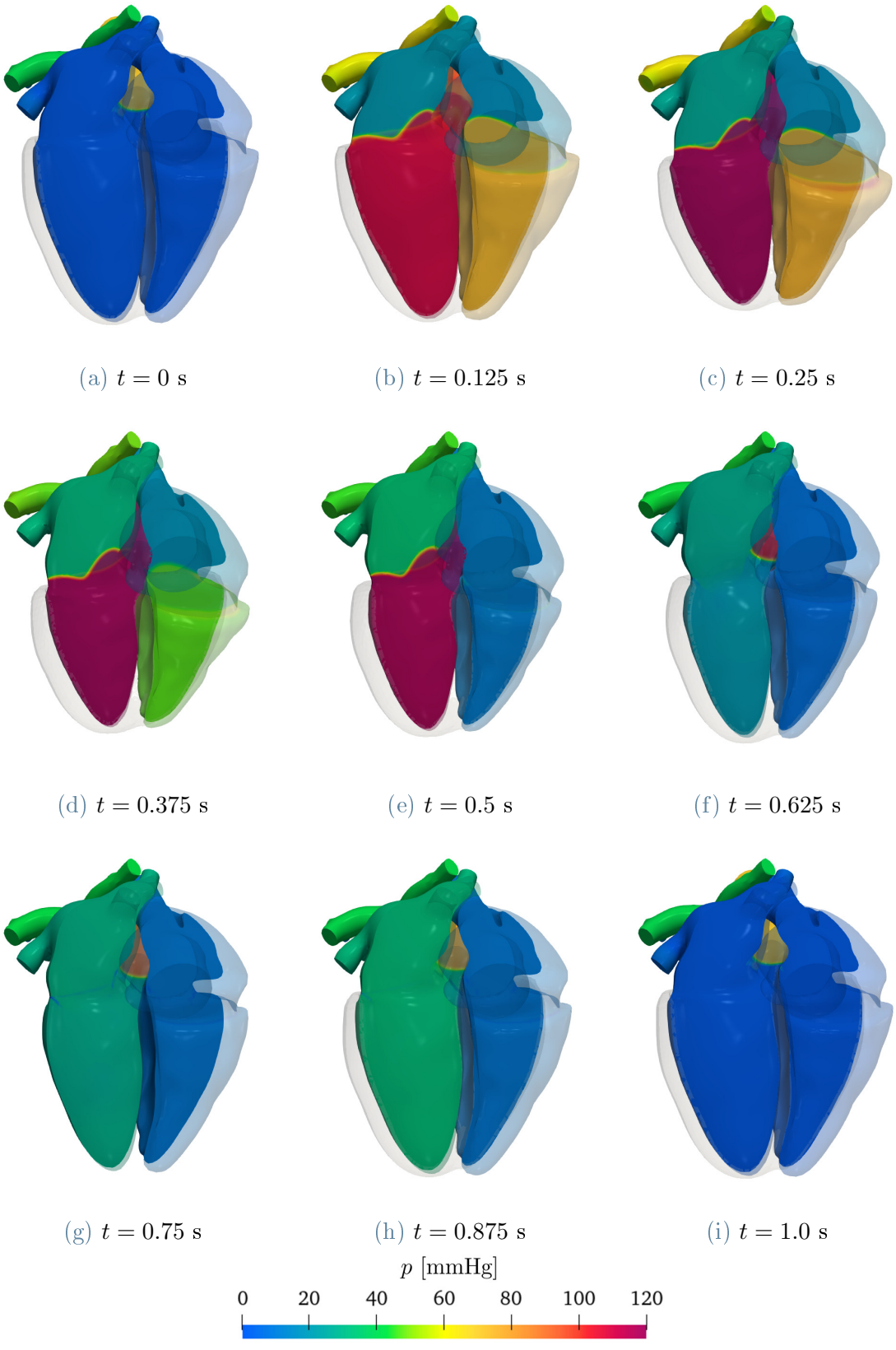

(a) $t = 0$ s (b) $t = 0.125$ s (c) $t = 0.25$ s

(d) $t = 0.375$ s (e) $t = 0.5$ s (f) $t = 0.625$ s

(g) $t = 0.75$ s (h) $t = 0.875$ s (i) $t = 1.0$ s

Figure 7.19: Pressure (rear view).

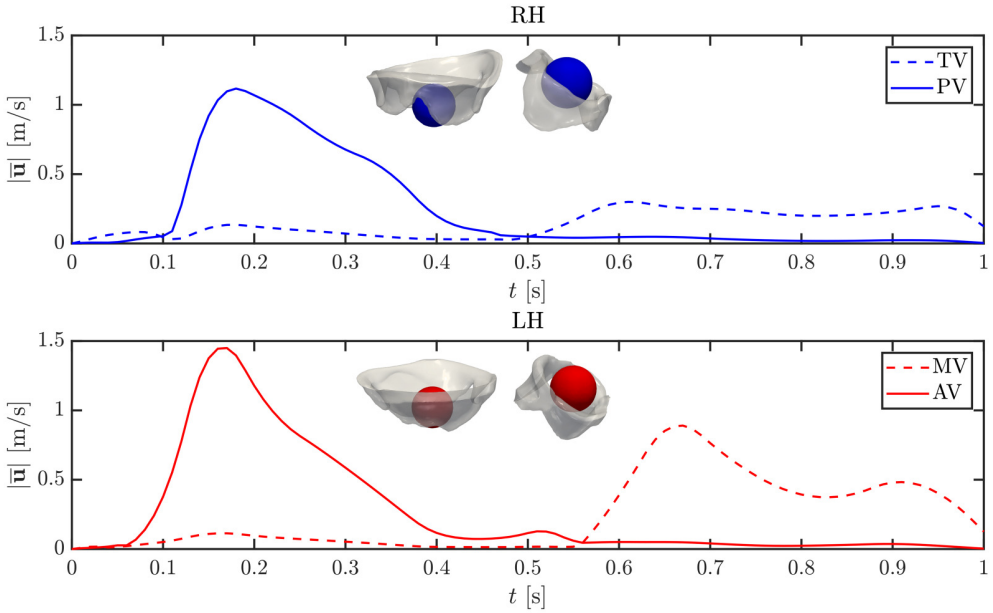

Figure 7.20: Averaged velocity in control volumes between the cardiac valves leaflets during a heart cycle.

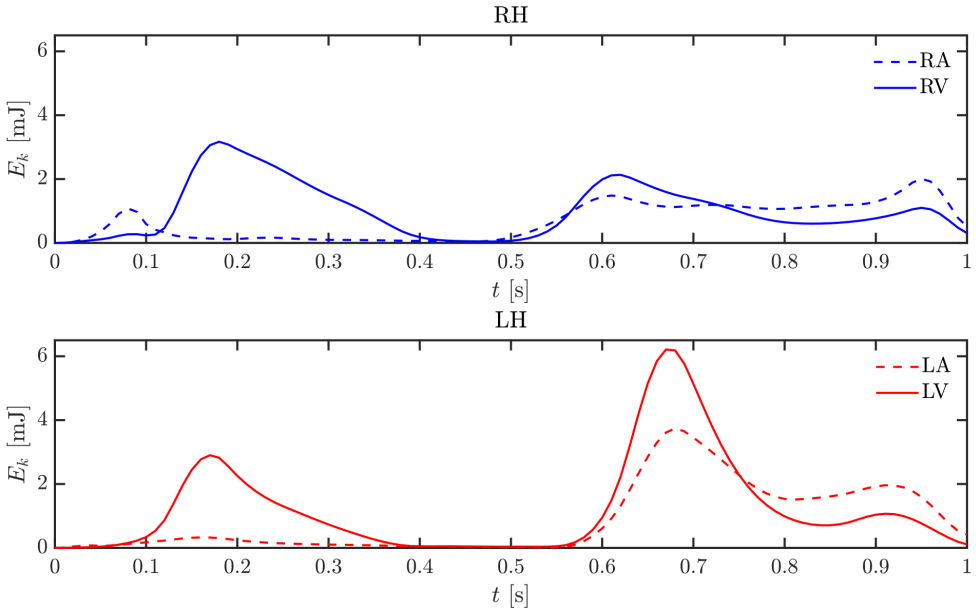

Figure 7.21: Turbulent kinetic energy in RA, RV (top) and LA, LV (bottom) during a heart cycle.

We consider a slice in the ventricular apico-basal direction and we project the vorticity $\nabla \times \boldsymbol{u}$ on the slice's normal direction, as we display in Figure 7.22. In the LH, we recognize the ring vortex formation under the MV section: the shear layers roll on the MV leaflets, enter in the ventricular cavity producing an "O" shaped vortex. Specifically, the flow rotates in the clockwise direction under the anterior leaflet, counterclockwise under the posterior one. This pattern has been found also in the LH simulation and compared with in-vivo data from the literature in Chapter 6. On the right side of the heart, we observe a weaker flow entering in the RV, with shear layers rolling on the leaflets of the TV. As shear layers roll through the anterior leaflet, the flow starts rotating in the clockwise direction; viceversa, on the poster leaflet, the flow rotates counterclockwise. However, differently from the LH, where the high speed mitral jet reaches the LV apex, the right ventricular flow is weaker and the rotation of the vortex is limited in the upper part of the RV. Our findings on the right ventricular flows are coherent with the numerical results obtained in [280], where CFD patient-specific simulations of the sole RV are carried out.

To better investigate the vorticity production in the different chambers, we display the enstrophy S in Figure 7.23. Specifically, we compute it as defined in Equation (5.21) by using the vorticity on the second heart cycle. The plot confirms that the main differences among the left and the right parts of the heart are mainly evident during diastole: the LA and LV are characterized by a larger vorticity production and dissipation with respect to the RA and RV. Thus, the early diastolic flow shows a similar pattern in terms of vortex formation; however, as the filling phase advances, the right vortex is weaker and does not enter in the core of the RV, breaking up in the upper part of the ventricle and dissipating the energy produced. Furthermore, by comparing the behavior of S in the atria, the LA is characterized by larger enstrophy values due to the formation, interaction and dissipation of the ring vortices coming from the pulmonary veins and impacting in the atrial chamber. We addressed these patterns in Chapter 5 for both idealized and patient-specific geometries. On the contrary, as we report in Figure 7.24, we found that the flow is much more unidirectional in the RA: shear layers form in the venae cavae, enter in the atrium, but the flow is then "sucked" by the RV through the TV without perturbation and coalescence of shear layers.

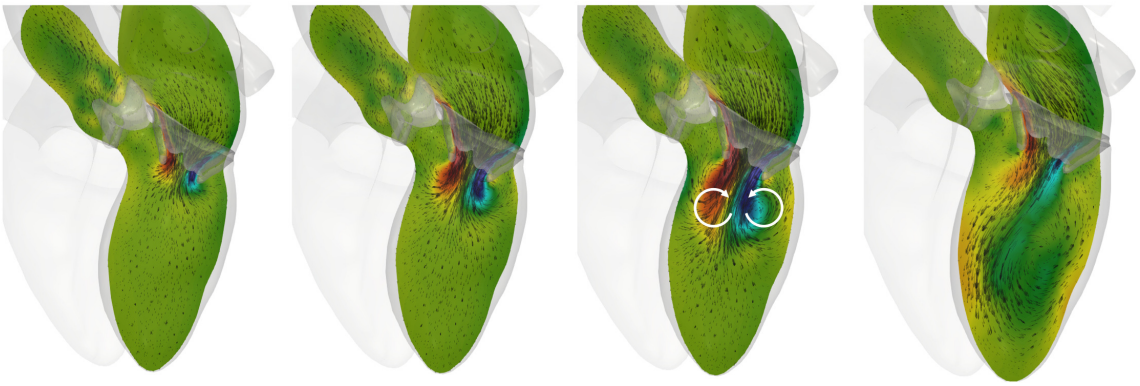

(a) LH

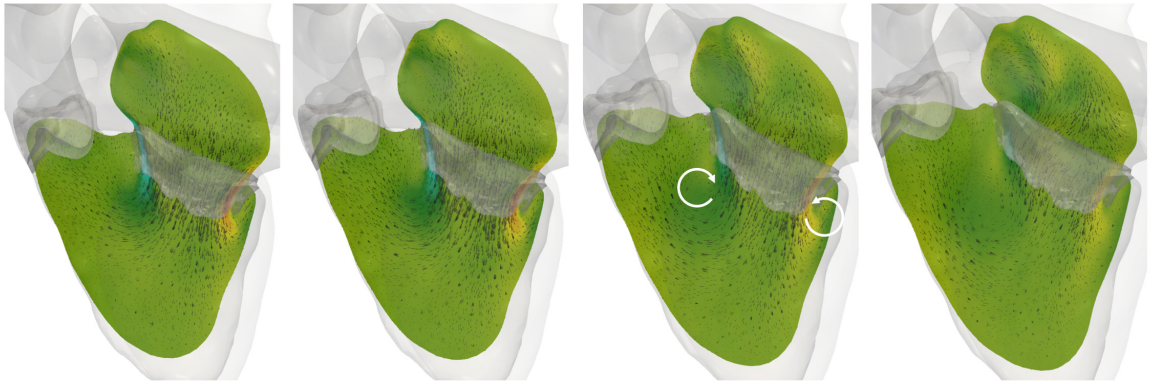

(b) RH

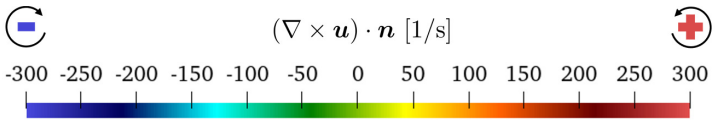

Figure 7.22: Slice in the ventricular apico-basal direction colored according to the projection of the vorticity on the normal direction (pointing towards the reader) with 2D glyphs oriented and scaled as the velocity. Snapshots acquired in diastole at times $t = 0.60$ s, $t = 0.62$ s, $t = 0.65$ s, $t = 0.72$ s. (a) LH; (b) RH.

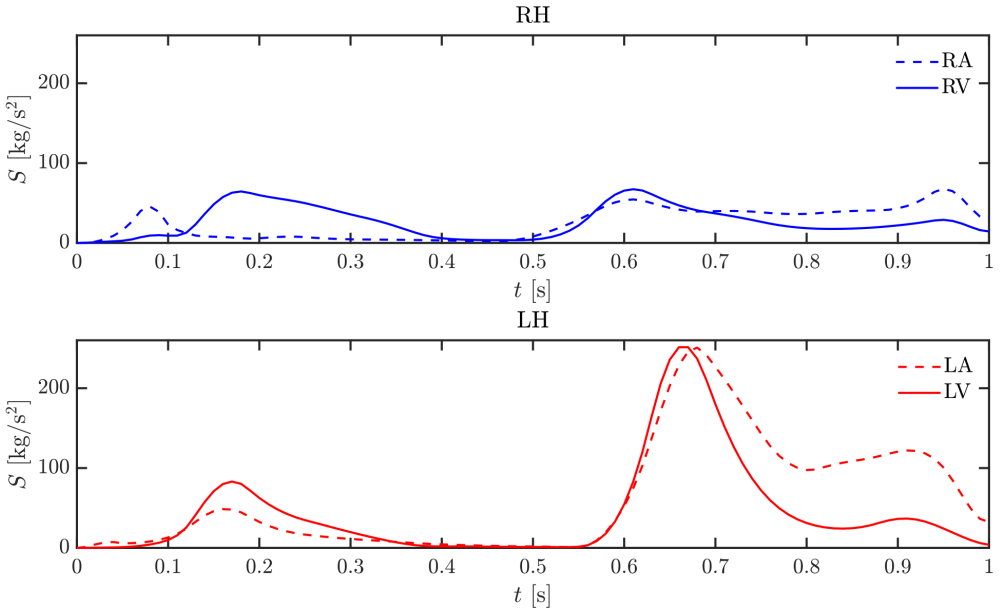

Figure 7.23: Enstrophy in RA, RV (top) and LA, LV (bottom) during a heart cycle.

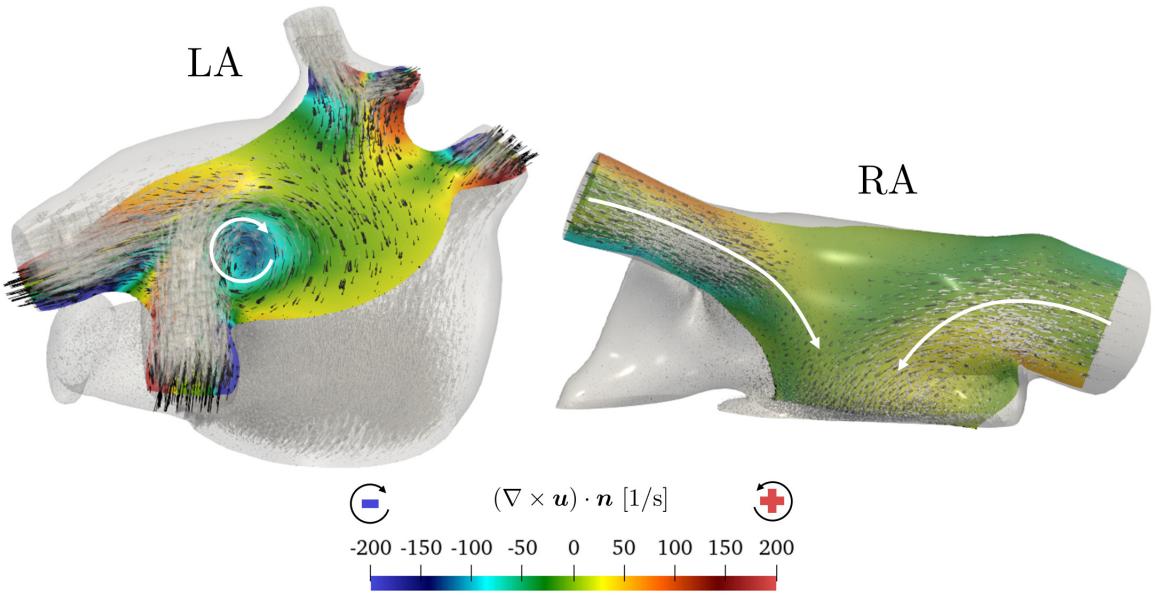

Figure 7.24: Projection of the vorticity in the normal direction of two planes with 2D glyphs: on the left a plane passing through the pulmonary veins; on the right a slice in the ventricular apico-basal direction passing through the venae cavae. Snapshot acquired at $t = 0.7$ s.

7.6. Concluding remarks

In this Chapter, we presented multiscale model for the hemodynamics of the whole heart coupled with the surrounding circulation. The cost to carry out a single heartbeat is approximately 5 days on a mesh made of 850K DOFs (linear FE) with 44 cores. We simulated a physiologic heart and we compared, when available, our numerical results with data coming from the literature, finding a good accordance in terms of averaged velocity and flow patterns. However, additional simulations are required to better calibrate the CFD model, especially to achieve more physiological pressures on the right side of the heart. A crucial role in this kind of simulations is played by the resistances, capacitance and inductance of the circulation model; thus, we believe that a proper sensitivity study may help the calibration of the model and the simulation of pathological scenarios. Different further directions could be undertaken in order to enhance the physiological significance of these simulations and also to reduce the computational cost. In Chapter 8, we list some possible future developments in this sense.

To conclude, the model presented in this chapter represents one of the few attempts in the literature to simulate the whole heart hemodynamics and, to the best of our knowledge, the first work in which the 3D CFD is also coupled to the remaining circulation. This yields a closed-loop model of the whole cardiocirculatory system in which the heart is modeled in 3D, with motion driven by electromechanics and accounting also for cardiac valves and transitional flow regime.

8 | Conclusions

In this thesis, we developed mathematical and numerical models for the computational fluid dynamics of the heart. Our goal is to carry out numerical simulations of the whole heart geometry by accounting for the main aspects that affect cardiac hemodynamics: transitional-turbulent blood flows, electromechanics, cardiac valves and mutual influence with the external blood circulation.

To model the transitional-flow regime of cardiac flows and to stabilize the Navier-Stokes equations discretized by means of Finite Elements, we employed residual-based strongly consistent stabilization methods, specifically the Streamline-Upwind Petrov-Galerkin (SUPG) and the Variational Multiscale - Large Eddy Simulation (VMS-LES) method. The latter also account for turbulence modeling according to the LES paradigm. Numerical code verification (by means of the Taylor-Green Vortex benchmark problem) and model validation (through the nozzle problem proposed by the Food and Drug Administration, FDA) showed a good agreement between the VMS-LES solutions and reference data, in either laminar and turbulent cases. However, the main issue in the turbulent case was related in accurately predicting the jet breakdown position: we found that the numerical solution is strongly influenced by parameters as the time-step size and the granularity of the mesh.

With the aim of improving the accuracy properties of stabilization and turbulence models, we proposed a novel methodology to compute the optimal stabilization parameters involved in this class of methods by means of artificial neural networks (ANNs). As a proof of concept, we considered the simpler case of advection-diffusion partial differential equations, discretized via finite element method and with the SUPG stabilization method. A universal definition of the stabilization parameter does not exist, formulas that ensure nodally exact solutions are designed for specific 1D problems only, and for more complex problems one tipically has to rely on some empirical extension of these expressions. Our numerical results on 1D and 2D test cases showed that the strategy based on ANNs produced more accurate results compared to numerical solutions with theoretical stabilization parameters. We envision extending this promising tool to learn the stabilization parameters in the VMS-LES method for the Navier-Stokes equations.

We investigated the role played by different stabilization methods, namely the SUPG

and VMS-LES method, by comparing the numerical results on the hemodynamics of a healthy left atrium. We produced a reference solution on a very fine mesh and we carried out numerical simulations on coarser grid levels with SUPG and VMS-LES methods. We found that if sufficiently fine meshes were employed, both methods are accurate and give comparable results. On the contrary, if coarse enough meshes were considered, the VMS-LES method better predicted the transitional-flow regime and cycle-to-cycle blood flow variations than the standard SUPG method, suggesting hence that the usage of VMS-LES method is necessary if coarse meshes are used.

Once we assessed the role of VMS-LES method in cardiac flows, we proposed a novel computational model of the left atrium for idealized and patient-specific geometries, either in physiological and pathological conditions. Specifically, we considered the atrial fibrillation pathology. The displacement is expressed via a volume-based definition, and we modeled the reduced atrial contractility induced by atrial fibrillation by conveniently tuning a 0D model of the whole cardiovascular system. We found that atrial fibrillation caused a slowing of the blood flow, vorticity reduction and an increment of blood stasis, especially in the auricle, where we also measured a large washout reduction. Furthermore, we found consistency with in-vivo data in terms of clinical biomarkers and flow patterns on healthy and pathologic cases.

We then extend our model to the left heart and, finally, to the whole heart. We introduced a novel preprocessing procedure to extend a given ventricular displacement on the whole heart (or left, or right) geometry and we accounted for the motion of the atria (or atrium) via a volume-based definition. Thus, in our computational model, the fluid dynamics is one-way coupled to the ventricle(s) electromechanics giving rise to a multiphysics system. We believe that this procedure might also be employed with displacement fields coming from different sources – as imaging data – and thus, be applied also to patient-specific studies. We accounted for the mutual influence between the heart hemodynamics and the remaining circulation by coupling our 3D multiphysics CFD problem with the surrounding circulation described by a 0D lumped parameter model. The output obtained by our numerical results on a healthy left heart match clinical data acquired in vivo with healthy subjects. Flowrates, velocity, pressures and indicators as the EA ratio are accurate when compared with in-vivo data, and the numerical simulations correctly predict the formation and intensity of the vortical structures in the heart. Furthermore, we simulated the pathological scenario of mitral regurgitation, allowing to compute different pathology indicators.

Whole heart CFD simulation is a research topic still at infancy, and the models and methods we developed in this thesis represent one of the few attempts in the scientific community to address this huge problem. However, a number of further developments can be undertaken to make the overall computational model more reliable, more accurate and less expensive from a computational point of view.

Additional CFD simulations of the whole heart should be carried out to achieve more physiological results, especially in terms of pressure in the right ventricle and in the

pulmonary trunk, as we observed too high pressure values in this part of the heart. We believe that better results might be achieved after a further calibration of the circulation model coefficients. However, large values of pressures may be also caused by a too fast ejection phase obtained in the electromechanical simulation. Thus, additional electromechanical simulations might be required to get more physiological haemodynamic results. In addition, introducing an electromechanical model of the whole heart would complete the description of the cardiac contractility and hence allow to relax some of the hypotheses we made on the atrial motion [44, 202].

Furthermore, in the present work we prescribed the electromechanics-based displacement on the boundary of the fluid dynamics domain, hence enforcing a kinematic coupling condition among the two physics. Since we are not including the dynamic balance in our model, the pressure would not be uniquely defined when both valves are closed. Thus, we discarded the isovolumetric phases of the heart cycle. Following the model proposed in [259], we are currently working on the introduction of an additional penalty term in the Navier-Stokes equations to control the intraventricular pressure during the isovolumetric phases.

A crucial aspect in in vitro simulation of the heart is the validation against images data. In this thesis we provided a validation of the CFD model on the cardiovascular benchmark test proposed by FDA, and validation of the CFD heart model by comparing the numerical results obtained on a realistic template left heart geometry against macro indicators and flow patterns acquired in-vivo in healthy subjects. This makes the computational framework meaningful and reliable; however, a more exhaustive validation process could consist of carrying out the CFD simulations on patient specific geometries and then compare the numerical results against imaging data acquired on the same patient (as 4D flow MRI).

Concerning the transitional blood flow regime, the accuracy of the stabilization - turbulence models employed in this thesis could be enhanced in several ways. One could extend the strategy devised based on ANNs to more complex and realistic cases, as learning subgrid models for LES methods or, for the case of the VMS-LES method, one could learn the stabilization parameters or directly the fine-scale solution.

Moreover, we found that the numerical scheme requires a small time step during systole, the phase of the heartbeat characterized by larger velocity values. We envision that the computational cost of a cardiac CFD simulation might be reduced by employing an adaptive time-advancing numerical scheme. Actually, adaptivity would allow to use a larger time step in diastole while satisfying the small time step requirement of systole.

Finally, we deem that the clinical routine might take full advantages of cardiac high-fidelity fluid dynamics simulations if relevant indicators are provided to clinicians in "real time". Thus, we believe that the development of reduced-order models for cardiac hemodynamics – by considering as input parameters the variability among patients – might be a promising tool to improve clinical treatments and therapeutics.

Bibliography

[1] URL https://bitbucket.org/lifev-dev/lifev-release/wiki/Home.

[2] URL https://gitlab.com/albertozingaro/ann-supg.

[3] URL https://commlab.uv.es/repository/.

[4] URL https://www.dealii.org/.

[5] URL https://www.fda.gov/science-research/science-and-research-special-topics/critical-path-initiative.

[6] URL https://lifex.gitlab.io/.

[7] URL https://www.3{D}s.com/products-services/simulia/solutions/life-sciences-healthcare/the-living-heart-project/.

[8] URL https://www.paraview.org/Wiki/PvPython_and_PvBatch.

[9] URL https://gitlab.com/albertozingaro/cfd-mesh.

[10] URL https://123sonography.com/ebook/pulmonary-acceleration-time-to-estimate-pulmonary-pressure.

[11] URL https://github.com/martemyev/tethex.

[12] URL https://trilinos.github.io.

[13] URL https://criticalecho.com/tutorial-6-assessment-of-lv-diastolic-function-and-filling-pressures.

[14] URL www.vmtk.org.

[15] Comprehensive transthoracic echocardiographic examination protocol. In *Pocket Guide to Echocardiography*, pages 1–5. Wiley-Blackwell, sep 2012. doi: 10.1002/9781118480007.ch1. URL https://doi.org/10.1002%2F9781118480007.ch1.

[16] M. Abadi, A. Agarwal, P. Barham, E. Brevdo, Z. Chen, C. Citro, G. Corrado, A. Davis, J. Dean, M. Devin, S. Ghemawat, I. Goodfellow, A. Harp, G. Irving, M. Isard, Y. Jia, R. Jozefowicz, L. Kaiser, M. Kudlur, J. Levenberg, D. Mané, R. Monga, S. Moore, D. Murray, C. Olah, M. Schuster, J. Shlens,

B. Steiner, I. Sutskever, K. Talwar, P. Tucker, V. Vanhoucke, V. Vasudevan, F. Viégas, O. Vinyals, P. Warden, M. Wattenberg, M. Wicke, Y. Yu, and X. Zheng. TensorFlow: Large-scale machine learning on heterogeneous systems. `http://tensorflow.org/`, 2015.

[17] N. Ahmed and S. Rubino. Numerical comparisons of finite element stabilized methods for a 2D vortex dynamics simulation at high Reynolds number. *Computer Methods in Applied Mechanics and Engineering*, 349:191–212, 2019.

[18] P. Alboni, S. Scarfò, G. Fucà, N. Paparella, and P. Yannacopulu. Hemodynamics of idiopathic paroxysmal atrial fibrillation. *Pacing and Clinical Electrophysiology*, 18:980–985.

[19] M. Alnæs, J. Blechta, J. Hake, A. Johansson, B. Kehlet, A. Logg, C. Richardson, J. Ring, M. Rognes, and G. Wells. The fenics project version 1.5. *Archive of Numerical Software*, 3(100), 2015. doi: 10.11588/ans.2015.100.20553.

[20] L. Antiga, M. Piccinelli, L. Botti, B. Ene-Iordache, A. Remuzzi, and D. A. Steinman. An image-based modeling framework for patient-specific computational hemodynamics. *Medical & Biological Engineering & Computing*, 46(11): 1097–1112, nov 2008. doi: 10.1007/s11517-008-0420-1. URL `https://doi.org/10.1007%2Fs11517-008-0420-1`.

[21] C. P. Appleton. Evaluation of diastolic function by two-dimensional and doppler assessment of left ventricular filling including pulmonary venous flow. In *Diastology*, pages 115–143. Elsevier, 2008. doi: 10.1016/b978-1-4160-3754-5.50016-0. URL `https://doi.org/10.1016%2Fb978-1-4160-3754-5.50016-0`.

[22] C. P. Appleton, J. M. Galloway, M. S. Gonzalez, M. Gaballa, and M. A. Basnight. Estimation of left ventricular filling pressures using two-dimensional and doppler echocardiography in adult patients with cardiac disease: Additional value of analyzing left atrial size, left atrial ejection fraction and the difference in furation of pulmonary venous and mitral flow velocity at atrial contraction. *Journal of the American College of Cardiology*, 22:1972–1982.

[23] P. M. Arvidsson, S. J. Kovács, J. Töger, R. Borgquist, E. Heiberg, M. Carlsson, and H. Arheden. Vortex ring behavior provides the epigenetic blueprint for the human heart. *Scientific Reports*, 6(1), 2016. doi: 10.1038/srep22021. URL `https://doi.org/10.1038%2Fsrep22021`.

[24] ASME V&V 40-2018. Assesing credibility of computational modeling through verification and validation: application to medical devices. Standard, The American Society of Mechanical Engineers, 2018.

[25] M. Astorino, J. Hamers, S. C. Shadden, and J.-F. Gerbeau. A robust and efficient valve model based on resistive immersed surfaces. *International Journal for*

Numerical Methods in Biomedical Engineering, 28(9):937–959, may 2012. doi: 10.1002/cnm.2474. URL https://doi.org/10.1002%2Fcnm.2474.

[26] C. M. Augustin, A. Crozier, A. Neic, A. J. Prassl, E. Karabelas, T. Ferreira da Silva, J. F. Fernandes, F. Campos, T. Kuehne, and G. Plank. Patient-specific modeling of left ventricular electromechanics as a driver for haemodynamic analysis. *EP Europace*, 18(suppl_4):iv121–iv129, 2016.

[27] B. Baccani, F. Domenichini, and G. Pedrizzetti. Vortex dynamics in a model left ventricle during filling. *European Journal of Mechanics-B/Fluids*, 21(5):527–543, 2002.

[28] Y. Bartosiewicz and M. Duponcheel. Large Eddy Simulation: Application to liquid metal fluid flow and heat transfer. In F. Roelofs, editor, *Thermal hydraulics aspects of liquid metal cooled nuclear reactors*, pages 245–271. Woodhead Publishing, 2018.

[29] A. M. Bavo, G. Rocatello, F. Iannaccone, J. Degroote, J. Vierendeels, and P. Segers. Fluid-structure interaction simulation of prosthetic aortic valves: comparison between immersed boundary and arbitrary Lagrangian-Eulerian techniques for the mesh representation. *PloS one*, 11(4):e0154517, 2016.

[30] J. D. Bayer, R. C. Blake, G. Plank, and N. A. Trayanova. A novel rule-based algorithm for assigning myocardial fiber orientation to computational heart models. *Annals of Biomedical Engineering*, 40(10):2243–2254, 2012.

[31] Y. Bazilevs, V. Calo, J. Cottrell, T. Hughes, A. Reali, and G. Scovazzi. Variational multiscale residual-based turbulence modeling for large eddy simulation of incompressible flows. *Computer Methods in Applied Mechanics and Engineering*, 197(1-4):173–201, 2007.

[32] Y. Bazilevs, J. Gohean, T. Hughes, R. Moser, and Y. Zhang. Patient-specific isogeometric fluid-structure interaction analysis of thoracic aortic blood flow due to implantation of the Jarvik 2000 left ventricular assist device. *Computer Methods in Applied Mechanics and Engineering*, 198(45-46):3534–3550, 2009.

[33] N. Bénard, J. Pons-Prats, J. Périaux, G. Bugeda, P. Braud, J. Bonnet, and E. Moreau. Turbulent separated shear flow control by surface plasma actuator: experimental optimization by genetic algorithm approach. *Experiments in Fluids*, 57:1–17, 2016.

[34] R. Bensow, M. Larson, and P. Vesterlund. Vorticity-strain residual-based turbulence modeling of the Taylor-Green vortex. *International Journal for Numerical Methods in Fluids*, 54:745–756, 06 2007. doi: 10.1002/fld.1485.

[35] L. Bertagna, S. Deparis, L. Formaggia, D. Forti, and A. Veneziani. The LifeV library: engineering mathematics beyond the proof of concept. *arXiv preprint arXiv:1710.06596*, 2017.

[36] C. Bertoglio and A. Caiazzo. A tangential regularization method for backflow stabilization in hemodynamics. *Journal of Computational Physics*, 261:162–171, 2014.

[37] P. J. Blanco and R. A. Feijoo. A 3D-1D-0D computational model for the entire cardiovascular system. *Mecanica Computacional*, 24:5887–5911, 2010.

[38] J. Blazek. *Computational Fluid Dynamics: Principles and Applications*. Elsevier Science, 2001.

[39] D. Bluestein and S. Einav. Transition to turbulence in pulsatile flow through heart valves - a modified stability approach. *Journal of Biomechanical Engineering*, 116 (4):477–487, 1994.

[40] P. B. Bochev, C. R. Dohrmann, and M. D. Gunzburger. Stabilization of low-order mixed finite elements for the Stokes equations. *SIAM Journal on Numerical Analysis*, 44(1):82–101, 2006. doi: 10.1137/S0036142905444482. URL `https://doi.org/10.1137/S0036142905444482`.

[41] D. Boffi, F. Brezzi, and M. Fortin. *Mixed finite element methods and applications*, volume 44. Springer, 2013.

[42] M. Brachet, D. Meiron, S. Orszag, G.N., R. Morf, and U. Frisch. Small-scale structure of the Taylor-Green vortex. *Journal of Fluid Mechanics*, 130:411–452, 1983.

[43] A. N. Brooks and T. J. R. Hughes. Streamline upwind/Petrov-Galerkin formulations for convection dominated flows with particular emphasis on the incompressible Navier-Stokes equations. *Computer Methods in Applied Mechanics and Engineering*, 32(1-3):199–259, 09 1982. doi: 10.1016/0045-7825(82)90071-8. URL `https://doi.org/10.1016%2F0045-7825%2882%2990071-8`.

[44] M. Bucelli, L. Dedé, and A. Quarteroni. Coupled computational modeling of cardiac electrophysiology, mechanics and fluid dynamics. In *MATHMOD Discussion Contribution Volume*. Technische Universität Wien, 2022.

[45] C. Canuto, M. Hussaini, A. Quarteroni, and T. Zang. *Spectral Methods. Fundamentals in Single Domains*. Springer-Verlag, Berlin, 2006.

[46] R. M. Carey and P. K. Whelton. Prevention, detection, evaluation, and management of high blood pressure in adults: synopsis of the 2017 American College of Cardiology/American Heart Association Hypertension Guideline. *Annals of internal medicine*, 168(5):351–358, 2018.

[47] C. Carmody, G. Burriesci, I. Howard, and E. Patterson. An approach to the simulation of fluid-structure interaction in the aortic valve. *Journal of Biomechanics*, 39(1):158–169, 2006.

[48] R. Chabiniok, V. Y. Wang, M. Hadjicharalambous, L. Asner, J. Lee, M. Sermesant, E. Kuhl, A. A. Young, P. Moireau, M. P. Nash, D. Chapelle, and D. A. Nordsletten. Multiphysics and multiscale modelling, data-model fusion and integration of organ physiology in the clinic: ventricular cardiac mechanics. *Interface focus*, 6(2):20150083, 2016.

[49] S. Chandra, N. M. Rajamannan, and P. Sucosky. Computational assessment of bicuspid aortic valve wall-shear stress: implications for calcific aortic valve disease. *Biomechanics and Modeling in Mechanobiology*, 11(7):1085–1096, 2012.

[50] R. Cheng, Y. G. Lai, and K. B. Chandran. Three-dimensional fluid-structure interaction simulation of bileaflet mechanical heart valve flow dynamics. *Annals of Biomedical Engineering*, 32(11):1471–1483, 2004.

[51] C. Chnafa, S. Mendez, and F. Nicoud. Image-based large-eddy simulation in a realistic left heart. *Computers & Fluids*, 94:173–187, 2014.

[52] Y. J. Choi, J. Constantino, V. Vedula, N. Trayanova, and R. Mittal. A new MRI-based model of heart function with coupled hemodynamics and application to normal and diseased canine left ventricles. *Frontiers in Bioengineering and Biotechnology*, 3:140, 2015.

[53] F. Chollet et al. Keras. `https://keras.io`, 2015.

[54] R. Codina. On stabilized finite element methods for linear systems of convection-diffusion-reaction equations. *Computer Methods in Applied Mechanics and Engineering*, 188(1):61–82, 2000. ISSN 0045-7825. doi: https://doi.org/10.1016/S0045-7825(00)00177-8. URL `https://www.sciencedirect.com/science/article/pii/S0045782500001778`.

[55] R. Codina. Analysis of a stabilized finite element approximation of the Oseen equations using orthogonal subscales. *Applied Numerical Mathematics*, 58(3):264–283, 2008. ISSN 0168-9274. doi: https://doi.org/10.1016/j.apnum.2006.11.011. URL `https://www.sciencedirect.com/science/article/pii/S0168927406002194`.

[56] R. Codina, J. Principe, O. Guasch, and S. Badia. Time dependent subscales in the stabilized finite element approximation of incompressible flow problems. *Computer Methods in Applied Mechanics and Engineering*, 196(21):2413–2430, 2007. ISSN 0045-7825. doi: https://doi.org/10.1016/j.cma.2007.01.002. URL `https://www.sciencedirect.com/science/article/pii/S0045782507000035`.

[57] R. Codina, J. Principe, O. Guasch, and S. Badia. Time dependent subscales in the stabilized finite element approximation of incompressible flow problems. *Computer Methods in Applied Mechanics and Engineering*, 196(21-24):2413–2430, 2007.

[58] D. Collia, L. Zovatto, G. Tonti, and G. Pedrizzetti. Comparative analysis of right ventricle fluid dynamics. *Frontiers in Bioengineering and Biotechnology*, 9, 2021.

[59] O. Colomés, S. Badia, R. Codina, and J. Principe. Assessment of variational multiscale models for the large eddy simulation of turbulent incompressible flows. *Computer Methods in Applied Mechanics and Engineering*, 285, 11 2014. doi: 10.1016/j.cma.2014.10.041.

[60] B. Colvert, M. Alsalman, and E. Kanso. Classifying vortex wakes using neural networks. *Bioinspiration & Biomimetics*, 2018.

[61] M. Corti. Effects of atrial fibrillation on left atrium haemodynamics: a patient specific computational fluid dynamics study. Master's thesis, Politecnico di Milano, 2021.

[62] J. A. Cottrell, T. J. R. Hughes, and Y. Bazilevs. *Isogeometric Analysis: Toward Integration of CAD and FEA*. John Wiley & Sons, 2009.

[63] C. T. Crowe, J. D. Schwarzkopf, M. Sommerfeld, and Y. Tsuji. *Multiphase Flows with Droplets and Particles*. CRC Press, 2 edition.

[64] C. F. Curtiss and J. O. Hirschfelder. Integration of stiff equations. *Proceedings of the National Academy of Sciences of the United States of America*, 38(3):235, 1952.

[65] J. De Hart, G. Peters, P. Schreurs, and F. Baaijens. A three-dimensional computational analysis of fluid-structure interaction in the aortic valve. *Journal of Biomechanics*, 36(1):103–112, 2003.

[66] L. Dean. Blood groups and red cell antigens. URL `https://www.ncbi.nlm.nih.gov/books/NBK2261/`.

[67] L. Dede', F. Menghini, and A. Quarteroni. Computational fluid dynamics of blood flow in an idealized left human heart. *International Journal for Numerical Methods in Biomedical Engineering*, dec 2019. doi: 10.1002/cnm.3287. URL `https://doi.org/10.1002%2Fcnm.3287`.

[68] Y. Delorme, K. Anupindi, and S. Frankel. Large eddy simulation of fda's idealized medical device. *Cardiovascular engineering and technology*, 4, 2013.

[69] S. Deparis, G. Grandperrin, and A. Quarteroni. Parallel preconditioners for the unsteady Navier-Stokes equations and applications to hemodynamics simulations. *Computers & Fluids*, 92:253–273, mar 2014. doi: 10.1016/j.compfluid.2013.10.034. URL `https://doi.org/10.1016%2Fj.compfluid.2013.10.034`.

[70] D. Dillon-Murphy, D. Marlevi, B. Ruijsink, A. Qureshi, H. Chubb, E. Kerfoot, M. O'Neill, D. Nordsletten, O. Aslanidi, and A. De Vecchi. Modeling left atrial

flow, energy, blood heating distribution in response to catheter ablation therapy. *Frontiers in physiology*, 9:1757, 2018.

[71] N. Discacciati, J. S. Hesthaven, and D. Ray. Controlling oscillations in high-order Discontinuous Galerkin schemes using artificial viscosity tuned by neural networks. *Journal of Computational Physics*, 409:109304, 2020.

[72] H. T. Dodge, F. T. Kirkham, and C. V. King. Ventricular dynamics in atrial fibrillation. *Circulation*, 15:335–347.

[73] M. Domanin, A. Buora, F. Scardulla, B. Guerciotti, L. Forzenigo, P. Biondetti, and C. Vergara. Computational fluid-dynamic analysis after carotid endarterectomy: patch graft versus direct suture closure. *Annals of vascular surgery*, 44: 325–335, 2017.

[74] F. Domenichini and G. Pedrizzetti. Intraventricular vortex flow changes in the infarcted left ventricle: numerical results in an idealised 3D shape. *Computer Methods in Biomechanics and Biomedical Engineering*, 14(01):95–101, 2011.

[75] F. Domenichini, G. Pedrizzetti, and B. Baccani. Three-dimensional filling flow into a model left ventricle. *Journal of fluid mechanics*, 539:179–198, 2005.

[76] J. Donea, S. Giuliani, and J.-P. Halleux. An arbitrary Lagrangian-Eulerian finite element method for transient dynamic fluid-structure interactions. *Computer Methods in Applied Mechanics and Engineering*, 33(1-3):689–723, 1982.

[77] J. Donea, A. Huerta, J.-P. Ponthot, and A. Rodriguez-Ferran. Arbitrary Lagrangian–Eulerian Methods. In R. d. B. Erwin Stein and T. J. Hughes., editors, *Encyclopedia of Computational Mechanics*, volume 1: Fundamentals, chapter 14, pages 413–437. John Wiley & Sons, 2004.

[78] R. Doste, D. Soto-Iglesias, G. Bernardino, A. Alcaine, R. Sebastian, S. Giffard-Roisin, M. Sermesant, A. Berruezo, D. Sanchez-Quintana, and O. Camara. A rule-based method to model myocardial fiber orientation in cardiac biventricular geometries with outflow tracts. *International journal for numerical methods in biomedical engineering*, 35(4):e3185, 2019.

[79] K. Duraisamy, G. Iaccarino, and H. Xiao. Turbulence modeling in the age of data. *Annual Review of Fluid Mechanics*, 51:357–377, 2019.

[80] P. Dyverfeldt, M. Bissell, A. J. Barker, A. F. Bolger, C.-J. Carlhäll, T. Ebbers, C. J. Francios, A. Frydrychowicz, J. Geiger, D. Giese, M. D. Hope, P. J. Kilner, S. Kozerke, S. Myerson, S. Neubauer, O. Wieben, and M. Markl. 4D flow cardiovascular magnetic resonance consensus statement. *Journal of Cardiovascular Magnetic Resonance*, 17(1), 2015. doi: 10.1186/s12968-015-0174-5. URL `https://doi.org/10.1186%2Fs12968-015-0174-5`.

[81] M. El Rafei, L. Könözsy, and Z. Rana. Investigation of numerical dissipation in classical and implicit large eddy simulations. *Aerospace*, 4(4):59, 2017.

[82] M. Enriquez-Sarano, K. S. Dujardin, C. M. Tribouilloy, J. B. Seward, A. P. Yoganathan, K. R. Bailey, and A. J. Tajik. Determinants of pulmonary venous flow reversal in mitral regurgitation and its usefulness in determining the severity of regurgitation. *The American journal of cardiology*, 83(4):535–541, 1999.

[83] J. Evans, D. Kamensky, and Y. Bazilevs. Variational multiscale modeling with discretely divergence-free subscales. *Computers & Mathematics with Applications*, 80, 04 2020. doi: 10.1016/j.camwa.2020.03.011.

[84] C. Farhat, A. Rajasekharan, and B. Koobus. A dynamic variational multiscale method for large eddy simulations on unstructured meshes. *Computer Methods in Applied Mechanics and Engineering*, 195(13-16):1667–1691, 2006.

[85] M. Fedele and A. Quarteroni. Polygonal surface processing and mesh generation tools for the numerical simulation of the cardiac function. *International Journal for Numerical Methods in Biomedical Engineering*, 37(4), jan 2021. doi: 10.1002/cnm.3435. URL `https://doi.org/10.1002%2Fcnm.3435`.

[86] M. Fedele, E. Faggiano, L. Dede', and A. Quarteroni. A patient-specific aortic valve model based on moving resistive immersed implicit surfaces. *Biomechanics and Modeling in Mechanobiology*, 16(5):1779–1803, jun 2017. doi: 10.1007/s10237-017-0919-1. URL `https://doi.org/10.1007%2Fs10237-017-0919-1`.

[87] M. A. Fernández, J.-F. Gerbeau, and V. Martin. Numerical simulation of blood flows through a porous interface. *ESAIM: Mathematical Modelling and Numerical Analysis*, 42(6):961–990, aug 2008. doi: 10.1051/m2an:2008031. URL `https://doi.org/10.1051%2Fm2an%3A2008031`.

[88] A. Ferrer, R. Sebastián, D. Sánchez-Quintana, J. F. Rodríguez, E. J. Godoy, L. Martínez, and J. Saiz. Detailed anatomical and electrophysiological models of human atria and torso for the simulation of atrial activation. *PloS one*, 10(11):e0141573, 2015.

[89] G. W. Fischer and P. Trigo. 15 - Mitral Valvular Disease. In D. L. Reich and G. W. Fischer, editors, *Perioperative Transesophageal Echocardiography*, pages 144–155. W.B. Saunders, Philadelphia, 2014. ISBN 978-1-4557-0761-4. doi: https://doi.org/10.1016/B978-1-4557-0761-4.00015-3. URL `https://www.sciencedirect.com/science/article/pii/B9781455707614000153`.

[90] L. Formaggia and F. Nobile. A stability analysis for the arbitrary Lagrangian Eulerian formulation with finite elements. *East-West Journal of Numerical Mathematics*, 7(2):105–131, 1999.

[91] L. Formaggia, J.-F. Gerbeau, F. Nobile, and A. Quarteroni. On the coupling of 3D

and 1d Navier-Stokes equations for flow problems in compliant vessels. *Computer Methods in Applied Mechanics and Engineering*, 191(6-7):561–582, 2001.

[92] L. Formaggia, D. Lamponi, and A. Quarteroni. One-dimensional models for blood flow in arteries. *Journal of engineering mathematics*, 47(3):251–276, 2003.

[93] D. Forti and L. Dede'. Semi-implicit bdf time discretization of the Navier–Stokes equations with vms-LES modeling in a high performance computing framework. *Computers & Fluids*, 117:168–182, 2015.

[94] L. P. Franca, S. L. Frey, and T. J. R. Hughes. Stabilized finite element methods: I. application to the advective-diffusive model. *Computer Methods in Applied Mechanics and Engineering*, 95(2):253–276, 1992.

[95] P. C. Franzone, L. F. Pavarino, and S. Scacchi. *Mathematical cardiac electrophysiology*, volume 13. Springer, 2014.

[96] P. C. Franzone, L. F. Pavarino, and S. Scacchi. Parallel multilevel solvers for the cardiac electro-mechanical coupling. *Applied Numerical Mathematics*, 95: 140–153, 2015.

[97] K. H. Fraser, M. E. Taskin, B. P. Griffith, and Z. J. Wu. The use of computational fluid dynamics in the development of ventricular assist devices. *Medical engineering & physics*, 33(3):263–280, 2011.

[98] S. Fresca and A. Manzoni. Real-time simulation of parameter-dependent fluid flows through deep learning-based reduced order models. *Fluids*, 6(7):1–25, 2021.

[99] S. Fresca, L. Dede', and A. Manzoni. A comprehensive deep learning-based approach to reduced order modeling of nonlinear time-dependent parametrized PDEs. *Journal of Scientific Computing*, 87(2):1–36, 2021.

[100] I. Fumagalli, M. Fedele, C. Vergara, L. Dede', S. Ippolito, F. Nicolò, C. Antona, R. Scrofani, and A. Quarteroni. An image-based computational hemodynamics study of the systolic anterior motion of the mitral valve. *Computers in Biology and Medicine*, 123:103922, aug 2020. doi: 10.1016/j.compbiomed.2020.103922. URL `https://doi.org/10.1016%2Fj.compbiomed.2020.103922`.

[101] A. Galeao, R. Almeida, S. Malta, and A. Loula. Finite element analysis of convection dominated reaction–diffusion problems. *Applied Numerical Mathematics*, 48(2):205–222, 2004.

[102] L. Gan, L. Yu, M. Xie, W. Feng, and J. Yin. Analysis of real-time three dimensional transesophageal echocardiography in the assessment of left atrial appendage function in patients with atrial fibrillation. *Experimental and Therapeutic Medicine*, 12:3323–3327.

[103] H. Gao, L. Feng, N. Qi, C. Berry, B. E. Griffith, and X. Luo. A coupled mitral

valve-left ventricle model with fluid-structure interaction. *Medical Engineering & Physics*, 47:128–136, 2017.

[104] D. Garcia, J. C. del Álamo, D. Tanné, R. Yotti, C. Cortina, É. Bertrand, J. C. Antoranz, E. Pérez-David, R. Rieu, F. Fernández-Avilés, and J. Bermejo. Two-dimensional intraventricular flow mapping by digital processing conventional color-doppler echocardiography images. *IEEE Transactions on Medical Imaging*, 29(10):1701–1713, oct 2010. doi: 10.1109/tmi.2010.2049656. URL `https://doi.org/10.1109%2Ftmi.2010.2049656`.

[105] F. Gaudenzi and A. P. Avolio. Lumped parameter model of cardiovascular-respiratory interaction. In *2013 35th Annual International Conference of the IEEE Engineering in Medicine and Biology Society (EMBC)*, pages 473–476. IEEE, 2013.

[106] A. Gerbi. *Numerical approximation of cardiac electro-fluid-mechanical models: Coupling strategies for large-scale simulation.* PhD thesis, Ecole Polytechnique Fédérale de Lausanne, 2018.

[107] M. Germano, U. Piomelli, P. Moin, and W. H. Cabot. A dynamic subgrid-scale eddy viscosity model. *Physics of Fluids A: Fluid Dynamics*, 3(7):1760–1765, 1991.

[108] C. Geuzaine and J. Remacle. Gmsh: A 3D finite element mesh generator with built-in pre- and post-processing facilities. *International Journal for Numerical Methods in Engineering*, 79:1309 – 1331, 2009.

[109] R. Glowinski, T.-W. Pan, and J. Periaux. A lagrange multiplier/fictitious domain method for the numerical simulation of incompressible viscous flow around moving rigid bodies:(i) case where the rigid body motions are known a priori. *Comptes Rendus de l'Académie des Sciences-Series I-Mathematics*, 324(3):361–369, 1997.

[110] I. Goodfellow, Y. Bengio, and A. Courville. *Deep Learning.* MIT Press, 2016. URL `http://www.deeplearningbook.org`.

[111] B. E. Griffith. Immersed boundary model of aortic heart valve dynamics with physiological driving and loading conditions. *International journal for numerical methods in biomedical engineering*, 28(3):317–345, 2012.

[112] J. M. Guccione and A. D. McCulloch. Finite element modeling of ventricular mechanics. In *Theory of Heart*, pages 121–144. Springer, 1991.

[113] G. S. Gulsin, A. Singh, and G. P. McCann. Cardiovascular magnetic resonance in the evaluation of heart valve disease. *BMC Medical Imaging*, 17(1), 2017. doi: 10.1186/s12880-017-0238-0. URL `https://doi.org/10.1186%2Fs12880-017-0238-0`.

[114] M. Guo and J. S. Hesthaven. Data-driven reduced order modeling for time-dependent problems. *Computer Methods in Applied Mechanics and Engineering*, 345:75–99, 2019.

[115] D. K. Gupta, A. M. Shah, R. P. Giugliano, C. T. Ruff, E. M. Antman, L. T. Grip, N. Deenadayalu, E. Hoffman, I. Patel, M. Shi, et al. Left atrial structure and function in atrial fibrillation: Engage af-timi 48. *European heart journal*, 35 (22):1457–1465, 2014.

[116] P. Hariharan, M. Giarra, V. Reddy, S. Day, K. Manning, S. Deutsc, S. Stewart, M. Myers, M. Berman, G. Burgreen, E. Paterson, and R. Malinauskas. Multilaboratory particle image velocimetry analysis of the FDAbenchmark nozzle model to support validation of computational fluid dynamics simulations. *Journal of biomechanical engineering*, 133:041002, 2011.

[117] P. Hariharan, M. Giarra, V. Reddy, S. Day, K. Manning, S. Deutsc, S. Stewart, M. Myers, M. Berman, G. Burgreen, E. Paterson, and R. Malinauskas. Multilaboratory particle image velocimetry analysis of the FDA benchmark nozzle model to support validation of computational fluid dynamics simulations. *Journal of biomechanical engineering*, 133:041002, 2011.

[118] S. Haßler, L. Pauli, and M. Behr. The variational multiscale formulation for the fully-implicit log-morphology equation as a tensor-based blood damage model. *International journal for numerical methods in biomedical engineering*, 35(12): e3262, 2019.

[119] E. Helps and D. McDonald. Observations on laminar flow in veins. *The Journal of physiology*, 124(3):631, 1954.

[120] J. S. Hesthaven and S. Ubbiali. Non-intrusive reduced order modeling of nonlinear problems using neural networks. *Journal of Computational Physics*, 363:55–78, 2018.

[121] H. A. Himburg, D. M. Grzybowski, A. L. Hazel, J. A. LaMack, X.-M. Li, and M. H. Friedman. Spatial comparison between wall shear stress measures and porcine arterial endothelial permeability. *American Journal of Physiology-Heart and Circulatory Physiology*, 286(5):H1916–H1922, 2004.

[122] J. Hiromi Spühler and J. Hoffman. An interface-tracking unified continuum model for fluid-structure interaction with topology change and full-friction contact with application to aortic valves. *International Journal for Numerical Methods in Engineering*, 2020.

[123] M. Hirschvogel, M. Bassilious, L. Jagschies, S. M. Wildhirt, and M. W. Gee. A monolithic 3D-0D coupled closed-loop model of the heart and the vascular system: Experiment-based parameter estimation for patient-specific cardiac mechanics. *International Journal for Numerical Methods in Biomedical*

Engineering, 33(8):e2842, feb 2017. doi: 10.1002/cnm.2842. URL `https://doi.org/10.1002%2Fcnm.2842`.

[124] D. I. Hollnagel, P. E. Summers, D. Poulikakos, and S. S. Kollias. Comparative velocity investigations in cerebral arteries and aneurysms: 3d phase-contrast MR angiography, laser doppler velocimetry and computational fluid dynamics. *NMR in Biomedicine: An International Journal Devoted to the Development and Application of Magnetic Resonance In vivo*, 22(8):795–808, 2009.

[125] T. J. Hughes. Multiscale phenomena: Green's functions, the dirichlet-to-neumann formulation, subgrid scale models, bubbles and the origins of stabilized methods. *Computer Methods in Applied Mechanics and Engineering*, 127(1-4): 387–401, 1995.

[126] T. J. Hughes, L. Mazzei, and K. E. Jansen. Large eddy simulation and the variational multiscale method. *Computing and visualization in science*, 3(1): 47–59, 2000.

[127] T. J. Hughes, A. A. Oberai, and L. Mazzei. Large eddy simulation of turbulent channel flows by the variational multiscale method. *Physics of fluids*, 13(6): 1784–1799, 2001.

[128] T. J. R. Hughes. *The finite element method: linear static and dynamic finite element analysis*. Courier Corporation, 2012.

[129] T. J. R. Hughes, V. M. Calo, and G. Scovazzi. Variational and multiscale methods in turbulence. In *Mechanics of the 21st Century*, pages 153–163. Springer, 2005.

[130] T. J. R. Hughes, G. Scovazzi, and L. P. Franca. Multiscale and stabilized methods. *Encyclopedia of Computational Mechanics Second Edition*, pages 1–64, 2018.

[131] J. Hunt, A. Wray, and P. Moin. Eddies, stream, and convergence zones in turbulent flows. *Studying Turbulence Using Numerical Simulation Databases-I1*, 193, 1988.

[132] P. A. Iaizzo. *Handbook of cardiac anatomy, physiology, and devices*. Springer Science & Business Media, 2009.

[133] Z. M. G. Inc. Zygote solid 3D heart generation ii developement report. tech. rep. 2014.

[134] R. K. Jarvik. The total artificial heart. *Scientific American*, 244(1):74–81, 1981.

[135] V. John and P. Knobloch. On spurious oscillations at layers diminishing (sold) methods for convection-diffusion equations: Part i–a review. *Computer Methods in Applied Mechanics and Engineering*, 196(17-20):2197–2215, 2007.

[136] A. Johnson and T. Tezduyar. Mesh update strategies in parallel finite element computations of flow problems with moving boundaries and interfaces. *Computer*

Methods in Applied Mechanics and Engineering, 119(1-2):73–94, nov 1994. doi: 10.1016/0045-7825(94)00077-8. URL https://doi.org/10.1016%2F0045-7825%2894%2900077-8.

[137] S. M. Joshi, T. Anandh, B. Teja, and S. Ganesan. On the choice of hyper-parameters of artificial neural networks for stabilized finite element schemes. *International Journal of Advances in Engineering Sciences and Applied Mathematics*, 13(2):278–297, 2021.

[138] D. Kamensky, M.-C. Hsu, D. Schillinger, J. A. Evans, A. Aggarwal, Y. Bazilevs, M. S. Sacks, and T. J. Hughes. An immersogeometric variational framework for fluid-structure interaction: Application to bioprosthetic heart valves. *Computer Methods in Applied Mechanics and Engineering*, 284:1005–1053, 2015.

[139] E. Karabelas, M. A. Gsell, C. M. Augustin, L. Marx, A. Neic, A. J. Prassl, L. Goubergrits, T. Kuehne, and G. Plank. Towards a computational framework for modeling the impact of aortic coarctations upon left ventricular load. *Frontiers in physiology*, 9:538, 2018.

[140] T. D. Karamitsos, J. M. Francis, S. Myerson, J. B. Selvanayagam, and S. Neubauer. The role of cardiovascular magnetic resonance imaging in heart failure. *Journal of the American College of Cardiology*, 54(15):1407–1424, oct 2009. doi: 10.1016/j.jacc.2009.04.094. URL https://doi.org/10.1016%2Fj.jacc.2009.04.094.

[141] R. Kaufmann, R. Rezar, B. Strohmer, B. Wernly, M. Lichtenauer, W. Hitzl, M. Meissnitzer, K. Hergan, and M. Granitz. Left atrial ejection fraction assessed by prior cardiac ct predicts recurrence of atrial fibrillation after pulmonary vein isolation. *Journal of Clinical Medicine*, 10:1–12.

[142] M. Kemp. Leonardo da vinci's laboratory: studies in flow. *Nature*, 571(7765): 322–324, 2019.

[143] H. B. Kim, J. R. Hertzberg, and R. Shandas. Development and validation of echo PIV. *Experiments in Fluids*, 36(3):455–462, mar 2004. doi: 10.1007/s00348-003-0743-5. URL https://doi.org/10.1007%2Fs00348-003-0743-5.

[144] H. J. Kim, I. E. Vignon-Clementel, C. A. Figueroa, J. F. LaDisa, K. E. Jansen, J. A. Feinstein, and C. A. Taylor. On coupling a lumped parameter heart model and a three-dimensional finite element aorta model. *Annals of Biomedical Engineering*, 37(11):2153–2169, 2009.

[145] W. Y. Kim, P. G. Walker, E. M. Pedersen, J. K. Poulsen, S. Oyre, K. Houlind, and A. P. Yoganathan. Left ventricular blood flow patterns in normal subjects: A quantitative analysis by three-dimensional magnetic resonance velocity mapping. *Journal of the American College of Cardiology*, 26(1):224–238, 1995. doi:

10.1016/0735-1097(95)00141-l. URL https://doi.org/10.1016%2F0735-1097%2895%2900141-l.

[146] W. Y. Kim, P. G. Walker, E. M. Pedersen, J. K. Poulsen, S. Oyre, K. Houlind, and A. P. Yoganathan. Left ventricular blood flow patterns in normal subjects: a quantitative analysis by three-dimensional magnetic resonance velocity mapping. *Journal of the American College of Cardiology*, 26(1):224–238, 1995.

[147] R. Koizumi, K. Funamoto, T. Hayase, Y. Kanke, M. Shibata, Y. Shiraishi, and T. Yambe. Numerical analysis of hemodynamic changes in the left atrium due to atrial fibrillation. *Journal of Biomechanics*, 48(3):472–478, 2015.

[148] A. N. Kolmogorov. The local structure of turbulence in incompressible viscous fluid for very large reynolds numbers. *Cr Acad. Sci. URSS*, 30:301–305, 1941.

[149] T. Korakianitis and Y. Shi. Numerical simulation of cardiovascular dynamics with healthy and diseased heart valves. *Journal of Biomechanics*, 39(11):1964–1982, 2006.

[150] S. J. Kovács, D. M. McQueen, and C. S. Peskin. Modelling cardiac fluid dynamics and diastolic function. *Philosophical Transactions of the Royal Society of London. Series A: Mathematical, Physical and Engineering Sciences*, 359(1783):1299–1314, 2001.

[151] A. Krämer, K. Küllmer, D. Reith, W. Joppich, and H. Foysi. Semi-Lagrangian off-lattice Boltzmann method for weakly compressible flows. *Phys. Rev. E*, 95, 02 2017. doi: 10.1103/PhysRevE.95.023305.

[152] D. N. Ku, D. P. Giddens, C. K. Zarins, and S. Glagov. Pulsatile flow and atherosclerosis in the human carotid bifurcation. positive correlation between plaque location and low oscillating shear stress. *Arteriosclerosis: An Official Journal of the American Heart Association, Inc.*, 5(3):293–302, 1985.

[153] P. K. Kundu, I. M. Cohen, and D. R. Dowling. *Fluid Mechanics*. Academic Press, 5 edition, 2014.

[154] K. Kunzelman, D. R. Einstein, and R. Cochran. Fluid-structure interaction models of the mitral valve: function in normal and pathological states. *Philosophical Transactions of the Royal Society B: Biological Sciences*, 362(1484):1393–1406, 2007.

[155] G. Kutyniok, P. Petersen, M. Raslan, and R. Schneider. A theoretical analysis of deep neural networks and parametric PDEs. *Constructive Approximation*, jun 2021. doi: 10.1007/s00365-021-09551-4. URL https://doi.org/10.1007%2Fs00365-021-09551-4.

[156] R. M. Lancellotti, C. Vergara, L. Valdettaro, S. Bose, and A. Quarteroni. Large

eddy simulations for blood dynamics in realistic stenotic carotids. *International journal for numerical methods in biomedical engineering*, 33(11):e2868, 2017.

[157] T. B. Le and F. Sotiropoulos. Fluid-structure interaction of an aortic heart valve prosthesis driven by an animated anatomic left ventricle. *Journal of Computational Physics*, 244:41–62, 2013.

[158] A. Lupo, I. Mokhov, S. Dostoglou, A. Kunz, and J. Burkhardt. Assessment of the impact of the planetary scale on the decay of blocking and the use of phase diagrams and enstrophy as a diagnostic. *Izvestiya, Atmospheric and Oceanic Physics*, 43(1):45–51, 2007.

[159] X. Ma, H. Gao, B. E. Griffith, C. Berry, and X. Luo. Image-based fluid-structure interaction model of the human mitral valve. *Computers & Fluids*, 71:417–425, 2013.

[160] A. Maceira, S. Prasad, M. Khan, and D. Pennell. Normalized left ventricular systolic and diastolic function by steady state free precession cardiovascular magnetic resonance. *Journal of Cardiovascular Magnetic Resonance*, 8(3):417–426, 2006.

[161] R. A. Malinauskas, P. Hariharan, S. W. Day, L. H. Herbertson, M. Büsen, U. Steinseifer, K. I. Aycock, B. C. Good, S. Deutsch, K. B. Manning, and B. Craven. FDAbenchmark medical device flow models for CFDvalidation. *ASAIO journal (American Society for Artificial Internal Organs : 1992)*, 63, 2017.

[162] J. Mangual, F. Domenichini, and G. Pedrizzetti. Describing the highly three dimensional right ventricle flow. *Annals of Biomedical Engineering*, 40(8):1790–1801, 2012.

[163] J. O. Mangual, E. Kraigher-Krainer, A. De Luca, L. Toncelli, A. Shah, S. Solomon, G. Galanti, F. Domenichini, and G. Pedrizzetti. Comparative numerical study on left ventricular fluid dynamics after dilated cardiomyopathy. *Journal of Biomechanics*, 46(10):1611–1617, 2013.

[164] M. Markl, M. Carr, J. Ng, D. C. Lee, K. Jarvis, J. Carr, and J. J. Goldberger. Assessment of left and right atrial 3D hemodynamics in patients with atrial fibrillation: a 4D flow MRI study. *International Society for Magnetic Resonance in Medicine*, 32:807–815, .

[165] M. Markl, D. C. Lee, N. Furiasse, M. Carr, C. Foucar, J. Ng, J. Carr, and J. J. Goldberger. Left atrial and left atrial appendage 4D blood flow dynamics in atrial fibrillation. *Circulation, Cardiovascular Imaging*, 9:e004984, .

[166] M. Markl, A. Frydrychowicz, S. Kozerke, M. Hope, and O. Wieben. 4D flow MRI. *Journal of Magnetic Resonance Imaging*, 36(5):spcone–spcone, oct 2012. doi: 10.1002/jmri.23556. URL `https://doi.org/10.1002%2Fjmri.23556`.

[167] G. Marom, H.-S. Kim, M. Rosenfeld, E. Raanani, and R. Haj-Ali. Fully coupled fluid-structure interaction model of congenital bicuspid aortic valves: effect of asymmetry on hemodynamics. *Medical & biological engineering & computing*, 51 (8):839–848, 2013.

[168] A. Masci, M. Alessandrini, D. Forti, F. Menghini, L. Dedé, C. Tommasi, A. Quarteroni, and C. Corsi. A patient-specific computational fluid dynamics model of the left atrium in atrial fibrillation: Development and initial evaluation. In *International Conference on Functional Imaging and Modeling of the Heart*, pages 392–400. Springer, 2017.

[169] A. Masci, L. Barone, L. Dede', M. Fedele, C. Tomasi, A. Quarteroni, and C. Corsi. The impact of left atrium appendage morphology on stroke risk assessment in atrial fibrillation: a computational fluid dynamics study. *Frontiers in physiology*, 9:1938, 2019.

[170] A. Masci, M. Alessandrini, D. Forti, F. Menghini, L. Dedé, C. Tomasi, A. Quarteroni, and C. Corsi. A proof of concept for computational fluid dynamic analysis of the left atrium in atrial fibrillation on a patient-specific basis. *Journal of Biomechanical Engineering*, 142(1), 2020.

[171] F. R. Menter, M. Kuntz, and R. Langtry. Ten years of industrial experience with the sst turbulence model. *Turbulence, heat and mass transfer*, 4(1):625–632, 2003.

[172] V. Mihalef, R. I. Ionasec, P. Sharma, B. Georgescu, I. Voigt, M. Suehling, and D. Comaniciu. Patient-specific modelling of whole heart anatomy, dynamics and haemodynamics from four-dimensional cardiac ct images. *Interface Focus*, 1(3): 286–296, 2011.

[173] M. Milano and P. Koumoutsakos. Neural network modeling for near wall turbulent flow. *Journal of Computational Physics*, 182(1):1–26, 2002. doi: https://doi.org/10.1006/jcph.2002.7146.

[174] V. Milišić and A. Quarteroni. Analysis of lumped parameter models for blood flow simulations and their relation with 1d models. *ESAIM: Mathematical modelling and numerical analysis*, 38(4):613–632, 2004.

[175] J. R. Mitchell and J.-J. Wang. Expanding application of the wiggers diagram to teach cardiovascular physiology. *Advances in physiology education*, 38(2):170–175, 2014.

[176] T. M. Mitchell. *Machine learning*. McGraw-hill New York, 1997.

[177] R. Mittal, J. H. Seo, V. Vedula, Y. J. Choi, H. Liu, H. H. Huang, S. Jain, L. Younes, T. Abraham, and R. T. George. Computational modeling of cardiac hemodynamics: Current status and future outlook. *Journal of Computational Physics*, 305:1065–1082, 2016. doi: 10.1016/j.jcp.2015.11.022. URL `https://doi.org/10.1016%2Fj.jcp.2015.11.022`.

[178] NASA. Problem C3.5 direct numerical simulation of the Taylor-Green vortex at Re = 1600. https://cfd.ku.edu/hiocfd/case_c3.5.pdf.

[179] P. Neittaanmäki and S. Repin. Artificial intelligence and computational science. *Intelligent Systems, Control and Automation: Science and Engineering*, 76:27–35, 2022. doi: 10.1007/978-3-030-70787-3_3. URL https://www.scopus.com/inward/record.uri?eid=2-s2.0-85113802679&doi=10.1007%2f978-3-030-70787-3_3&partnerID=40&md5=bb88fbe938df734647a2393e41b22a36.

[180] M. T. Ngo, C. I. Kim, J. Jung, G. H. Chung, D. H. Lee, and H. S. Kwak. Four-dimensional flow magnetic resonance imaging for assessment of velocity magnitudes and flow patterns in the human carotid artery bifurcation: Comparison with computational fluid dynamics. *Diagnostics*, 9(4):223, 2019.

[181] F. Nicoud, C. Chnafa, J. Siguenza, V. Zmijanovic, and S. Mendez. Large-eddy simulation of turbulence in cardiovascular flows. In *Biomedical Technology*, pages 147–167. Springer, 2018.

[182] M. Nobili, U. Morbiducci, R. Ponzini, C. Del Gaudio, A. Balducci, M. Grigioni, F. M. Montevecchi, and A. Redaelli. Numerical simulation of the dynamics of a bileaflet prosthetic heart valve using a fluid-structure interaction approach. *Journal of Biomechanics*, 41(11):2539–2550, 2008.

[183] G. Novati, L. Mahadevan, and P. Koumoutsakos. Controlled gliding and perching through deep-reinforcement-learning. *Phys. Rev. Fluids*, 4, 2019. doi: 10.1103/PhysRevFluids.4.093902.

[184] U. of Illinois at Urbana-Champaign. Center for Supercomputing Research, Development, and G. Cybenko. *Continuous valued neural networks with two hidden layers are sufficient*. 1988.

[185] J.-i. Okada, T. Washio, S. Sugiura, and T. Hisada. Clinical and pharmacological application of multiscale multiphysics heart simulator, UT-heart. *The Korean Journal of Physiology & Pharmacology*, 23(5):295–303, 2019.

[186] K. M. Olsson, N. P. Nickel, J. Tongers, and M. M. Hoeper. Atrial flutter and fibrillation in patients with pulmonary hypertension. *International Journal of Cardiology*, 167:2300–2305.

[187] L. H. Opie. *Heart physiology: from cell to circulation*. Lippincott Williams & Wilkins, 2004.

[188] J. A. Ormiston, P. M. Shah, C. Tei, and M. Wong. Size and motion of the mitral valve annulus in man. *Circulation*, 64:113–120, 1981.

[189] S. Osher and J. A. Sethian. Fronts propagating with curvature-dependent speed: Algorithms based on hamilton-jacobi formulations. *Journal of Computational Physics*, 79(1):12–49, 1988.

[190] E. Ovsyannikova and V. Kashirin. Blood flow modeling with a finite element living heart model in the flowvision software complex. In *IOP Conference Series: Materials Science and Engineering*, volume 747, page 012070. IOP Publishing, 2020.

[191] S. Pant, C. Corsini, C. Baker, T.-Y. Hsia, G. Pennati, and I. E. Vignon-Clementel. A lumped parameter model to study atrioventricular valve regurgitation in stage 1 and changes across stage 2 surgery in single ventricle patients. *IEEE Transactions on Biomedical Engineering*, 65(11):2450–2458, nov 2018. doi: 10.1109/tbme.2018.2797999. URL `https://doi.org/10.1109%2Ftbme.2018.2797999`.

[192] F. Pashakhanloo, D. A. Herzka, H. Ashikaga, S. Mori, N. Gai, D. A. Bluemke, N. A. Trayanova, and E. R. McVeigh. Myofiber architecture of the human atria as revealed by submillimeter diffusion tensor imaging. *Circulation Arrhythmia and Electrophysiology*, 9:e004133.

[193] T. Passerini, A. Quaini, U. Villa, A. Veneziani, and S. Canic. Validation of an open source framework for the simulation of blood flow in rigid and deformable vessels. *International journal for numerical methods in biomedical engineering*, 29, 2013.

[194] A. S. Patelli, L. Dede', T. Lassila, A. Bartezzaghi, and A. Quarteroni. Isogeometric approximation of cardiac electrophysiology models on surfaces: An accuracy study with application to the human left atrium. *Computer Methods in Applied Mechanics and Engineering*, 317:248–273, 2017.

[195] L. Pauli. *Stabilized finite element methods for computational design of blood-handling devices*. Verlag Dr. Hut, 2016.

[196] P. Pellicori, E. Lukaschuk, A. Joseph, C. V. Bourantas, N. Sherwi, P. H. Loh, A. Rigby, J. Zhang, A. L. Clark, and J. G. F. Cleland. Clinical significance of left atrial ejection fraction measured by MRI in patients with suspected heart failure. *European Heart Journal*, 34:P1492.

[197] S. Perdoncin. Numerical validation of a variational multiscale-LES turbulence model for blood flows. Master's thesis, Politecnico di Milano, 2020.

[198] K. Perktold, E. Thurner, and T. Kenner. Flow and stress characteristics in rigid walled and compliant carotid artery bifurcation models. *Medical & biological engineering & computing*, 32(1):19–26, 1994.

[199] C. S. Peskin. Flow patterns around heart valves: a numerical method. *Journal of Computational Physics*, 10(2):252–271, 1972.

[200] C. S. Peskin. Fluid dynamics of the heart and its valves. In *APS Division of Fluid Dynamics Meeting Abstracts*, pages 3INV–02, 1997.

[201] C. S. Peskin. The immersed boundary method. *Acta numerica*, 11:479–517, 2002.

[202] R. Piersanti. *Mathematical and Numerical Modeling of Cardiac Fiber Generation and Electromechanical Function: Towards a Realistic Simulation of the Whole Heart*. PhD thesis, Politecnico di Milano, 2022.

[203] R. Piersanti, P. C. Africa, M. Fedele, C. Vergara, L. Dede', A. F. Corno, and A. Quarteroni. Modeling cardiac muscle fibers in ventricular and atrial electrophysiology simulations. *Computer Methods in Applied Mechanics and Engineering*, 373:113468, 2021.

[204] R. Piersanti, F. Regazzoni, M. Salvador, A. F. Corno, L. Dede', C. Vergara, and A. Quarteroni. 3D-0D closed-loop model for the simulation of cardiac biventricular electromechanics. *arXiv preprint arXiv:2108.01907*, 2021.

[205] S. B. Pope. *Turbulent flows*. IOP Publishing, 2001.

[206] A. Quarteroni. Diffusion-transport-reaction equations. In *Numerical Models for Differential Problems*, pages 291–338. Springer Milan, 2014. doi: 10.1007/978-88-470-5522-3_12. URL `https://doi.org/10.1007%2F978-88-470-5522-3_12`.

[207] A. Quarteroni. *Numerical Models for Differential Problems*, volume 16. Springer International Publishing, 2017.

[208] A. Quarteroni. *Numerical Models for Differential Problems*, volume 16. Springer, 2017.

[209] A. Quarteroni and A. Valli. *Numerical Approximation of Partial Differential Equations*. Springer–Verlag, Berlin and Heidelberg, 1994.

[210] A. Quarteroni, R. Sacco, and F. Saleri. *Numerical mathematics*, volume 37. Springer Science & Business Media, 2010.

[211] A. Quarteroni, A. Veneziani, and C. Vergara. Geometric multiscale modeling of the cardiovascular system, between theory and practice. *Computer Methods in Applied Mechanics and Engineering*, 302:193–252, 2016.

[212] A. Quarteroni, T. Lassila, S. Rossi, and R. Ruiz-Baier. Integrated heart. coupling multiscale and multiphysics models for the simulation of the cardiac function. *Computer Methods in Applied Mechanics and Engineering*, 314:345–407, 2017.

[213] A. Quarteroni, L. Dede', A. Manzoni, and C. Vergara. *Mathematical modelling of the human cardiovascular system: data, numerical approximation, clinical applications*, volume 33. Cambridge University Press, 2019.

[214] M. Raissi and G. E. Karniadakis. Hidden physics models: Machine learning of nonlinear partial differential equations. *Journal of Computational Physics*, 357: 125–141, 2018.

[215] M. Raissi, P. Perdikaris, and G. E. Karniadakis. Machine learning of linear differential equations using Gaussian processes. *Journal of Computational Physics*, 348:683–693, 2017.

[216] M. Raissi, P. Perdikaris, and G. E. Karniadakis. Physics-informed neural networks: A deep learning framework for solving forward and inverse problems involving nonlinear partial differential equations. *Journal of Computational Physics*, 378:686–707, 2019.

[217] T. C. Rebollo and B. M. Dia. A variational multi-scale method with spectral approximation of the sub-scales: Application to the 1D advection–diffusion equations. *Computer Methods in Applied Mechanics and Engineering*, 285:406–426, 2015. ISSN 0045-7825. doi: https://doi.org/10.1016/j.cma.2014.11.025. URL `https://www.sciencedirect.com/science/article/pii/S0045782514004514`.

[218] F. Regazzoni. *Mathematical modeling and Machine Learning for the numerical simulation of cardiac electromechanics*. PhD thesis, Politecnico di Milano, 2020.

[219] F. Regazzoni, L. Dede', and A. Quarteroni. Machine learning for fast and reliable solution of time-dependent differential equations. *Journal of Computational Physics*, 397:108852, 2019.

[220] F. Regazzoni, L. Dede', and A. Quarteroni. Machine learning of multiscale active force generation models for the efficient simulation of cardiac electromechanics. *Computer Methods in Applied Mechanics and Engineering*, 370:113268, 2020. ISSN 0045-7825. doi: https://doi.org/10.1016/j.cma.2020.113268. URL `https://www.sciencedirect.com/science/article/pii/S0045782520304539`.

[221] F. Regazzoni, L. Dede', and A. Quarteroni. Biophysically detailed mathematical models of multiscale cardiac active mechanics. *PLoS computational biology*, 16 (10):e1008294, 2020.

[222] F. Regazzoni, L. Dede', and A. Quarteroni. Machine learning of multiscale active force generation models for the efficient simulation of cardiac electromechanics. *Computer Methods in Applied Mechanics and Engineering*, 370:113268, 2020.

[223] F. Regazzoni, M. Salvador, P. C. Africa, M. Fedele, L. Dede', and A. Quarteroni. A cardiac electromechanics model coupled with a lumped parameters model for closed-loop blood circulation. part ii: numerical approximation. *arXiv preprint arXiv:2011.15051*, 2020.

[224] F. Regazzoni, M. Salvador, P. C. Africa, M. Fedele, L. Dede', and A. Quarteroni. A cardiac electromechanics model coupled with a lumped parameters model for closed-loop blood circulation. part i: model derivation. *arXiv preprint arXiv:2011.15040*, 2020.

[225] C. H. Roney, R. Bendikas, F. Pashakhanloo, C. Corrado, E. J. Vigmond, E. R.

McVeigh, N. A. Trayanova, and S. A. Niederer. Constructing a human atrial fibre atlas. *Annals of Biomedical Engineering*, 49:233–250.

[226] H.-G. Roos, M. Stynes, and L. Tobiska. *Numerical Methods for Singularly Perturbed Differential Equations*. Springer, Berlin and Heidelberg, 1996. doi: 10.1007/978-3-662-03206-0. URL https://doi.org/10.1007%2F978-3-662-03206-0.

[227] A. Rutkowski, David R. ad Glukhov and A. Roldán-Alzate. Abstract 15940: Wall shear stress and vorticity in atrial fibrillation, pulmonary hypertension, and normal atrial anatomy models. *Circulation*, 142:A15940.

[228] P. Sagaut. *Large eddy simulation for incompressible flows: an introduction*. Springer Science & Business Media, 2006.

[229] M. Salvador, L. Dede', and A. Quarteroni. An intergrid transfer operator using radial basis functions with application to cardiac electromechanics. *Computational Mechanics*, 66(2):491–511, 2020. doi: 10.1007/s00466-020-01861-x. URL https://doi.org/10.1007%2Fs00466-020-01861-x.

[230] S. Scarsoglio, A. Guala, C. Camporeale, and L. Ridolfi. Impact of atrial fibrillation on the cardiovascular system through a lumped-parameter approach. *Medical and Biological Engineering and Computing*, 52:905–920.

[231] K. E. Schober, V. L. Fuentes, J. D. Mcewan, and A. T. French. Pulmonary venous flow characteristics as assessed by transthoracic pulsed doppler echocardiography in normal dogs. *Veterinary Radiology & Ultrasound*, 39(1):33–41, 1998.

[232] C. Schwab. *p- and hp-FEM. Theory and Application to Solid and Fluid Mechanics*. Oxford University Press, 1998.

[233] G. Scovazzi, M. Christon, T. J. R. Hughes, and J. Shadid. Stabilized shock hydrodynamics: I. a Lagrangian method. *Computer Methods in Applied Mechanics and Engineering*, 196(4):923–966, 2007. ISSN 0045-7825. doi: https://doi.org/10.1016/j.cma.2006.08.008. URL https://www.sciencedirect.com/science/article/pii/S0045782506002374.

[234] G. Scovazzi, B. Carnes, X. Zeng, and S. Rossi. A simple, stable, and accurate linear tetrahedral finite element for transient, nearly, and fully incompressible solid dynamics: a dynamic variational multiscale approach. *International Journal for Numerical Methods in Engineering*, 106(10):799–839, 2016. doi: https://doi.org/10.1002/nme.5138. URL https://onlinelibrary.wiley.com/doi/abs/10.1002/nme.5138.

[235] J. H. Seo and R. Mittal. Effect of diastolic flow patterns on the function of the left ventricle. *Physics of Fluids*, 25(11):110801, 2013.

[236] J. H. Seo, V. Vedula, T. Abraham, A. C. Lardo, F. Dawoud, H. Luo, and R. Mit-

tal. Effect of the mitral valve on diastolic flow patterns. *Physics of fluids*, 26(12): 121901, 2014.

[237] Y. Shi and T. Korakianitis. Numerical simulation of cardiovascular dynamics with left heart failure and in-series pulsatile ventricular assist device. *Artificial organs*, 30(12):929–948, 2006.

[238] Y. Shi, P. Lawford, and R. Hose. Review of zero-D and 1-D models of blood flow in the cardiovascular system. *Biomedical engineering online*, 10(1):1–38, 2011.

[239] E. B. Shim, J. Y. Sah, and C. H. Youn. Mathematical modeling of cardiovascular system dynamics using a lumped parameter method. *The Japanese Journal of Physiology*, 54(6):545–553, 2004. doi: 10.2170/jjphysiol.54.545. URL `https://doi.org/10.2170%2Fjjphysiol.54.545`.

[240] M. Spartera, G. Pessoa Amorim, A. Stracquadanio, A. Von Ende, A. Fletcher, P. Manley, S. Neubauer, V. M. Ferreira, B. Casadei, A. T. Hess, and R. S. Wijesurendra. Left atrial 4D flow cardiovascular magnetic resonance: a reproducibility study in sinus rhythm and atrial fibrillation. *Journal of Cardiovascular Magnetic Resonance*, 23:29.

[241] P. D. Stein and H. N. Sabbah. Turbulent blood flow in the ascending aorta of humans with normal and diseased aortic valves. *Circulation research*, 39(1): 58–65, 1976.

[242] S. Stella, C. Vergara, L. Giovannacci, A. Quarteroni, and G. Prouse. Assessing the disturbed flow and the transition to turbulence in the arteriovenous fistula. *Journal of biomechanical engineering*, 141(10), 2019.

[243] S. Stewart, E. Paterson, G. Burgreen, P. Hariharan, M. Giarra, V. Reddy, S. Day, K. Manning, S. Deutsch, M. Berman, M. Myers, and R. Malinauskas. Assessment of CFD performance in simulations of an idealized medical device: Results of FDA's first computational interlaboratory study. *Cardiovascular Engineering and Technology*, 3:139–160, 2012.

[244] B. Su, L. Zhong, X.-K. Wang, J.-M. Zhang, R. San Tan, J. C. Allen, S. K. Tan, S. Kim, and H. L. Leo. Numerical simulation of patient-specific left ventricular model with both mitral and aortic valves by FSI approach. *Computer methods and programs in biomedicine*, 113(2):474–482, 2014.

[245] T. Sugimoto, R. Dulgheru, A. Bernard, F. Ilardi, L. Contu, K. Addetia, L. Caballero, N. Akhaladze, G. Athanassopoulos, D. Barone, M. Baroni, N. Cardim, A. Hagendorff, K. Hristova, T. Lopez, G. de la Morena, B. Popescu, M. Moonen, M. Penicka, T. Ozyigit, J. Rodrigo Carbonero, N. van de Veire, R. von Bardeleben, D. Vinereanu, J. Zamorano, Y. Go, M. Rosca, A. Calin, J. Magne, B. Cosyns, S. Marchetta, E. Donal, G. Habib, M. Galderisi, L. Badano, R. Lang, and P. Lancellotti. Echocardiographic reference ranges for normal left ventricular

2D strain: results from the EACVI NORRE study. *European Heart Journal-Cardiovascular Imaging*, 18(8):833–840, 2017.

[246] S. M. Szilágyi, L. Szilágyi, and Z. Benyó. A patient specific electro-mechanical model of the heart. *Computer methods and programs in biomedicine*, 101(2): 183–200, 2011.

[247] A. Tagliabue, L. Dedé, and A. Quarteroni. Fluid dynamics of an idealized left ventricle: the extended nitsche's method for the treatment of heart valves as mixed time varying boundary conditions. *International Journal for Numerical Methods in Fluids*, 85(3):135–164, 2017.

[248] A. Tagliabue, L. Dede', and A. Quarteroni. Complex blood flow patterns in an idealized left ventricle: A numerical study. *Chaos: An Interdisciplinary Journal of Nonlinear Science*, 27(9):093939, 2017.

[249] A. Tagliabue, L. Dede', and A. Quarteroni. Fluid dynamics of an idealized left ventricle: the extended Nitsche's method for the treatment of heart valves as mixed time varying boundary conditions. *International Journal for Numerical Methods in Fluids*, 85(3):135–164, 2017.

[250] T. Tassi. Stabilization methods for transport dominated problems enhanced by artificial neural networks: towards LES turbulence modelling. Master's thesis, Politecnico di Milano, 2021.

[251] T. Tassi, A. Zingaro, and L. Dede'. A Machine Learning approach to enhance the SUPG stabilization method for advection-dominated differential problems. *MOX Report*, 58, 2021.

[252] C. A. Taylor, T. J. Hughes, and C. K. Zarins. Finite element analysis of pulsatile flow in the abdominal aorta under resting and exercise conditions. *ASME-PUBLICATIONS-BED*, 33:81–82, 1996.

[253] C. A. Taylor, T. J. Hughes, and C. K. Zarins. Finite element modeling of blood flow in arteries. *Computer Methods in Applied Mechanics and Engineering*, 158 (1-2):155–196, 1998.

[254] G. Taylor and A. Green. Mechanism of the production of small eddies from large ones. *Proceedings of the Royal Society London*, 1937. doi: http://doi.org/10.1098/rspa.1937.0036.

[255] K. H. Ten Tusscher and A. V. Panfilov. Alternans and spiral breakup in a human ventricular tissue model. *American Journal of Physiology-Heart and Circulatory Physiology*, 291(3):H1088–H1100, 2006.

[256] T. Tezduyar and S. Sathe. Stabilization parameters in SUPG and PSPG formulations. *Journal of computational and applied mechanics*, 4(1):71–88, 2003.

[257] T. E. Tezduyar and Y. Osawa. Finite element stabilization parameters computed from element matrices and vectors. *Computer Methods in Applied Mechanics and Engineering*, 190(3-4):411–430, 2000.

[258] A. This. *Image/model fusion for the quantification of mitral regurgitation severity.* PhD thesis, Sorbonne université, 2019.

[259] A. This, L. Boilevin-Kayl, M. A. Fernández, and J.-F. Gerbeau. Augmented resistive immersed surfaces valve model for the simulation of cardiac hemodynamics with isovolumetric phases. *International Journal for Numerical Methods in Biomedical Engineering*, 36(3), sep 2019. doi: 10.1002/cnm.3223. URL https://doi.org/10.1002%2Fcnm.3223.

[260] A. This, H. G. Morales, O. Bonnefous, M. A. Fernández, and J.-F. Gerbeau. A pipeline for image based intracardiac CFD modeling and application to the evaluation of the PISA method. *Computer Methods in Applied Mechanics and Engineering*, 358:112627, jan 2020. doi: 10.1016/j.cma.2019.112627. URL https://doi.org/10.1016%2Fj.cma.2019.112627.

[261] P. Tripathi. Pathophysiological mechanism behind diabetic cardiovascular disorders. *International Journal of Current Research*, 6(1):4426–4436, 2014.

[262] M. Umeki. Numerical simulation of plane Poiseuille turbulence. *Fluid dynamics research*, 13(2):67, 1994.

[263] F. N. Van de Vosse and N. Stergiopulos. Pulse wave propagation in the arterial tree. *Annual Review of Fluid Mechanics*, 43:467–499, 2011.

[264] R. J. van der Geest and P. Garg. Advanced analysis techniques for intra-cardiac flow evaluation from 4D flow MRI. *Current Radiology Reports*, 4(7), 2016. doi: 10.1007/s40134-016-0167-7. URL https://doi.org/10.1007%2Fs40134-016-0167-7.

[265] R. van Loon, P. D. Anderson, and F. N. van de Vosse. A fluid-structure interaction method with solid-rigid contact for heart valve dynamics. *Journal of Computational Physics*, 217(2):806–823, 2006.

[266] V. Vedula, R. George, L. Younes, and R. Mittal. Hemodynamics in the left atrium and its effect on ventricular flow patterns. *Journal of biomechanical engineering*, 137(11), 2015.

[267] A. Veneziani and C. Vergara. Flow rate defective boundary conditions in haemodynamics simulations. *International Journal for Numerical Methods in Fluids*, 47(8-9):803–816, 2005.

[268] C. Vergara, D. Le Van, M. Quadrio, L. Formaggia, and M. Domanin. Large eddy simulations of blood dynamics in abdominal aortic aneurysms. *Medical engineering & physics*, 47:38–46, 2017.

[269] A. Verkaik, A. Bogaerds, F. Storti, and F. Van De Vosse. A coupled overlapping domain method for the computation of transitional flow through artificial heart valves. In *ASME 2012 Summer Bioengineering Conference (SBC 2012)*, pages 217–218. American Society of Mechanical Engineers, 2012.

[270] J. A. Viecelli. A method for including arbitrary external boundaries in the MAC incompressible fluid computing technique. *Journal of Computational Physics*, 4 (4):543–551, 1969.

[271] I. E. Vignon-Clementel, C. Figueroa, K. Jansen, and C. Taylor. Outflow boundary conditions for 3D simulations of non-periodic blood flow and pressure fields in deformable arteries. *Computer methods in biomechanics and biomedical engineering*, 13(5):625–640, 2010.

[272] F. Viola, V. Meschini, and R. Verzicco. Fluid-structure-electrophysiology interaction (FSEI) in the left-heart: a multi-way coupled computational model. *European Journal of Mechanics-B/Fluids*, 79:212–232, 2020.

[273] F. Viola, V. Meschini, and R. Verzicco. Effects of stenotic aortic valve on the left heart hemodynamics: a fluid-structure-electrophysiology approach. *arXiv preprint arXiv:2103.14680*, 2021.

[274] F. Viola, V. Spandan, V. Meschini, J. Romero, M. Fatica, M. D. de Tullio, and R. Verzicco. FSEI-GPU: GPU accelerated simulations of the fluid-structure-electrophysiology interaction in the left heart. *arXiv preprint arXiv:2103.15187*, 2021.

[275] P. Virtanen, R. Gommers, T. Oliphant, M. Haberland, T. Reddy, D. Cournapeau, E. Burovski, P. Peterson, W. Weckesser, J. Bright, S. van der Walt, M. Brett, J. Wilson, K. Millman, N. Mayorov, A. Nelson, E. Jones, R. Kern, E. Larson, C. Carey, I. Polat, Y. Feng, E. Moore, J. VanderPlas, D. Laxalde, J. Perktold, R. Cimrman, I. Henriksen, E. Quintero, C. Harris, A. Archibald, A. Ribeiro, F. Pedregosa, P. van Mulbregt, and SciPy 1.0 Contributors. SciPy 1.0: Fundamental Algorithms for Scientific Computing in Python. *Nature Methods*, 17: 261–272, 2020. doi: 10.1038/s41592-019-0686-2.

[276] Y. Wang, Y. Qiao, Y. Mao, C. Jiang, J. Fan, and K. Luo. Numerical prediction of thrombosis risk in left atrium under atrial fibrillation. *Mathematical Biosciences and Engineering*, 17:2348–2360.

[277] H. Watanabe, S. Sugiura, H. Kafuku, and T. Hisada. Multiphysics simulation of left ventricular filling dynamics using fluid-structure interaction finite element method. *Biophysical journal*, 87(3):2074–2085, 2004.

[278] C. Wiggers. *Circulation in Health & Diseases*. Lea & Febiger, Philadelphia, 1915.

[279] D. C. Wilcox. *Turbulence modeling for CFD*, volume 2. DCW industries La Canada, CA, 1998.

[280] H. Wiputra, C. Q. Lai, G. L. Lim, J. J. W. Heng, L. Guo, S. M. Soomar, H. L. Leo, A. Biwas, C. N. Z. Mattar, and C. H. Yap. Fluid mechanics of human fetal right ventricles from image-based computational fluid dynamics using 4D clinical ultrasound scans. *American Journal of Physiology-Heart and Circulatory Physiology*, 311(6):H1498–H1508, 2016.

[281] C. Xie, J. Wang, K. Li, and C. Ma. Artificial neural network approach to large-eddy simulation of compressible isotropic turbulence. *Physical Review E*, 99(5): 053113, 2019.

[282] C. Xie, J. Wang, and E. Weinan. Modeling subgrid-scale forces by spatial artificial neural networks in large eddy simulation of turbulence. *Physical Review Fluids*, 5(5):054606, 2020.

[283] L. Yang, S. Badia, and R. Codina. A pseudo-compressible variational multiscale solver for turbulent incompressible flows. *Computational Mechanics*, 58: 1051–1069, 2016. doi: 10.1007/s00466-016-1332-9.

[284] B. Yegnanarayana. *Artificial neural networks*. PHI Learning Pvt. Ltd., 2009.

[285] O. Yousefian, S. Carlson, A. Keibel, R. Doshi, and L. Saxon. Effect of atrial fibrillation on pulmonary artery pressures in ambulatory heart failure patients. *Journal of Cardiac Failure*, 23:S61.

[286] M. Zancanaro, M. Mrosek, G. Stabile, C. Othmer, and G. Rozza. Hybrid neural network reduced order modelling for turbulent flows with geometric parameters. *arXiv preprint arXiv:2107.09591*, 2021.

[287] J. Zhang, Z. Chen, B. P. Griffith, and Z. J. Wu. Computational characterization of flow and blood damage potential of the new maglev CH-VAD pump versus the HVAD and HeartMate II pumps. *The International journal of artificial organs*, 43(10):653–662, 2020.

[288] S. Zhao, P. Papathanasopoulou, Q. Long, I. Marshall, and X. Xu. Comparative study of magnetic resonance imaging and image-based computational fluid dynamics for quantification of pulsatile flow in a carotid bifurcation phantom. *Annals of Biomedical Engineering*, 31(8):962–971, 2003.

[289] X. Zheng, J. Seo, V. Vedula, T. Abraham, and R. Mittal. Computational modeling and analysis of intracardiac flows in simple models of the left ventricle. *European Journal of Mechanics-B/Fluids*, 35:31–39, 2012.

[290] Z. Zhou, G. He, S. Wang, and G. Jin. Subgrid-scale model for large-eddy simulation of isotropic turbulent flows using an artificial neural network. *Computers & Fluids*, 195:104319, 2019.

[291] A. Zingaro, L. Dede', F. Menghini, and A. Quarteroni. Hemodynamics of the

heart's left atrium based on a variational multiscale-LES numerical method. *European Journal of Mechanics-B/Fluids*, 89:380–400, 2021.

[292] A. Zingaro, I. Fumagalli, L. Dede', M. Fedele, P. C. Africa, A. F. Corno, and A. Quarteroni. A multiscale CFD model of blood flow in the human left heart coupled with a lumped parameter model of the cardiovascular system. *arXiv preprint arXiv:2110.02114*, 2021.

[293] V. Zmijanovic, S. Mendez, V. Moureau, and F. Nicoud. About the numerical robustness of biomedical benchmark cases: Interlaboratory FDA's idealized medical device. *International Journal for Numerical Methods in Biomedical Engineering*, 33, 03 2016. doi: 10.1002/cnm.2789.

Acronyms and Abbreviations

AA	Ascending Aorta
AF	Atrial Fibrillation
ALE	Arbitrary Lagrangian Eulerian
ANN	Artificial Neural Network
aSIMPLE	Approximated Semi-Implicit Method for Pressure Linked Equations
AV	Aortic Valve
BC	Boundary Condition
BDF	Backward Differentiation Formula
BiV	Biventricular
CMR	Cardiac Magnetic Resonance
CFD	Computational Fluid Dynamics
DNS	Direct Numerical Simulation
DOF	Degree Of Freedom
DPM	Discrete Parcel Method
DTMRI	Diffusion Tensor Magnetic Resonance Imaging
EDV	End Diastolic Volume
EJ	Ejection Fraction
EM	Electromechanics
ESV	End Systolic Volume
FE	Finite Element
FD	Fictitious Domain
FDA	Food and Drug Administration
FS	Flow Stasis
FSI	Fluid-Structure-Interaction
GMRES	Generalized Minimal Residual
IB	Immersed Boundary
L-BFGS-B	Limited memory Broyden-Fletche–Goldfarb-Shanno with Bound constraints
LA	Left Atrium
LAA	Left Atrium Appendage
LAAEF	Left Atrium Appendage Ejection Fraction
LAEF	Left Atrium Ejection Fraction
LES	Large Eddy Simulation

LH	Left Heart
LV	Left Ventricle
LIC	Line Integral Convolution
ML	Machine Learning
MRI	Magnetic Resonance Imaging
MV	Mitral Valve
NS	Navier-Stokes
ODE	Ordinary Differential Equation
OSI	Oscillatory Shear Index
PDE	Partial Differential Equation
PH	Physiological
PINN	Physics Informed Neural Network
PISA	Proximal Isovelocity Surface Area
PT	Pulmonary Trunk
PV	Pulmonary Valve
RA	Right Atrium
RANS	Reynolds-Averaged Navier-Stokes
RF	Regurgitant Fraction
RH	Right Heart
RIIS	Resistive Immersed Implicit Surface
RIS	Resistive Immersed Surface
RRT	Relative Residence Time
RTT	Reynolds Transport Theorem
RV	Right Ventricle
RVol	Regurgitant Volume
SGD	Stochastic Gradient Descent
SV	Stroke Volume
SUPG	Streamline Upwind Petrov Galerkin
TAWSS	Time-Averaged Wall Shear Stress
TGV	Taylor Green Vortex
TV	Tricuspid Valve
VMS	Variational Multiscale
WSS	Wall Shear Stress

List of Figures

List of Tables